A Michelson-Morley Test of Lorentz Invariance Using a Rotating Optical Cavity

DISSERTATION

zur Erlangung des akademischen Grades
doctor rerum naturalium
(Dr. rer. nat.)
im Fach Physik

eingereicht an der
Mathematisch-Naturwissenschaftlichen Fakultät I
Humboldt-Universität zu Berlin

von
Herr Dipl.-Phys. Sven Herrmann
geboren am 06.02.1975 in Spaichingen

Präsident der Humboldt-Universität zu Berlin:
Prof. Dr. Dr. h.c. Christoph Markschies

Dekan der Mathematisch-Naturwissenschaftlichen Fakultät I:
Prof. Dr. Christian Limberg

Gutachter:

1. Prof. Achim Peters, PhD
2. Prof. Dr. Fritz Riehle
3. Prof. John L. Hall

eingereicht am: 24. Oktober 2006
Tag der mündlichen Prüfung: 12. März 2007

Abstract

This thesis presents a modern Michelson-Morley experiment, which provides improved limits on test parameters that model a violation of Lorentz invariance in electrodynamics. The measurement thereby sets an upper limit on an anisotropy of the speed of light at a level of $\Delta c/c \sim 10^{-16}$.

The experiment compares the resonance frequencies of two optical high-finesse cavities, one of them continuously rotating on a turntable. To read out their resonance frequencies, two Nd:YAG lasers are frequency-stabilized to these cavities. On the timescale of a turntable rotation ($\sim 45\,\mathrm{s}$), a relative frequency stability of $\sim 1 \times 10^{-14}$ is achieved, limited by thermal noise of the cavity mirrors.

An anisotropic propagation of light would cause a modulation of the rotating cavity's resonance at twice the turntable rotation rate, additionally modulated by Earth's rotation and orbital revolution. Two test theories are applied here, to derive such an anisotropy signal as a consequence of a violation of Lorentz invariance. These test theories are an extension of the standard-model of particle physics, based on work by V.A. Kostelecký *et al.*, and a kinematic formalism by H.P. Robertson, R. Mansouri and R.U. Sexl.

Previously as well as simultaneously performed Michelson-Morley experiments were severely affected by systematic effects arising from the rotation of the setup on a turntable. Several systematic effects have been identified within the present experiment as well. These systematics are described in detail, together with the measures that have been taken to suppress systematic signal amplitudes below $1\,\mathrm{Hz}$. This is a reduction by up to a factor of 100 as compared to preceding experiments.

During the course of one year, 27 frequency comparisons of the rotating with the non-rotating cavity have been performed, each spanning $24\,\mathrm{h}$ to $100\,\mathrm{h}$ of continuous measurement. In total, the measurement includes $\sim 10^5$ rotations. An analysis of this data within the two test models is presented and limits on the relevant test parameters are deduced. These limits restrict an anisotropy of the speed of light at a level of 10^{-16}, which is a factor of ten more stringent as compared to results of previous such measurements.

Further improved limits on a violation of Lorentz invariance might be ob-

tained within the near future. An improved setup with new cavities, that exhibit lower thermal noise, and first data from this setup are already presented here. The relative frequency stability has been enhanced to 2×10^{-15} at the timescale of a turntable rotation. This opens the door to another order of magnitude improvement of the experiment's sensitivity within a long-term measurement aiming for the $\Delta c/c \sim 10^{-17}$ level of accuracy.

Zusammenfassung

Diese Arbeit präsentiert ein modernes Michelson-Morley Experiment, welches genauere Grenzwerte für Testparameter liefert, die eine hypothetische Verletzung der Lorentzinvarianz modellieren. Die Messung setzt einen oberen Grenzwert für eine Anisotropie der Lichtgeschwindigkeit im Bereich von $\Delta c/c \sim 10^{-16}$.

Das hier beschriebene Experiment vergleicht die Frequenzen zweier optischer Hoch-Finesse Resonatoren, wobei einer dieser Resonatoren kontinuierlich auf einem Drehtisch rotiert. Um die Eigenfrequenzen der Resonatoren abzufragen, werden die Frequenzen zweier Nd:YAG-Laser aktiv auf die Resonatoren stabilisiert. Die dabei erreichte relative Frequenzstabilität auf der Zeitskala einer Tischdrehung ($\sim 45\,\mathrm{s}$) liegt bei $\sim 1 \times 10^{-14}$, limitiert durch das thermische Rauschen der Resonatorspiegel.

Durch eine Anisotropie der Lichtgeschwindigkeit würde sich eine Modulation der Eigenfrequenz des auf dem Drehtisch rotierenden Resonators ergeben, zusätzlich moduliert durch die Erddrehung und den Erdorbit. Um ein derartiges Signal im Rahmen einer Verletzung der Lorentzinvarianz zu modellieren, wurden zwei verschiedene Testtheorien herangezogen. Diese sind eine die Lorentzinvarianz explizit verletzende Erweiterung des Standardmodells der Teilchenphysik, basierend auf Arbeiten von V.A. Kostelecký *et al.*, so wie ein kinematischer Formalismus, welcher auf Arbeiten von H.P. Robertson sowie R. Mansouri und R.U. Sexl fußt.

Sowohl vorangegangene als auch parallel durchgeführte derartige Experimente waren in ihrer Genauigkeit durch systematische Effekte limitiert, die mit der Drehung des Experiments auf einem Drehtisch einhergehen. Verschiedene derartige systematische Effekte wurden auch in diesem Experiment identifiziert. Diese systematischen Effekte und die Unterdrückung entsprechender Signalamplituden auf unter $1\,\mathrm{Hz}$ sind im Detail dargestellt. Im Vergleich zu vorhergehenden Messungen konnten derartige Effekte um bis zu einem Faktor 100 reduziert werden.

Insgesamt wurden 27 Datensätze eines Frequenzvergleichs des rotierenden mit dem nicht rotierenden Resonator aufgenommen, welche sich jeweils über $24\,\mathrm{h}$ bis $100\,\mathrm{h}$ erstrecken. Dabei gingen mehr als 10^5 Tischumdrehungen in die Gesamtmessung ein.

Es wird eine Analyse dieser Daten im Rahmen beider Testtheorien präsentiert, und Grenzwerte auf die relevanten Parameter werden bestimmt. Diese Grenzwerte schränken eine Anisotropie der Lichtgeschwindigkeit im Bereich von 10^{-16} ein, d.h. etwa 10 mal genauer als die Ergebnisse vorangegangener Messungen.

Auf dieser Grundlage sollte sich in nächster Zukunft eine weitere deutliche Steigerung der Messgenauigkeit erzielen lassen. Der Aufbau eines verbesserten derartigen Experiments, welches neue Resonatoren mit geringerem thermischen Rauschen zum Einsatz bringt, sowie erste verbesserte Resultate werden hier bereits präsentiert. Die relative Frequenzstabilität über eine Tischdrehung gemittelt konnte auf 2×10^{-15} verbessert werden. Damit steht der Weg offen für eine weitere Langzeit-Messung, welche die Grenze für eine Anisotropie der Lichtgeschwindigkeit bis in den Bereich von $\Delta c/c \sim 10^{-17}$ drücken wird.

Contents

x

List of Figures

xiii

List of Tables

Chapter 1

Introduction

1.1 Putting Lorentz invariance to the test

Lorentz invariance has served as a guiding principle in constructing fundamental physics theory, ever since its validity throughout all of physics has been revealed by Einstein's pioneering work on special relativity in 1905 [Ein05]. The principle of special relativity formulated there gives an operational definition of Lorentz invariance. It basically states that the outcome of an experiment does not depend on the uniform velocity and orientation of the inertial reference frame it is referred to.

Today, Lorentz invariance is a cornerstone of quantum field theory, which has been tested experimentally to astonishing precision. Nevertheless, experimental physics continues to put Lorentz invariance to the test at ever increasing precision. These efforts are motivated in the first place by the fundamental importance of Lorentz invariance, which obliges experimental physics to reconsider the established test experiments, while technical progress allows for more and more sensitive measurements. In addition, there have indeed been theoretical suggestions that Lorentz invariance might not be an exact symmetry at all energies. This possibility has been considered by several theoreticians working to formulate a fundamental theory beyond the standard-model of particle physics. The latter fails to provide a quantum description of gravity and many different approaches for a unifying theory have been pursued so far. Among them are string theories [Kak99] or loop quantum gravity [NPZ05] and the fate of Lorentz symmetry in these models has been posed to discussion by some authors. For instance, it has been shown that a spontaneous breaking of Lorentz invariance might occur in string theories even with the general dynamics of the theory preserving Lorentz symmetry [KS89]. Also, for loop quantum gravity the issue of a pos-

sible Lorentz violation has been raised [AMU02, GP99a]. Other models, such as noncommutative field theory [DN01] implicitly incorporate a violation of Lorentz invariance [CHK$^+$01]. Given the possibility of such a violation at presumably rather high energies the question remains, whether it extends into the low-energy four dimensional world. So far only few qualitative and almost no quantitative predictions exist. Thus, a broad range of test experiments are currently pursued, all aiming to detect some minuscule low-energy remnants of a hypothetical Lorentz violation. The revelation of only a tiny such signal might provide important input to the formulation of a quantum gravity theory.

Among the most sensitive tests for Lorentz invariance are a variety of clock-comparison experiments, applying clocks of different constitution and orientation and moving at a velocity $\vec{v}$, e. g. due to Earth's rotation and orbital revolution. Such comparisons have been performed applying many different clocks e. g. Hydrogen masers [PHM$^+$01, HPM$^+$03], Xenon and Helium masers [CBR$^+$04, BSW$^+$00], atomic fountain clocks [WCBC06], and frequency standards based on optical [BMP$^+$02, MHB$^+$03a] or microwave cavities [WBC$^+$04, WTB$^+$04]. Further test experiments have been performed on high energy particles [HMW05, CG99], on spin polarized matter [HNL03, BK00] and on charged particles either trapped in a Penning trap [MID99, GKH$^+$99, BKR99] or within a storage ring [SKE$^+$03, Lan05]. Finally, numerous validations of Lorentz invariance are also inferred from astronomical observations [Alt06, EMN00, KM01], provided with extraordinary sensitivities due to the enormous length and timescales accessible there.

1.2 Modern Michelson-Morley experiments

This thesis now presents another clock-comparison test of Lorentz invariance which is often referred to as a modern Michelson-Morley experiment. In this sense, it can be viewed as a descendant of the well known experiment performed by Albert A. Michelson and Edward W. Morley in 1887 [MM87]. Using a rotatable Michelson interferometer, they tried to provide evidence for an ether medium, which they believed to cause an anisotropic light propagation in the two interferometer arms. However, no such effect could be found. Still, their experiment subsequently gained reputation as one of special relativity's most prominent confirmations. Numerous repetitions of this experiment have been performed so far and have increased the sensitivity to an anisotropy of the speed of light by six orders of magnitude, corresponding to an upper limit on the order of $\Delta c/c \sim 10^{-15}$ (see Figure 1.1).

A schematic of the principle setup of a modern Michelson-Morley experiment
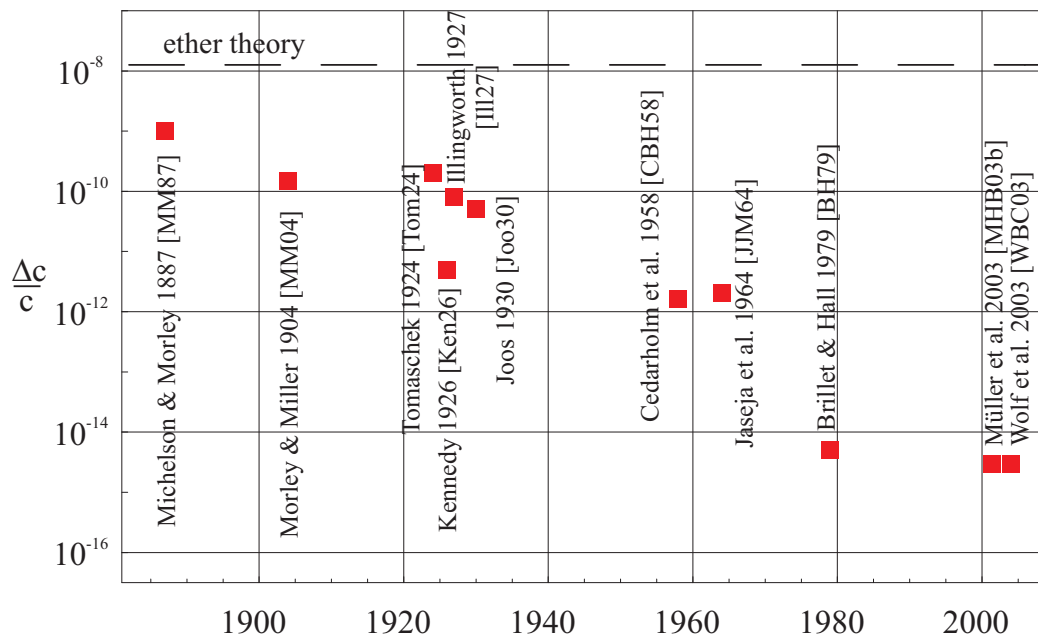
Figure 1.1: *Improvements of the Michelson-Morley experiment since 1887. The last classic interferometer experiment is the one performed by Joos [Joo30] in 1930. Later experiments achieved higher sensitivity applying rotating electromagnetic cavities.*

is shown in Figure 1.2 to the right. This simplified scheme especially points out the evolution of the modern version of the experiment from the original. Modern Michelson-Morley experiments typically apply high-quality electromagnetic resonators with an eigenfrequency that depends on the speed of light c, e.g. $\nu_C = mc/2L$ for a linear optical Fabry-Pérot cavity of length L (with $m \, \epsilon \, \mathbb{N}$). Using lasers this frequency can be read out at a relative accuracy of down to one part in 10^{15}. If the cavity is rotated, an anisotropy of the speed of light would cause a modulation of its frequency at twice the rotation rate. Thus, a comparison of the frequencies of two rotating cavities, as depicted in Figure 1.2, should reveal such an anisotropy within the measurement of $\Delta\nu = \nu_{C,x} - \nu_{C,y}$.

A landmark experiment of this kind was performed by Alain Brillet and John L. Hall in 1979 [BH79]. It provided a tremendous increase in measurement sensitivity as compared to earlier experiments. They compared a methane stabilized laser to the frequency of a cavity rotating on a turntable once in $10\,\mathrm{s}$. After that more than twenty years passed until further experiments of the Michelson-Morley type were resumed again. These new attempts came along with a general revival of test experiments for Lorentz invariance, which was strongly inspired by the advent of a new test formalism, that models a possible violation of Lorentz invariance as an extension to the standard-model of particle physics [CK98]. Initially, these recent Michelson-Morley experiments [LNW$^+$03, MHB$^+$03a, WBC$^+$03] lacked the possibility of active rotation on a turntable which forced them to rely on Earth's rotation instead. Thus, they had to apply cryogenically cooled resonators that feature a high long-term stability. Nonetheless, they succeeded to achieve an improvement in measurement sensitivity as compared to the experiment by Brillet and Hall.

Now, the present experiment for the first time since Brillet and Hall applies a continuously rotating setup again. As compared to measurements relying on Earth's rotation, actively rotating the setup allows to match the rotation rate to the timescale of optimal frequency stability and to integrate over a significantly enlarged number of rotations. However, previous actively rotating experiments have been severely affected by systematic effects arising from turntable rotation. Therefore, besides high frequency stability the suppression of systematic effects is the most important issue within such an experiment.

The basic scheme of the present setup is depicted in Figure 1.3. It is similar to the one of [BH79], in that only one rotating resonator (R1) is applied. The stationary frequency reference is provided by a second cavity (R2), and a measurement of $\Delta\nu = \nu_{\mathrm{R1}} - \nu_{\mathrm{R2}}$ is performed while the cavity R1 rotates on a turntable. Consequently, the fundamental signal that indicates a violation
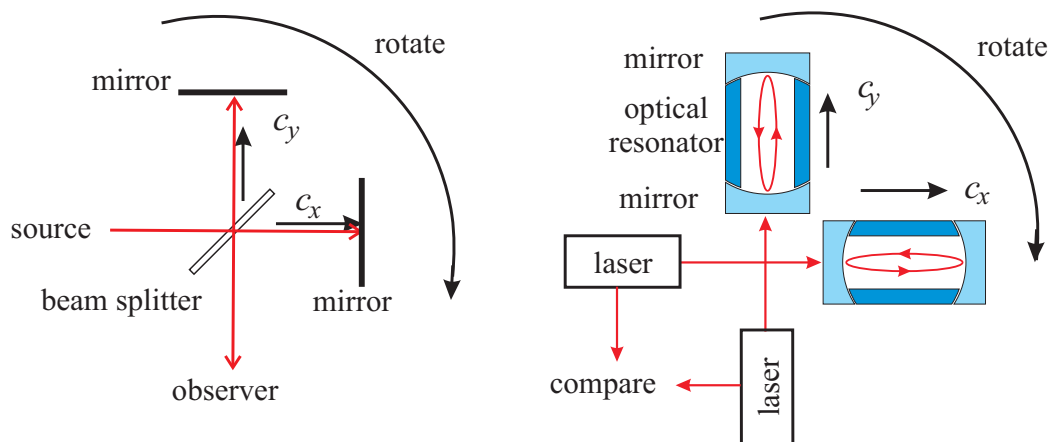
Figure 1.2: *Principle of classic and modern Michelson-Morley experiments. The classic experiments (left) search for a shift in the interference pattern (intensity measurement) while the experiment rotates. Modern optical experiments (right) perform a direct frequency measurement between lasers stabilized to rotating electromagnetic cavities ($\nu_R \sim c/2L$ for a linear cavity). An anisotropy of light propagation would then lead to an oscillation of the difference frequency at twice the rotation frequency.*

of Lorentz invariance is expected at the $2\omega_{\text{rot}}$ Fourier component. Within a long-term measurement, Earth's rotation and orbital motion further shift the anisotropy signal to the sidereal sidebands of this $2\omega_{\text{rot}}$ component. The specific form of an anisotropy signal arising from a violation of Lorentz invariance, can be modeled according to certain test models for a violation of Lorentz invariance. Two such test models are applied for the analysis of the present experiment. The first is an extension of the standard-model of particle physics (SME = standard-model extension), which incorporates effects from a violation of Lorentz invariance [CK98]. The second is a kinematic formalism that has been formulated by H.P. Robertson as early as 1949 [Rob49] and has been extended by R. Mansouri and R.U. Sexl [MS76] later on. It is denoted the Robertson-Mansouri-Sexl (RMS) formalism here. Both test models provide parameters which can be restricted by an analysis of the measurement data. The experiment thereby aims to significantly improve the present level of accuracy achieved by the recent experiments which relied on Earth's rotation only.
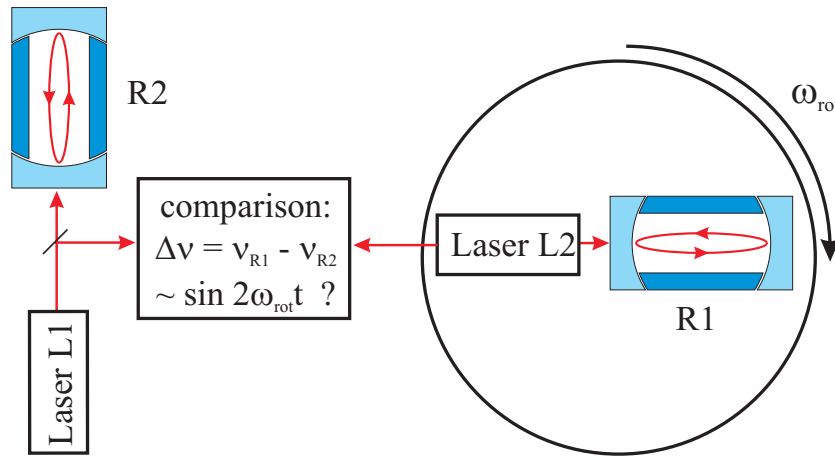
Figure 1.3: *Basic setup of this experiment comparing the resonance frequency of a single rotating cavity to that of a stationary cavity.*

1.3   Outline of this thesis

In **Chapter 2** the search for a violation of Lorentz invariance is motivated in more detail and the two test theories applied for an evaluation of the experiment are introduced: The standard-model extension and the formalism of Robertson, Mansouri and Sexl.

According to these test theories, in **Chapter 3** the specific signals of Lorentz violation within the present experiment are derived.

Chapter 4 then describes the experimental setup and discusses the limitations on the achieved frequency stability. The special precautions taken in order to enable an active rotation of the complete setup on a turntable are also addressed in detail.

In **Chapter 5** special emphasis is put to systematic effects which arise from active rotation. The prevention of such effects is essential for the performance of the measurement and a large part of the experimental work was spent on this issue.

Chapter 6 gives an analysis of the measured data according to the adopted test models and deduces limits on the relevant test parameters. It concludes with an evaluation of these results and a comparison to previous and concurrent work.

Finally, in **Chapter 7** a new setup aiming for a further improvement of the achieved sensitivity is presented. This setup has already provided first improved measurements from which preliminary results on test parameters could be obtained.

Chapter 2

Test theories for a violation of Lorentz invariance

Numerous experiments and even every-day applications like the Global Positioning System verify Lorentz invariance. However, it is often not trivial to separate consequences of Lorentz invariance from other aspects involved in a particular measurement. Consider, for instance, the successful prediction of the lepton g factor: to what extent does this verify Lorentz invariance as opposed to the validity of the underlying quantization procedures?

Therefore, a test theory has to be applied, which models a violation of Lorentz invariance and links it to observable quantities, ideally in an unambiguous way. Such a test theory allows to judge the sensitivity of a specific experiment to Lorentz violation and to distinguish it from experiments testing different aspects.

Two commonly adopted test theories for Lorentz violation are applied in the present work. The first is an extension of the standard-model of particle physics, referred to as standard-model extension (SME) [CK98]. The second is a kinematic formalism by H.P. Robertson [Rob49], later extended by R. Mansouri and R.U. Sexl [MS76], referred to as Robertson-Mansouri-Sexl formalism (RMS). Both formalisms provide test parameters that can be bounded specifically by a Michelson-Morley experiment. In this chapter, an introduction into these formalisms is given, as far as necessary for an analysis of the experiment.

2.1 Possible origins of a violation of Lorentz invariance

The idea of a violation of Lorentz invariance has been put forward by theories beyond the standard-model, aiming to formulate a quantum gravity theory. Most of these theories, such as string theories or loop quantum gravity, preserve Lorentz symmetry or a higher dimensional Poincaré symmetry in the first place. Nonetheless, some of these models suggest the possibility of a breaking of Lorentz symmetry at some energy scale. In that case, Lorentz symmetry would have to be considered an approximate low-energy phenomenon. Consequently, minuscule Lorentz violating effects might be detected as low-energy remnants within test experiments for Lorentz violation.

Possible Magnitude

The relevant energy scale of Lorentz violation within a quantum gravity theory is usually assumed to be the Planck energy $E_{\text{Pl}} \sim 10^{19}$ GeV. Accordingly, effects from Lorentz violation in a laboratory experiment at energy scale E can be estimated to be suppressed by factors $\mathcal{O}(E/E_{\text{Pl}})$. Within experiments that apply photons of $E \sim 1$ eV, this is on the order of 10^{-28}, which is currently far beyond the sensitivity of test experiments as the one described here. However, there is a large uncertainty with respect to both, the actual energy scales that have to be applied, and the scaling of the suppression of Lorentz violation effects. Models such as [ADD99] discuss significantly lower energy scales for a quantum gravity theory, and [Vol01] consider the possibility of a reentrance of Lorentz violation at very low energy scale. Consequently, also the improvement of a measurement sensitive at a level of 10^{-15}, such as the Michelson-Morley experiment described here, by one or two orders of magnitude appears to be worthwhile within this context.

String theories

The theory of the basic bosonic string [Wit86] requires a 26-dimensional space-time for consistency and consequently applies a multidimensional Poincaré symmetry. However, the transition to the low-energy limit, which involves compactification of the extra dimensions resulting in a four-dimensional flat space-time, is not yet understood. Generally it is believed that 26-dimensional Poincaré symmetry transforms into exact Lorentz symmetry in flat space-time. However, the question has been raised, whether along this transition a breakdown of the symmetry takes place, leaving only an approximate Lorentz symmetry in four dimensions.

In [KS89] V.A. Kostelecký and S. Samuel have investigated whether a spontaneous breaking of Lorentz symmetry could occur in string theories. Indeed, they presented a potential mechanism for this breaking. With respect to symmetry breaking for string theories, the same concept applies as for particle field theories. There, spontaneous breaking of a symmetry of the Lagrangian occurs, if the ground state of a particle field does not obey this symmetry. This is the case for an unstable vacuum, where some of the fields acquire non-zero expectation values. In [KS89] a mechanism for such breaking is presented, that is ruled out within particle physics due to gauge invariance and renormalizability, but might apply to string or superstring theories.

Loop quantum gravity

The canonical quantization procedure for gravity fails due to non-renormalizable divergencies within a perturbation series in Newton's constant. One attempt to circumvent this is followed in loop quantum gravity (LQG) [NPZ05], which aims to quantize gravity non-perturbatively. The propagation of photons in a semiclassical background based on a LQG approach is considered in [AMU02]. They present modified effective low-energy Maxwell equations that are not Lorentz covariant. From these equations dispersion relations can be deduced, that involve Lorentz violating corrections. Similar dispersion relations have also been discussed by [GP99a], starting from LQG, and by [EMN00], based on a string theory approach. These Lorentz violating terms would give rise to birefringence and dispersion of the vacuum. As discussed in [GP99b, AEM+98, EMN99], these effects are expected to be suppressed by a factor of E/E_{Pl} with the Planck energy $E_{\mathrm{Pl}} \sim 10^{19}$ GeV. However, in highly energetic gamma ray bursts from distant cosmological sources [BFM+92] they could be detectable at the present level of measurement accuracy.

Noncommutative field theories

Noncommutative field theories have gained more and more interest during recent years, especially since the discovery that noncommutative gauge theories directly emerge from limits of string theories and M-theory [CDS98, KS02]. This group of theories assumes that space-time coordinates are intrinsically noncommutative, which in the most simple case can be expressed by

$$[x^\mu, x^\nu] = i\theta^{\mu\nu}, \tag{2.1}$$

where $\theta^{\mu\nu}$ is an antisymmetric tensor of dimension (length)^2. This conflicts with Lorentz invariance, and effects of this breaking of Lorentz symmetry might become observable at length scales as small as that of $\theta^{\mu\nu}$, naturally

expected to be on the order of the Planck length $l_{\text{Pl}} \sim 10^{-35}\,\text{m}$. The issue of Lorentz violation in noncommutative theories has been given a closer consideration in [CHK$^+$01], and results from several existing test experiments for Lorentz invariance have been used to provide bounds on $\theta^{\mu\nu}$ down to $(10^{-27}\,\text{m})^2$.

Effects from curved space-time

The theory of special relativity considers physics in inertial frames and flat space-time only. As shown by the theory of general relativity, gravity does not fit into special relativity. Instead, it requires a replacement of the flat Minkowski metric by a curved metric, which becomes a dynamical field. Still, special relativity applies locally, i.e. when considering an apparatus of sufficiently small size, where space-time can be considered approximately flat. Consequently, if space-time curvature comes into play, Lorentz invariance is denoted local Lorentz invariance. An interesting question is, at what level of sensitivity effects from curved space-time would affect the present experiment.

For an earthbound classical Michelson-Morley interferometer, the effect of space-time curvature have been considered in [TR02]. They start from an expression for a light cone within an axially symmetric, static field caused by a central rotating body of mass M and angular momentum J:

$$0 = g_{tt}dt^2 + 2g_{t\phi}dtd\phi + g_{rr}dr^2 + g_{\theta\theta}d\theta^2 + g_{\phi\phi}d\phi^2. \tag{2.2}$$

The elements of the metric can be approximated for weak fields according to [MTW73] as

$$g_{tt} \approx c^2(1 - \frac{\mu}{r}),$$

$$g_{t\phi} \approx \frac{\mu c}{r}a\sin^2\theta,$$

$$g_{rr} \approx -1 - \frac{\mu}{r} + \frac{\sin^2\theta}{r^2}a^2,$$

$$g_{\theta\theta} \approx -r^2 - a^2\cos^2\theta,$$

$$g_{\phi\phi} \approx -(r^2 + a^2)\sin^2\theta, \tag{2.3}$$

where $a = J/Mc$, and $\mu = 2GM/c^2$ denotes the Schwarzschild radius of the source.

From this ansatz, the time delay due to gravity and rotation of the Earth for a free (i.e. geodesic) light beam, that travels a distance L in the equatorial plane, has been calculated in [TR02] to be:

$$\Delta t \sim \frac{l^3\mu}{8cR^4}(\frac{3}{4}\mu - \frac{a^2}{R}). \tag{2.4}$$

Choosing L = 1 m and the Earth as the source of the gravitational field, yields a value on the order of $\Delta t = 10^{-41}$ s, which is far below the sensitivity of any current Michelson interferometer. Note, that it is only relevant to consider geodesic light rays here. This has been disregarded by some authors, which then derive effects that are orders of magnitude larger than the above result given by [TR02].

2.2 Standard-model extension (SME)

During recent years, a framework has been elaborated which models violations of Lorentz invariance in a general and consistent way. This work formulates a Lorentz and CPT violating extension of the standard-model, briefly referred to as standard-model extension (SME) here. An outline of the SME has been given by D. Colladay and V.A. Kostelecký in [CK97, CK98].

The idea of the SME is to add to the Lagrangian of each sector of the standard-model of particle physics all CPT and Lorentz violating expressions that can be formed from the particle fields and general Lorentz tensors. Restrictions on these terms are set by preserving the gauge structure based on $SU(3) \times U(2) \times U(1)$ symmetry, renormalizability, observer Lorentz invariance, energy-momentum conservation and other desirable features. Thus, the extra terms are limited to a finite and manageable number. The consequences of these terms are then evaluated in the standard way i.e. minimizing the action applying variation techniques. This very general ansatz in principle allows to model the outcome of any experiment, assuming that (particle) Lorentz invariance is violated and taking into account all relevant consequences. Finally, the SME allows to design specific test experiments, that provide clean and desirably unambiguous limits on certain subsets of the Lorentz violation parameters. The classic test experiments such as the Michelson-Morley experiment, can be described within the SME, and indeed the latter proofs to be a sensitive test for several of the parameters of the SME.

2.2.1 Photonic sector of the SME

The most general form of a Lorentz violating extension to the Lagrangian of the photonic sector of the SME can be formulated as [CK98, KM02]

$$\mathcal{L} = -\frac{1}{4}F^{\mu\nu}F_{\mu\nu} - \frac{1}{4}(k_F)_{\kappa\lambda\mu\nu}F^{\kappa\lambda}F^{\mu\nu} + \frac{1}{2}(k_{AF})^{\kappa}\epsilon_{\kappa\lambda\mu\nu}A^{\lambda}F^{\mu\nu}, \qquad (2.5)$$

where A^λ is the electrodynamic 4-potential and $F_{\mu\nu}$ the electromagnetic field tensor. The second and third term obey observer Lorentz invariance (i.e. they are scalar), but explicitly violate particle Lorentz invariance. The magnitude of this violation is encoded in the tensors k_F and k_{AF} of degree four and one. Further scalar expressions can be formed from photonic fields and other tensors and have been considered in [CK98]. They have been shown to raise severe theoretical problems though, such as violations of energy and momentum conservation.

k_{AF} has the dimension of mass and the associated extension to the Lagrangian does not preserve CPT symmetry. Its problematic theoretical implications, leading to negative contributions to the energy density and a contribution to the energy-momentum tensor which is not gauge invariant, have been pointed out in [JK99]. In addition, astronomical measurements set strict limits of $< 10^{-42}$ GeV [CFJ90] on this parameter. Thus, considerations are restricted to the first CPT even term here, reducing the Lagrangian to

$$\mathcal{L} = -\frac{1}{4}F^{\mu\nu}F_{\mu\nu} - \frac{1}{4}(k_F)_{\kappa\lambda\mu\nu}F^{\kappa\lambda}F^{\mu\nu}. \tag{2.6}$$

The symmetries of k_F are the same as for the Riemann tensor. Consequently, its independent dimensionless components are restricted to a number of 19.[1] Proceeding from equation (2.6) in the usual way, i.e. applying variational techniques to minimize the action, results in a new set of Maxwell equations. The inhomogeneous equations are

$$\partial_\alpha F^\alpha_\mu + (k_F)_{\mu\alpha\beta\gamma}\partial^\alpha F^{\beta\gamma} = 0, \tag{2.7}$$

while the homogeneous equations remain unaltered.

These equations are analogous to standard Maxwell equations in anisotropic media: the parameters of k_F can be arranged within linear combinations

$$(\kappa_{DE})^{jk} = -2(k_F)^{0j0k},$$
$$(\kappa_{HB})^{jk} = \frac{1}{2}\epsilon^{jpq}\epsilon^{krs}(k_F)^{pqrs},$$
$$(\kappa_{DB})^{jk} = (k_F)^{0jpq}\epsilon^{kpq},$$
$$(\kappa_{HE})^{jk} = -(\kappa_{DB})^{kj}, \tag{2.8}$$

and analogous to standard electrodynamics, new fields $\vec{D}$ and $\vec{H}$ can be defined by

$$\begin{pmatrix} \vec{D} \\ \vec{H} \end{pmatrix} = \begin{pmatrix} 1 + \kappa_{DE} & \kappa_{DB} \\ \kappa_{HE} & 1 + \kappa_{HB} \end{pmatrix} \begin{pmatrix} \vec{E} \\ \vec{B} \end{pmatrix}, \tag{2.9}$$

[1]Basically these symmetries leave 20 independent parameters, however an additional normalization condition, namely taking out the $F^{\mu\nu}F_{\mu\nu}$ part, further reduces the number of free parameters to 19.

which allows to write down the complete set of Maxwell equations in the familiar form

$$
\begin{aligned}
\nabla \times \vec{H} - \partial_0 \vec{D} &= 0, \\
\nabla \times \vec{E} - \partial_0 \vec{B} &= 0, \\
\nabla \vec{D} &= 0, \\
\nabla \vec{B} &= 0.
\end{aligned}
\tag{2.10}
$$

Thus, Lorentz violation in the photonic sector can be considered to effectively turn the vacuum into an anisotropic medium. The properties of this medium are fixed by the values of the matrices introduced in equations (2.8), which can be considered to be remnants of a Planck scale structure of space-time.

For the description of test experiments it is convenient to further group these SME parameters into subsets that can be accessed by different test experiments. Therefore, they are usually rearranged into four 3×3 matrices and one scalar according to

$$
\begin{aligned}
(\tilde{\kappa}_{e+})^{jk} &= \frac{1}{2}(\kappa_{DE})^{jk} + (\kappa_{HB})^{jk}, \\
(\tilde{\kappa}_{e-})^{jk} &= \frac{1}{2}(\kappa_{DE})^{jk} - (\kappa_{HB})^{jk} - \frac{1}{3}\delta^{jk}(\kappa_{DE}^{ll}), \\
(\tilde{\kappa}_{o+})^{jk} &= \frac{1}{2}(\kappa_{DB})^{jk} + (\kappa_{HE})^{jk}, \\
(\tilde{\kappa}_{o-})^{jk} &= \frac{1}{2}(\kappa_{DB})^{jk} - (\kappa_{HE})^{jk}, \\
\tilde{\kappa}_{tr} &= \frac{1}{3}\delta^{jk}(\kappa_{DE}^{ll}).
\end{aligned}
\tag{2.11}
$$

The subscript e refers to matrices containing only parity even, o to matrices containing only parity odd parameters. Using these expressions the Lagrangian of equation (2.6) can be expressed as

$$
\begin{aligned}
\mathcal{L} = &\frac{1}{2}\left[(1 + \tilde{\kappa}_{tr})\vec{E}^2 - (1 - \tilde{\kappa}_{tr})\vec{B}^2\right] + \frac{1}{2}\vec{E}\left[\tilde{\kappa}_{e+} + \tilde{\kappa}_{e-}\right]\vec{E} \\
&- \frac{1}{2}\vec{B}\left[\tilde{\kappa}_{e+} - \tilde{\kappa}_{e-}\right]\vec{B} + \vec{E}\left[\tilde{\kappa}_{o+} + \tilde{\kappa}_{o-}\right]\vec{B}.
\end{aligned}
\tag{2.12}
$$

The effect of $\tilde{\kappa}_{tr}$ is a rotationally invariant modification of the speed of light, which can be removed by appropriate coordinate transformations and field redefinitions. However, the Lorentz violation associated with this coefficient can not be eliminated by this redefinition. Instead it is simply

shifted to other sectors of the SME, i.e. the matter sector instead of the photonic sector. It can be shown further [KM02], that such field redefinitions are also suitable to transform the effect of $\tilde{\kappa}_{e-}$ and $\tilde{\kappa}_{o+}$ to the matter sector. However, this does not apply to the coefficients $\tilde{\kappa}_{e+}$ and $\tilde{\kappa}_{o-}$. Consequently, an analysis of different experiments reveals that measurements that compare light to light, such as birefringence measurements, are insensitive to the nine parameters encoded in $\tilde{\kappa}_{e-}$, $\tilde{\kappa}_{o+}$ and $\tilde{\kappa}_{tr}$. These can only be determined by experiments that compare light with matter, such as cavity experiments.

Choice of reference frame

Following the conventions given in [KM02], all $\tilde{\kappa}$-matrices are referred to a Sun-centered celestial equatorial coordinate frame (SCCEF), which has the X-axis pointing towards vernal equinox and the Z-axis pointing towards the celestial North pole (all taken in the J2000.0 frame). The Y-axis is chosen accordingly to complete the right-handed dreibein (see Figure 2.1). On the relevant timescales of terrestrial experiments this reference frame is inertial to sufficient approximation. Matrix elements and axes referring to this coordinate frame are labeled by capital indices in the following. The coordinate axes x, y, z for the Earth-based laboratory, where the experiment takes place, are chosen such that the x-axis points South, the y-axis points East and the z-axis vertically upwards. Transformation from the SCCEF to the laboratory frame applies a Lorentz transformation

$$\Lambda^{\mu}_{\nu} = \begin{pmatrix} 1 & -\beta^1 & -\beta^2 & -\beta^3 \\ -(\tilde{R} \cdot \vec{\beta})^1 & R^{11} & R^{12} & R^{13} \\ -(\tilde{R} \cdot \vec{\beta})^2 & R^{21} & R^{22} & R^{23} \\ -(\tilde{R} \cdot \vec{\beta})^3 & R^{31} & R^{32} & R^{33} \end{pmatrix} \tag{2.13}$$

composed from a boost

$$\vec{\beta} = \beta_{\oplus} \begin{pmatrix} \sin \Omega_{\oplus} T' \\ -\cos \eta \cos \Omega_{\oplus} T' \\ -\sin \eta \cos \Omega_{\oplus} T' \end{pmatrix} + \beta_L \begin{pmatrix} -\sin \Omega_{\oplus} T' \\ \cos \Omega_{\oplus} T' \\ 0 \end{pmatrix} \tag{2.14}$$

and a rotation

$$R = \begin{pmatrix} \cos \chi \cos \omega_{\oplus} T_{\oplus} & \cos \chi \sin \omega_{\oplus} T_{\oplus} & -\sin \chi \\ -\sin \omega_{\oplus} T_{\oplus} & \cos \omega_{\oplus} T_{\oplus} & 0 \\ \sin \chi \cos \omega_{\oplus} T_{\oplus} & \sin \chi \sin \omega_{\oplus} T_{\oplus} & \cos \chi \end{pmatrix}. \tag{2.15}$$

Here, $\beta_{\oplus} = v_{\oplus}/c \approx 10^{-4}$ is Earth's orbital boost factor, $\beta_L \approx 10^{-6}$ is the laboratory boost factor due to Earth's rotation and $\omega_{\oplus}$ is the frequency of
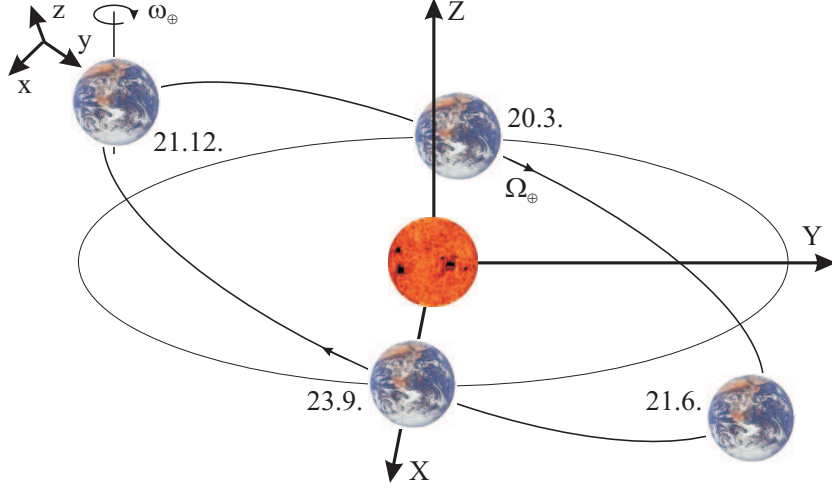
Figure 2.1: *Laboratory frame and Sun-centered celestial equatorial coordinate frame (SCCEF) adopted for the analysis of the experiment.*

a sidereal day. The time axis $T_\oplus$ is fixed by $T_\oplus = 0$, which can be chosen at any instant when the laboratory y-axis and the SCCEF Y-axis coincide. The time axis T' is set by $T' = 0$ at the instant when the Earth crosses the celestial equatorial plane on a descending trajectory in the year 2000.

Within the following all matrices referring to the laboratory frame are labeled by $(\tilde\kappa)_{\text{lab}}$ and their matrix elements by small indices. Matrices referring to the SCCEF remain unlabeled and their elements are given capital indices. Finally, matrices referred to the laboratory are transformed into expressions referred to the SCCEF according to [KM02] as given by

$$(\kappa_{DE})^{jk}_{\text{lab}} = T_0^{jkJK}(\kappa_{DE})^{JK} - T_1^{(jk)JK}(\kappa_{DB})^{JK},$$
$$(\kappa_{HB})^{jk}_{\text{lab}} = T_0^{jkJK}(\kappa_{HB})^{JK} - T_1^{(jk)KJ}(\kappa_{DB})^{JK},$$
$$(\kappa_{DB})^{jk}_{\text{lab}} = T_0^{jkJK}(\kappa_{DB})^{JK} + T_1^{kjJK}(\kappa_{DE})^{JK} + T_1^{jkJK}(\kappa_{HB})^{JK}, \qquad (2.16)$$

where

$$T_0^{jkJK} = R^{jJ}R^{kK}, \qquad T_1^{jkJK} = R^{jP}R^{kJ}\epsilon^{KPQ}\beta^Q. \qquad (2.17)$$

Limits set by astrophysical observations

From astrophysical measurements the terms $\tilde{\kappa}_{e+}$ and $\tilde{\kappa}_{o-}$ containing $5 + 5 = 10$ independent parameters have been restricted to values down to 10^{-32} [KM02, Alt06]. These limits are deduced from:

- Observations of pulsed light from distant sources. The violation of Lorentz invariance encoded in the matrices $\tilde{\kappa}_{e+}$ and $\tilde{\kappa}_{o-}$ modifies the dispersion relation of photons. This dispersion relation then features two different solutions, corresponding to distinct propagation modes of perpendicular polarization and different phase velocity. This would give rise to birefringence i.e. light pulses from pulsars (ms to μs in duration, at distances of kpc) or gamma ray bursts (several seconds in duration, at distances of Gpc) would split into two distinct pulses of perpendicular polarization. The arrival times of these should be separated according to $\Delta t = \Delta v L$, where the huge distance L effectively amplifies a possible tiny Lorentz violating Δv. The observation of only one pulse from a certain source and the inclusion of several sources distributed all over the sky, thus probing different directions, allows to deduce a limit on the involved parameters of $|\tilde{\kappa}| < 10^{-16}$.

- Polarization measurements of polarized light from distant sources at different wavelengths. The observed phase shift among the two polarization modes caused by a potential Lorentz violating birefringence depends on the wavelength of the emitted radiation. The observation of polarized light from distant sources emitted in a broad band of wavelengths, thus allows to set tight bounds on the same components as above at a level of $|\tilde{\kappa}| < 10^{-32}$. This estimate can be applied without knowledge of the initial polarization of the light, if one assumes that light is emitted at the same polarization for different wavelengths.

Limits set by laboratory tests

The non-birefringent terms of $\tilde{\kappa}_{e-}$, $\tilde{\kappa}_{o+}$ and $\tilde{\kappa}_{tr}$, contain $5 + 3 + 1 = 9$ free parameters. As pointed out above, they cannot be determined from astrophysical birefringence experiments, but have to be determined from experiments that compare light with matter, i.e. laboratory experiments. The limits thus deduced do not reach the same high accuracy as those found by astrophysical measurements. However, laboratory experiments offer full control of experimental conditions and do not rely on a priori assumptions of astrophysical models.

Several experimenters have provided bounds on these SME parameters from

parameter	[MHB$^+$03a]	[WBC$^+$04]
$\tilde{\kappa}_{e-}^{XX} - \tilde{\kappa}_{e-}^{YY}$	8.9 ± 4.9	-3.2 ± 4.6
$\tilde{\kappa}_{e-}^{ZZ}$	-	-
$\tilde{\kappa}_{e-}^{XY}$	1.7 ± 2.6	-5.7 ± 2.3
$\tilde{\kappa}_{e-}^{XZ}$	-6.3 ± 12.4	-3.2 ± 1.3
$\tilde{\kappa}_{e-}^{YZ}$	3.6 ± 9.0	0.5 ± 1.3
$\tilde{\kappa}_{o+}^{XY}$	14.0 ± 14.0	-1.8 ± 1.5
$\tilde{\kappa}_{o+}^{XZ}$	-1.2 ± 2.6	-1.4 ± 2.3
$\tilde{\kappa}_{o+}^{YZ}$	0.1 ± 2.7	2.7 ± 2.2

Table 2.1: *Experimental status of the photonic sector of the SME. All $\tilde{\kappa}_{e-}$ values are $\times 10^{-15}$, $\tilde{\kappa}_{o+}$ values are $\times 10^{-11}$. The birefringent terms of $\tilde{\kappa}_{e+}$ and $\tilde{\kappa}_{o-}$ are not listed, since they have been shown to be $< 10^{-32}$ from astrophysical observations and are assumed to be zero here. $\tilde{\kappa}_{tr}$ is not listed as well as it is not subject to cavity experiments.*

different types of clock-comparison experiments. The strongly bounded bire-fringent parameters $\tilde{\kappa}_{e+}$ and $\tilde{\kappa}_{o-}$ are assumed to be zero within the analyses of these laboratory experiments. J. Lipa *et al.* [LNW$^+$03] performed a comparison of two superconducting cryogenic microwave resonators. The difference frequency of these cavities undergoing Earth's rotation and orbital motion was analyzed for a time spanning three months. From this measurement they deduce limits on linear combinations of seven photonic SME parameters down to a level of 10^{-13}.

A comparison of two cryogenic optical Fabry-Pérot resonators by H. Müller *et al.* [MHB$^+$03a, MHB$^+$03b] improved on this result by about two orders of magnitude. Furthermore, this experiment was able to set independent limits on these seven SME parameters, because it relied on a data basis spanning $> 1\,\text{year}$. Similar results were achieved by P. Wolf *et al.* [WBC$^+$03, WBC$^+$04], who compared a Hydrogen maser to a cryogenically cooled sapphire cavity operating at $\sim 11\,\text{GHz}$ in a whispering gallery mode. The limits on photonic SME parameters deduced from these measurements are summarized in Table 2.1. All of these experiments solely applied Earth's rotation and relied on the high long-term stability of cryogenically cooled resonators. As Earth's rotation axis coincides with the SCCEF Z-axis, these experiments were not able to provide a bound on $\tilde{\kappa}_{e-}^{ZZ}$.

The rotationally invariant parameter $\tilde{\kappa}_{tr}$ cannot be bounded by a Michelson-Morley experiment. The current limit on this parameter of $\tilde{\kappa}_{tr} < 2.2 \times 10^{-7}$ has been set by an Ives-Stilwell type experiment [TWFH05, HGL$^+$07].

2.2.2   Matter sector of the SME

The extended Lagrangian for a Fermion within the SME is given by [KL99]

$$\mathcal{L} = \frac{1}{2} i \overline{\psi} \Gamma_\nu \partial^\nu \psi - \overline{\psi} M \psi, \tag{2.18}$$

where

$$M = m^w + a_\mu^w \gamma^\mu + b_\mu^w \gamma_5 \gamma^\mu + \frac{1}{2} H_{\mu\nu}^w \sigma^{\mu\nu},$$

$$\Gamma_\nu = \gamma_\nu + c_{\mu\nu}^w \gamma^\mu + d_{\mu\nu}^w \gamma_5 \gamma^\mu + \frac{1}{2} g_{\lambda\mu\nu}^w \sigma^{\lambda\mu}. \tag{2.19}$$

m is the particle mass and $\gamma_\mu, \gamma_5, \sigma^{\mu\nu}$ are the conventional Dirac matrices. The index w denotes the particle species, which is either p = proton, n = neutron or e = electron. The parameters entering M are of dimension mass, those entering Γ are dimensionless. The implications of these extra terms for clock-comparison experiments have been elaborated in a paper by V.A. Kostelecký and C.D. Lane [KL99]. They explicitly show that Lorentz violation shifts the electronic energy levels within the clock transitions of atomic clocks. These shifts depend on velocity and orientation and introduce a sidereal time variation of the clock's frequency according to Earth's rotation. Comparison of clocks e.g. based on different atomic species can then be used to provide limits on the parameters of equation (2.19). As atomic clocks typically utilize atoms that are composed by several protons, neutrons and electrons, the derivation of an unambiguous limit on a single parameter of equation (2.19) becomes very complicated, unless simplified models are used. In [KL99] such calculations are given and the components of the Lorentz violating tensors are grouped into irreducible linear combinations according to their appearance within experiments. These linear combinations are denoted by a tilde throughout the following.

Limits on SME parameters of the matter sector

From results of several clock-comparison measurements [PBIW85, LJH+86, CHL+89, BHK+95], limits on many SME parameter combinations of the matter sector have been deduced in [KL99] and elsewhere [PHM+01, WCBC06]. Other precision measurements have provided stringent limits on further parameters. These experiments applied electrons in a Penning trap [BKR99, MID99, DMVS99], spin-polarized torsion pendulums on a turntable [HNL03, BK00] and Doppler shift measurements on Lithium ions [SKE+03, Lan05]. An overview of the results obtained by these measurements is given in Table 2.3.

parameter	limit ($\times 10^{-15}$)
$c_{(YZ)}$	0.21 ± 0.46
$c_{(XZ)}$	-0.16 ± 0.63
$c_{(XY)}$	0.76 ± 0.35
$c_{XX} - c_{YY}$	1.15 ± 0.64

Table 2.2: *Limits on electron parameters deduced from cavity experiments [Mül05]. Expressions $c_{(ik)}$ denote the symmetric combinations $c_{ik} + c_{ki}$.*

Cavity experiments of the type described in this thesis, provide limits on some of the SME electron parameters c_{ij}, which are not restricted by any of the other precision measurements discussed above. These limits are obtained by combining results from different experiments, that apply cavities made from different materials. In [Mül05] the data of the previous Michelson-Morley experiments of [BH79] (cavities made from ULE = ultra-low expansion glass ceramics), [WBC$^+$03] (whispering gallery resonators made from sapphire) and [MHB$^+$03a] (vacuum cavities made from sapphire) are combined and limits on several combinations of SME electron parameters are extracted as given in Table 2.2.

2.3   Test theory of Robertson, Mansouri and Sexl (RMS)

Previous Michelson-Morley experiments were often analyzed applying a kinematical test theory based on work done by H.P. Robertson [Rob49] and later extended by R. Mansouri and R.U. Sexl [MS76]. This test theory assumes the existence of a preferred isotropic frame Σ, commonly taken to be the cosmic microwave background (CMB). In [MS76], the Lorentz transformations are replaced by general parameterized transformations between Σ (X, Y, Z, T) and a laboratory frame S (x, y, z, t), as given by

$$
\begin{aligned}
t &= a(v)T - \frac{v}{c^2}x, \\
x &= b(v)(X - vT), \\
y &= d(v)Y, \\
z &= d(v)Z,
\end{aligned}
\tag{2.20}
$$

where S moves at a velocity $\vec{v}$ along X-direction relative to Σ and c is the isotropic speed of light in Σ. The coefficient v/c^2 that appears in the transformation of t reflects the choice of Einstein synchronization here. Isotropy

SME parameter	p	n	e
$\tilde{b}_X, \tilde{b}_Y$	10^{-27} [HPM+03]	10^{-31} [BSW+00]	10^{-29} [HNL03]
$\tilde{b}_Z$	-	-	10^{-28} [HNL03]
$\tilde{b}_T, \tilde{g}_T, \tilde{H}_{JT}, d_\pm$	-	10^{-27} [CBR+04]	-
$\tilde{d}_Q, \tilde{d}_{XY}, \tilde{d}_{YZ}$	-	10^{-27} [CBR+04]	-
$\tilde{d}_X, \tilde{d}_Y$	10^{-25} [KL99]	10^{-29} [CBR+04]	10^{-22} [KL99]
$\tilde{d}_{XZ}, \tilde{d}_Z$	-	-	-
$\tilde{g}_{D,X}, \tilde{g}_{D,Y}$	10^{-25} [KL99]	10^{-29} [CBR+04]	10^{-22} [KL99]
$\tilde{g}_{D,Z}, \tilde{g}_{JK}$	-	-	-
$\tilde{g}_c$	-	10^{-27} [CBR+04]	-
$\tilde{g}_-, \tilde{g}_Q, \tilde{g}_{TJ}$	-	-	-
$\tilde{c}_Q$	10^{-22} [WCBC06]	-	10^{-15} [Alt06]
$\tilde{c}_X, \tilde{c}_Y$	10^{-25} [WCBC06]	10^{-25} [KL99]	10^{-19} [Mül05]
$\tilde{c}_Z, \tilde{c}_-$	10^{-25} [WCBC06]	10^{-27} [KL99]	10^{-19} [Mül05]
$\tilde{c}_{TJ}$	10^{-21} [WCBC06]	-	10^{-16} [Alt06]

Table 2.3: *Order of magnitude of experimental limits on SME parameters from the matter sector, stated in GeV. The coefficients stated here denote linear combinations of the parameters of equations (2.19) which are accessible from clock-comparison experiments. Indices J,K run over X,Y,Z. D and Q denote dipole respectively quadrupole contributions. For explicit definitions of these parameters see [KL99].*

of Σ further implies that a, b and d are even functions of v. For low velocities $a(v), b(v)$ and $d(v)$ can be expanded into a Taylor series

$$a(v) = 1 + \alpha \frac{v^2}{c^2} + ...,$$
$$b(v) = 1 + \beta \frac{v^2}{c^2} + ...,$$
$$d(v) = 1 + \delta \frac{v^2}{c^2} + ... \qquad (2.21)$$

If Lorentz invariance remains preserved, these transformations reduce to the Lorentz transformations and the first order test parameters take the values $\alpha = -\frac{1}{2}, \quad \beta = \frac{1}{2}$ and $\delta = 0$. Deviations from these values describe modifications in time dilation and lead to an anisotropy as well as a boost dependence of light propagation in S, as given by [MS76]:

$$\Delta c(v, \theta)/c = -(\alpha - \beta + 1)\frac{v^2}{c^2} - (\beta + \delta - \frac{1}{2})\frac{v^2}{c^2}\sin^2\theta(t), \qquad (2.22)$$

where θ is the angle between the direction of light propagation and $\vec{v}$. In order to determine the complete set of test parameters α, β, δ, three experiments are required: the Kennedy–Thorndike experiment [KT32] is sensitive to a velocity dependence of $c = c(v)$, thus it tests the parameter combination $(\alpha - \beta + 1) \equiv P_{\mathrm{KT}}$; the Michelson–Morley experiment [Mic81, MM87, MM97] tests for an anisotropy of the speed of light $c = c(\theta)$ described by the term $(\beta + \delta - \frac{1}{2}) \equiv P_{\mathrm{MM}}$; the Ives–Stilwell experiment [IS38, IS42] determines the parameter $(\alpha + \frac{1}{2}) \equiv P_{\mathrm{IS}}$ from a measurement of the quadratic Doppler effect.

Experimental limits on RMS parameters

Table 2.4 gives an overview of the experimental status with respect to the RMS test parameters. In [HH90], D. Hils and J.L. Hall have carried out a comparison of the frequency of an optical cavity to an iodine standard. They deduce a limit on the Kennedy-Thorndike parameter P_{KT} ny analyzing this frequency for a signal that would originate from a variation of v due to Earth's rotation. In [BMP+02], the high long-term stability of a cryogenic optical resonator, compared to an iodine standard during half a year of measurement span, allowed to improve this result by taking into account the larger variation of v due to Earth's orbital motion. Another order of magnitude improvement on this was achieved by Wolf *et al.* [WBC+03], who also applied a cryogenically cooled resonator, however in the microwave regime, and compared it to a Hydrogen maser.

experiment	limit	reference + year
$(\beta + \delta - \frac{1}{2})$	$< 5 \times 10^{-9}$	[BH79] 1979
$(\beta + \delta - \frac{1}{2})$	$(2.2 \pm 1.5) \times 10^{-9}$	[MHB$^+$03a] 2003
$(\beta + \delta - \frac{1}{2})$	$(1.2 \pm 2.2) \times 10^{-9}$	[WBC$^+$03] 2003
$(\alpha - \beta + 1)$	$< 6.6 \times 10^{-5}$	[HH90] 1990
$(\alpha - \beta + 1)$	$(1.9 \pm 2.1) \times 10^{-5}$	[BMP$^+$02] 2002
$(\alpha - \beta + 1)$	$(1.6 \pm 3.0) \times 10^{-7}$	[WBC$^+$03] 2003
$(\alpha + \frac{1}{2})$	$< 1.1 \times 10^{-6}$	[GKH$^+$94] 1994
$(\alpha + \frac{1}{2})$	$< 1.8 \times 10^{-7}$	[SKE$^+$03] 2003

Table 2.4: *Experimental limits on the test parameters of the RMS formalism.*

A limit on P_{MM} can be deduced from a series of Michelson-Morley experiments (Figure 1.1). One of the most advanced of these was performed by A. Brillet and J.L. Hall [BH79]. They compared a methane-stabilized laser to a cavity rotating on a turntable at a rate of 0.1 Hz. The more recent experiments, performed to provide limits on SME parameters in the first place [MHB$^+$03a, WBC$^+$03], allowed to improve this limit on P_{MM} as well.

Finally, the Ives-Stilwell parameter P_{IS} is currently best restricted by a measurement done by Saathoff *et al.* [SKE$^+$03], who measured the relativistic Doppler shift on Lithium ions at $v/c \sim 0.064$ at the heavy ion storage ring in Heidelberg, Germany.

Chapter 3

Signals of a violation of Lorentz invariance

An anisotropy of the speed of light as a consequence of Lorentz violation would cause a modulation of the resonance frequency of the rotating cavity at twice the table rotation frequency ω_{rot}. The basic signal thus is expected to take the form

$$\frac{\Delta\nu}{\nu_0} = B \sin 2\omega_{\text{rot}}t + C \cos 2\omega_{\text{rot}}t, \tag{3.1}$$

where $\Delta\nu = \nu_{\text{R1}} - \nu_{\text{R2}}$ is the frequency difference of the rotating (R1) and the stationary (R2) cavity, and ν_0 is the fundamental cavity frequency $\nu_{\text{R1}} \approx \nu_{\text{R2}} \approx \nu_0 = 2.82 \times 10^{14}\,\text{Hz}$. The additional rotation of the setup due to Earth's rotation ($\omega_\oplus$) and Earth's orbital motion around the Sun ($\Omega_\oplus$) adds to the turntable rotation. Thus, the amplitudes B and C may be modulated at $\omega_\oplus$ and $2\omega_\oplus$:

$$\begin{aligned} B = B_0 &+ B_{\text{s1}} \sin \omega_\oplus t + B_{\text{c1}} \cos \omega_\oplus t \\ &+ B_{\text{s2}} \sin 2\omega_\oplus t + B_{\text{c2}} \cos 2\omega_\oplus t, \end{aligned} \tag{3.2}$$

$$\begin{aligned} C = C_0 &+ C_{\text{s1}} \sin \omega_\oplus t + C_{\text{c1}} \cos \omega_\oplus t \\ &+ C_{\text{s2}} \sin 2\omega_\oplus t + C_{\text{c2}} \cos 2\omega_\oplus t, \end{aligned} \tag{3.3}$$

and the respective amplitudes B_k and C_k again vary on an annual timescale. In this chapter the two test theories introduced above, SME and RMS, will be applied to derive expressions for B_k and C_k in terms of Lorentz violation test parameters. This will allow a consistent quantitative analysis of the experiment as a test of Lorentz invariance.

3.1   The Michelson-Morley experiment in the SME framework

3.1.1   Cavity resonance frequency with Lorentz violation in the photonic sector

Let $\vec{E}_0 e^{i\omega t}$ and $\vec{B}_0 e^{i\omega t}$ be the solutions of the fully Lorentz invariant Maxwell equations, while $\vec{E} e^{i\omega t}$ and $\vec{B} e^{i\omega t}$ describe the fields that are perturbed from these states to first order due to the effect of a small Lorentz violation. Within classical electrodynamics, the relative frequency change of a cavity when slightly perturbing the electrodynamic fields can be calculated from

$$\frac{\delta\nu}{\nu_0} = -\frac{1}{\langle U \rangle} \int_V [\vec{E}_0^* \vec{D} - \vec{D}_0^* \vec{E} - \vec{B}_0^* \vec{H} + \vec{H}_0^* \vec{B}] d^3x, \qquad (3.4)$$

where

$$\langle U \rangle = \frac{1}{2} \int_V (\vec{E}_0 \vec{D}_0^*) d^3x. \qquad (3.5)$$

The above expression applies with the periodic boundary conditions, set by the cavity geometry, unaltered. This is assumed to hold for small perturbations. As given in [KM02] and shown explicitly in [Gök04], the evaluation of this expression using equations (2.9) results in

$$\frac{\delta\nu}{\nu_0} = -\frac{1}{\langle U \rangle} \int_V [\vec{E}_0^*(\kappa_{DE})_{\text{lab}} \vec{E}_0^* - \vec{B}_0^*(\kappa_{HB})_{\text{lab}} \vec{B}_0^*] d^3x. \qquad (3.6)$$

The terms involving the "off diagonal" matrices $(\kappa_{DB})_{\text{lab}} = -(\kappa_{HE})_{\text{lab}}^T$ vanish, because of the preserved orthogonality of electric and magnetic fields within the cavity.

The fields in equation (3.6) depend on the experimental setup according to the orientation and geometry of the cavity and the polarization of the light. For a linear Fabry-Pérot cavity (index of refraction $n = 1$) oriented along the direction of a unit vector $\hat{N}$ and linearly polarized light, evaluation of equation (3.6) results in

$$\frac{\delta\nu}{\nu_0} = \frac{\vec{E}_0^*(\kappa_{DE})_{\text{lab}} \vec{E}_0 - \epsilon(\hat{N} \times \vec{E}_0^*)(\kappa_{HB})_{\text{lab}}(\hat{N} \times \vec{E}_0^*)}{2\epsilon |E_0^2|}. \qquad (3.7)$$

In accordance with the present experimental setup, the optical axis $\hat{N}$ is taken within the xy-plane at an angle θ with respect to the laboratory x-axis. The polarization $\hat{E}$ is oriented horizontally at right angle with respect to $\hat{N}$. Note, that the cavity configuration applied here differs from that considered in [KM02]. There, $\vec{E}_0$ is assumed to be polarized along the laboratory

z-direction. However, for a vacuum cavity with index of refraction $n = 1$ the relevant results remain unaltered compared to those derived in [KM02]. Substitution of κ_{DE} and κ_{HB} by the matrices defined in (2.11) and transformation of these matrices to the SCCEF using (2.16) yields an expression of the form

$$\frac{\delta\nu}{\nu_0} = A + B\sin 2\theta + C\cos 2\theta, \tag{3.8}$$

where the amplitudes A, B and C exhibit a time dependence due to Earth's rotation $\omega_\oplus$ within the SCCEF as given by

$$\begin{aligned}
A = A_0 &+ A_{\mathrm{s1}}\sin\omega_\oplus T_\oplus + A_{\mathrm{c1}}\cos\omega_\oplus T_\oplus \\
&+ A_{\mathrm{s2}}\sin 2\omega_\oplus T_\oplus + A_{\mathrm{c2}}\cos 2\omega_\oplus T_\oplus,
\end{aligned} \tag{3.9}$$

$$\begin{aligned}
B = B_0 &+ B_{\mathrm{s1}}\sin\omega_\oplus T_\oplus + B_{\mathrm{c1}}\cos\omega_\oplus T_\oplus \\
&+ B_{\mathrm{s2}}\sin 2\omega_\oplus T_\oplus + B_{\mathrm{c2}}\cos 2\omega_\oplus T_\oplus,
\end{aligned} \tag{3.10}$$

$$\begin{aligned}
C = C_0 &+ C_{\mathrm{s1}}\sin\omega_\oplus T_\oplus + C_{\mathrm{c1}}\cos\omega_\oplus T_\oplus \\
&+ C_{\mathrm{s2}}\sin 2\omega_\oplus T_\oplus + C_{\mathrm{c2}}\cos 2\omega_\oplus T_\oplus.
\end{aligned} \tag{3.11}$$

The amplitudes A_k, B_k and C_k exhibit a modulation due to Earth's orbital motion ($\Omega_\oplus$) and depend on linear combinations of elements of $\tilde{\kappa}_{e-}$, $\tilde{\kappa}_{e+}$, $\tilde{\kappa}_{o-}$, $\tilde{\kappa}_{o+}$ and $\tilde{\kappa}_{tr}$ as given in Appendix B.

3.1.2 Frequency comparison of a rotating to a stationary cavity

The frequency shift described by equation (3.8) refers to a single cavity at rest in the laboratory frame. As described in chapter 4, the experiment features comparison of the frequencies of one actively rotated cavity R1 and one stationary cavity R2. Based on the above results, the relative frequency variation of these cavities is derived now. Rotation of R1 is described by adopting $\theta = \omega_{\mathrm{rot}}T$, with $T = 0$ when the resonator axis and the laboratory x-axis coincide. In accordance with the measurement, the derivation of the signal assumes counterclockwise rotation ($+\omega_{\mathrm{rot}}$). The frequency difference between R1 and R2 oriented North-South ($\theta = 0$) applying equation (3.7) then is

$$\frac{\delta\nu_{\mathrm{rot}} - \delta\nu_{\mathrm{stat}}}{\nu_0} = B\sin 2\omega_{\mathrm{rot}}T + C\cos 2\omega_{\mathrm{rot}}T - C. \tag{3.12}$$

The last term C can be considered constant on the timescale of one or few rotations since $\omega_{\mathrm{rot}} \gg \omega_\oplus$. For short data sets this term contributes to the arbitrary offset only. Thus, we are left with

$$\frac{\Delta\nu}{\nu_0} = B\sin 2\omega_{\mathrm{rot}}T + C\cos 2\omega_{\mathrm{rot}}T, \tag{3.13}$$

where B and C can be obtained from equations (3.10) and (3.11) and the coefficients B_k and C_k therein can be found in Appendix B. Note, that $\tilde{\kappa}_{tr}$ only enters the rotationally invariant term A, which drops out in this frequency comparison. Therefore, $\tilde{\kappa}_{tr}$ cannot be determined from the present experiment.

In Table 3.1 the relevant signal amplitudes are stated to first order in orbital boost, neglecting $\tilde{\kappa}_{e+}$ and $\tilde{\kappa}_{o-}$, which are taken to be zero based on astrophysical observations. One element of $\tilde{\kappa}_{e-}$ enters each coefficient C_k respectively B_k. Additionally, two or three elements of $\tilde{\kappa}_{o+}$ enter each coefficient in various combinations. The $\tilde{\kappa}_{o+}$ terms are associated with boost dependent Lorentz violation. Thus, they are suppressed by factors $\beta_\oplus$ to first order and exhibit a sidereal modulation at $\Omega_\oplus$ due to Earth's orbital motion. Note that the same linear combinations of SME parameters appear in each B_k and its associated C_k coefficient. Consequently, there are only five independent combinations of eight SME parameters. The sidereal modulation of the $\tilde{\kappa}_{o+}$-terms within these linear combinations can in principle be used to determine independent limits on these parameters. However, this requires a measurement spanning more than one year.

Frequency comparison of two rotating cavities

As described in chapter 4, the experimental setup offered the possibility to alternatively compare the frequencies of two rotating resonators oriented perpendicular to each other. The signal obtained from this comparison can be derived from equation (3.7) adopting $\theta_1 = \omega_{\text{rot}}T$ and $\theta_2 = \omega_{\text{rot}}T + \pi/2$. This yields

$$
\begin{aligned}
\frac{\delta\nu_{\text{rot},1} - \delta\nu_{\text{rot},2}}{\nu_0} = {} & B \sin 2\omega_{\text{rot}}T - B \sin 2(\omega_{\text{rot}}T + \pi/2) \\
& + C \cos 2\omega_{\text{rot}}T - C \cos 2(\omega_{\text{rot}}T + \pi/2),
\end{aligned}
\tag{3.14}
$$

which can be summarized as a Lorentz violation signal of the form

$$
\frac{\Delta\nu}{\nu_0} = 2B \sin 2\omega_{rot}T + 2C \cos 2\omega_{\text{rot}}T.
\tag{3.15}
$$

A comparison of this expression with equation (3.13) reveals, that this exactly equals the signal of equation (3.1), apart from a factor of two in favor of the sensitivity of this configuration. However, as will become evident below, the bad performance of one of the rotating resonators compromised this possibly increased sensitivity, and all measurements were ultimately obtained from a comparison of a rotating to a stationary resonator only.

	SME amplitude
C_0	$\gamma_0 \left(\frac{3}{2}\tilde{\kappa}_{e-}^{ZZ} - \beta_\oplus[(\cos\eta\,\tilde{\kappa}_{o+}^{XZ} + 2\sin\eta\,\tilde{\kappa}_{o+}^{XY})\cos\Omega_\oplus T' + \tilde{\kappa}_{o+}^{YZ}\sin\Omega_\oplus T'] \right)$
C_{s1}	$\gamma_1 \left(-\tilde{\kappa}_{e-}^{YZ} + \beta_\oplus[\cos\eta\,\tilde{\kappa}_{o+}^{XY} - \sin\eta\,\tilde{\kappa}_{o+}^{XZ}]\cos\Omega_\oplus T' \right)$
C_{c1}	$\gamma_1 \left(-\tilde{\kappa}_{e-}^{XZ} + \beta_\oplus[\sin\eta\,\tilde{\kappa}_{o+}^{YZ}\cos\Omega_\oplus T' - \tilde{\kappa}_{o+}^{XY}\sin\Omega_\oplus T'] \right)$
C_{s2}	$\gamma_2 \left(\tilde{\kappa}_{e-}^{XY} - \beta_\oplus[\cos\eta\,\tilde{\kappa}_{o+}^{YZ}\cos\Omega_\oplus T' + \tilde{\kappa}_{o+}^{XZ}\sin\Omega_\oplus T'] \right)$
C_{c2}	$\gamma_2 \left(\frac{1}{2}[\tilde{\kappa}_{e-}^{XX} - \tilde{\kappa}_{e-}^{YY}] - \beta_\oplus[\cos\eta\,\tilde{\kappa}_{o+}^{XZ}\cos\Omega_\oplus T' - \tilde{\kappa}_{o+}^{YZ}\sin\Omega_\oplus T'] \right)$
B_0	0
B_{s1}	$\frac{\gamma_3}{\gamma_1}C_{c1}$
B_{c1}	$-\frac{\gamma_3}{\gamma_1}C_{s1}$
B_{s2}	$-\frac{\gamma_4}{\gamma_2}C_{c2}$
B_{c2}	$\frac{\gamma_4}{\gamma_2}C_{s2}$

Table 3.1: *Modulation amplitudes according to equations (3.10) and (3.11) related to photonic SME parameters. $\gamma_0 = \frac{1}{4}\sin^2\chi$, $\gamma_1 = \frac{1}{2}\cos\chi\sin\chi$, $\gamma_2 = \frac{1}{4}(1 + \cos^2\chi)$, $\gamma_3 = -\frac{1}{2}\sin\chi$ and $\gamma_4 = \frac{1}{2}\cos\chi$. Relations are stated to first order in orbital boost. $\beta_\oplus = 10^{-4}$ is the boost parameter, $\chi = 37°$ is the colatitude of the Berlin laboratory and $\eta = 23°$ is the tilt of Earth's axis relative to the SCCEF Z-axis.*

Fourier spectrum of a Lorentz violation signal

Alternatively, the Lorentz violation signal shall also presented as it would appear in a Fourier spectrum of a beat frequency measurement spanning a few days. This presentation has been adopted in several publications on similar cavity tests of Lorentz invariance.

The modulation of the basic signal at $2\omega_{\mathrm{rot}}$ due to Earth's rotation and orbital motion generates sidereal sidebands, that appear within a Fourier spectrum of the beat frequency measurement as depicted in Figure 3.1. Analysis of a data set spanning ~ 1 day, requires expressions for the Fourier amplitudes at the sidereal sidebands $\pm\omega_\oplus$ including the contributions of $\omega_\oplus \pm \Omega_\oplus$, which cannot be fully resolved from less than one year of measurement. These expressions are derived by inserting the amplitudes of Table 3.1 into equations (3.10) and (3.11). This is used to evaluate (3.13) and to separate the resulting expression into contributions at ω_{rot} and the sidebands at $\pm\omega_\oplus$. The obtained signal then is of the form

$$\frac{\Delta\nu}{\nu_0} = \sum_{k=-2}^{2} (\tilde{B}_k \sin[((2\omega_{\mathrm{rot}} - k\omega_\oplus)T - \phi_k] + \tilde{C}_k \cos[((2\omega_{\mathrm{rot}} - k\omega_\oplus)T - \phi_k]).$$

(3.16)

The unresolved annual variation is still present in the time dependence of the Fourier amplitudes varying on an annual timescale. The respective phase differences due to the different time axes T, T' and $T_\oplus$ have to be traced carefully and are absorbed in ϕ_k here. The determination of ϕ_k can be simplified, if the measurement data is referred to the time axis $T_\oplus$, with $T_\oplus = 0$ at any instant when the laboratory y-axis and SCCEF Y-axis coincide. This time can be calculated from the data on Earth's orbit available from [US 06] for a certain day of the measurement. The most convenient choice is $T_\oplus = 0$ on March 20th, 2000, 11 h 14 min UTC (coordinated universal time). This is only $\delta T = 3$ h 39 min after the instant of vernal equinox at $T' = 0$ (March 20th, 2000, 7 h 35 min UTC) and allows to set $T' \approx T_\oplus$ within calculations. All phase factors due to this shift in time axes are on the order of $\Omega_\oplus \delta T \sim 5 \times 10^{-3}$ and thus are negligible ($\phi_k = 0$). Finally, adopting $T_\oplus$ as the common time axis, the sideband amplitudes given in Table C.2 are obtained. These amplitudes apply to short data sets (~ 1 day) taken at a time T' on the annual timescale.
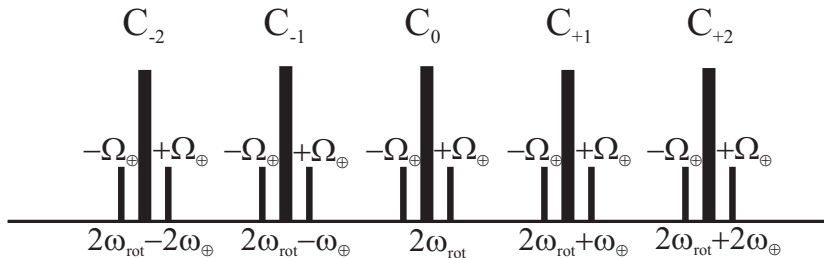
Figure 3.1: *A Lorentz violation signal would appear at the turntable frequency and the sidebands at plus and minus once and twice the sidereal rotation frequency of the Earth. The amplitudes of the respective sidebands are listed in Table C.2. According to this picture a full independent measurement of all signal components requires a measurement of > 1 year, as the frequency resolution of one day does not allow to resolve the sidebands at $\pm\Omega_\oplus$.*

3.1.3 Cavity resonance frequency with Lorentz violation in the electronic sector

So far, the effect of a violation of Lorentz invariance to the resonance frequency of a cavity of unaltered boundary conditions has been considered. However, one might wonder whether a violation of Lorentz invariance in the matter sector could lead to a change of the cavity dimensions or the index of refraction for a matter filled cavity. This would as well contribute to the change of the cavity resonance frequency.

The consequences of Lorentz violation in the electronic sector of the SME within cavity experiments have been studied in [MHS+03a] and [Mül05]. As shown in [KL99], a non-relativistic Hamiltonian $h' = h + \delta h$ can be derived from the Lagrangian (2.19) for a free electron, where δh includes the corrections arising from Lorentz violation. In [MHS+03a] it has been shown, that for N electrons within a crystal (neglecting interactions) the only non-vanishing contribution from δh to the expectation value of h' arises from

$$\delta h = \frac{1}{m} E'_{ij} \sum_{a=1}^{N} (p_a)_i (p_a)_j, \tag{3.17}$$

where $i, j = x, y, z$, p_a denotes the a_{th} particle's momentum, the sum runs over all N electrons, and

$$E'_{ij} = -c_{ij} - \frac{1}{2} c_{00} \delta_{jk} \tag{3.18}$$

is the Lorentz violating tensor containing the SME parameters c_{ij} of equation (2.19). The modified total energy of the crystal is derived from the expecta-

tion value of h' using a Bloch wave ansatz for the single electron wave function in a crystal. The resulting lowest order contributions to changes in crystal dimensions are then determined from a minimization of this energy. Thereby, the specific elastic properties of the cavity spacer material are applied. Finally, a material specific sensitivity matrix $\mathcal{M}_{\Gamma\Xi}$ is derived, which links the Lorentz violation parameters of $E'_{ij} \equiv E'_{\Xi}$ to the strain $dx_i/dx_j = e_{ij} \equiv e_{\Gamma}$ on the cavity spacer:

$$e_{\Gamma} = \mathcal{M}_{\Gamma\Xi}E'_{\Xi}. \tag{3.19}$$

$\Gamma, \Xi = \hat{x}\hat{x}, \hat{y}\hat{y}, \hat{z}\hat{z}, \hat{x}\hat{y}, \hat{x}\hat{z}, \hat{y}\hat{z}$ label the orientations within a cavity fixed reference frame. Thus, given the material's sensitivity matrix for a certain spacer material, the frequency change of a Fabry-Pérot cavity can be derived. For instance, if the optical axis coincides with the cavity $\hat{x}$-axis, one obtains

$$(\frac{\delta\nu}{\nu_0})_{e-} = \mathcal{M}_{\hat{x}\hat{x}\Xi}E'_{\Xi}. \tag{3.20}$$

The general form of the sensitivity matrix for isotropic materials according to [MHS⁺03a] is given by

$$\mathcal{M} = \begin{pmatrix} \mathcal{M}_{11} & \mathcal{M}_{12} & \mathcal{M}_{12} & 0 & 0 & 0 \\ \mathcal{M}_{12} & \mathcal{M}_{11} & \mathcal{M}_{12} & 0 & 0 & 0 \\ \mathcal{M}_{12} & \mathcal{M}_{12} & \mathcal{M}_{11} & 0 & 0 & 0 \\ 0 & 0 & 0 & \mathcal{M}_{44} & 0 & 0 \\ 0 & 0 & 0 & 0 & \mathcal{M}_{44} & 0 \\ 0 & 0 & 0 & 0 & 0 & \mathcal{M}_{44} \end{pmatrix}. \tag{3.21}$$

Fused materials are intrinsically isotropic on a macroscopic scale, because they present an ensemble of randomly oriented microcrystals. The derivation of the sensitivity matrix (3.21) for fused silica thus involves the calculation of matrix elements for crystalline silica and subsequent averaging over all orientations. This yields ([Mül05]):

$$\mathcal{M}_{11} = 2.64, \quad \mathcal{M}_{12} = -0.32, \quad \mathcal{M}_{44} = 3.95. \tag{3.22}$$

The relative length change along the optical axis, which is assumed to coincide with the cavity $\hat{x}$-axis, can then be obtained from

$$(\frac{\delta\nu}{\nu_0})_{e-} = \mathcal{M}_{11}E'_{\hat{x}\hat{x}} + \mathcal{M}_{12}(E'_{\hat{y}\hat{y}} + E'_{\hat{z}\hat{z}}). \tag{3.23}$$

Applying the same transformations as in section 3.1.1, the frequency change for a stationary cavity in the laboratory frame with the optical axis at an angle θ to the laboratory x-axis can be calculated. The resulting expression

can be arranged in an analogous form to that of equation (3.8). If one restricts to terms of lowest order in orbital boost, the inclusion of the electronic terms into the signal amplitudes of Table 3.1 can be obtained by simply replacing the test parameters according to

$$\tilde{\kappa}_{e-}^{IJ} \rightarrow \tilde{\kappa}_{e-}^{IJ} + 2\mathcal{M}_{\text{fs}}c_{(IJ)},$$
$$\tilde{\kappa}_{o+}^{IJ} \rightarrow \tilde{\kappa}_{o+}^{IJ}.$$

Note, that boost dependence for $\tilde{\kappa}_{e-}^{IJ}$ and $c_{(IJ)}$ is only a second order effect, whereas it is a first order effect for $\tilde{\kappa}_{o+}$. The effective sensitivity coefficient for fused silica is $\mathcal{M}_{\text{fs}} = \mathcal{M}_{11} - \mathcal{M}_{12} = 3.96$.

3.2 The Michelson-Morley experiment in the RMS framework

The relative frequency change between two resonators oriented relative to $\vec{v}$ at angles $\theta_1(t)$ and $\theta_2(t)$ can be obtained from equation (2.22) as

$$\frac{\Delta\nu}{\nu_0} = P_{\text{MM}}\frac{v^2}{c^2}\left[\sin^2\theta_1(t) - \sin^2\theta_2(t)\right]. \tag{3.24}$$

In order to determine the explicit time dependence of this expression, all vectors are referred to the SCCEF and the relation

$$\sin^2\theta_i(t) = 1 - \left(\frac{\vec{v}(t)\vec{e}_i(t)}{v}\right)^2, \tag{3.25}$$

is applied, where $\vec{e}_1(t)$ is the unit vector along the axis of the rotating resonator R1 and $\vec{e}_2(t)$ that along the stationary resonator R2. Adopting the above conventions about the laboratory frame, one can write:

$$(\vec{e}_1)_{\text{lab}} = \begin{pmatrix} \cos\omega_{\text{rot}}T \\ \sin\omega_{\text{rot}}T \\ 0 \end{pmatrix} \quad , \quad (\vec{e}_2)_{\text{lab}} = \begin{pmatrix} 1 \\ 0 \\ 0 \end{pmatrix}. \tag{3.26}$$

$\vec{v}(t)$ is the velocity of the laboratory relative to the CMB. The major contributions to $\vec{v}(t)$ are the solar system's motion relative to the CMB at $v_c \sim 370\,\text{km/s}$ [LTS$^+$96] and Earth's orbital motion at $v_\oplus \sim 30\,\text{km/s}$. The term due to Earth's rotation is of order $300\,\text{m/s}$ and is considered negligible here. The orientation of $\vec{v}(t)$ in the SCCEF is given by

$$\vec{v}(t) = v_c\begin{pmatrix} \cos\alpha\cos\beta \\ \sin\alpha\cos\beta \\ -\sin\beta \end{pmatrix} + v_\oplus\begin{pmatrix} \sin\Omega T \\ \cos\Omega T\cos\eta \\ -\cos\Omega T\sin\eta \end{pmatrix}, \tag{3.27}$$

where $\alpha = 168°$, $\beta = -6°$ [LTS$^+$96]. Adopting the same conventions about the different time axes T, T' and $T_\oplus$ as above, an evaluation of equation (3.24) to first order in $v_\oplus$ uses the transformation (2.13) and arranges the resulting Lorentz violation signal analogous to equations (3.10) and (3.11). This yields the signal components given in Table 3.2. The alternative representation of this signal by means of Fourier amplitudes according to equation (3.16) is given in Table C.3.

	RMS amplitude $(\times P_{\mathrm{MM}} \frac{v_c^2}{c^2})$
C_0	$\frac{1}{2}\gamma_0(-1 + 3\cos 2\beta)$ $+2\frac{v_\oplus}{v_c}\gamma_0(\sin\alpha\cos\beta\cos\eta - 2\sin\beta\sin\eta)\cos\Omega_\oplus T'$ $+2\frac{v_\oplus}{v_c}\gamma_0\cos\beta\cos\alpha\sin\Omega_\oplus T'$
$C_{\mathrm{s}1}$	$-\gamma_1\sin\alpha\sin 2\beta$ $-2\frac{v_\oplus}{v_c}\gamma_1(\sin\beta\cos\eta + \sin\alpha\cos\beta\sin\eta)\cos\Omega_\oplus T'$
$C_{\mathrm{c}1}$	$-\gamma_1\cos\alpha\sin 2\beta$ $-2\frac{v_\oplus}{v_c}\gamma_1\cos\alpha\cos\beta\sin\eta\cos\Omega_\oplus T'$ $-2\frac{v_\oplus}{v_c}\gamma_1\sin\beta\sin\Omega_\oplus T'$
$C_{\mathrm{s}2}$	$-\gamma_2\sin 2\alpha\cos^2\beta$ $-2\frac{v_\oplus}{v_c}\gamma_2\cos\alpha\cos\beta\cos\eta\cos\Omega_\oplus T'$ $-2\frac{v_\oplus}{v_c}\gamma_2\sin\alpha\cos\beta\sin\Omega_\oplus T'$
$C_{\mathrm{c}2}$	$-\gamma_2\cos 2\alpha\cos^2\beta$ $+2\frac{v_\oplus}{v_c}\gamma_2\sin\alpha\cos\beta\cos\eta\cos\Omega_\oplus T'$ $-2\frac{v_\oplus}{v_c}\gamma_2\cos\alpha\cos\beta\sin\Omega_\oplus T'$
B_0	0
$B_{\mathrm{s}1}$	$\frac{\gamma_3}{\gamma_1}C_{\mathrm{c}1}$
$B_{\mathrm{c}1}$	$-\frac{\gamma_3}{\gamma_1}C_{\mathrm{s}1}$
$B_{\mathrm{s}2}$	$-\frac{\gamma_4}{\gamma_2}C_{\mathrm{c}2}$
$B_{\mathrm{c}2}$	$\frac{\gamma_4}{\gamma_2}C_{\mathrm{s}2}$

Table 3.2: *Modulation amplitudes according to equations (3.10) and (3.11) related to the RMS parameter P_{MM}. $\gamma_0 = \frac{1}{4}\sin^2\chi$, $\gamma_1 = \frac{1}{2}\sin\chi\cos\chi$, $\gamma_2 = \frac{1}{4}(1 + \cos^2\chi)$, $\gamma_3 = -\frac{1}{2}\sin\chi$ and $\gamma_4 = \frac{1}{2}\cos\chi$. χ denotes the laboratory colatitude, η the tilt of Earth's axis relative to the SCCEF Z-axis. Terms varying with Earth's orbital motion are suppressed by $v_\oplus/v_c \sim 0.08$.*

3. Signals of a violation of Lorentz invariance

Chapter 4

The setup

The basic scheme of the experiment is depicted in Figure 1.3. The resonance frequency of a continuously rotating cavity R1 is read out using a laser L1, and is compared to the frequency of a stationary cavity R2, which is read out using a laser L2. A violation of Lorentz invariance would then be indicated by a modulation of the beat frequency $\Delta\nu = \nu_{R1} - \nu_{R2}$ at twice the turntable rotation rate $2\omega_{\mathrm{rot}}$, as described by equation (3.13).

The first part of this chapter presents the laser stabilization setup applied to read out the cavity frequencies. The essential components are described and some fundamental aspects of frequency stabilization to cavities are discussed. Finally, the achieved performance and the limitations set to frequency stability of the applied cavities are discussed. The second part of this chapter describes how the active rotation of a part of the setup is achieved. The associated systematic effects that affect the beat frequency measurement are then described in the next chapter in full detail.

4.1 The cavities

4.1.1 Fabry-Pérot resonators

Consider an optical Fabry-Pérot resonator of length L and a plane wave $\vec{E}_{\mathrm{in}} = \vec{E}_0 e^{i\omega t}$ incident on this resonator as depicted in Figure 4.1. The transmission and reflection coefficients of the front and back mirror for the laser field are r_1 and t_1, respectively r_2 and t_2. If mirror loss is neglected energy conservation implies for each mirror:

$$r_i^2 + t_i^2 = 1. \tag{4.1}$$

In addition a coefficient a is introduced, that accounts for losses during half a round trip $(|E(\vec{L})| = a|E(\vec{0})|)$, i.e. $a = 1$ corresponds to no loss. For

the steady state the resonating field can then be written as the sum of the transmitted incident field and the field that has completed one round trip, thereby accumulating a phase $\delta = 4\pi\nu L/c$:

$$\vec{E}_{\text{res}} = t_1\vec{E}_{\text{in}} + r_1 r_2 a^2 \vec{E}_{\text{res}} e^{i\delta}. \tag{4.2}$$

This equation allows to determine the resonating field $\vec{E}_{\text{res}}$ in terms of $\vec{E}_{\text{in}}$. The reflected and transmitted fields then can be obtained from

$$\vec{E}_{\text{r}} = r_1\vec{E}_{\text{in}} - a^2 t_1 r_2 \vec{E}_{\text{res}}, \tag{4.3}$$

$$\vec{E}_{\text{t}} = a t_2 \vec{E}_{\text{res}}. \tag{4.4}$$
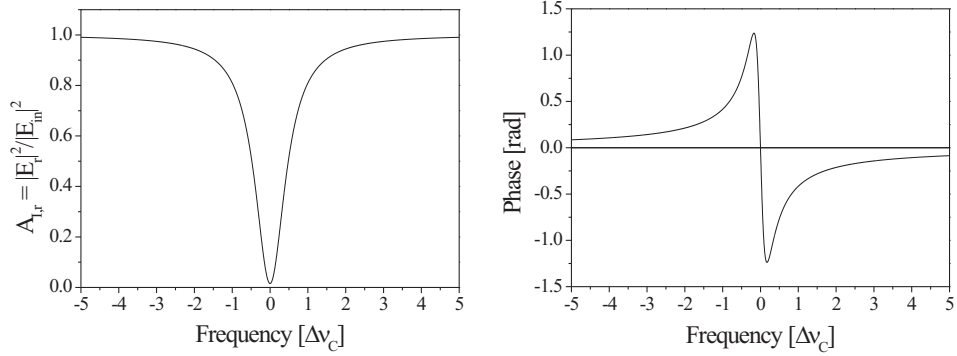
Figure 4.1: *Basic scheme of a Fabry-Pérot resonator and transfer functions for intensity (top left) and phase (top right) of the light reflected from a Fabry-Pérot resonator.*

Combination of all above equations yields the steady state transfer functions $A_{E,r/t} = |\vec{E}_{r/t}|/|\vec{E}_{in}|$ for the transmitted and reflected amplitudes:

$$A_{E,r} = \frac{r_1 - r_2 a^2 e^{i\delta}}{1 - r_1 r_2 a^2 e^{i\delta}}, \tag{4.5}$$

$$A_{E,t} = \frac{\sqrt{1 - r_2^2}\sqrt{1 - r_1^2}}{1 - r_1 r_2 a^2 e^{i\delta}}. \tag{4.6}$$

The phase ϕ of the reflected and transmitted fields can be obtained from

$$\tan \phi_r = \frac{\Im[\vec{E}_r]}{\Re[\vec{E}_r]}, \tag{4.7}$$

$$\tan \phi_t = \frac{\Im[\vec{E}_t]}{\Re[\vec{E}_t]}. \tag{4.8}$$

The intensity transfer functions $A_{I,r/t}$ are obtained by taking the absolute square of equations (4.5) and (4.6). This results in

$$A_{I,r} = 1 - \left(1 - \left[\frac{r_1 - r_2 a^2}{1 - r_1 r_2 a^2}\right]^2\right) F(\delta), \tag{4.9}$$

$$A_{I,t} = \frac{(1 - r_2^2)(1 - r_1^2)}{(1 - r_1 r_2 a^2)^2} F(\delta). \tag{4.10}$$

Here, $F(\delta)$ is the Airy function which describes the dependence of the transmitted and reflected power on the detuning $\delta = 4\pi\nu L/c$:

$$F(\delta) = \frac{1}{1 + (\frac{2\mathcal{F}}{\pi})^2 \sin^2 \delta/2} \tag{4.11}$$

with the so-called Finesse

$$\mathcal{F} = \frac{\pi(r_1 r_2 a^2)^{\frac{1}{4}}}{1 - \sqrt{r_1 r_2 a^2}}. \tag{4.12}$$

The frequency separation of two maxima of equation (4.11) is denoted the free spectral range (FSR), given by $c/2L$. For small detunings δ equation (4.11) can be approximated using $\sin(\delta/2) \approx \delta/2$ resulting in a Lorentzian function:

$$F(\delta) = \frac{1}{1 + (\frac{\mathcal{F}}{\pi}\delta)^2}. \tag{4.13}$$

The full width at half maximum $\Delta\nu_C$ of this Lorentzian curve with respect to frequency is given by

$$\Delta\nu_C = \frac{\text{FSR}}{\mathcal{F}}. \tag{4.14}$$

37

Optical impedance matching

Equations (4.9) and (4.10) yield maximum transmitted respectively minimum reflected power, if an input mirror reflection of $r_1 = r_2 a^2$ is chosen. If this condition is met the cavity is optimally impedance matched and the difference in reflectivity of front and back mirror just compensates for the cavity round trip losses. Fabrication of a high-finesse cavity ($\mathcal{F} > 10^5$) requires mirror reflectivities of better than $(1 - 10^{-4})$. Thus, very accurate control of mirror coating quality and mirror substrate losses is needed, in order to obtain optimum impedance matching. Indeed, the fabrication of a high-finesse cavity with $\mathcal{F} > 500000$ and an impedance matching which allows for a coupling $> 50\%$ is extremely delicate and reaches the limit of state of the art coating technology. A bad impedance matching results in a decreased coupling of only a few percent of the incident light or worse. Typically, this occurs due to mirror losses and comes along with a degradation of the Finesse.

Gaussian cavity modes

The mode spectrum of Hermite-Gaussian modes of a vacuum Fabry-Pérot cavity of length L and mirror curvatures R_a and R_b can be calculated from [KL66]

$$\nu_{q,m,n} = \frac{c}{2L} \left[q + \frac{m+n+1}{\pi} \arccos \sqrt{g_a g_b} \right]. \tag{4.15}$$

Here, q is the longitudinal, m and n are the transverse electromagnetic (TEM) mode numbers, and $g_{a,b} = (1 - L/R_{a,b})$. The desired cavity mode for frequency stabilization is the transverse mode with $m = n = 0$ (TEM$_{00}$), because it is non-degenerate and best matches the intensity profile of the laser beam incident onto the cavity.

4.1.2   Properties of the applied cavities

The specific properties of the applied cavities R1 and R2 are listed in Table 4.1. All resonators are made from a cylindrical fused silica spacer with a center bore hole and mirrors optically contacted to each side (see Figure 4.2). The mirrors are BK7 substrates coated with a dielectric high-reflectivity (HR) coating at 1064 nm. With the resonators mounted inside an evacuated chamber, the light confined between the mirrors travels in vacuum. The quality of the two resonators turned out to differ substantially. Only resonator R1 exhibits a Finesse > 100000, whereas the Finesse of the TEM$_{00}$ mode of R2 is affected by a damage of the HR mirror coating. This also affected the

property	symbol	R1	R2
spacer material		fused silica	fused silica
mirror substrate		BK7	BK7
index of refraction	n	1	1
length	L [cm]	2.85	10
ROC	R [cm]	50	50
Finesse (TEM$_{00}$)	$\mathcal{F}$	170000	20000
linewidth (TEM$_{00}$)	$\Delta\nu_C$ [kHz]	30	70
FSR	$c/2L$ [GHz]	5	1.5
TEM$_{00}$/TEM$_{10}$ separation	$\nu_{00} - \nu_{10}$	554 MHz	307 MHz
waist	w_0 [μm]	170	225
operation		rotating	stationary

Table 4.1: *Properties of the two resonators R1 and R2 applied in this experiment. ROC = radius of curvature.*

impedance matching of the cavity, limiting the maximum achievable coupling to $\sim 10\%$.

4.1.3 Mounting of the cavities

The cavity R1 is placed inside a copper mount as shown in Figure 4.3. The mount has been plated with gold to prevent oxidation and ensure a good thermal contact to the cavity. To provide a well defined two-line contact between the resonator and the copper mount, the resonator is supported on a u-profile and fixed by two copper strips, slightly pressing it from above. Together with R1 another identical resonator was placed inside the copper mount, with its optical axes oriented perpendicular to R1. This third cavity was added to enable comparison of two rotating resonators. However, it turned out to be damaged and featured a linewidth of only 400 kHz for the TEM$_{00}$ mode. Thus, it was of no further use during this experiment.

The whole assembly is mounted in vacuum inside a liquid-Helium bath cryostat, operated at room temperature. The cryostat's design is sketched in Figure 4.5. As the experiment evolved from a setup using cryogenically cooled resonators [MHB$^+$03a], the straight forward approach was to make use of the cryostat applied there. Used as a simple vacuum chamber, it provides excellent thermal insulation also at room temperature. The time constant for ambient temperature fluctuations penetrating to the probe chamber is about 6 h. Optical access to couple the laser light to the resonators is provided
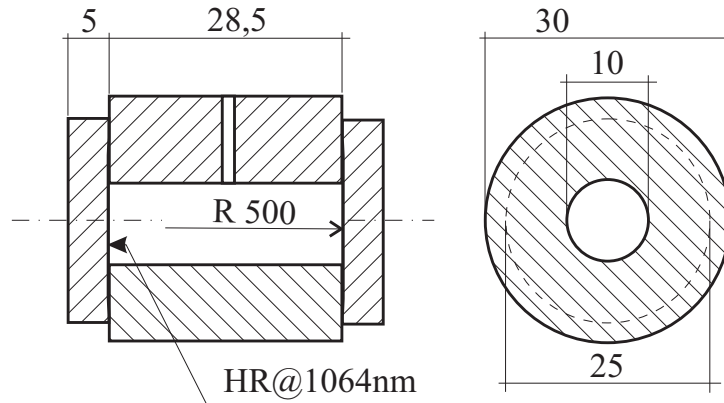
Figure 4.2: *Schematic assembly of resonator R1. Numbers are in units of mm. The mirrors are BK7 substrates with a curvature of $R = 500\,$mm, coated with a high reflection (HR) coating at 1064 nm and optically contacted to the fused silica spacer. The design of R2 is the same, apart form the length of the spacer which is $L = 100\,$mm there.*
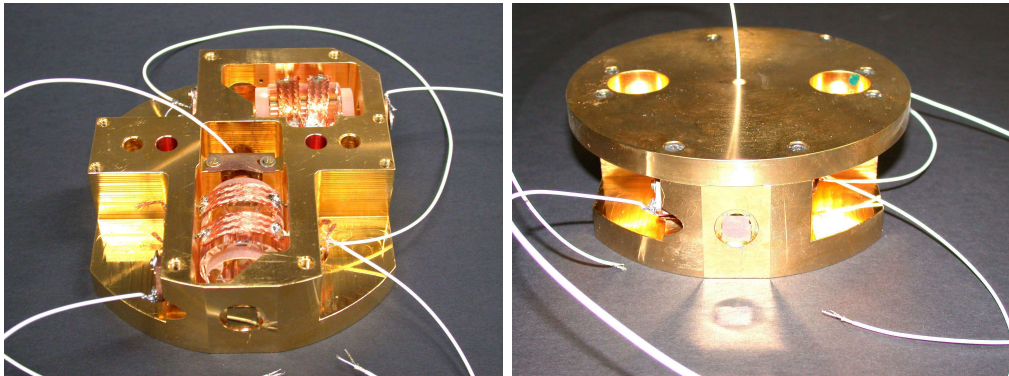
Figure 4.3: *Mounting of resonator R1 and an additional identical resonator. The resonators are placed inside a massive gold-plated copper mount to provide a homogenous temperature for both resonators. The resonators' optical axes are oriented perpendicular to each other. The mount is equipped with polarizers in front of the resonators and photodiodes to detect the reflected and transmitted light.*
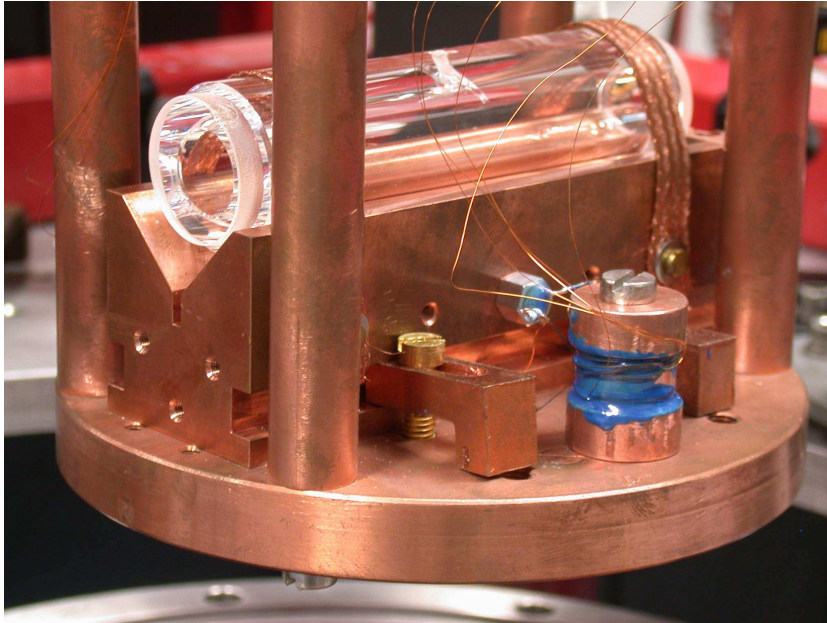
Figure 4.4: *Mounting of resonator R2 inside the second non-rotating vacuum chamber.*

through windows on opposite sides of the chamber. The resonator mount is equipped with a polarizer and a beam splitter in front of the resonator, as well as two InGaAs photodiodes to detect the transmitted and reflected light. The reflected and transmitted signals are transferred to the outside via coaxial cables and an electrical feedthrough on top of the chamber.

The stationary reference resonator R2 is placed inside a second identical cryostat, supported by a v-shaped copper mount (Figure 4.4). This second cryostat was operated at room temperature as well. Optical access is provided from both sides through windows, and transmitted and reflected signals can be accessed outside the chamber.

4.2   Laser frequency stabilization setup

A schematic drawing of the complete setup for frequency stabilizing laser L1 to R1 and laser L2 to R2 is given in Figure 4.11. The stationary setup with R2 and L2 resided in another laboratory and light from L2 was transferred to the setup of L1 and R1 using a polarization-maintaining single-mode fiber of 40 m in length. Details of these setups and some basic issues of frequency stabilization are described in the following.

electrical feedthroughs

vacuum pump

pressure gauge
fitting

LHe tank / 13 l
(empty)

thermal shield
(stainless steel)

bellows

180 cm

flange

LHe tank / 1 l
(empty)

thermal shields
(copper)

thermal sensors

heaters

copper holder

resonators inside
copper mount

optical access

windows

26 cm
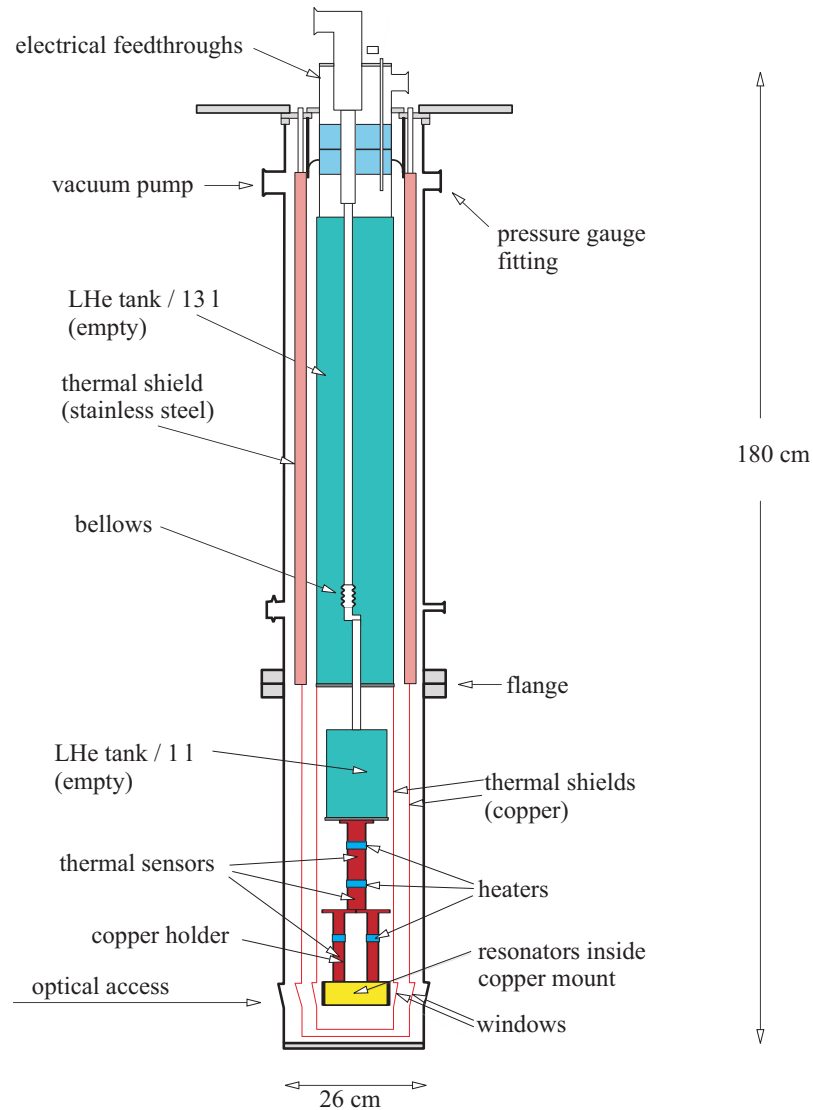
Figure 4.5: *Schematic of the vacuum chamber which actually is a liquid-Helium bath cryostat that had been used during past work applying cryogenically cooled resonators [MHB+03a]. The cryostat proofed to be suitable for this experiment, as it provides good thermal insulation at room temperature with a time constant of ∼6 h.*

4.2.1 The Nd:YAG lasers

Two Nd:YAG lasers with 1064 nm emission wavelength are applied to interrogate the resonance frequencies of the two cavities. Both are based on the non-planar ring oscillator design (NPRO, [KB85]). Thus, they are of compact dimensions and offer good intrinsic free-running frequency stability (~ 10 kHz linewidth at 1 ms).

Tuning of the laser frequency is achieved in two different ways. A piezo-electric crystal attached to the NPRO allows fast tuning of the laser frequency by means of varying strain of the NPRO. This channel offers a tuning range of several ten MHz at a rate of a up to a few MHz. A frequency span of 40 GHz is accessible by tuning the laser crystal temperature in a range of 20° C to 40° C. The mode-hop-free tuning range is about 15 GHz.

Laser	L1	L2
model	LWE 122	Innolight GmbH (LZH)
max output power	200 mW	2 W
tuning coeff. piezo	4.4 MHz/V	2 MHz/V
tuning coeff. temp.	3.1 GHz/K	5 GHz/K
noise eater	yes	no

Table 4.2: *Characteristics of the NPRO Nd:YAG lasers used in this experiment. Laser L1 is used in the rotating setup, laser L2 in the stationary setup. LWE: Lightwave Electronics Inc. LZH: Laserzentrum Hannover.*

4.2.2 Optics setup

Each of the two lasers is followed by a two-stage optical isolator (> 60 dB isolation), in order to prevent back reflections of light into the laser crystal. A good optical isolation is especially important because even tiny such reflections are known to strongly disturb the laser output frequency. Behind the optical isolator, a polarizing beam splitter (PBS) cube in combination with a $\lambda/2$-plate in every system serves for adjusting the laser intensity and allows to split off < 10 mW of the laser light for frequency comparison to the other laser. The horizontal polarization is sent to the cavity. Note, that the cavities' resonance frequencies for s- and p-polarization are non-degenerate at several kHz frequency difference. This is partly due to deviations of the mirror curvature along different orientations. Furthermore, time dependent effects from relocation processes within the mirror coating [Sto98] have been observed. Thus, rotations of polarization of less than 1° can result in frequency deviations of a few Hertz. Consequently, Polarcor polarizers were
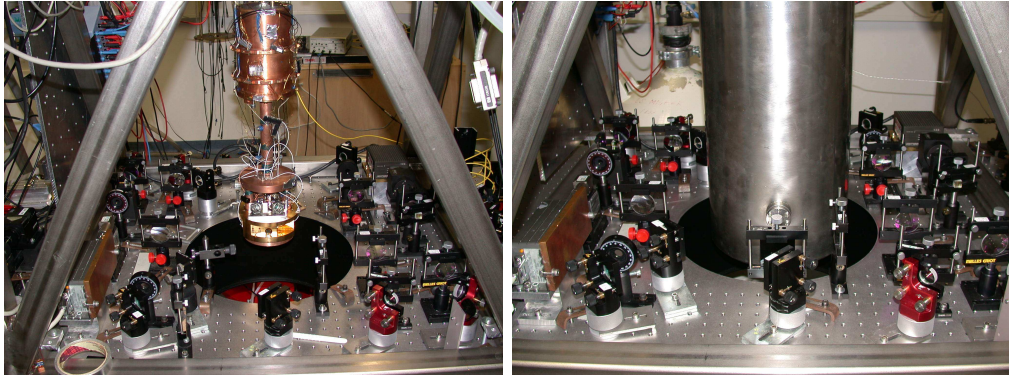
Figure 4.6: *The rotating optical setup before and after closing the vacuum chamber. Laser L1 and the optics for coupling the light to R1 can be seen to the right side in the pictures. To the left in each picture, another laser system for stabilization to the second (damaged) resonator can be seen, which was not used for the actual measurements. For more details see Figure 4.11.*

placed as the last optical element in front of the resonators, in order to provide a well defined linear polarization .

Coupling the laser light to a resonator TEM_{00} mode required a good mode matching, i.e. to form a Gaussian beam that matches the mode defined by the cavity geometry. Special care has been spent on this in setting up an appropriate telescope in front of the resonator. A beam waist can be generated outside the cavity, which matches the waist required for the cavity, and which is then imaged onto the cavity site. However despite all efforts, no coupling of more than 10% of the light impinging the cavities could be achieved, due to the bad impedance matching of the cavities.

The laser power coupled to the cavities was $\sim 10 \, \mu W$. This reduces possible thermal effects from dissipation of laser power, that could affect the cavity frequency stability. Still, it is enough light to generate an error signal of sufficient signal to noise ratio.

Last but not least, all parasitic etalons have to be avoided within the laser beam path. Thus, only anti-reflection coated lenses, windows etc. have been applied and have been tilted with respect to the incident laser beam if possible.

Photodetectors

Beam movements with respect to the photodiode's sensitive surface have been observed to produce phase shifts of the detected signal [Tro05], which lead to frequency deviations of several Hertz. To prevent this effect good pointing

stability must be achieved e.g. by mounting the photodiodes close to the cavity preferably inside the vacuum chamber. However, with the detectors inside the chamber, an adjustment of the photodiode position is not possible after the chamber has been closed. As a consequence, large area photodiodes had to be used, contributing a capacity of about 500 pF, which can be reduced to $\sim$ 200 pF applying reverse bias. This capacity is further increased by about 200 pF due to the long (2 m) coaxial cable that connects the photodiode with the front end amplifier, directly attached to the electrical feedthrough on top of the chamber. This large input capacity of $\sim$ 400 pF disfavors the use of transimpedance amplifiers. This is because the complex impedance of cable and detector favors oscillations of the amplifier and the high capacity strongly amplifies voltage noise at the amplifier input. Thus, a photodetector with very low voltage noise is required. Such a photodetector has been developed especially for this application by H. Müller [Mül04], applying eight paralleled MOSFETs that feature high transconductance and low input capacitance. The input noise of this detector was measured to be as low as $3 \, \text{pA}/\sqrt{\text{Hz}}$.
For the stationary resonator R2 the photodiodes were not mounted inside the vacuum chamber. Instead, a photodetector front end was placed outside, in front of the chamber window, to detect the signal reflected from the cavity. A transimpedance amplifier design was chosen here, based on an integrated circuit (NE/SA5211) with an internal 28 kΩ impedance and a 3 dB bandwidth of 180 MHz. This circuit is specified for a dark current noise of $1.8 \, \text{pA}/\sqrt{\text{Hz}}$. Finally, within both setups special attention was spent to slightly tilt the photodiode surface with respect to the incident laser beam, in order to avoid parasitic resonances with the cavity mirror.

4.2.3 Free-running frequency stability

Due to a sophisticated compact design, the NPRO Nd:YAG lasers provide light of excellent intrinsic frequency stability. However, residual frequency fluctuations and drift arise due to vibrations, temperature fluctuations and instabilities in the driving current of the pump laser diodes. Typical drifts are about 1 MHz/h, while fluctuations on timescales of ms are on the order of several kHz. The spectral noise density of frequency fluctuations of the free-running laser L1 is shown in Figure 4.7, which is representative for L2 as well. The bottom graph there gives the corresponding Allan deviation.

A fundamental limit for the free-running frequency stability of a laser is set by spontaneously emitted photons, which incoherently add to the laser field and cause a random phase diffusion. This is called the Schawlow-Townes

limit [ST58]. Its spectral noise density in units of $\mathrm{Hz}/\sqrt{\mathrm{Hz}}$ is given by

$$S_{f,ST} = \delta\nu_R\sqrt{\frac{2h\nu}{P}}. \tag{4.16}$$

$\delta\nu_R$ is the laser resonator linewidth, ν the laser's frequency and P the output power of the laser. Naturally, $S_{f,ST}$ scales with the inverse of the square root of laser power, as contributions of spontaneously emitted photons to the phase of the laser field become less relevant with increasing coherent laser power. Inserting the values for laser L1 ($P = 200\,\mathrm{mW}$, $\delta\nu_R = 100\,\mathrm{MHz}$) yields

$$S_{f,ST} = 0.1\,\mathrm{Hz}/\sqrt{\mathrm{Hz}} \tag{4.17}$$

or a corresponding Schawlow-Townes linewidth of

$$\Delta\nu_{ST} = \pi S_{f,ST}^2 = 0.03\,\mathrm{Hz}. \tag{4.18}$$

As evident from Figure 4.7, the free-running frequency stability below $100\,\mathrm{Hz}$ is orders of magnitude above the fundamental Schawlow-Townes limit. An extrapolation of the $1/f$-behavior of frequency noise towards higher frequencies shows that it might only be reached above $100\,\mathrm{kHz}$. However, using active feedback it is possible to suppress frequency fluctuations, in principle even below the Schawlow-Townes limit.

4.2.4 Basics of a control loop for laser frequency stabilization

Stabilization of the laser frequency ν_L to the cavity resonance ν_C is done using active feedback. The basic scheme of such a laser stabilization control loop is depicted in Figure 4.8. The laser frequency ν_L is continuously compared to the resonator resonance frequency ν_C. The deviation $e = \nu_C - \nu_L$ is converted to an error signal by means of a discriminator of slope $D(\omega)$ (given in V/Hz). This error signal is processed by the servo electronics with a transfer function $G(\omega)$. The control signal generated from this is fed back to the laser by means of an actuator. In the present setup this is the piezo-electric crystal attached to the NPRO. It allows to tune the laser frequency with a transfer function $K(\omega)$.
In the open loop a deviation $e = \nu_C - \nu_L$ will thus cause a correction of the laser output frequency ν_L' given by

$$\nu_L' = KGDe. \tag{4.19}$$
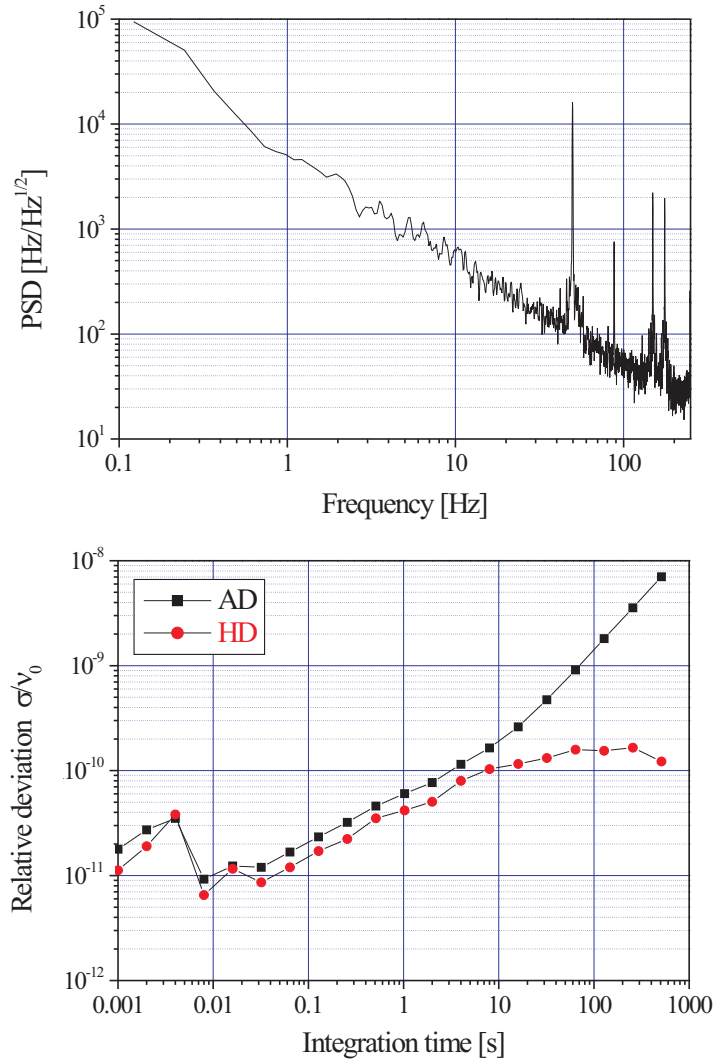
Figure 4.7: *Free-running frequency stability of laser L1. Top: The power spectral density falls off $\sim 1/f$ towards higher frequencies, presumably reaching the Schawlow-Townes limit above $\sim100\,kHz$. Bottom: The corresponding Allan (AD) and Hadamard (HD) deviations show random walk frequency noise up to $\tau = 10\,s$ and a large drift on timescales above.*

47
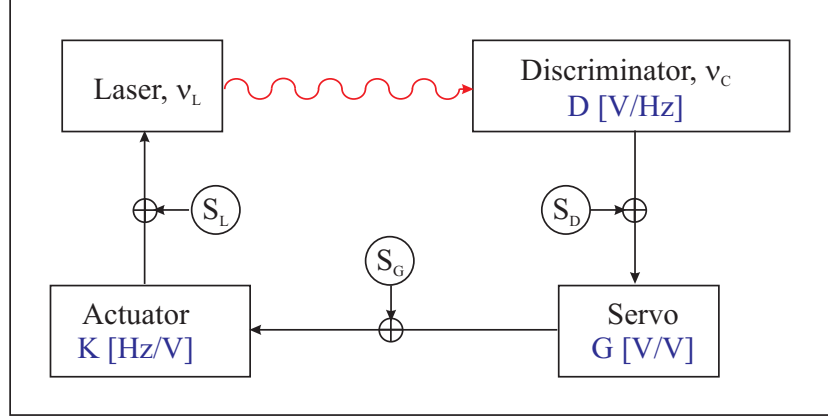
Figure 4.8: *Block diagram for laser frequency stabilization applying active feedback (see text for details).*

KGD is referred to as the open loop gain. If the feedback loop is closed ($\nu_L = \nu'_L$) one obtains

$$\nu_L = \frac{KGD}{1 + KGD}\nu_C. \tag{4.20}$$

Thus, high open loop gain is required to achieve a reliable tracking of the reference frequency. Even more, variations of the open loop gain do not affect tracking of the reference frequency as long as $KGD \gg 1$. However, in practice feedback gain in a closed loop cannot be increased infinitely. Delays in the feedback path cause a phase shift, which typically increases with frequency. Therefore, every closed feedback loop starts to oscillate, if the gain at frequencies with 180° phase shift is increased beyond unity. Consequently, a feedback loop must apply appropriately shaped transfer functions that provide sufficient gain at the relevant frequencies while still matching this stability requirement.

Noise contributions within the feedback loop

In a closed feedback loop additional noise sources such as servo noise S_G and discriminator noise S_D, contribute to the total laser frequency noise $S_{L,cl}$. Geometrically adding all noise sources according to Figure 4.8 yields

$$S_{L,cl}^2 = \frac{S_L^2 + K^2 S_G^2 + K^2 G^2 S_D^2}{|1 + KGD|^2}. \tag{4.21}$$

Considering the ideal case of infinite open loop gain KGD, this expression reduces to

$$S_{L,cl} = \frac{S_D}{D}. \tag{4.22}$$
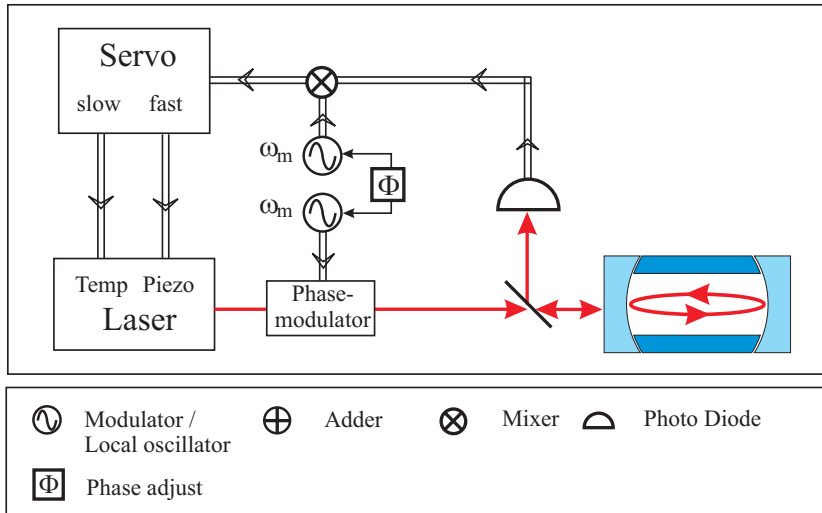
Figure 4.9: *Basic setup of PDH frequency stabilization. The laser light is phase-modulated at ω_m. The light reflected from the cavity is detected and the beat note between sidebands and carrier is demodulated phase-sensitively. The signal obtained for $\Phi = 90°$ and $\omega_m \gg 2\pi\Delta\nu_C$ is an error signal as shown in Figure 4.10. This signal is fed back to the laser for tuning its frequency to the cavity resonance.*

Thus, within a well designed feedback loop the only limit for suppression of laser frequency fluctuations arises from the discriminator properties, as long as enough loop gain can be applied.

4.2.5 Pound-Drever-Hall frequency discrimination

In the present experiment frequency discrimination is implemented following a scheme that was developed by R.V. Pound [Pou46] for microwave applications, and later transferred to and realized for optical frequencies by R. Drever and J.L. Hall [DHK+83]. Thus, it is referred to as the Pound-Drever-Hall (PDH) locking scheme here. There is an extensive literature on frequency stabilization using the PDH-technique, and most of the relevant aspects here are described in detail elsewhere [SHH88, DGB92, ZH93, YCIB99]. The principle setup is shown in Figure 4.9. The laser phase is modulated at an rf frequency ω_m, which can be written as a sum over sidebands at multiples

of ω_m:

$$E(t) = E_0 e^{-i\omega_L t} e^{-i\beta \sin(\omega_m t)}$$
$$= E_0 \sum_{k=-\infty}^{\infty} J_k(\beta) e^{-i(\omega_L + k\omega_m)t}, \tag{4.23}$$

where $J_k(\beta)$ are the Bessel functions of order k, and β denotes the modulation index. Coupling the modulated laser light to the resonator causes amplitude and phase shifts of the reflected and transmitted carrier and sidebands. These can be described using the transfer functions $A_{E,r}(\omega)$ and $A_{E,t}(\omega)$ of section 4.1.1. If only the first order sidebands in reflection are considered, one obtains

$$E_r(t) = E_0 e^{-i\omega_L t} \left[J_0(\beta)|A_r^{(0)}|e^{-i\phi^0} \right.$$
$$\left. -J_1(\beta)|A_r^{(-1)}|e^{i(\omega_m t - \phi_{-1})} + J_1(\beta)|A_r^{(+1)}|e^{-i(\omega_m t - \phi_{+1})} \right], \tag{4.24}$$

where the transfer functions have been decomposed into phase and amplitude contributions: $A_r = |A_r^{(k)}|e^{-i\phi_k}$. The phase shifts ϕ_k depend on the respective detuning $e = \nu_C - \nu_L$ from the cavity resonance as shown in Figure 4.1. From squaring equation (4.24) the beat note signal between reflected carrier and sidebands can be derived:

$$S \sim 2|E_0|^2 \mathrm{Re}\left(J_0(\beta)J_1(\beta)e^{i\omega_m t}[e^{i(\phi_0 - \phi_{+1})} - e^{i(\phi_{-1} - \phi_0)}] \right). \tag{4.25}$$

According to Figure 4.1 for $\omega_m \gg 2\pi\Delta\nu_C$ one finds $\phi_{+1} \approx -\phi_{-1}$ and the above expression can be rearranged to

$$S \sim 4|E_0|^2 J_0(\beta)J_1(\beta)\sin(\phi_0)\sin(\omega_m t - \phi_1). \tag{4.26}$$

Thus, the dispersive properties of the resonator effectively turn the phase modulation of the laser light into an amplitude modulation. Demodulating this signal at ω_m to DC results in an error signal, which according to the term $\sin(\phi_0)$ in equation (4.26) exactly vanishes and changes sign for zero detuning ($\phi_0 = 0$) at the cavity resonance. Details on calculating the full expressions for PDH error signals that go beyond the simple approximation of equation (4.26) can be found e.g. in [Mül04]. Figure 4.10 compares a calculated and a measured error signal obtained for resonator R1 in reflection. The center slope of this error signal is already accurately predicted by the simple approximation of equation (4.26) for $\omega_m \gg 2\pi\Delta\nu_C$.
In terms of photocurrent it can be expressed in units of A/Hz [DGB92] as

$$D = \frac{8J_0(\beta)J_1(\beta)}{\Delta\nu_C} \frac{e\eta\kappa P_i}{h\nu}, \tag{4.27}$$
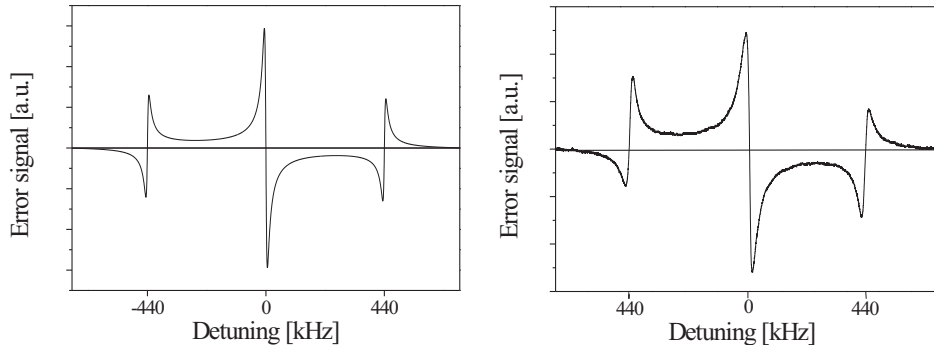
Figure 4.10: *A calculated (left) and measured (right) PDH error signal from R1. Note that the calculation only includes the first order sidebands. The cavity linewidth is about 30 kHz and a modulation frequency of $\omega_m/2\pi = 440$ kHz is applied. The modulation index is adjusted to ~ 1.*

where P_i is the power incident on the cavity, $\Delta\nu_C$ is the cavity linewidth and η is the quantum efficiency of the photodetector. The factor $\kappa < 1$ has been included to account for the actual impedance matching of the cavity. The error signal slope reaches a maximum value for a modulation index $\beta = 1.08$. With $\Delta\nu_C = 30$ kHz, $P_i = 100\,\mu$W, $\eta = 0.7$ and $\kappa = 0.1$ this results in an error signal slope of ~ 1 nA/Hz.

Implementation of the PDH scheme

A modulation frequency of $\omega_m/2\pi = 444$ kHz was chosen for laser L1, corresponding to the highest pronounced resonance of the piezo-electric actuator. This modulation is provided by a signal generator HP 33120A. The photodetector signal at this frequency is amplified to > 0 dBm using the front end amplifiers described above, followed by commercial low-noise amplifiers (MiniCircuits, ZFL500LN). The PDH error signal is generated using a double-balanced mixer (MiniCircuits, ZFM3) and a local oscillator (HP 331208), which is phase-locked to the modulation signal at ω_m with a phase offset of 90°. The error signal is low-pass filtered with a corner frequency of 100 kHz at the mixer output and fed into the servo electronics.

The same scheme was applied for laser L2. There a higher resonance of the piezo actuator at $\omega_m/2\pi = 770$ kHz was used, which is more favorable, as laser intensity noise decreases with increasing frequency. Different other schemes with modulation at frequencies > 1 MHz or demodulation at the

third harmonic of ω_m have been tried as well, but offered no improvement. The latter method is insensitive to a residual amplitude modulation (RAM) at ω_m. This RAM leads to an offset of the error signal as shown in [Mül04]. In the present setup however, the piezo-electric actuators yield very low RAM on the order of 10^{-4} to 10^{-5}.

4.2.6 Loop filter and frequency transducers

Given a PDH error signal of sufficient signal-to-noise ratio, the decisive issue is the design of the loop filter transfer function $G(\omega)$ implemented in the servo electronics. The aim here is to provide maximum gain at the relevant frequencies and sufficient locking bandwidth, while still meeting the stability requirement. In the present experiment, the relevant regime for frequency stability is below a few Hertz and the required locking bandwidths are on the order of several ten kHz only. This is due to the intrinsically narrow free-running laser linewidth of the NPRO Nd:YAG laser ($\sim 10\,\mathrm{kHz}$). Thus, the piezo-electric crystals attached to the NPRO were used as the only fast frequency actuators here, which limits the locking bandwidth to below $100\,\mathrm{kHz}$ because of mechanical resonances of the piezo.

The loop filter comprises a variable proportional gain and two integrators. The first integrator's corner frequency could be varied among six discrete frequencies between $f_{I1} = 70$ and $150\,\mathrm{kHz}$. The second integrator was set at $f_{I2} = 6\,\mathrm{kHz}$. This provided sufficient gain and locking bandwidth ($\sim 30\,\mathrm{kHz}$) to suppress residual error signal fluctuations at frequencies $< 1\,\mathrm{kHz}$ below a level of $1\,\mathrm{Hz}$. Other combinations of integrators and low-pass filters or notch filters to circumvent the first piezo resonance which limits the locking bandwidth have been tried, but did not achieve a further increase of the locking bandwidth. However, the fundamental limitation of the achieved frequency stability is not attributed to the limited locking bandwidth or the performance of the lock electronics in general. Thus, the implementation of more elaborate schemes to improve on this has been postponed for a future setup. Such schemes applying a combination of various faster actuators have been described in [ZH93, DGB92, SHH88]. Further general ideas about the optimum loop filter design for frequency stabilization can be found in [HTY99] and references therein.

4.2.7 Beat frequency measurement

Measurements of the relative frequency stability of R1 and R2 are performed by generating direct beat notes between light of the two frequency-stabilized lasers. A small fraction of laser light ($\sim 1\,\mathrm{mW}$) from each system is overlapped

on a fast photodiode (New Focus, 1537, 6 GHz). Selection of appropriate TEM$_{00}$ modes of the cavities always allows to obtain a difference frequency within the frequency range ≤ 2 GHz of the available synthesizer (Marconi, 2031). This synthesizer serves as a local oscillator to mix down the beat note to < 250 MHz, which can then be counted directly using a SRS SR620 counter. A low-pass filter at 250 MHz prevents aliasing of harmonics above the bandwidth of the frequency counter of 300 MHz.

In its standard mode of operation, the counter samples the beat frequency applying a gate time of 1 s. Alternatively, it can be operated in a "fast mode", which allows to record the beat frequency at gate times as low as 1 ms. Both counter and local oscillator are phase-locked to an external frequency reference. The latter is a rubidium-based atomic clock (Efratom, FRT) with a relative frequency stability of 10^{-11} above integration times of 1 s. This is sufficient to provide a local oscillator frequency, stable to better than 0.01 Hz. Thus, laser frequency stability at 1 s and above can in principle be determined down to Allan deviations as low as 3×10^{-17}.

4.3   Relative frequency stability of R1 and R2

A typical 24 hour measurement of the beat frequency of R1 and R2 is presented in Figure 4.12. This measurement has been done without rotating R1. A large average drift of ~ -40 Hz/s is observed, caused by relative temperature changes of the resonators. The bottom graph shows the residual frequency fluctuations after a removal of the drift by filtering the data with a numerical high-pass filter of corner frequency $f_c = 1/(200\,\text{s})$ (see section 4.6 for details on the data processing). The frequency measurement exhibits flicker noise with rms-fluctuations on the order of 20 Hz.

In order to give a quantitative measure of frequency stability, the Allan and Hadamard deviation are calculated here [Rut78]. The first is the most common measure of frequency stability in the time domain, while the latter is a similarly defined three-point variance, which is insensitive to linear frequency drift (see Appendix A for definitions). Such a linear drift can easily be discerned from a Lorentz violation signal. Therefore, the Hadamard deviation is more appropriate to point out the limitations of this experiment. Figure 4.13 presents the Allan and Hadamard deviations calculated from a ~ 1000 s subset of the data of Figure 4.12. The Allan deviation is dominated by linear drift down to integration times as low as 1 s. The Hadamard deviation, however, reaches a minimum of 1.5×10^{-14} at $\tau = 30$ s, and nonlinear drift becomes relevant for $\tau > 100$ s only.
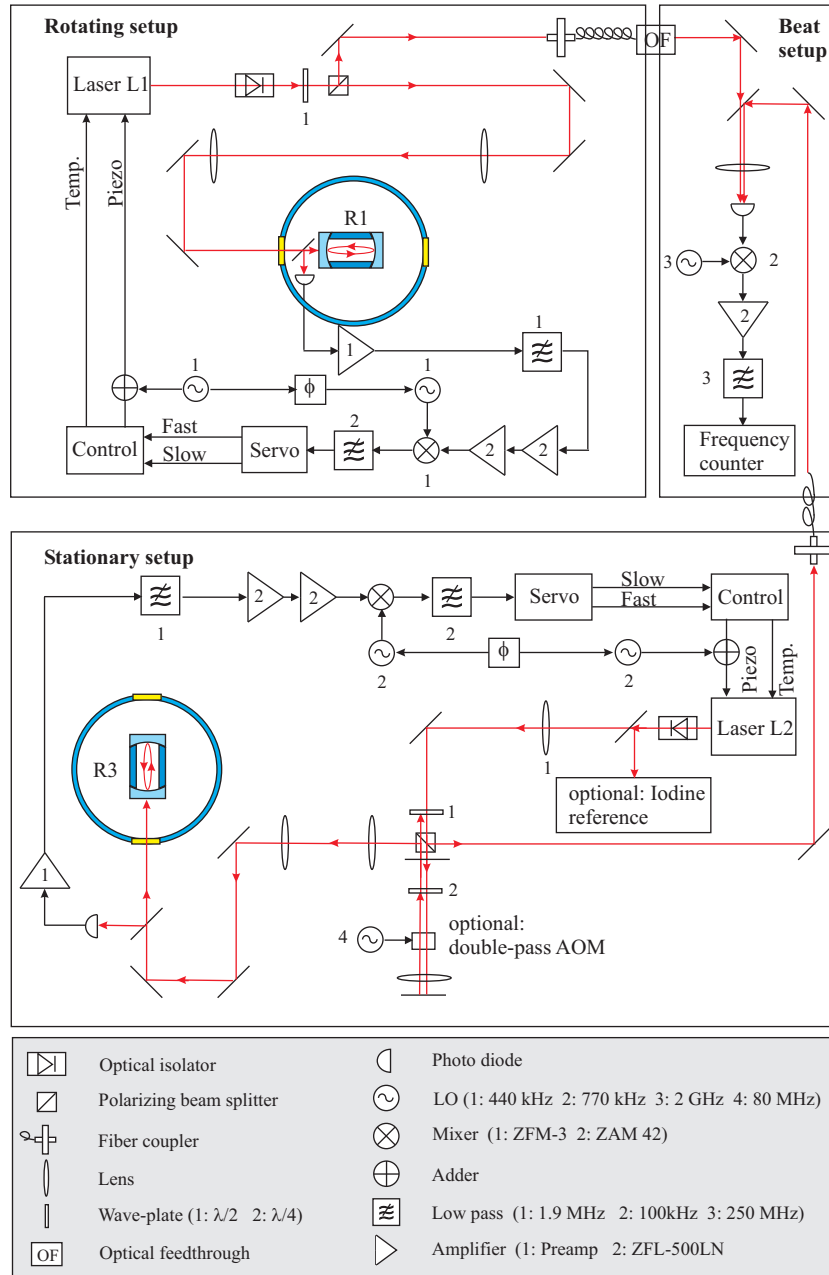
Figure 4.11: *Complete laser stabilization setup for comparison of R1 (complete setup rotating on a turntable) and R2. Light from L2 was transferred to the beat setup using a polarization-maintaining single-mode fiber of L = 40 m. The optical feedthrough is described in section 4.5.2. The optional double-pass AOM and the iodine standard were used for the measurements described in section 4.4.3. Further details of the setup are described in section 4.2.*
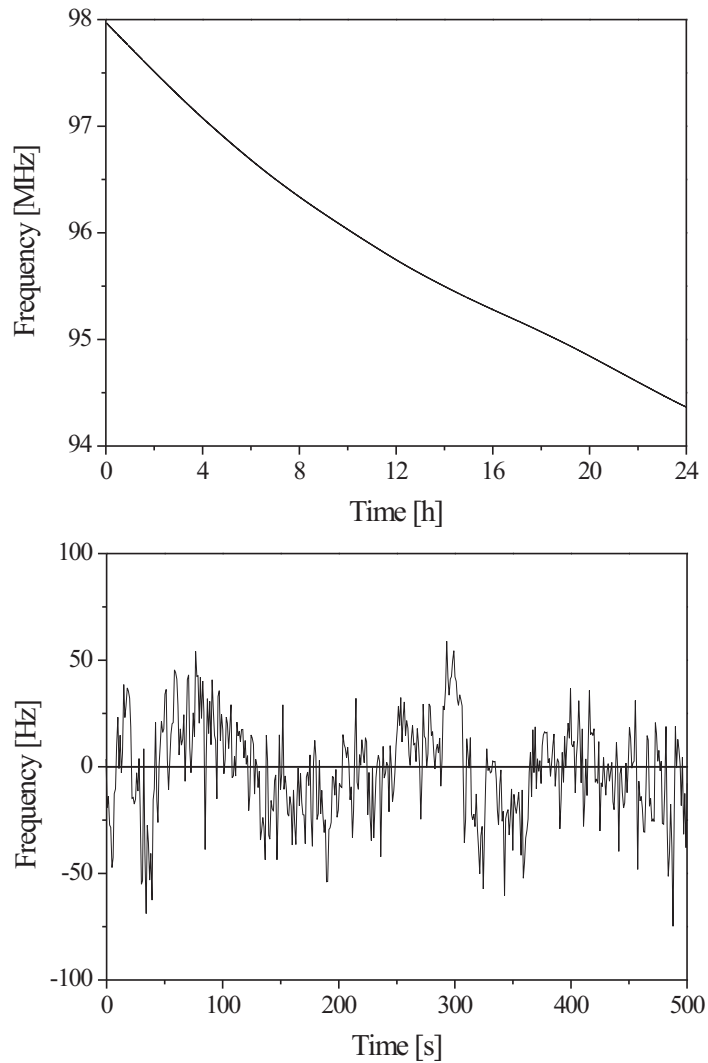
Figure 4.12: *Example of a 24 h beat frequency measurement. The beat frequency gives the frequency fluctuations of R1 relative to R2. Top: The total measurement exhibits a large drift of several MHz during 24 h. Bottom: A 500 s extract from this measurement after removal of drift, applying a numerical low-pass filter with a corner frequency of $f_c = 1/(200\,s)$ to the data.*
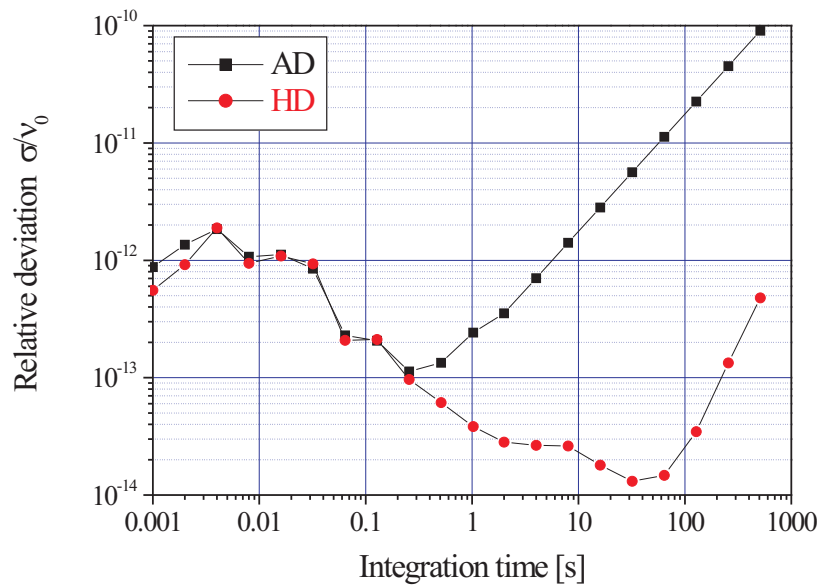
Figure 4.13: *Relative Allan and Hadamard deviation characterize the frequency stability of R1 and R2. The latter is insensitive to the large linear drift present in the measurement. Both curves have been calculated from an extract of* ∼ 2000 s *of the measurement of Figure 4.12 using AlaVar 5.2* *[Mak06].*

4.4 Limitations

Different limitations of the achieved frequency stability have been identified. Accordingly, the relative Hadamard deviation shown in Figure 4.13 can be divided into three regimes:

- Up to an integration time of 1 s the graph exhibits a bumpy structure, indicating the presence of oscillations at several discrete frequencies due to vibrations. This becomes even more evident from an FFT of the beat frequency measurement as shown in Figure 4.14

- From 1 s to 100 s integration time the Hadamard deviation turns into a flicker floor close to the 10^{-14} level. This flicker noise is caused by thermal noise of the cavity mirrors, which exhibits a $1/f$ dependence.

- Above 100 s quadratic and higher order drift due to temperature creep set in.

In what follows a closer look is spent on these regimes and the different limitations on frequency stability will be discussed.

4.4.1 Short-term stability

Doppler effect

The vacuum chamber was originally designed as a cryostat and features suspension of the resonator mount at the bottom of a thin-walled steel tube. This tube is fixed at the top of the cryostat (see Figure 4.5) and in effect constitutes a pendulum of two meters in length. Thus, the resonator mount had to be fixed against the surrounding thermal shields to dampen the pendulum resonance. Still, a resonant oscillation at about 7 Hz and harmonics could not be suppressed. These oscillations relative to the optical table contribute to frequency noise due to the Doppler effect, as is revealed by a Fourier spectrum of a frequency measurement with 1 ms gate time (bottom graph in Figure 4.14). Assuming an amplitude of 0.01 mm displacement for the pendulum oscillation at 7 Hz, the velocity amplitude for the resonator movement is $v = \pm 0.4$ mm/s and the relative Doppler shift is

$$\frac{\Delta \nu}{\nu_0} = \frac{v}{c} = 1.3 \times 10^{-12} \equiv 360 \,\text{Hz}, \tag{4.28}$$

with $\nu_0 = 2.82 \times 10^{14}$. This could well account for the peak at 7 Hz and its harmonics in Figure 4.14.

Vibrations

Vibrations of the laboratory floor are dampened by the pendulum resonance to some extent. Still, they cause strain on the cavity as estimated in e.g. [HTY99]. Several peaks in Figure 4.14 presumably originate from such vibrations. In addition to the peak due to line power exactly at $50\,\text{Hz}$ there are frequency oscillations at $\sim 49\,\text{Hz}$ and $\sim 24.5\,\text{Hz}$. These can be attributed to vibrations of the laboratory floor, caused by heavy duty electrical motors. Such motors are present all over the building e.g. in vacuum pumps, elevators or the air conditioning system. The presence of these vibrations is independently revealed by a seismometer measurement (top graph in Figure 4.14).

Suppression of such vibrations was achieved in a reconstruction of the setup by use of an active vibration isolation and an improved mounting of the (new) cavities. This will be presented in chapter 7.

Further limitations of short-term stability

Vibrations present the main limitation of short-term frequency stability in this setup. Nonetheless, other possible sources of frequency noise are analyzed here as well. In an improved setup applying new cavities as described in chapter 7 these limitations to frequency stability might become relevant.

The minimum spectral density of laser frequency noise in the closed loop is determined by the discriminator properties only, as long as enough feedback gain is provided. The relevant parameters therefore are the discriminator slope as given in equation (4.27) and the **photocurrent shot noise** of the photodetector. According to [DGB92] the latter is given by (in units of $A/\sqrt{\text{Hz}}$):

$$S_A = \sqrt{2}\sqrt{2eI} = \sqrt{2}\sqrt{2e(2J_1(\beta)J_0(\beta)\frac{e\eta P}{h\nu})} \tag{4.29}$$

Combining this with equation (4.27) results in a frequency noise density (in units of $\text{Hz}/\sqrt{\text{Hz}}$) of

$$S_f = \Delta\nu_C\sqrt{\frac{h\nu}{8J_0(\beta)J_1(\beta)\eta\kappa P}} \tag{4.30}$$

where $P_i = \kappa P$ is the optical power incident on the photodetector. Inserting the parameters for R2, $P = 10\,\mu\text{W}$, $\eta = 0.7$ and a coupling of $\kappa = 0.1$ of the laser light into the cavity mode, this sets a fundamental limit of

$$S_f = 0.07\frac{\text{Hz}}{\sqrt{\text{Hz}}} \tag{4.31}$$
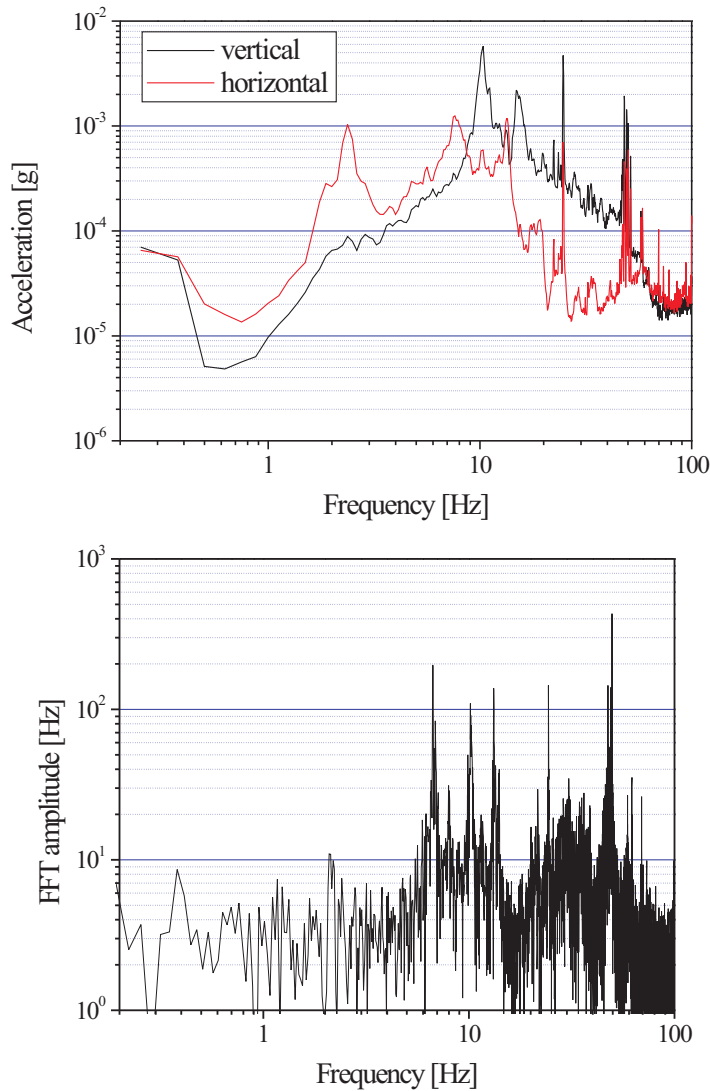
Figure 4.14: *Influence of vibrations on beat frequency short-term stability. The Fourier transform of a beat frequency measurement sampled at 1 ms reveals oscillations at several discrete frequencies of ∼100 Hz in amplitude (bottom graph). Corresponding vibrations are revealed in an FFT of a seismometer measurement (top graph, measured using a seismometer of Güralp Systems Ltd., model CMG-6T).*

Another contribution to discriminator noise is the **photodetector noise** adding $3.6\,\mathrm{pA}/\sqrt{\mathrm{Hz}}$ to the signal photocurrent (referred to the photodetector input). Conversion by means of the discriminator slope (4.27) gives the associated frequency noise:

$$S_f = 0.17 \frac{\mathrm{Hz}}{\sqrt{\mathrm{Hz}}} \tag{4.32}$$

Technical intensity noise of the laser presents another limitation on frequency stabilization. Laser L1 is equipped with a noise eater that monitors and actively suppresses intensity noise via pump-diode current feedback. The relative intensity noise spectrum of laser L2 is shown in Figure 4.15. A large relaxation peak is present at $\sim 300\,\mathrm{kHz}$, since this laser is not equipped with a noise eater. This relaxation peak is a characteristic feature of these lasers and is caused by oscillations of the population inversion of the lasing transition. Above $300\,\mathrm{kHz}$ intensity noise decreases as $1/f$ and approaches the shot noise limit at $f > 4\,\mathrm{MHz}$. Thus, problems due to intensity noise can in principle be avoided by operating with signals sufficiently above $300\,\mathrm{kHz}$. According to the measurement of Figure 4.15, the intensity noise of laser L2 at $\omega_m = 770\,\mathrm{kHz}$ contributes approximately $1\,\mathrm{pA}/\sqrt{\mathrm{Hz}}$ to the total photocurrent noise. Conversion to frequency noise results in

$$S_f = 0.05 \frac{\mathrm{Hz}}{\sqrt{\mathrm{Hz}}}. \tag{4.33}$$

Intensity noise of laser L1, which applies a noise eater, has been estimated to be below this value despite the lower modulation frequency of $440\,\mathrm{kHz}$.

The above noise densities can be converted to Allan deviations, assuming white frequency noise using the relation

$$\sigma_f = \frac{S_f}{\sqrt{2\tau}}. \tag{4.34}$$

The largest contribution, which is detector noise, thereby sets a limit to the relative Allan deviation at $\sim 4 \times 10^{-16}$ at an integration time of $1\,\mathrm{s}$.

Last but not least, frequency noise arises because light is transferred via optical fibers to the beat measurement system. The optical fibers are exposed to all kinds of ambient influences that alter the optical path length and impose **fiber phase noise** on the transmitted light. Here, fiber phase noise was measured according to the scheme described in [MYH94]. The light is sent through the optical fiber, is shifted in frequency by a double-pass AOM after the fiber by $2 \times 80\,\mathrm{MHz}$, is sent back along the same path
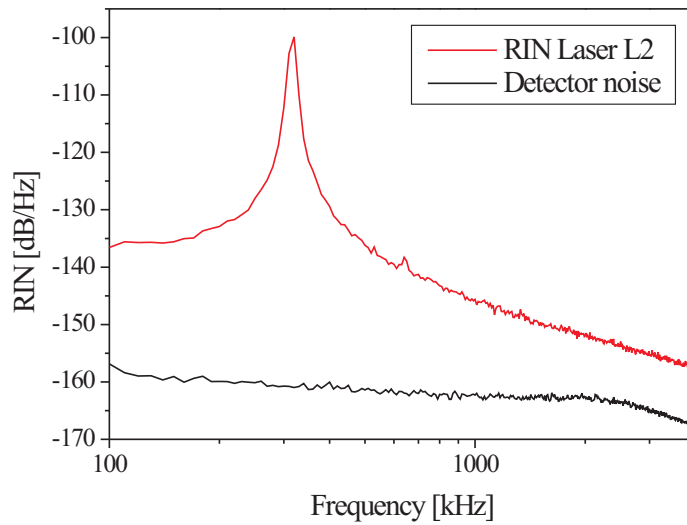
Figure 4.15: *Technical intensity noise of laser L2 expressed in terms of relative intensity noise (RIN). This is defined as the Fourier transform of the autocorrelation function $C_{pp}(\tau) = \frac{\delta P(t)\delta P(t+\tau)}{P^2}$ stated in dB. A large relaxation peak is present at $\sim 300\,kHz$. Its magnitude and frequency depend on the pump diode current and wavelength. The technical noise falls off towards higher frequencies as $1/f$, approaching the shot noise level at $f > 4\,MHz$. For laser L1, intensity noise is suppressed by a noise eater.*
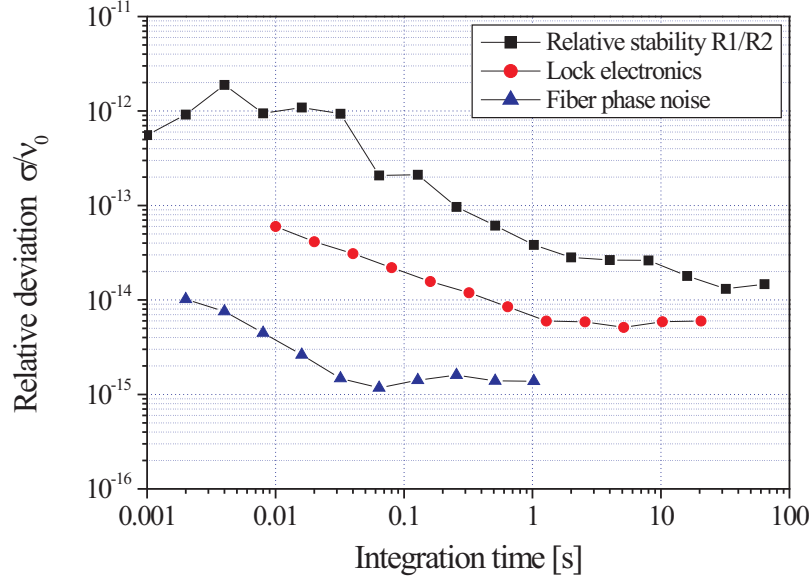
Figure 4.16: *The top curve shows the achieved stability (linear drift removed). The curve to the middle gives the Allan deviation for a comparison of laser L1 to L2, both locked to neighboring TEM$_{00}$ modes of R2. This essentially represents the lock electronics' performance. The Allan deviation determined from a measurement of fiber phase noise is also given. Both, electronics and fiber phase noise currently are not the relevant limitation to the observed frequency stability.*

and a beat note of light before and after double passing the fiber is generated. The frequency stability of this signal at 160 MHz is dominated by fiber phase noise, as all other frequency fluctuations are common mode and cancel. The Allan deviation calculated from such a measurement, using the 40 m polarization-maintaining single-mode fiber that transfers the light of L2 to the beat system, is given in Figure 4.16. As evident from this graph there is a flicker noise floor at 10^{-15} for $\tau > 0.1$ s. This does not limit the performance at the current level of sensitivity, but could become important for a future version of the experiment.

4.4.2 Flicker noise

Thermal noise

In the present setup, frequency stability above integration times of $1\,$s is limited by thermal noise of the cavities. Two kinds of thermal noise are considered here. These are thermal noise due to Brownian motion [Sau90] and thermoelastic noise [BGV99].

The effect of thermal noise arising from **Brownian motion** has been investigated extensively for high-sensitivity torsion pendulums and gravitational wave detectors [Sau90, SBS98]. It has only recently been identified as an important issue for frequency stabilization to Fabry-Pérot cavities [NKC04, NML$^+$06]. The idea is that at a finite temperature T the mechanical resonances of a macroscopic body, e.g. resonances of a mirror substrate or a complete optical resonator, are excited to a certain extent. A model to describe these resonances has been given by Saulson [Sau90], which considers structural damping as opposed to viscous damping. The fundamental difference between viscous and structural damping is elaborated briefly in what follows.

A viscously damped harmonic oscillator obeys an equation of motion of the form

$$m\ddot{x} + f\dot{x} + kx = F_{th}. \tag{4.35}$$

As a simple model, consider a mass suspended from a spring of spring constant k with a frictional damping force $F = -f\dot{x}$. F_{th} is the external force caused by thermally driven Brownian motion. Following Saulson [Sau90] the displacement spectral noise density S_x^2 expressed in m^2/Hz can be derived using the Fluctuation Dissipation Theorem (FDT) [CG52]. The latter relates the dissipation in the system, expressed by the mechanical conductance $\sigma(\omega)$, to S_x^2 as described by

$$S_x^2(\omega) = \frac{4k_B T}{\omega^2}\sigma(\omega). \tag{4.36}$$

An expression for $\sigma(\omega)$ can be derived from the above equation of motion (4.35) as follows: for a harmonic time dependence, the impedance Z defined by $F = Z\dot{x}$ is

$$Z = i(\omega m - \frac{k}{\omega}) + f. \tag{4.37}$$

The inverse of the impedance is called admittance Y and is given by

$$Y = Z^{-1} = \frac{\omega^2 f + im(\omega\omega_0^2 - \omega^3)}{m^2(\omega_0^2 - \omega^2)^2 + \omega^2 f^2} \tag{4.38}$$

using $k = m\omega_0^2$. The real part of the admittance Y is the mechanical conductance σ. Insertion into equation (4.36) gives

$$S_x^2 = \frac{4k_B T f}{m^2[(\omega_0^2 - \omega^2)^2 + \omega^2 f^2]},$$
(4.39)

which for representative values is plotted in Figure 4.17. As shown there, the displacement noise approaches a constant, low value towards far off-resonant low frequencies.

As opposed to viscous damping, structural damping does not include a frictional damping term. Instead, it can be described by a complex spring constant given by

$$k \rightarrow k(1 + i\phi(\omega)),$$
(4.40)

where ϕ is the so-called loss angle. This gives rise to dissipation within the system, and is related to the quality factor Q of the oscillator by

$$\phi = \frac{1}{Q}.$$
(4.41)

The equation of motion with an external driving force F then is

$$m\ddot{x} + k(1 + i\phi(\omega))x = F.$$
(4.42)

The mechanical impedance Z according to this equation is found to be

$$Z = i(\omega m - \frac{k}{\omega}) - \frac{k\phi}{\omega},$$
(4.43)

which is similar to equation (4.37) with f replaced by $-k\phi/\omega$. Proceeding as above and applying (4.36) results in

$$S_x^2(\omega) = \frac{4k_B T \omega_0^2 \phi}{\omega m[(\omega_0^2 - \omega^2)^2 + \omega_0^4 \phi^2]}.$$
(4.44)

The frequency dependence of this expression is displayed in Figure 4.17 as well, assuming a frequency independent loss angle. According to this model thermal noise increases towards zero as $1/\omega$, which does not average out with increasing integration time and leads to a so called flicker noise floor in the Allan deviation.

A detailed evaluation of Brownian thermal noise for realistic cavities, comprising mirror substrates, mirror coatings and spacer has been given in
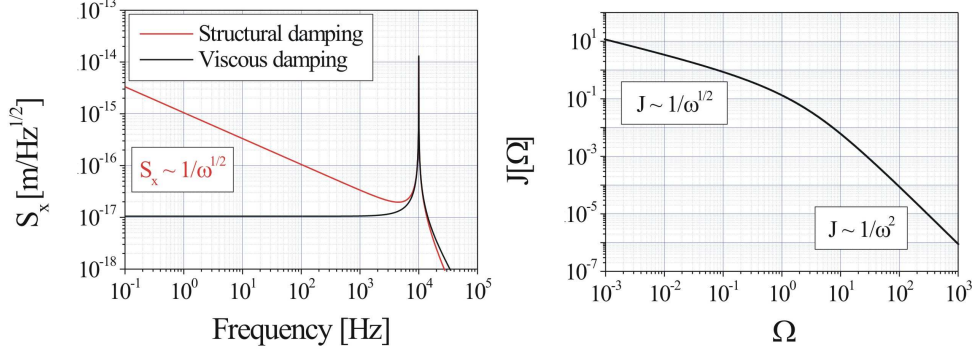
Figure 4.17: *Left: Frequency dependence of Brownian thermal noise assuming either viscous damping or structural damping. Calculations assume m = 5 g, $\phi = 3 \times 10^4$ and $\omega_0 = 10\,kHz$. Right: Shape function for thermoelastic damping.*

[NKC04]. They obtain expressions for thermal noise densities of mirror substrates with coating ($S_{x,\mathrm{BM}}^2$) and spacer ($S_{x,\mathrm{BS}}^2$) as given by

$$S_{x,\mathrm{BS}}^2(\omega) = \frac{4k_BT}{\omega}\frac{L}{3\pi R^2 E}\phi_\mathrm{S}, \tag{4.45}$$

$$S_{x,\mathrm{BM}}^2(\omega) = \frac{4k_BT}{\omega}\frac{1-\sigma^2}{\sqrt{\pi}Ew_0}\phi_\mathrm{M}\left(1 + \frac{2d(1-2\sigma)\phi_\mathrm{C}}{\sqrt{\pi}(1-\sigma)\phi_\mathrm{M}}w_0\right), \tag{4.46}$$

where E is Young's modulus, R is the spacer radius, L is the spacer length and d is the coating thickness. The indices S, M and C denote spacer, mirror substrate and coating, respectively. Note, that the effective thermal noise density attributed to the mirrors includes averaging over the area that is covered by the laser beam of waist $w_0(= 1/\mathrm{e}^2$ diameter).

Another type of thermal noise is **thermoelastic noise**. It arises from the thermodynamical fluctuations of a finite temperature T in a given volume V

$$< \delta T^2 >= \frac{k_BT^2}{\rho c_p V}, \tag{4.47}$$

where c_p is the specific heat capacity, ρ the material density and k_B the Boltzmann constant. These fluctuations couple to mechanical fluctuations via the coefficient of thermal expansion (CTE) α. The implications of thermoelastic noise on optomechanical devices in general have been elaborated in [CCHP01, BGV99]. They derive an expression for the spectral noise density of length fluctuations x of a mirror substrate. Again, these fluctuations are

65

averaged over the area covered by a laser beam of waist w_0. They obtain an expression

$$S_{x,\text{TM}}^2(\omega) = \frac{8}{\sqrt{2\pi}}\alpha^2(1+\sigma)^2\frac{k_B T^2 w_0}{2\kappa}J(\Omega),\tag{4.48}$$

where κ is the thermal conductivity and σ is Poisson's ratio. $J(\Omega)$ is a shape function with $\Omega = \omega/\omega_C$, where the critical frequency ω_C is the frequency for which the thermal diffusion length

$$l_t = \sqrt{\frac{2\pi\kappa}{\rho c_p \omega}}\tag{4.49}$$

becomes comparable to the beam waist w_0. It is given as $\omega_C = 2\kappa/(\rho c_p w_0^2)$. According to [CCHP01], the shape function $J[\Omega]$ can be calculated from

$$J[\Omega] = \sqrt{\frac{2}{\pi^3}}\int_0^\infty du \int_{-\infty}^\infty dv \frac{u^3 e^{-u^2/2}}{(u^2+v^2)[(u^2+v^2)^2+\Omega^2]}.\tag{4.50}$$

As evident from a plot of $J(\Omega)$ given in Figure 4.17, thermoelastic noise of a mirror substrate beyond the critical frequency converges as $1/\omega^2$. This is because the thermal diffusion length decreases with frequency and length fluctuations are averaged over the area covered by the laser beam. In this regime, the effect of thermoelastic noise can be decreased by increasing the beam waist w_0 ($S_{x,\text{MT}}^2 \sim 1/w_0^3$). However, below the critical frequency the thermal diffusion length is larger than the beam waist. Consequently, the effect of thermoelastic noise does not depend on w_0 in this regime.

The role of thermoelastic noise within the spacer of an optical cavity remains to be studied. Usually these spacers are fabricated from materials of low CTE which makes contributions of thermoelastic noise negligible. To our knowledge, no study of its influence within the cavity spacer has been done yet.

So far, all experimental observations agree with equations (4.45), (4.46) and (4.48) within a factor of ~ 2 over a frequency range from 10^{-2} to 10^4 s [NAY+03, NML+06]. Therefore, we apply these equations to obtain an estimate of the limitation set by thermal noise for this experiment. The critical cavity properties are the thermal expansion coefficient α and the loss angles $\phi = 1/Q$ of the mirror substrate, coating and the spacer. These values are obtained from the literature here, since no accurate direct measurement of the mechanical quality of the resonators was done. A very simple measurement performed on R2 as described in [Mül04] excited the mechanical resonance of the mirror by a piezo attached to the mirror. This measurement yielded a Q-factor on the order of 10^3, which agrees with the literature value, if we

take into account that the loss angles are increased due to the cavity support and the optical bonding of the mirrors.

Estimates of thermal noise for mirror substrates of different materials are presented in Table 4.3. The values there give the calculated displacement noise densities at $1\,\mathrm{Hz}$, (using equations (4.45), (4.46) and (4.48)), averaged over a laser beam waist of $200\,\mu\mathrm{m}$. In accordance with [NAY+03], a loss angle of $\sim 3 \times 10^{-4}$ was adopted for the BK7 substrates of the present cavities. The coating loss angle can be assumed to be on the order of 4×10^{-4} [CCG+04]. Its contribution is negligible, if the substrate is of similar low mechanical quality and if the beam radius is substantially larger than the depth of the coating. With respect to thermoelastic noise of BK7, one finds that the thermal diffusion length at $1\,\mathrm{Hz}$ is on the order of $10^{-3}\,\mathrm{m}$, which is slightly larger than the considered beam waist. Consequently, the cutoff frequency for thermoelastic noise is $\omega_C \sim 25\,\mathrm{Hz}$ which at $f = 1\,\mathrm{Hz}$ results in $\Omega = 0.25$ and $J(\Omega) = 0.65$. Note, that for the present experiment the thermoelastic noise model is only applicable for frequencies $> 0.01\,\mathrm{Hz}$. For frequencies below, the thermal diffusion length becomes comparable to the dimensions of the cavities and correlations among the thermal noise fluctuations of the cavity mirrors are to be expected.

Adding all noise contributions, it turns out that BK7 is a particularly unfavorable material due to both, a relatively large CTE and low mechanical quality. Materials of high mechanical Q-factors and lower CTE, such as fused silica or ULE, feature a thermal noise level which is up to a factor of five lower. Indeed, for high Q materials the coating loss presents the limiting factor.

Based on equations (4.45), (4.46) and (4.48), the effect of thermal noise for different cavity schemes is considered in Table 4.4. These estimates include thermal noise of both mirrors and spacer assuming no correlations. The displacement noise density S_x can be converted into a frequency noise density S_f using $\Delta L/L \sim \Delta f/f$. The Allan deviation σ can then be obtained from

$$\sigma^2 = 2\ln(2)S_f^2 f. \tag{4.51}$$

This relation holds for a frequency dependence $S_f^2 \sim 1/f$ as predicted for Brownian thermal noise. For thermoelastic noise this is only approximately fulfilled at $\Omega \sim 1$ as evident from Figure 4.17. For the cavity scheme of R1 (scheme A) thermal noise should cause a flicker noise floor at a relative Allan deviation of

$$\sigma/\nu_0 = 1.3 \times 10^{-14}, \tag{4.52}$$

with $\nu_0 = 2.82 \times 10^{14}$. If we ignore linear frequency drift, we can compare this to the Hadamard deviation calculated from the actual measurements,

material	Q	α [K^{-1}]	$S_{x,TE}$	$S_{x,M}$	$S_{x,C}$	$S_{x,T}$
BK7	3×10^3	7×10^{-6}	1.3	1.6	0.4	2.1
FS	1×10^6	6×10^{-7}	0.1	0.1	0.4	0.4
ULE	6×10^4	$< 10^{-8}$	< 0.01	0.4	0.4	0.6
Zerodur	3×10^3	$< 10^{-8}$	< 0.01	1.8	0.4	1.8

Table 4.3: *Thermal noise budget for different mirror substrate materials. Q denotes the mechanical quality factor, α the coefficient of thermal expansion. All noise density values S_x are $\times 10^{-16} \frac{m}{\sqrt{Hz}}$ at 1 Hz and refer to a single mirror. $S_{x,TE}$ refers to thermoelastic, $S_{x,M}$ and $S_{x,C}$ to Brownian thermal noise of the substrate and the coating, and $S_{x,T}$ to the total thermal noise density. Calculations assume a beam waist of $w_0 = 200\,\mu m$ and a coating thickness of $10\,\mu m$.*

which is at a level of $\sigma/\nu_0 \sim 1.5 \times 10^{-14}$ and agrees well with this estimate on thermal noise.

The question remains, how to overcome this thermal noise limit. An obvious solution would be cooling the resonators to liquid-Helium temperature $T = 4\,K$. According to the FDT, relative frequency instabilities are expected to scale with $\sqrt{T}$, allowing for a factor of ~ 8 improvement. Further benefits could be expected from an increased mechanical Q-factor at lower temperature. However, this does not hold for fused silica [JKR64]. On the other hand, continuously operating the rotating experiment at cryogenic temperature introduces further experimental difficulties and is rather cost-intensive. Thus, it was decided to replace the cavities by new ones, which feature an optimized design for room temperature application within a Michelson-Morley experiment. This optimum configuration features a material of high mechanical Q, such as fused silica, at reasonable low CTE and a larger cavity length. An increased length a priori reduces relative frequency instabilities due to mirror displacement noise such as thermal noise. In addition, it leads to a larger beam diameter at the mirrors which reduces the effect of thermal noise even more. This new set of resonators is described in chapter 7.

Performance of the lock electronics

A comparison of the frequencies of laser L1 and L2, stabilized to two neighboring TEM$_{00}$ modes of R2 was performed to test the performance of the stabilization electronics. All cavity length fluctuations in this measurement are common mode. Thus, frequency stability is limited by the performance of the lock electronics only. As shown in Figure 4.16, the Allan deviation for this measurement features a flicker floor at a level of 5×10^{-15}, which is better

scheme	material	L [cm]	w_0 [μm]	Allan deviation σ/ν_0
A	BK7	3	170	1.3×10^{-14}
B	BK7	10	225	3.3×10^{-15}
C	Zerodur	5.5	200	4.8×10^{-15}
D	FS	5.5	200	1.4×10^{-15}
E	ULE	5.5	200	1.9×10^{-15}
F	ULE	24	270	3.4×10^{-16}

Table 4.4: *Thermal noise budget for different cavity configurations. All calculations assume $\lambda = 1064\,nm$ and include the effect of spacer thermal noise. The latter is usually negligible compared to mirror thermal noise, except for Zerodur. Cavity schemes A and B are those for R1 and R2. The estimate of thermal noise for cavity R1 is in good agreement with the observed flicker noise. Schemes C, D and E correspond to a new set of resonators implemented in an improved version of the experiment (see 7). Scheme F corresponds to the cavity used by [YCIB99], who reported on the lowest cavity frequency stability obtained so far. They observed a flicker floor above 1 s at a level of 2×10^{-16}, which agrees with the calculated value within a factor of two.*

than the comparison of R1 to R2 by a factor of three. As will be shown in chapter 7, the origin of this flicker noise has been identified to be instabilities of beam pointing. Fluctuations of beam pointing on the photodetector have been observed to cause fluctuations of the phase of the error signal [Tro05]. These in turn shift the lock point and lead to frequency instabilities on the order of several Hertz per degree phase shift. For a comparison of two lasers locked to one resonator described in chapter 7, an Allan deviation down to 5×10^{-16} has been obtained, applying the same lock electronics but with improved beam pointing stability of the laser beams.

4.4.3 Frequency drift

Long-term frequency drift is mainly caused by temperature drift. This has been verified for R2 by comparing its frequency to an iodine frequency standard [Sch03], which provides an independent long-term stable frequency reference. A fraction of the light of laser L2 is frequency-doubled and used for stabilizing the laser to a transition in molecular iodine (see [Sch03] for details). The light at 1064 nm is sent through a double-pass AOM, driven at f_{AOM}, before it is coupled to a TEM$_{00}$ mode of R2. The voltage controlled oscillator that generates f_{AOM} is controlled by the PDH error signal of R2 in

order to track the cavity resonance. Thus, $2f_{\text{AOM}}$ always equals the relative deviation of the cavity frequency with respect to the long-term stable iodine transition.

The top graph in Figure 4.18 shows a recording of $2f_{\text{AOM}}$ during a long-term measurement of seven days. In direct comparison the temperature changes of the resonator mount, measured using a $10\,\text{k}\Omega$ thermistor, are also shown. The correlation among the two becomes evident from the lower graph in Figure 4.18. According to this measurement a CTE of $(6.82 \pm 0.28) \times 10^{-7}\,/\text{K}$ can be deduced.

Furthermore, this measurement allows to estimate the temperature independent drift due to material ageing. If we assume that this effect contributes a constant linear frequency drift, we can evaluate an approximately linear section of the graph in Figure 4.18, which shows that material ageing contributes $< 0.1\,\text{Hz/s}$ to the total drift rate. This low value suggests, that an improved temperature stability could directly provide a significant improvement of long-term frequency stability. Thus, attempts to set up an active temperature stabilization have been undertaken here and are described in [Sen06]. However, the temperature stability required to achieve frequency stability at the Hertz level is on the order of $\sim 100\,\text{nK}$. This is far from the level that could be achieved applying an active stabilization. However, for a future version of the experiment significantly improved temperature stability has been targeted, based on an advanced passive thermal isolation in a new vacuum chamber (see Appendix F).
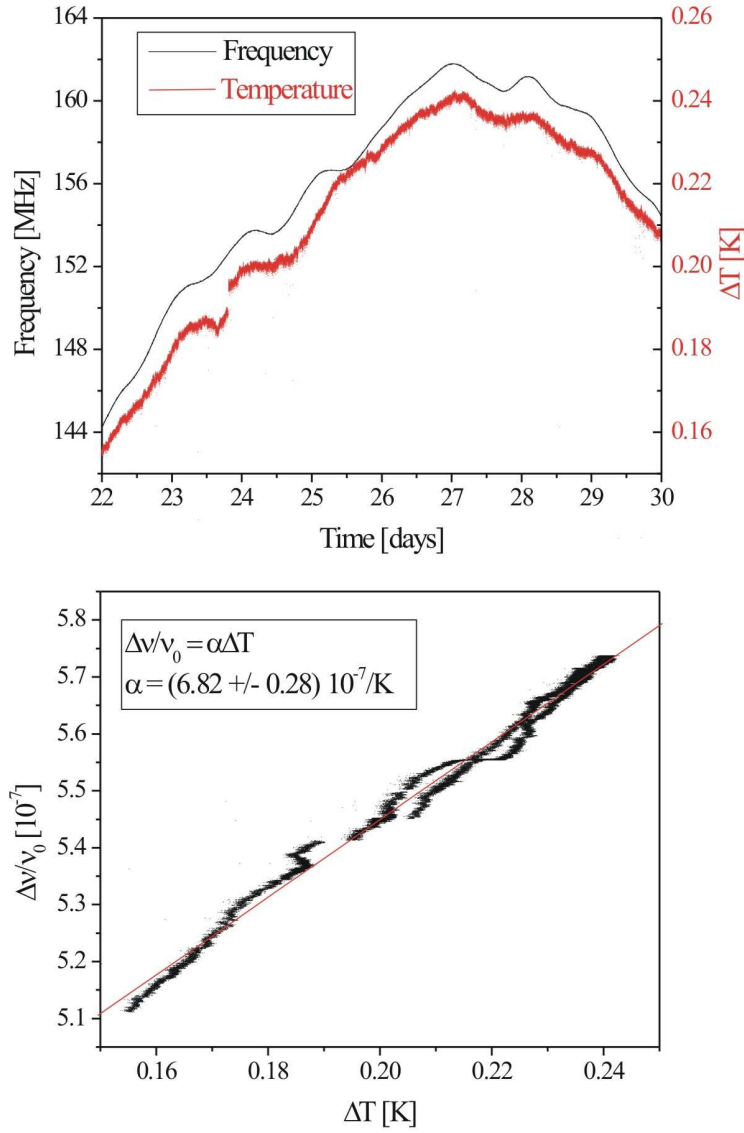
Figure 4.18: *Top: Frequency and temperature drift of R2. Bottom: The correlation of frequency drift of R2 to temperature variations inside the vacuum chamber allows to deduce the effective CTE of resonator R2.*

Figure 4.19: *Precision turntable for rotating the laser stabilization setup for R1. Specifications are given in Table 4.5.*

4.5   Active rotation of the setup

4.5.1   The turntable

A turntable of extraordinary precision (Kugler GmbH, RTV600) is applied to rotate the complete laser stabilization setup for resonator R1. This turntable features minimum axial and planar runout, even when applying a heavy off-center load. Some specifications of the turntable are given in Table 4.5. The hemispherical rotor has a diameter of 60 cm and hovers on an air bear-

specification	value
rotor diameter	60 cm
weight	400 kg
maximum applicable load	1000 kg
air bearing pressure	4 - 6 bar
rotation axis wobble	$< 1\mu\text{rad}$
planar runout	$<0.1\,\text{nm}$
axial stiffness	300 N/μm
angular readout accuracy	0.02°

Table 4.5: *Specifications of the precision turntable.*

ing generated by compressed air. Compressed air of six bar is supplied by a compressor (Hydrovane, HV01) located in a neighboring room. The air bearing gap between rotor and stator measures $< 10\,\mu$m. The table is equipped with a port for connecting a vacuum pump, which allows to pump on the air bearing which sets the table under an effective pre-load equal to 1000 kg. This increases the stiffness of the table and makes it less sensitive to varying loads.

The table rests on three aluminum rods which are 20 cm in height and 10 cm in diameter. These rods are supported by a flat tripod that is welded from three steel beams, each 120 cm in length. The tripod distributes the weight of the setup (~ 840 kg in total), which was necessary, given a maximum allowed load for the laboratory floor of $700\,$kg/m^2. The tripod again rests on three wedge shoes, which allow to level the complete setup at an accuracy of few μrad. The position of the wedge shoes coincides with lines of structural steel beams in the laboratory concrete floor to minimize bending of the floor. The table is equipped with a DC-motor by the manufacturer, connected by a flat rubber belt smoothly wrapped around the rotor. However, using two simple 12-V DC-motors (Shayang Ye Industrial, RB350200) that drive rubber friction wheels of 2 cm in diameter yielded a tighter connection between motor and turntable rotor. The two motors are mounted at opposite sides of the table. In this way no asymmetric force is applied to the rotor and rotational true run is preserved.

The table is equipped with an encoder that reads out the instantaneous rotation angle. This encoder consists of a Zerodur disk etched with 18000 radial lines and a photo sensor. This sensor's readout is turned into sinusoidal quadrature signals with an angular resolution of $360°/18000 = 0.02°$ per period of the encoder signal. Additionally, the encoder gives out a single peak on a third channel every time the table rotor passes its "zero"-position marked on the Zerodur disk.

4.5.2 Setup on the turntable

A high-performance optical breadboard with a center hole of 360 mm in diameter is placed on the turntable. This allows access to the center bore hole of the turntable (2 cm diameter), which was used to transfer light from L1 to the laboratory as described in section 4.5.2. Additionally, it allows to remove or close the bottom shield of the vacuum chamber during assembly of the setup. Lasers and optics are mounted on the breadboard as shown in Figure 4.11. It also carries a steel beam construction that supports the vacuum chamber and racks for the electronic equipment. A turbomolecular pump is directly attached to a side flange of the vacuum chamber (see Figure 4.21),

backed by a stationary roughing pump from outside via a rotating vacuum feedthrough.

Rotating electric and vacuum feedthrough

A rotating electric feedthrough is used (Fabricast Inc., 19815) to supply the rotating setup with line power. This feedthrough consists of a pile of 15 slip rings of 4 cm in diameter on the rotor side, and silver graphite brushes on the stator side. Three channels are used for the transfer of line power and the additional channels for transfer of measurement signals between the laboratory and the rotating setup. The rotor of this assembly is attached to a vertical brass tube centered on the rotation axis and connected to a vacuum feedthrough (Turian Eng.) on top of the electric feedthrough. This vacuum feedthrough allows to rough-pump the turbomolecular pump, which is directly attached to a flange of the vacuum chamber.

The feedthrough is not rigidly attached to the rotating table, and is rotated by another DC-motor instead (Shayang Ye Industrial, RB350200). A simple control scheme is applied, in order to make it exactly follow the table rotation: as shown in Figure 4.20 differential rotation of feedthrough and table turns a potentiometer on axis below the assembly, which adjusts the pulse-contact control that drives the motor. This simple direct control achieved stable and reliable rotation of the feedthrough together with the table. This was especially important, as otherwise small forces are mediated between table and feedthrough, which distort rotational true run of the table. As discussed in chapter 5, the centrifugal forces caused by such a distortion give rise to a systematic variation of the beat frequency.

For the case of a malfunction of the feedthrough control, two emergency switches are implemented on top of the rotating setup. If the feedthrough lacks behind or runs ahead by 90° with respect to the table, a lever arm connected to the feedthrough rotor triggers these switches, which shuts down the power supply that drives both the table and feedthrough rotation motors.

Optical feedthrough

The center bore hole of the turntable is used to transfer a fraction of the light of L1 from the rotating setup to the beat measurement setup in the laboratory rest frame. Since for the beat frequency measurement the light has to be focussed on a small area photodiode, the beams have to be aligned with the rotation axis to < 0.1 mrad. This provides sufficient pointing stability, such that the amplitude of the beat signal remains within a range of 0 dBm to 5 dBm during a table rotation. This signal level is required for an
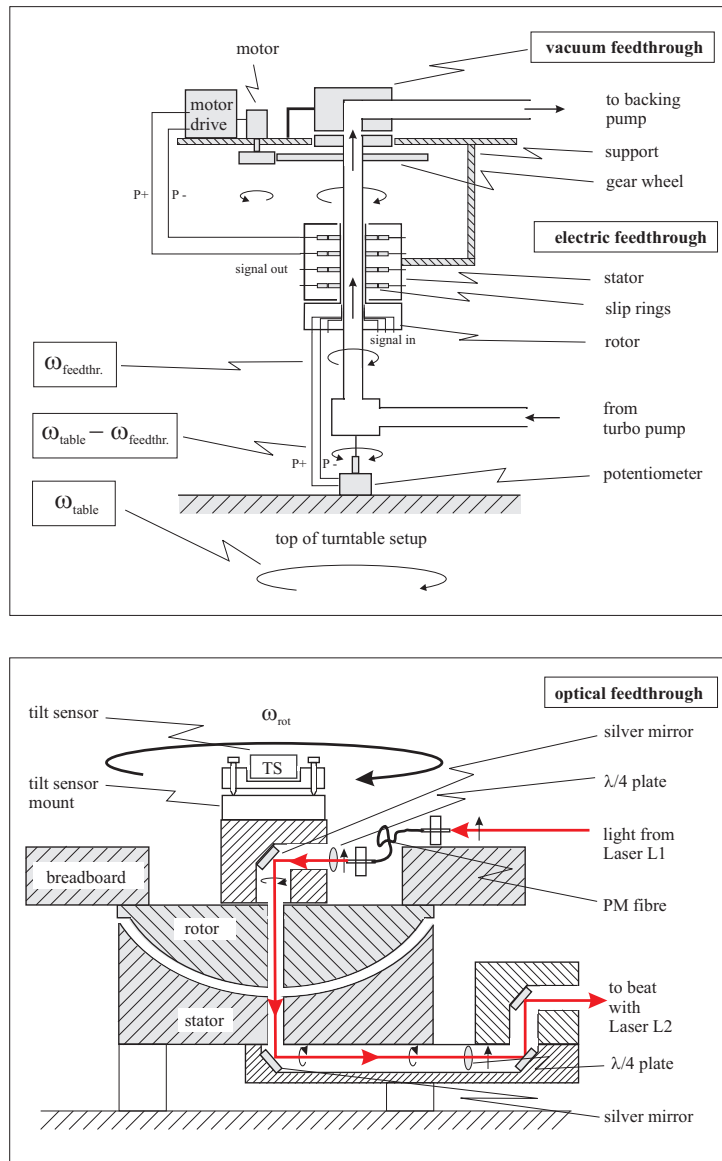
Figure 4.20: *Top: Schematic of the electric and vacuum feedthrough at the top of the setup. The potentiometer mounted on axis below the feedthrough adjusts the feedthrough motor drive such that it exactly follows table rotation. Bottom: Schematic of the optical feedthrough. Light from laser L1 is transferred along the rotation axis to the beat measurement system on a stationary platform at the bottom of the turntable. For the transfer the linear polarization is turned into circular polarization, which can again be converted into a linear polarization of fixed orientation in the laboratory.*

accurate frequency measurement.

Special care was spent on the polarization of the transferred light. Without any precautions the linear polarization of the transferred beam would rotate with table rotation in the laboratory frame. Generation of a beat signal with light from L2 however requires fixed parallel linear polarizations. This is achieved using the configuration shown in Figure 4.20. The linear polarization of light from L1 is turned into circular polarization by a first $\lambda/4$-plate. Then, the light is directed along the rotation axis towards the beat measurement platform beneath the table, using two silver mirrors. These metallic mirrors preserve the circular polarization in contrast to standard dielectric mirrors. Upon passing a second $\lambda/4$-plate, the light is turned to fixed linear polarization parallel to that of L2. Note, that in this scheme the frequency of the light is shifted by the table rotation frequency of $\nu_{\mathrm{rot}} = 0.02\,\mathrm{Hz}$. This is however only a constant shift and yet beyond the sensitivity of this experiment.

4.6 Beat frequency measurements with a rotating setup

Basically, all measurements consist of a record of the beat frequency of the rotating cavity R1 with the stationary cavity R2, recorded with a gate time of one second. A complete measurement always extends over at least 24 hours of continuous rotation and involves acquisition of time, tilt of the rotation axis and rotation angle. Thus, each data point of the frequency measurement can be assigned the exact time and orientation of the rotating cavity R1.

4.6.1 Optimum table rotation rate

The optimum table rotation rate has been determined as follows: According to Figure 4.13 the timescale of best frequency stability is at $\tau \sim 30\,\mathrm{s}$. The rotation rate can be chosen at one turn per $60\,\mathrm{s}$, such that $2\omega_{\mathrm{rot}}$ corresponds to this regime. Since flicker noise is prevalent in this time regime, the Hadamard deviation increases towards shorter integration times with a slope < -1. Thus, faster rotation rate can more than compensate for reduced frequency stability at shorter integration times, because it allows to increase the number of measurements and thus to improve the statistics. Consequently, the rotation period was set to $T = 45...50\,\mathrm{s}$. Even faster rotation turned out to increase the level of systematic effects, due to the influence of centrifugal

forces (see chapter 5). Rotation was performed counterclockwise for all measurements, which is required by the presence of a screw joint in the vacuum feedthrough. Clockwise rotation, as has been tried once, loosens this screw joint and breaks the vacuum after few hours of rotation.

4.6.2 Measurement procedure

Figure 4.21 gives a schematic of the complete turntable setup together with a simplified scheme of the data acquisition system and the control loops applied. Each measurement is initiated as follows: First, the PDH control loop CL1 for frequency stabilization is closed and the table rotation is started by closing the control loop CL2 (see chapter 5 for details). The electric feedthrough motor control CL3 starts automatically with table rotation. The computer readout of frequency and other data is started by an encoder trigger pulse, that indicates the table's zero position and is read out via a channel of the voltmeter (Agilent, 34970A). Two counters (SRS, SR620) are applied to record the beat frequency of R1 with R2, and optionally the beat frequency of R1 or R2 with another frequency reference. A third counter (HP 5334B) records the rotation angle by reading in the turntable encoder. The voltmeter offers several additional channels to register further data, such as the signals received from the tilt sensor on the table. These are routinely monitored and used as input for further control loops (CL4+5) for leveling the rotation axis. A detailed description of this tilt control system is given in chapter 5.
When the data acquisition is stopped after $> 24\,\text{h}$, the program continues to record data until it receives the next encoder trigger pulse. This guarantees, that each data set consists of an integer number of rotations.

4.6.3 Systematic effects arising from table rotation

Actively rotating the laser stabilization setup on a turntable, causes a number of systematic effects that compromize the beat frequency stability. Mainly, these are caused by direct forces that act on the resonators, which are usually either gravitational or centrifugal. Further influences arise from modulation of ambient conditions, which affect other parts of the setup, e.g. the servo electronics. Figure 4.23 gives an impression of how systematic frequency variations appeared in the first measurements obtained from a rotating setup. Typically, the amplitude of systematic frequency oscillations at ω_{rot} was as large as $10\,\text{Hz}$ and more. A detailed description of the sources of such effects and their suppression below $1\,\text{Hz}$ is presented in chapter 5.
The spectral distribution of amplitude and phase of systematics has been
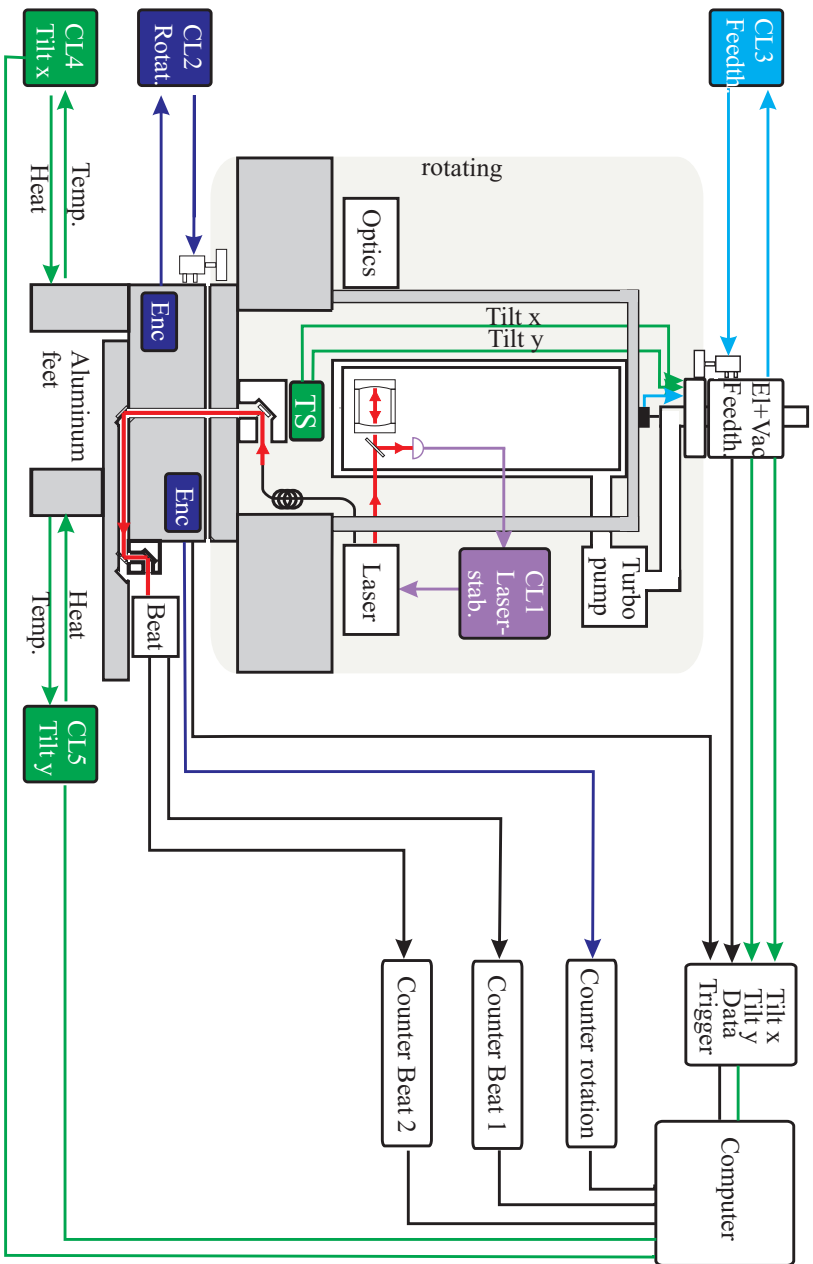
Figure 4.21: *Schematic of the rotating setup in total. The data acquisition and the different control loops applied are depicted schematically. CL1 is the Pound-Drever-Hall frequency stabilization according to section 4.2.5. The electric feedthrough, the optical feedthrough and CL3 are described in section 4.5.2. Details on tilt control (CL4+5) and rotation rate control (CL2) are given in chapter 5. Data acquisition covers one or two beat frequencies, rotation angle, rotation axis tilt as well as the trigger signal indicating the table's zero position.*
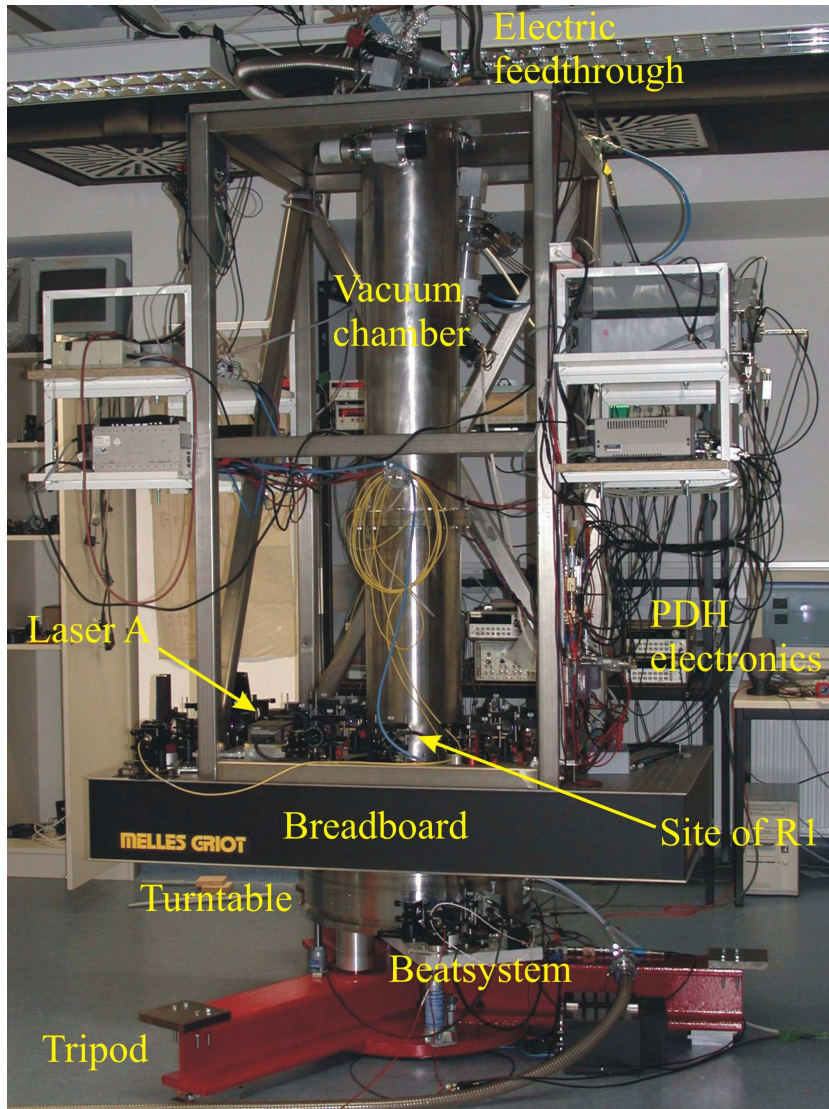
Figure 4.22: *Picture of the complete rotating setup.*

studied applying two methods of analyzing the data:

- Fourier transformations of the beat frequency data, as shown in Figure 4.24 to the top.

- Periodical averages of the beat frequency modulo 360°, as presented in Figure 4.24 to the bottom. Here, subsequent samples of the beat frequency measurement, each extending over exactly one table rotation, are averaged to picture the average frequency variation during a table rotation. These plots are briefly denoted "periodical averages" within the following.

Both methods are applied to data that has been high-pass filtered with a corner frequency of $f_c = 1/(200\,\mathrm{s})$, in order to remove the large frequency drift. Thus, spectral features $< \omega_{\mathrm{rot}}/4$ are not displayed in these plots. The high-pass filter has been realized by subtraction of a running average from the data, calculated from the 200 next neighbors for each data point. Possible signal distortions and phase shifts due to this filtering are not considered further here and these periodical averages and FFT plots are only used to obtain a rough estimate of the systematic effect throughout the following.
Note further, that the periodical average as displayed in Figure 4.24 is limited to the description of a systematic effect of constant phase. A systematic effect of varying phase will partially or completely average out in these these plots.
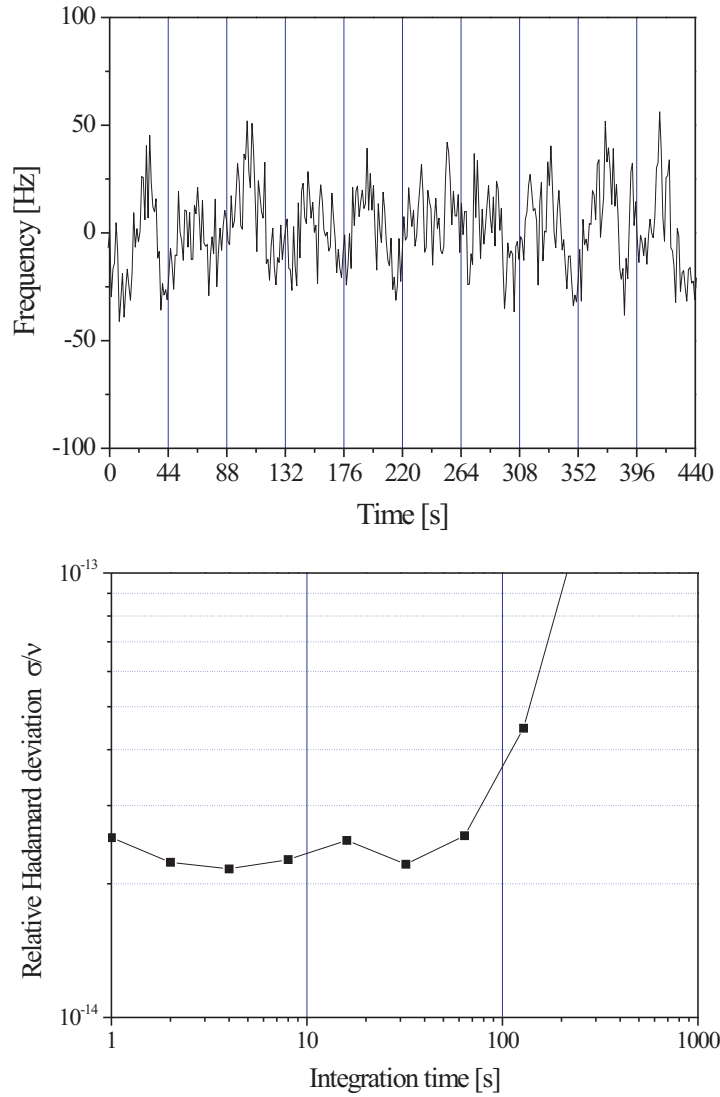
Figure 4.23: *A typical example for a measurement affected by systematic effects as observed within initial measurements. Top: An extract of the beat frequency measurement, after application of a numerical high-pass filter to the data ($f_c = 1/(200\,s)$). The rotation rate was set to 44 s. A systematic variation can be recognized superimposed by flicker noise. Bottom: The Hadamard deviation calculated from this measurement. A bump at $\sim T_{\rm rot}/2$ indicates the presence of a systematic oscillation at a period of $T_{\rm rot}$.*
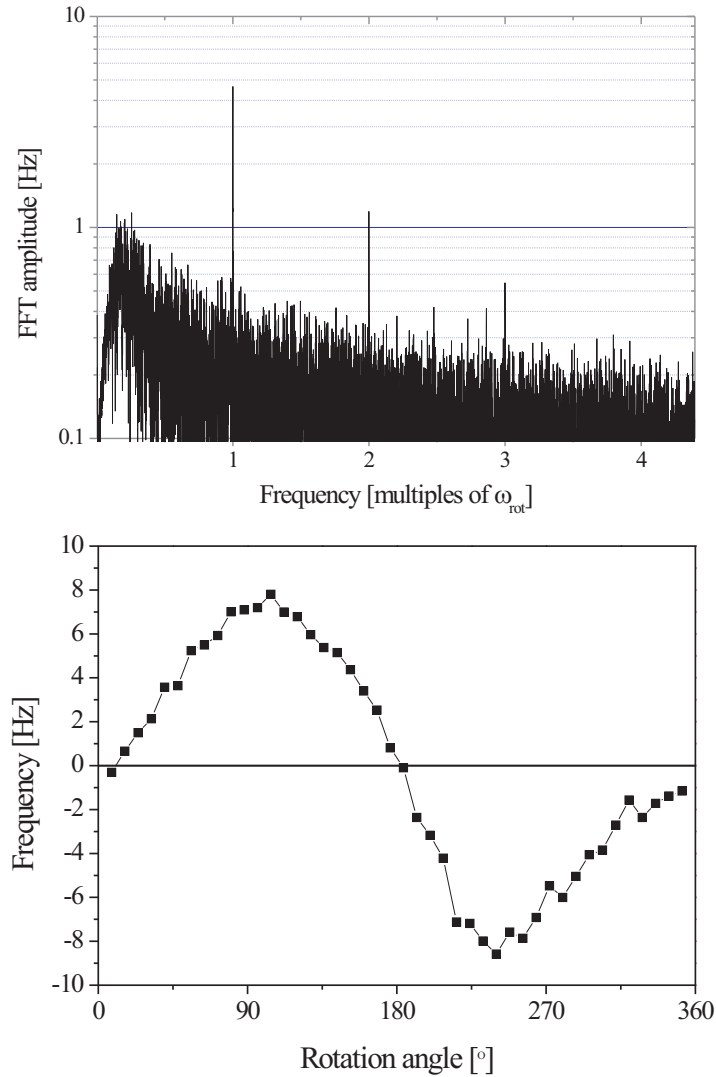
Figure 4.24: *Bottom: A periodical average of the beat frequency measurement of Figure 4.23 including ~ 2000 rotations shows the average frequency variation during a table rotation. The frequency exhibits a distorted sinusoidal oscillation at ω_{rot}. The absolute amplitude of the systematic oscillation at ω_{rot} is $\sim 7\,Hz$. Top: The Fourier transform of this beat frequency measurement shows peaks at the turntable rotation rate ω_{rot} and its harmonics. Below $\omega_{rot}/4$ the spectrum is cut off due to the application of the high-pass filter.*

Chapter 5

Systematic effects

The dominant systematic effect was observed at once the frequency of table rotation $\omega_{\rm rot}$ rather than at $2\omega_{\rm rot}$, the period of a Lorentz violation signal. Furthermore, for a measurement spanning more than one day, most of the Lorentz violation signal is contained in the sidereal sidebands of the $2\omega_{\rm rot}$ component (see Figure 3.1). Still, harmonics of the systematic effect at $\omega_{\rm rot}$ compromize the $2\omega_{\rm rot}$ component and, if this systematic effect is modulated with a 12 or 24 hour period, the sidereal sidebands as well. Consequently, systematics must be considered carefully here. The various systematic effects identified throughout the course of this work and the precautions taken to suppress them are described in this chapter.

5.1 Rotation axis tilt

5.1.1 Model

Tilting the cavity axis against the horizontal leads to a deformation of the cavity geometry due to the gravitational force. If we approximate the cavity as a solid cylinder, a simple estimate of the effect can be obtained as follows. Let the cavity axis be tilted at a constant angle α with respect to the horizontal. Deformation of its length then occurs in two ways: First, there is the strain along the cavity axis due to $F_G \sin\alpha$ (see Figure 5.1). Second, there is the orthogonal force $F_G \cos\alpha$, which causes an additional deformation along the cavity axis due to the finite Poisson ratio η of the material. If the cavity is fixed in the middle, the first deformation splits into two exactly cancelling contributions from the left and the right part. More generally, we consider the case that the cavity is fixed at a position displaced from the middle by
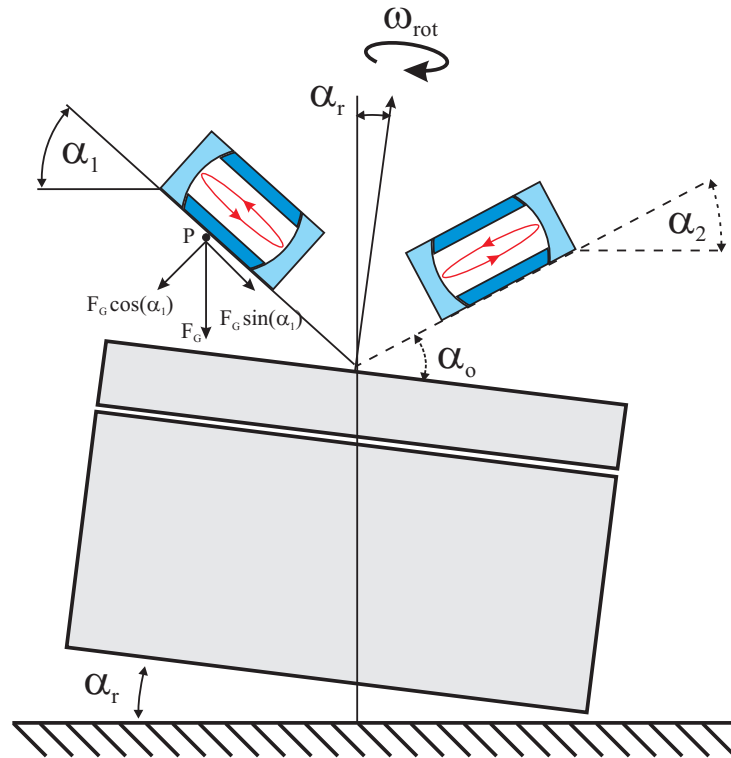
Figure 5.1: *Illustration of rotation axis tilt. Let the resonator be fixed at a single point P. During a rotation of the table the optical axis of the cavity is tilted against the horizontal by a maximum and a minimum angle of $\alpha_{1,2} = \alpha_0 \pm \alpha_r$. The gravitational force that deforms the cavity can be split into components $F_g \sin\alpha_{1,2}$ and $F_g \cos\alpha_{1,2}$, which vary systematically with rotation. For zero rotation axis tilt the cavity tilt remains constant during table rotation ($\alpha_{1,2} = \alpha_0$) and the forces acting on the cavity do not vary.*

$\gamma L/2$ with $0 < \gamma < 1$. Then, for variations of the tilt angle $\alpha \pm \Delta\alpha$, cavity deformation along the optical axis can be modeled as

$$\frac{\Delta L}{L} = \frac{\gamma\rho Lg}{E}\sin(\alpha + \Delta\alpha) + \frac{\eta\rho dg}{E}\cos(\alpha + \Delta\alpha), \tag{5.1}$$

where L is the cavity length, d is the diameter, E is Young's modulus, g is the gravitational acceleration and ρ is the material density. An expansion of this expression for small $\alpha + \Delta\alpha$ up to terms of second order results in

$$\frac{\Delta L}{L} = \frac{\gamma\rho Lg}{E}[\alpha + \Delta\alpha] + \frac{\eta\rho dg}{E}[1 - \frac{\alpha^2}{2} - \frac{\Delta\alpha^2}{2} - \alpha\Delta\alpha]. \tag{5.2}$$

Disregarding the constant offset terms that do not involve $\Delta\alpha$ results in

$$\frac{\Delta L}{L} = \frac{\rho Lg}{E}[\gamma\Delta\alpha - \frac{\eta d}{L}\alpha\Delta\alpha - \frac{\eta d}{L}\frac{\Delta\alpha^2}{2}]. \tag{5.3}$$

After rearranging this equation and using $\Delta L/L = \Delta\nu/\nu_0$ the tilt sensitivity can be modeled as

$$\frac{\Delta\nu}{\nu_0} = A\Delta\alpha + B\Delta\alpha^2, \tag{5.4}$$

with

$$A = \frac{\rho Lg}{E}[\gamma - \frac{\eta d}{L}\alpha], \tag{5.5}$$

$$B = \frac{\eta\rho dg}{2E}. \tag{5.6}$$

For a symmetry factor $\gamma = 0.05$ and a negligible offset tilt ($\alpha < 100\,\mathrm{mrad}$ is sufficient), insertion of values for R1 leads to

$$A = 4.3 \times 10^{-16}/\mu\mathrm{rad}, \tag{5.7}$$

$$B = 8.9 \times 10^{-22}/\mu\mathrm{rad}^2. \tag{5.8}$$

Referred to $\Delta\nu$ using $\nu_0 = 2.82 \times 10^{14}$ this corresponds to

$$A = 120\,\mathrm{mHz}/\mu\mathrm{rad}, \tag{5.9}$$

$$B = 0.03\,\mathrm{mHz}/\mu\mathrm{rad}^2. \tag{5.10}$$

In the next step, the case of a tilted cavity rotating on a turntable is considered. If the rotation axis is vertical, the tilt angle against the horizontal is not modulated, even with non-vanishing offset tilt α (see Figure 5.1). Only if the rotation axis is tilted by α_r, this leads to a modulated cavity tilt $\Delta\alpha = \alpha_r \sin\omega_{\mathrm{rot}}t$. Inserting this into equation (5.4) and neglecting constant

offset terms leads to a systematic frequency variation at once and twice the table rotation:

$$\frac{\Delta\nu}{\nu_0} = A\alpha_r \sin\omega_{\mathrm{rot}}t + B\frac{\alpha_r^2}{2}\cos 2\omega_{\mathrm{rot}}t \qquad (5.11)$$

According to this model, the dominant effect occurs at ω_{rot} as long as $\alpha_r \ll 2A/B \sim 8\,\mathrm{mrad}$. Furthermore, an observable systematic effect of $> 1\,\mathrm{Hz}$ at $2\omega_{\mathrm{rot}}$ is only expected for rotation axis tilts $> 260\,\mu\mathrm{rad}$. However in practice, harmonics of the ω_{rot} component at $2\omega_{\mathrm{rot}}$ can never be fully suppressed. Thus, accurate control of rotation axis tilt is required. Typical changes of the laboratory floor tilt are shown in Figure 5.4 to the top. They are on the order of $10\,\mu\mathrm{rad}$ per day, which over few days of measurement accumulates to a systematic error of several Hertz at ω_{rot}.

5.1.2 Active control of rotation axis tilt

An electronic two-axis bubble-level tilt sensor (Applied Geomechanics, 755-1129) is mounted at the center of the turntable in order to measure the rotation axis tilt α_r. The angular resolution of this sensor is $0.1\,\mu\mathrm{rad}$. The sensor mount enables leveling in two axes x and y, in order to minimize an offset tilt α_o of the sensor relative to the table platform. If the rotation axis is tilted, the output of the two sensor channels oscillates with table rotation. The peak-amplitude of this oscillation equals α_r, whereas the offset corresponds to α_o, which does not systematically affect the beat frequency. The tilt signals are amplified by a factor of 100 and read out via two channels of the rotating electric feedthrough. After low-pass filtering with $1\,\mathrm{Hz}$ corner frequency, a voltmeter (Agilent, 34970A) converts these signals into digitized data. The voltmeter is read out by the computer at a rate of one sample per second. As the tilt is measured on the rotating table, the computer needs to transform the sensor output into the laboratory frame. This is done using a transformation

$$\begin{pmatrix} \alpha_{r,x} \\ \alpha_{r,y} \end{pmatrix} = \begin{pmatrix} \sin\phi_{\mathrm{rot}} & -\cos\phi_{\mathrm{rot}} \\ \cos\phi_{\mathrm{rot}} & \sin\phi_{\mathrm{rot}} \end{pmatrix} \begin{pmatrix} \alpha_{r,x_{\mathrm{rot}}} \\ \alpha_{r,y_{\mathrm{rot}}} \end{pmatrix},$$

where ϕ_{rot} is the instantaneous rotation angle given by the encoder read out. The transformed signals again vary sinusoidally with table rotation, however the offset of this signal now corresponds to α_r whereas the amplitude of the variation gives α_o.

In order to zero rotation axis tilt, a simple actuator has been realized by placing the table upon three aluminum cylinders, each $20\,\mathrm{cm}$ in length and $10\,\mathrm{cm}$ in diameter. This allows to control the table tilt in two axes by means
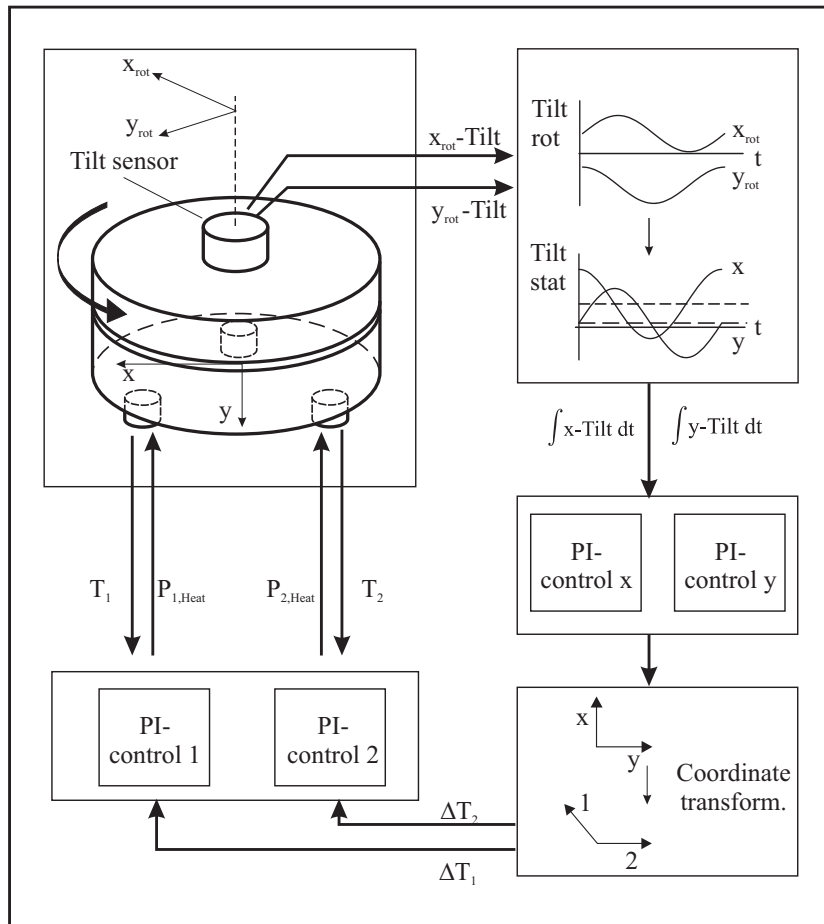
Figure 5.2: *Schematic outline of the two-stage tilt control system. See text for a description.*
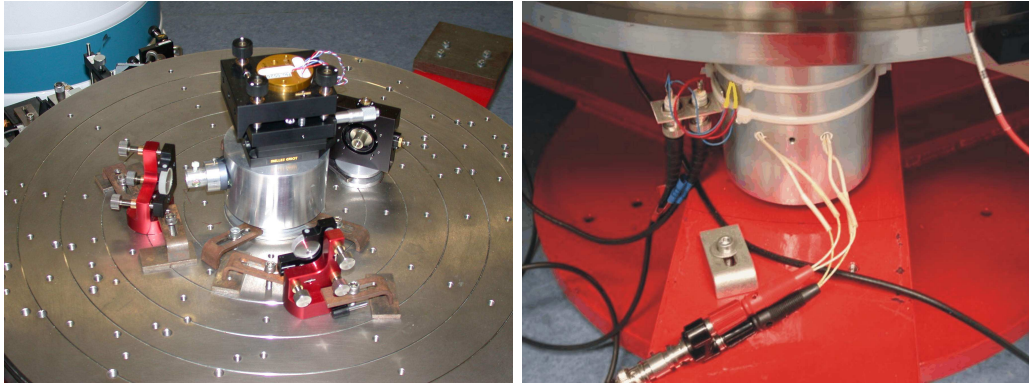
Figure 5.3: *Details of the tilt control system. Left: The two-axis bubble-level tilt sensor mounted at the turntable center in a horizontal mirror mount. Beneath and surrounding are components of the optical feedthrough (compare to Figure 4.20). Right: One of the aluminum feet, equipped with two 100 W heat cartridges and a Pt100 thermistor.*

of the thermal expansion of these legs. The temperature of two of these legs can be set in a range from $30°$ C to $70°$ C. The coefficient of thermal expansion for aluminum is 2.5×10^{-5}/K. Thus, varying the temperature by ± 20 K results in length changes of ± 0.1 mm. With the feet placed at a distance $r = 250$ mm from the center, α_r can thus be varied by $\pm 400 \, \mu$rad.

A feedback loop for tilt control is implemented in a two-stage configuration as sketched in Figure 5.2. This nested control loop scheme was a natural choice, since commercial digital PID-controllers (LakeShore, Autotuning Temperature Controller 330) were applied for stabilizing the temperature of the aluminum feet. The optimum operating temperature is about $50°$ C, for which the cooling and heating rate are approximately equal. Adjustment of the feet temperature by several tenths of a Kelvin typically takes about ~ 10 seconds.

Within a second, outer feedback loop the computer then adjusts the setpoint temperature for both temperature controllers, such that the rotation axis tilt is reduced below $1 \, \mu$rad. A new appropriate setpoint temperature is derived from the tilt measurement once every rotation. This is done using a digital PI-algorithm, which generates a correction signal (c_x, c_y) from the measured α_r. As the legs (labeled 1 and 2) are set up in a triangular configuration, the two actuators are correlated in their effect on tilt along the x- and y-axis. Thus, another coordinate transformation is applied which distributes the corrections referred to the laboratory frame axes (c_x, c_y) to the axes defined by

the legs (c_1, c_2)

$$\begin{pmatrix} c_1 \\ c_2 \end{pmatrix} = \begin{pmatrix} 2 & 0 \\ -\sqrt{3} & 1 \end{pmatrix} \begin{pmatrix} c_x \\ c_y \end{pmatrix}.$$

The tilt control loop's setpoint is $\alpha_r = 0$ by default, but arbitrary setpoints resulting in a constant non-vanishing α_r can be chosen as well. To prevent interference with the slow time constants ($\sim 10\,\mathrm{s}$) of the temperature control loop, an adjustment every second or third rotation only would be advisable. Nonetheless, also with the temperature adjusted every rotation, rotation axis tilt could be reliably reduced below $1\,\mu$rad as evident from the bottom graph in Figure 5.4. There, the step response to a large $100\,\mu$rad step in rotation axis tilt along one axis is shown. With the feedback parameters adjusted to a slight underdamping, the tilt is reduced below $1\,\mu$rad within ~ 6 hours (480 rotations). The insert shows the residual long-term variations of tilt with active control applied. Variations are below $1\,\mu$rad, which corresponds to a systematic effect at ω_{rot} of $< 0.1\,\mathrm{Hz}$ according to equation (5.4). This performance is sufficient at the present level of accuracy and is limited by noise of the tilt signals e.g. by vibrations and the slow bandwidth of the control loop. Within a future setup the application of high-load piezo actuators might allow a significantly faster and more sensitive tilt control.

Experimental determination of tilt sensitivity

The accurate tilt control eventually allowed to determine the tilt sensitivity coefficients of equation (5.11). For this purpose the tilt feedback loop was set to a discrete offset tilt of α_r along the y-axis. For $\alpha_r = 200\,\mu$rad a periodical average of the resulting beat frequency involving ~ 1000 rotations is shown in Figure 5.5 to the top. Similar periodical averages of the beat frequency have been obtained for other values of α_r ranging from 0 to $250\,\mu$rad. The amplitudes of the corresponding frequency variation at ω_{rot} respectively $2\omega_{\mathrm{rot}}$ have been determined from fits to these averages. The reaults are plotted as a function of α_r in Figure 5.5 to the bottom. The resulting linear dependence ($A \sim 0.1\,\mathrm{Hz}/\mu$rad) for the signal at ω_{rot} is agrees with the simple estimate of equation (5.4) if $\gamma \sim 0.05$ is assumed. The effect at $2\omega_{\mathrm{rot}}$ is about 10% of that at ω_{rot}. However, no significant quadratic dependence can be observed. Thus, the effect at $2\omega_{\mathrm{rot}}$ must be attributed to harmonics of the effect at ω_{rot} only. The second order coefficient B of equation (5.11) cannot be determined from this data. According to the above estimate a determination of B would have to apply larger tilt values on the order of several mrad in order to produce observable systematic effects of $\gg 1\,\mathrm{Hz}$ at $2\omega_{\mathrm{rot}}$.
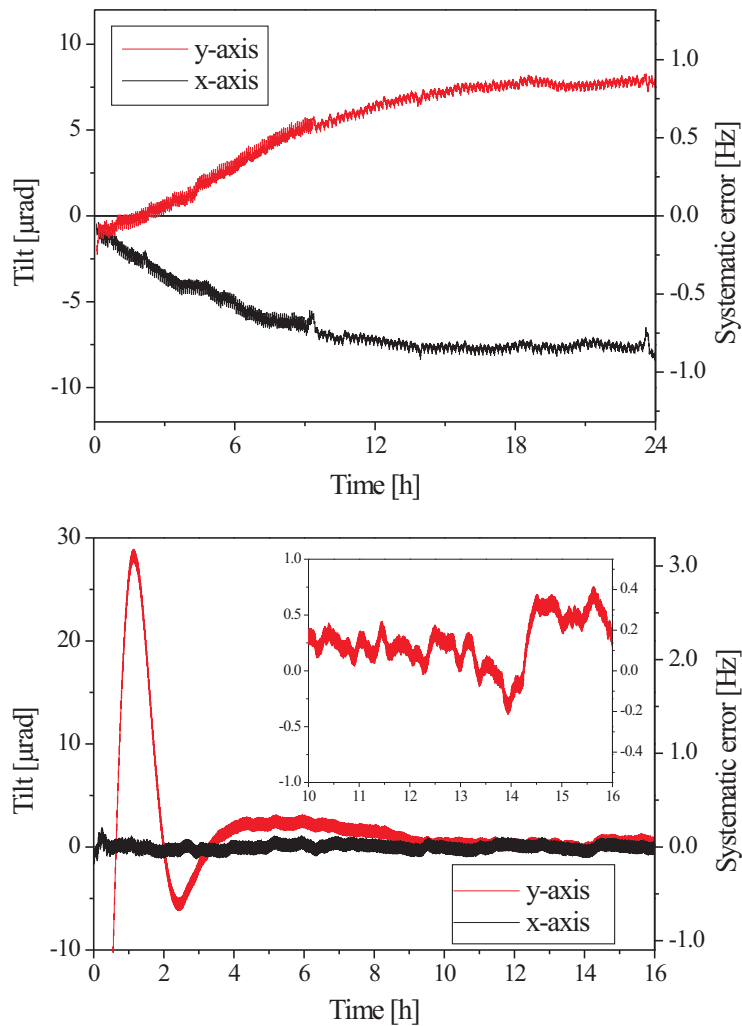
Figure 5.4: *Top graph: Typical variations of rotation axis tilt extend over ten or more μrad. These variations are caused by small movements of the building, where the experiment resides in a laboratory on the eighth floor. Bottom graph: Step response of tilt to an abrupt change of 100 μrad in y-axis tilt with active feedback applied. Insert: Residual long-term variations of tilt after 10 hours do not exceed 1 μrad. Note that the data has been smoothed to reduce measurement noise on the order of 1 μrad (peak).*
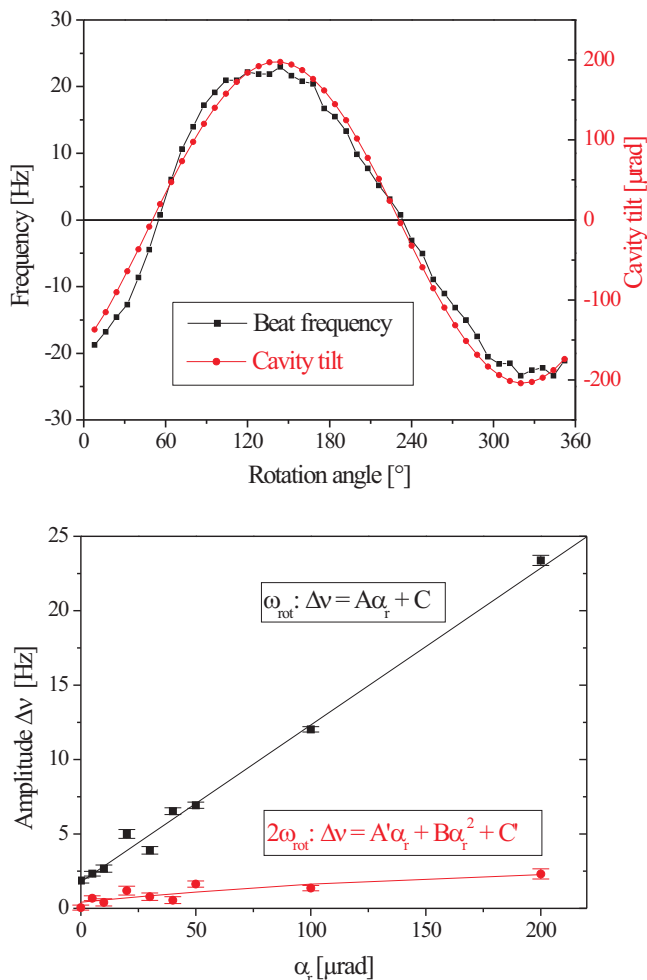
Figure 5.5: *Effect of large rotation axis tilt on the beat frequency. Top: Here, the setpoint of the rotation axis tilt control system was set to $\alpha_r = 200\,\mu rad$ along the laboratory y-axis. Thus, cavity tilt and beat frequency are modulated with turntable rotation as described by equation (5.11). The graph presents the periodical averages of the rotating tilt sensor's output and the beat frequency calculated from ~ 2000 rotations. Bottom: The systematic amplitudes as obtained for several values of rotation axis tilt. From a fit to this data, the tilt sensitivity coefficients of equation (5.11) can be determined. A' is included to model the leakage of the effect at ω_{rot} to $2\omega_{rot}$. C and C' correspond to the residual systematic effect at ω_{rot} and $2\omega_{rot}$ at zero rotation axis tilt. The fit results in $A = (105 \pm 4)\,mHz/\mu rad$, $C = 1.7\,Hz$, and $A' = (15 \pm 8)\,mHz/\mu rad$, $B < 1\,mHz/\mu rad^2$, $C' < 0.5\,Hz$.*

91

5.1.3 Axial runout

Modulation of cavity tilt due to axial runout (wobble) during a single rotation is not compensated by the slow tilt control described above. The table's specification on axial runout is $< 1\mu$rad with a high stiffness ($300\,\mathrm{N}/\mu\mathrm{m}$) even for heavy off-center loads. However, this only holds if the table is operated at the specified air pressures, preloaded by permanent vacuum pumping on the air bearing. The latter requires use of a heavy duty rotary vane pump next to the experiment. Since ambient vibrations deteriorate resonator frequency stability it was decided to omit such pumping. The effect of axial runout without vacuum preloading remained to be determined though. Thus, special care was taken to balance the center-of-mass of the rotating setup.

This further helped to minimize the effect of deformations of the supporting steel beam tripod, which vary with table rotation. The steel beams are not infinitely stiff and are estimated to bend by $\sim 100\,\mu\mathrm{m}$. Thus, systematic variations of only 1% of this value suffice to cause axis wobble on the order of $1\,\mu$rad. Thereby, the threefold symmetry of the supporting tripod favors systematic effects at $3\omega_\mathrm{rot}$ or $6\omega_\mathrm{rot}$ respectively. On the other hand, the twofold symmetry of the setup, mounted on the $1200 \times 900\,\mathrm{mm}^2$ breadboard, might cause an effect at the critical frequency $2\omega_\mathrm{rot}$.

The total load on the turntable is approximately $450\,\mathrm{kg}$. The rotation table itself contributes $390\,\mathrm{kg}$. This gives a total load of $\sim 840\,\mathrm{kg}$ on the tripod. To be able to balance the center-of-mass of the setup, three flat strain gauges are attached to the bottom of the table. When the table rotates, these strain gauges sense the periodical deformations of the supporting tripod. The amplitudes of the strain gauge signals oscillate with table rotation, which provides a measure for the offset of the center-of-mass. With loads of $0.5\,\mathrm{kg}$ to $10\,\mathrm{kg}$ each, placed at different positions on the rotating setup, these variations of strain during table rotation can be minimized. With the optimum distribution of balancing weights on the table, it is enough to add another $0.5\,\mathrm{kg}$ at $\sim 0.5\,\mathrm{m}$ distance from the center to causes an observable shift in the center-of-mass. Thus, for the balanced table the offset of the center-of-mass from the rotation axis r_o is approximately given by

$$r_o < \frac{0.5\,\mathrm{kg} \times 0.5\,\mathrm{m}}{450\,\mathrm{kg}} = 0.5\,\mathrm{mm}. \tag{5.12}$$

The sensitivity of the beat frequency to off-center loads has been studied as shown in Figure 5.6. Here, after balancing the table, a compact steel block of $13\,\mathrm{kg}$ was placed onto the top plate of the rack that supports the vacuum chamber. For different distances from the center, the resulting shift r_o of the center-of-mass was estimated as in equation 5.12 and a beat frequency measurement over ~ 1000 rotations for each value of r_o was recorded.

92
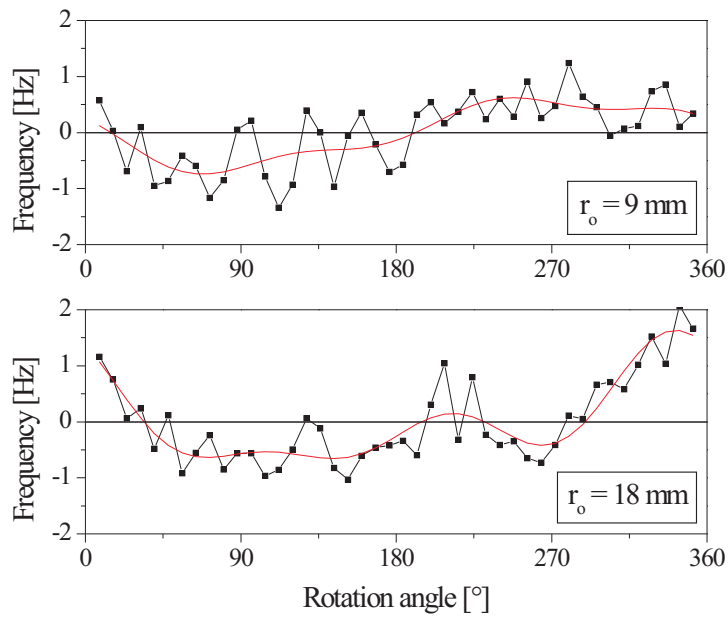
Figure 5.6: *Effect of translating the center-of-mass of the turntable setup. The periodical averages give the average beat frequency variation over a single rotation for different displacements r_0 (± 0.5 mm) of the center-of-mass from the turntable center. Each periodical average is calculated from ~ 1000 rotations.*

The periodical averages calculated from these measurements do not show an increase of the systematic effect at ω_{rot} or $2\omega_{\mathrm{rot}}$ above 2 Hz. Thus, the sensitivity to axial runout is conservatively estimated to be below 1 Hz per mm center-of-mass displacement. With a carefully balanced table ($r_o < 0.5\,\mathrm{mm}$) the effect is $< 0.5\,\mathrm{Hz}$.

5.2 Centrifugal forces

5.2.1 Model

Centrifugal forces can cause a systematic effect if they are modulated due to table rotation runout. The effect of centrifugal forces can be modeled in a simplified manner, treating the cavity as a fused silica cylinder of length L. The cavity is placed on the turntable with its optical axis aligned in radial direction. The inner end of the cylinder is at a distance a_1 from the rotation axis and the outer end is at a distance $a_2 = a_1 + L$. ρ is the material density and E is Young's modulus. The table rotates at an angular frequency ω and the cavity is assumed to be fixed at a single point P at a linear offset of $a_1 + (\gamma + 1)L/2$ from the turntable center, where $0 < \gamma < 1$. The relative length changes are calculated separately for the inner and outer part as referred to P.

The centrifugal deformation of a cavity segment of length dr at a distance r from the rotation axis is

$$d\left(\frac{\Delta L}{L}\right) = \frac{\rho\omega^2}{E}r\,dr. \qquad (5.13)$$

This expression is integrated from $r = a_1$ to $r = a_1 + (\gamma+1)L/2$ for the inner part, respectively from $r = a_1 + (\gamma+1)L/2$ to $r = a_1 + L$ for the outer part. The difference of the resulting expressions is given by

$$\left(\frac{\Delta L}{L}\right)_\omega = \frac{\rho\omega^2}{E}[\gamma a_1 L + \frac{L^2}{4}(\gamma^2 + 2\gamma - 1)]. \qquad (5.14)$$

According to this model a change of the rotation rate ω to $\omega' = \omega + \Delta\omega$ alters the cavity frequency by

$$\left(\frac{\Delta\nu}{\nu_0}\right)_{\Delta\omega} = \left(\frac{\Delta L}{L}\right)_{\omega+\Delta\omega} - \left(\frac{\Delta L}{L}\right)_\omega$$
$$= \frac{\rho}{E}[\gamma a_1 L + \frac{L^2}{4}(\gamma^2 + 2\gamma - 1)](2\omega\Delta\omega + \Delta\omega^2), \qquad (5.15)$$

where again $\Delta L/L = \Delta\nu/\nu_0$ was applied. For small variations in rotation rate $\Delta\omega \ll 2\omega$ and symmetric mounting of the cavity ($\gamma = 0$), this reduces to a linear effect of

$$\left(\frac{\Delta\nu}{\nu_0}\right)_{\Delta\omega} = A\Delta\omega \qquad (5.16)$$

with

$$A = \frac{\rho L^2}{2E}\omega. \qquad (5.17)$$

Insertion of values for R1 and $\omega = 2\pi/45\,\mathrm{s}^{-1}$ yields the relative sensitivity

$$A = 200 \times 10^{-14}/\frac{\mathrm{rad}}{\mathrm{s}}. \qquad (5.18)$$

Conversion to sensitivity of $\Delta\nu$ with $\nu_0 = 2.82 \times 10^{14}\,\mathrm{Hz}$ yields:

$$A = 560\,\mathrm{Hz}/\frac{\mathrm{rad}}{\mathrm{s}}. \qquad (5.19)$$

Thus, systematic variations of $\omega_{\mathrm{rot}} = 2\pi/45\,\mathrm{s}^{-1}$ have to be kept at $\Delta\omega < 10^{-3}\,\mathrm{rad/s}$ corresponding to $\Delta\omega/\omega < 1\%$, in order to suppress systematic frequency fluctuations below a level of $1\,\mathrm{Hz}$. Note however, that this estimate holds for a cavity fixed at a single point at the center only, while the actual effect largely depends on the mounting of the cavity.

5.2.2 Active stabilization of rotation rate

An active stabilization of the turntable rotation rate was implemented in order to (i) provide constant rotation rate throughout a measurement and (ii) minimize variations of centrifugal forces. Constant rotation rate (i) substantially simplifies the analysis of the data for a Lorentz violation signal, though in principle only accurate knowledge of table position at any instant of the measurement is required. With respect to (ii) a modulation at $2\omega_{\mathrm{rot}}$ is especially critical, which might be caused by interactions with a badly synchronized electric feedthrough rotation.

The rotation rate can be determined from the output of the encoder, which is a sinusoidal signal with 18000 periods per turn (see Section 4.5.1). This corresponds to a frequency of $400\,\mathrm{Hz}$ at the desired rotation period of $45\,\mathrm{s}$. Stabilization of the rotation rate is achieved by phase-locking this encoder signal to a stable reference (HP 33120A). The encoder output and the reference signal are fed into a digital phase detector, that determines the relative phase of the two signals unambiguously in a range of $127 \times 2\pi$. This corresponds to $5°$ deviation in angular table position. The instantaneous phase
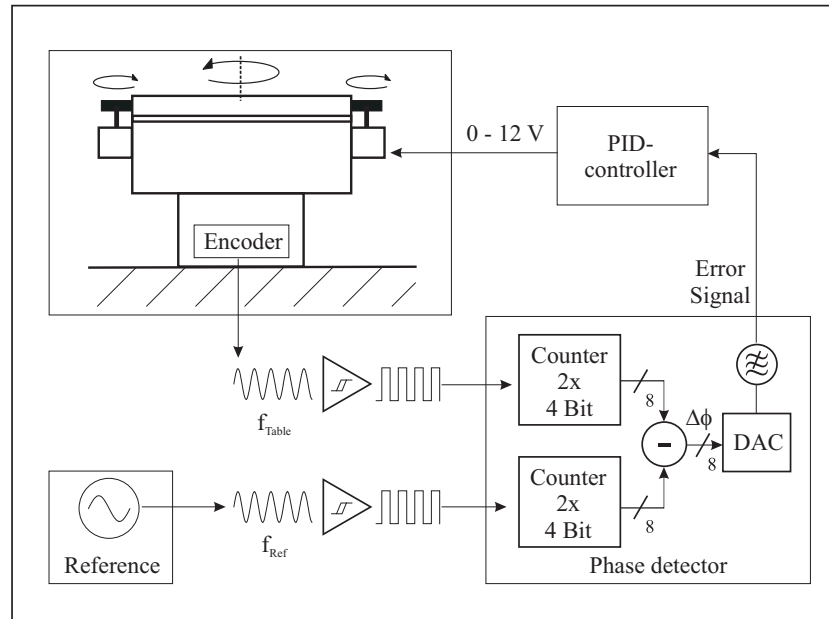
Figure 5.7: *Schematic outline of the rotation rate control system. See text for a description.*

difference is converted to an analog output by a digital-to-analog converter and a low-pass filter. Thus, angular deviations from ideal rotation even below $360°/18000 = 0.02°$ can be resolved. The analog output of the phase detector serves as input to a PID-controller, which control the two DC-motors that rotate the table. The table's large inertia thereby served as an effective low-pass suppressing any high-frequency $(> \sim 1\,\mathrm{Hz})$ noise on the rotation rate. This substantially simplified the realization of the phase lock.

The performance of this active rotation rate control is illustrated in Figure 5.8. To the top, the initial settling of the rotation rate at the onset of table rotation is shown. After five table rotations deviations from the setpoint rotation rate remain below 1%. To the bottom, periodical averages of the remaining deviations in rotation rate are given for slow $(T_{\mathrm{rot}} = 88\,\mathrm{s})$ and fast $(T_{\mathrm{rot}} = 36\,\mathrm{s})$ rotation rate. At faster rotation a modulation of the rotation rate at ω_{rot} appears with an average systematic peak deviation in rotation angle on the order of $0.2°$. The corresponding systematic effect on the beat frequency is on the order of $0.2\,\mathrm{Hz}$.
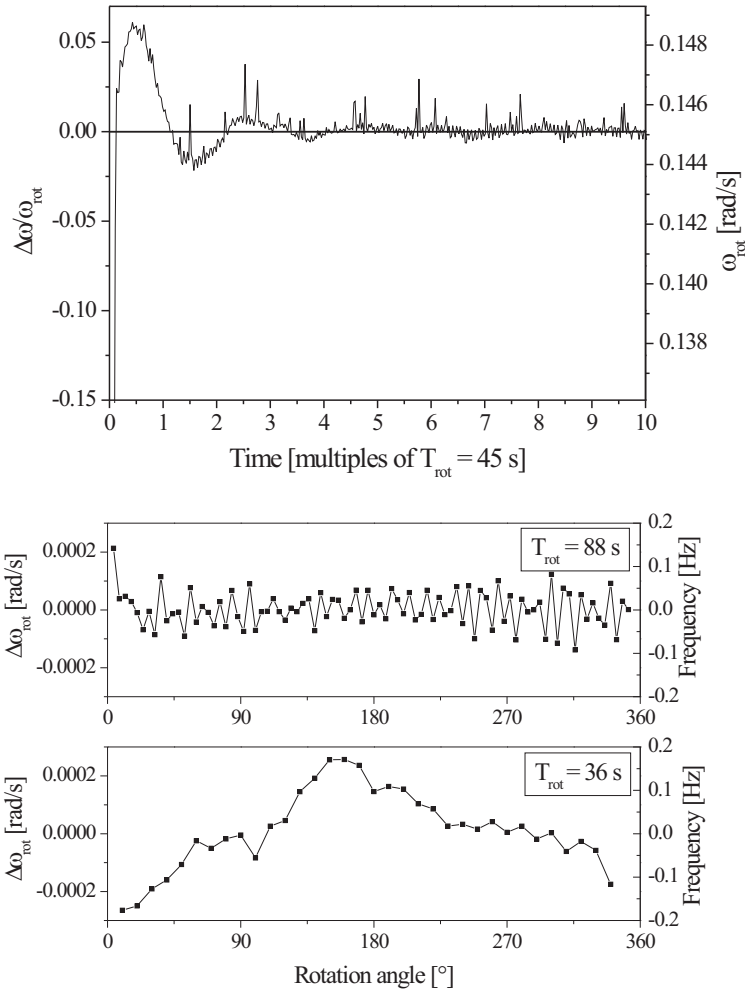
Figure 5.8: *Performance of rotation rate control. Top: It takes about five full rotations after starting the table rotation until the rotation rate is adjusted to the setpoint. The spikes are an artefact arising from synchronization of the counter gate time. Bottom graph: Residual deviations from constant rotation rate for fast ($T_{rot} = 36\,s$) and slow ($T_{rot} = 88\,s$) rotation rate. Periodical averages of the the deviation from the setpoint rotation rate are shown, each obtained from more than 1000 rotations. The average systematic peak deviation in rotation angle is below 0.2° in the worst case. The axis to the right gives the estimated associated systematic frequency deviation according to the experimentally determined sensitivity. For fast rotation ($T_{rot} < 40\,s$), residual centrifugal forces contribute a systematic effect at ω_{rot} on the order of 0.2 Hz.*

Experimental determination of sensitivity to centrifugal forces

The accurate control of the table rotation rate allowed a determination of the parameter A in equation (5.16). Slowly sweeping the table rotation rate up and down produced a beat frequency variation as shown in Figure 5.9. The amplitude of this beat frequency modulation $\Delta\nu$ was determined from periodical averages involving several hundred sweeps. This amplitude can be related to the span of the rotation rate sweep $\Delta\omega_{\mathrm{rot}}$. In total five such measurements with different spans $\Delta\omega_{\mathrm{rot}}$ were performed. A linear fit to this data yields

$$A = (666 \pm 84)\,\mathrm{Hz}/\frac{\mathrm{rad}}{\mathrm{s}}, \tag{5.20}$$

which is only slightly larger than the value estimated from the simple model above. This value of A corresponds to a beat frequency change of $\sim 2\,\mathrm{Hz}$ when changing $T_{\mathrm{rot}} = 45$ by $\Delta T = 1\,\mathrm{s}$. A closer consideration of the data in Figure 5.9 however reveals, that the five data points do not agree well with the linear fit. One reason might be the fact that data from two measurement runs has been combined here, which seem to exhibit different sensitivity to centrifugal forces. Thus, the data from the two measurements has been fitted separately as a second approach. Furthermore, since the applied values of $\Delta\omega$ do not meet the requirement $\Delta\omega \ll 2\omega$, a quadratic term (A') has been included into these fits. Finally, for $\Delta\omega_{\mathrm{rot}} \to 0$ the two measurements show a linear dependence with $A = 966\,\mathrm{Hz}/(\mathrm{rad/s})$ and $A = 648\,\mathrm{Hz}/(\mathrm{rad/s})$ respectively. Of course, the significance of these fits that rely on such few data points remains questionable. Still, they might given an estimate of the order of magnitude of the effect.

5.3 Electromagnetic interference

The very first measurements taken with a rotating table showed systematic effects due to variations of the electronic offset on the error signal. This was caused by electric stray fields at the PDH modulation frequency ω_m, which added to the error signal. A source of such electric stray signals is the local oscillator (LO) for demodulation of the error signal, which produces a high-level signal at ω_m. Interference of the error signal with reflections of LO stray fields depends on the orientation of the setup. Thus, the error signal offset gets modulated when the table is rotated, which causes a systematic beat frequency variation (see Figure 5.13). Initially, for a comparison of R1 to the identical co-rotating resonator, an effect on the order of $100\,\mathrm{Hz}$ as shown in Figure 5.11 could be observed. The most sensitive spot to such interference is the preamplifier stage, where the error signal is weakest. Enclosure of this
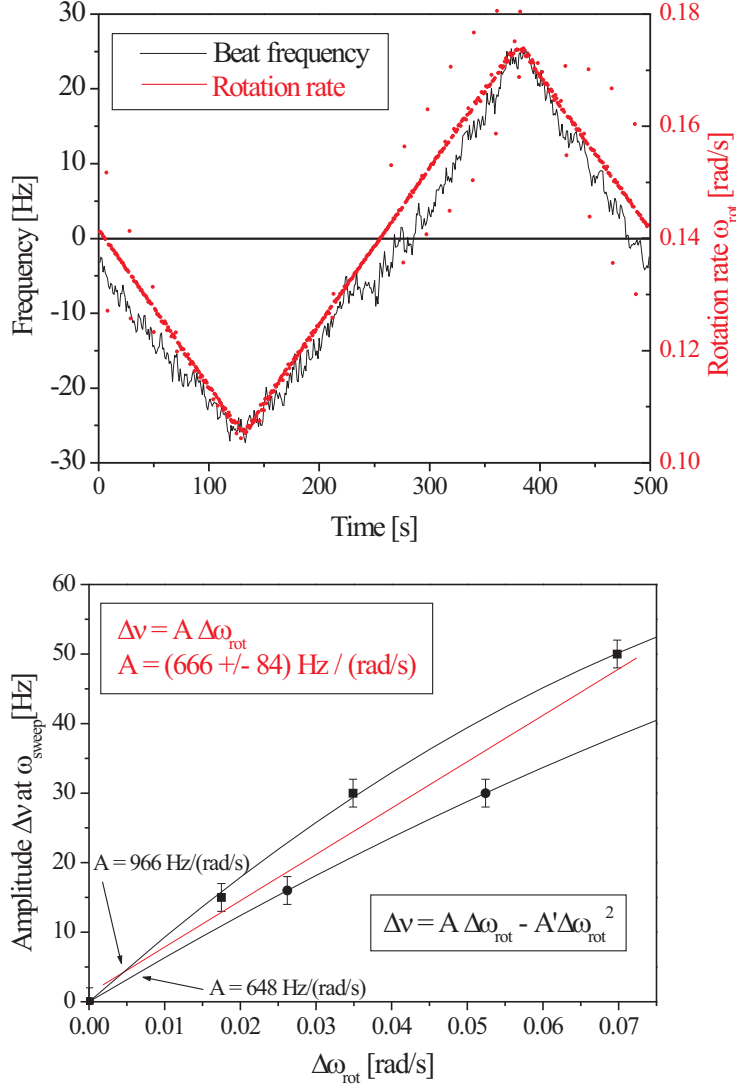
Figure 5.9: *Effect of a varying rotation rate on the beat frequency. Top: The rotation rate $\omega_{\mathrm{rot}} = 0.14\,\mathrm{rad/s}$ has been swept by $\Delta\omega_{\mathrm{rot}}/2 = \pm 0.035\,\mathrm{rad/s}$ with a period of $500\,\mathrm{s}$. The graph shows the corresponding periodical average of the simultaneously recorded beat frequency and the instantaneous rotation rate over ~ 200 sweeps. Bottom: The beat frequency variation $\Delta\nu$ (peak to peak) has been determined from similar measurements for several values of $\Delta\omega_{\mathrm{rot}}$. An average linear dependence $\Delta\nu = A\Delta\omega_{\mathrm{rot}}$ has been fitted to the data which gives $A = (666 \pm 84)\,\mathrm{Hz/(rad/s)}$ (see text for details on the additional fits).*

99

Figure 5.10: *A view of the neighboring building gives an impression of the rather noisy environment regarding to electromagnetic stray signals.*

preamplifier in a well-sealed steel-plate box, and the use of some additional aluminum foil, sufficed to significantly reduce the effect. Further, this effect scales with the cavity linewidth and thus was much less pronounced for R1 than for the (damaged) corotating cavity. To circumvent any residual problems from such interference of LO stray fields, the error signal was shifted to a different frequency after amplification and before demodulation, using an additional mixer and another local oscillator as sketched in Figure 5.12. At the cost of an additional local oscillator, this scheme guarantees that LO stray signals are separated in frequency from the sensitive error signal at ω_m.

5.4   Temperature gradients

The presence of a permanent temperature gradient in the laboratory causes a modulation of ambient temperature of the setup when the table rotates. Such a gradient could be caused by the air conditioning which features an outlet of cooled air in the laboratory ceiling, close to one side of the setup. Sensitive components to temperature variations are (i) the resonators inside the chamber (ii) the servo electronics (iii) the mixer in the PDH setup and (iv) the optical setup. With respect to resonator temperature the good ther-
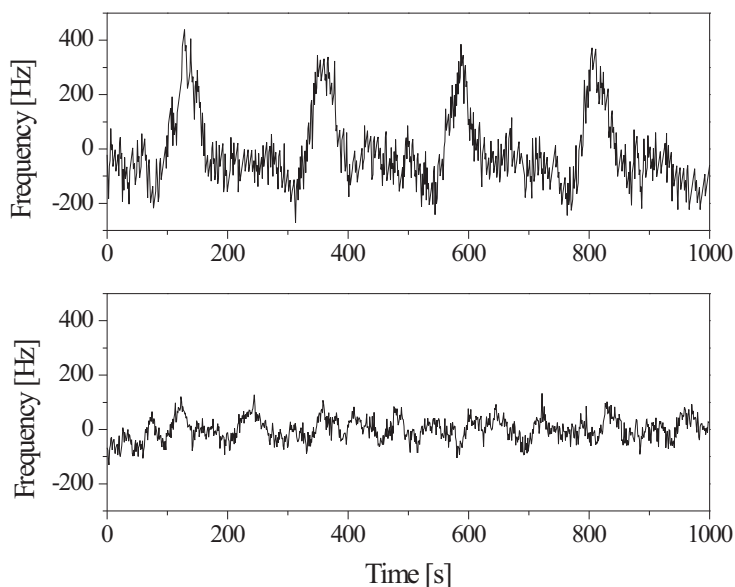
Figure 5.11: *Illustration of the effect of electromagnetic stray signals. Top: An extract of 1000 s taken from one of the first beat frequency measurement that was obtained from the rotating setup, comparing the two rotating resonators. The rotation period was set to 200 s here and systematic frequency variations are on the order of several 100 Hz. Bottom: A measurement of the beat frequency after improved shielding of the first preamplifier. Here, the rotation period was set to ∼100 s.*
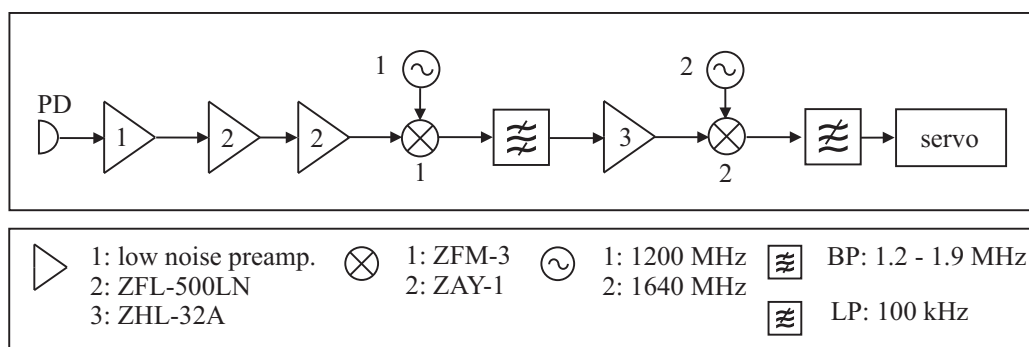
Figure 5.12: *Reconstruction of the lock electronics in order to avoid interference with local oscillator stray signals. With an additional mixer and local oscillator (1), the signal is shifted from 440 kHz to 1644 kHz before demodulation to DC.*

101

mal isolation effectively suppresses modulations at a period of 45 s and no indication for a modulation of resonator temperature with table rotation has been observed.

A modulation of the temperature of the electronic circuits (ii) and (iii) affects the mixer offset voltage and OpAmp offset voltages in the range of 100 nV/°C, possibly amplified by subsequent stages. Also variations of resistor and capacity values, which set the servo gain, might be caused. Heating these components by > 10°C with a heat gun, produced a beat frequency change on the order of several Hertz. Thus, we estimate that no systematic effect > 1 Hz should be caused, as long as temperature gradients do not exceed 0.1°C.

For the optical setup (iv), temperature variation causes frequency shifts due to varying parasitic etalons. Such etalons are formed between lenses, windows, photodiode surface and cavity mirrors etc., and effectively add a small offset to the PDH error signal. Thermal expansion of the setup alters the length of these parasitic etalons and leads to a varying offset and a varying lock point frequency. Thus, great care has been spent to avoid such parasitic etalons by tilting windows, lenses and photodiodes. Heating different parts of the optical setup by several degrees with a heat gun finally did not produce an effect of more than ~ 5 Hz/°C. Thus, with a temperature modulation of < 0.1°C per turn, corresponding systematic beat frequency variations are below 0.5 Hz.

5.5   Modulation of error signal amplitude and offset

Temperature gradients and electric stray signals, as discussed above, both shift the lockpoint by changing the error signal offset and amplitude. Other unknown systematic influences might affect the beat frequency in the same way. Thus, two measurements were performed here, to at least estimate the extent of such effects irrespective of their actual origin.

Given a symmetric error signal and no offset, a decrease in error signal amplitude should not affect the lock point as illustrated in Figure 5.13 (a). For a non-vanishing offset however, a decreased error signal amplitude leads to a shift of the lock point frequency (Figure 5.13 (c)). For small lock point shifts $\nu_2 - \nu_1 \ll \Delta\nu_C$, the error signal slope can be approximated to be $2A/\Delta\nu_C$ and a variation of error signal amplitude leads to

$$\Delta\nu = \nu_2 - \nu_1 = \frac{O}{2A}\Delta\nu_c(\frac{1}{x} - 1), \tag{5.21}$$

102
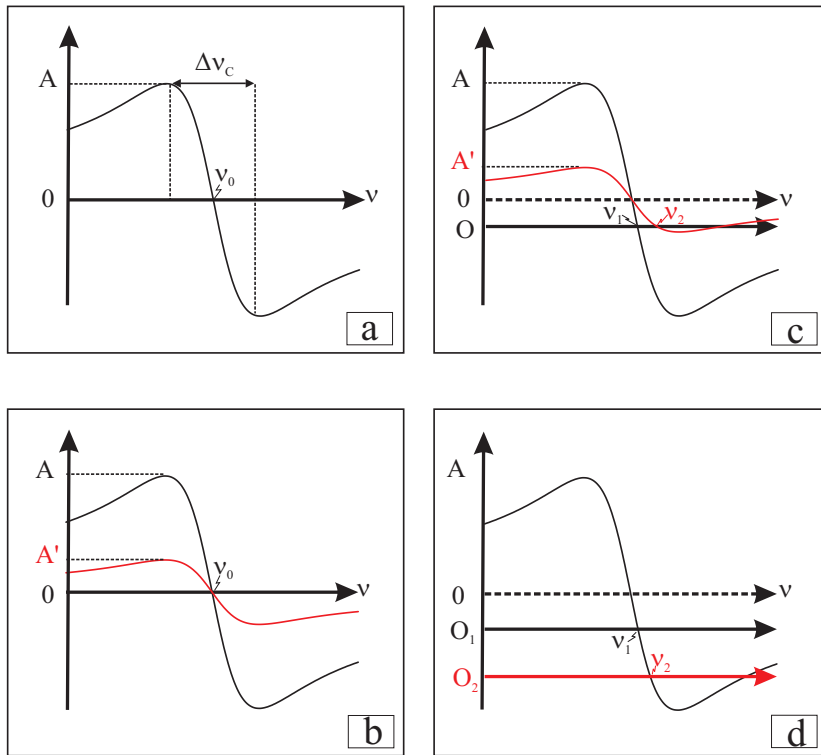
Figure 5.13: *Frequency shift $\Delta\nu = \nu_1 - \nu_2$ of the lock point due to electronic error signal offset. Graphs b and c illustrate the lock point shifts due to a varying error signal amplitude A with zero offset (b) and a finite offset O (c). Graph d illustrates the lock point shifts due to a variation of the error signal offset.*

where A is the error signal peak amplitude, $A' = xA$ is the decreased error signal amplitude, O is the offset on the error signal and $\Delta\nu_c$ is the cavity linewidth. Assuming a systematic variation of the error signal amplitude of 1% (x = 0.99) and an offset of $O = 0.01 \times 2A$ (e.g. 2.5 mV for $A = 125$ mV at the mixer output), the systematic frequency shift is

$$\Delta\nu = 10^{-4}\Delta\nu_c. \tag{5.22}$$

This turns into a systematic effect of ~ 3 Hz for the rotating cavity R1.
Vice versa, the measurement of the beat frequency provides a sensitive tool to determine the relative magnitude of variations of the error signal amplitude with turntable rotation. A deliberately generated large offset enhances the systematic effect caused by small variations of the amplitude. Consequently, approximately 1000 rotations have been performed with an error signal amplitude $A = 125$ mV and the offset O adjusted to 0 mV, 10 mV or 20 mV respectively. The corresponding systematic effect can be determined from periodical averages of the beat frequency for each of these measurements (see Figure 5.14). While for zero offset no effect > 1 Hz is found, an offset of 20 mV a leads to a systematic effect as large as $\Delta\nu = 5 \pm 1$ Hz. Insertion of this value into equation (5.21) together with $O/2A = 0.08$ yields $x = 0.9979 \pm 0.0004$. This corresponds to an absolute fluctuation of 250 ± 50 μV and a relative fluctuation of $\sim 0.21 \pm 0.04$%. As the effect scales linearly with offset voltage, the offset has to be kept below 4 mV or $O/A < 3$%, in order to keep the systematic variation of the beat frequency below 1 Hz.

The above consideration assumes constant offset. However, a modulation of the offset with table rotation might occur as well. This affect the beat frequency, even if the error signal amplitude is kept constant (see Figure 5.13 (d)). A systematic variation of the error signal offset $\Delta O = O_1 - O_2$ leads to a systematic frequency shift of

$$\Delta\nu = \nu_2 - \nu_1 = \frac{\Delta O}{2A}\Delta\nu_c. \tag{5.23}$$

Thus, for the rotating resonator R1 an offset variation during one rotation of $\Delta O/2A = 10^{-4}$ only, produces a systematic error of ~ 3 Hz. Analogous to the above measurement, the effect of a systematically varying offset ΔO on the beat frequency can be enhanced by reducing the error signal amplitude A. However, this requires to tune the amplitude without varying the offset. If the offset is of purely electronic origin (e.g. mixer offset), this can be achieved by reducing the power of the incident laser light. Consequently, a measurement including 1000 rotations at five times decreased light power
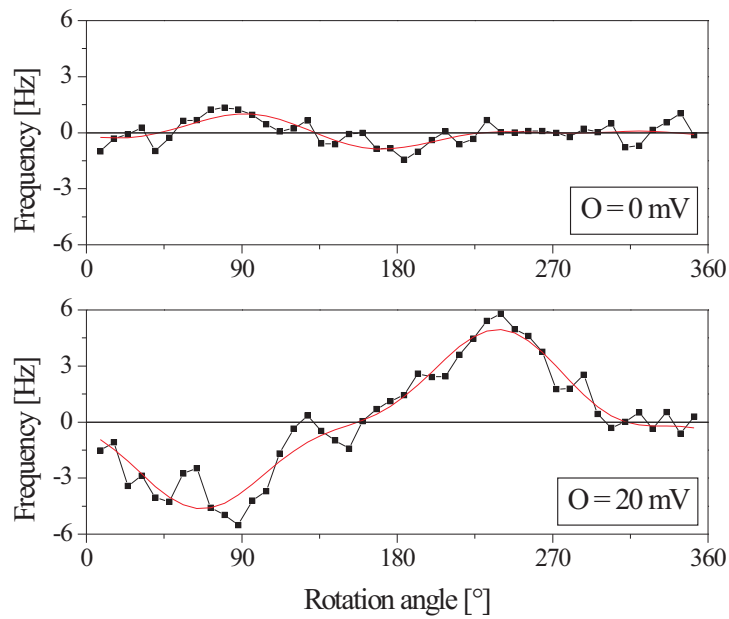
Figure 5.14: *Effect of systematic error signal amplitude fluctuations in the presence of an electronic offset. An electronic offset O was superimposed onto the error signal. The error signal amplitude was 250 mVpp. The periodical averages have been calculated from ~ 1000 rotations each and give the average frequency variation over a single turntable rotation. The increased systematic variation for $O = 20$ mV can be attributed to small fluctuations of the error signal amplitude (assuming constant offset during a single rotation).*

was performed ($A \sim 25\,\mathrm{mV}$). However, this did not reveal any effect $> 1\,\mathrm{Hz}$. Thus, systematic electronic offset fluctuations ΔO are estimated to be below $1\,\mu\mathrm{V}$ corresponding to $\Delta O/2A = 4 \times 10^{-5}$. Note however, that this measurement does not include a variation of the error signal offset by purely optical means, such as varying parasitic etalons.

In conclusion, the above effects do not contribute a systematic error $> 1\,\mathrm{Hz}$, as long as offsets are kept below $\sim 3\%$ of the error signal amplitude and show no systematic variations $> 0.01\%$ of the error signal amplitude ($> 5\,\mu\mathrm{V}$ for the typically applied error signal amplitude). These conditions are currently met without active stabilization of the offset or the coupling of to the resonators. Note however, that long-term drifts of the error signal offset exceed the specified limits within few days. Thus, in order to perform a long-term measurement within a future setup, an active stabilization of offset is advisable. This could be implemented following a scheme that has been applied in a previous measurement and is described in [MHS+03b]. Furthermore, a stabilization of the coupling to the resonator has been described in [Mül04], which could also help to improve future performance.

5.6   Failure of counter synchronization

Some of the initial measurements showed abrupt steps of the beat frequency of several Hertz, which occurred systematically with turntable rotation. This characteristic feature was caused by a failure in data acquisition due to bad initialization of the counter. If not reset properly, data from a preceding measurement is buffered in the counter's memory, which in effect distorts the synchronization. As a consequence, for the initial sampling gate time of each turntable rotation a delay of several ms is caused, which compromises the result of the frequency measurement during this interval. A correlation of this systematic effect and a delayed initial gate time was indeed observed. In accordance with these observations, the magnitude of the effect is was found to depend on the instantaneous beat frequency drift. However, the effect was not studied in detail, as it disappeared after proper initialization of the counter. Still, it shows quite plainly that the synchronization of the data acquisition is a critical issue, especially in the presence of a large frequency drift.

5.7 Earth's magnetic field

Magnetostriction within Earth's magnetic field is an effect that plagued many previous versions of Michelson-Morley experiments. Some of these experiments were especially sensitive to this effect, because they applied masers featuring metallic microwave cavities [JJMT64] or spacers for the interferometer arms made from Invar. Rotation in the Earth's magnetic field then results in a periodic contraction of the setup, which causes a signal at the critical frequency of $2\omega_{\mathrm{rot}}$. Indeed, to avoid such a magnetostriction effect, G. Joos for his experiment [Joo30] explicitly avoided the use of Invar, and applied a quartz glass construction to support the interferometer arms.

In the present setup magnetostriction should not affect the rotating cavity directly, because it is fabricated from fused silica, and to our knowledge no magnetostriction (possibly due to magnetic impurities) has been observed for this or other fused glass material so far. Still, Earth's magnetic field could affect other components of the rotating setup. However, no indication was found that such an effect might be relevant at this level of accuracy. Nonetheless, the sensitivity to magnetic fields remains to be studied in detail within a future setup.

5.8 Summary

Table 5.1 gives an overview of all systematic effects identified throughout this work and the level of suppression achieved for each effect. The values are stated for the dominant systematic effects at ω_{rot}, where it is understood that the effect at $2\omega_{\mathrm{rot}}$ is less or at most equal in magnitude. The progress with respect to suppression of systematic effects during the first 250 days of the measurement can be read off from Figure 5.15. During the gap from day 50 to 100 the stationary resonator R2 was implemented. The measurements before have been obtained from a comparison of the rotating to the second co-rotating resonator. The schemes for tilt control and rotation rate control were implemented in a basic version from beginning on, however, steadily improved and modified during the course of the measurements. The graph gives the systematic effects for all data sets acquired during this time. Out of these measurements, only those from R1 compared to R2, extending over > 24 hours and not affected by obvious malfunctions of control systems entered the final analysis. From December 2004 on (day ~ 150), residual systematic effects are on the order of a few Hertz and often below $1\,\mathrm{Hz}$, corresponding to a relative instability of $< 3 \times 10^{-15}$. As an example, consider the Fourier transform of a four-day data set shown in Figure 5.15, as com-

107

pared to the Fourier transform of an initial measurement shown in Figure 4.24. The peaks that indicate a systematic effect have been reduced below 1 Hz at ω_{rot}, respectively below the level of measurement noise at $2\omega_{\mathrm{rot}}$. This is a major achievement of the present work, as similar previous experiments were affected by systematic effects on the order of 10^{-13} [BH79] and also concurrent work has been reported, that reaches a suppression on the order of 3×10^{-14} only [SKE+03, AOGS05b].
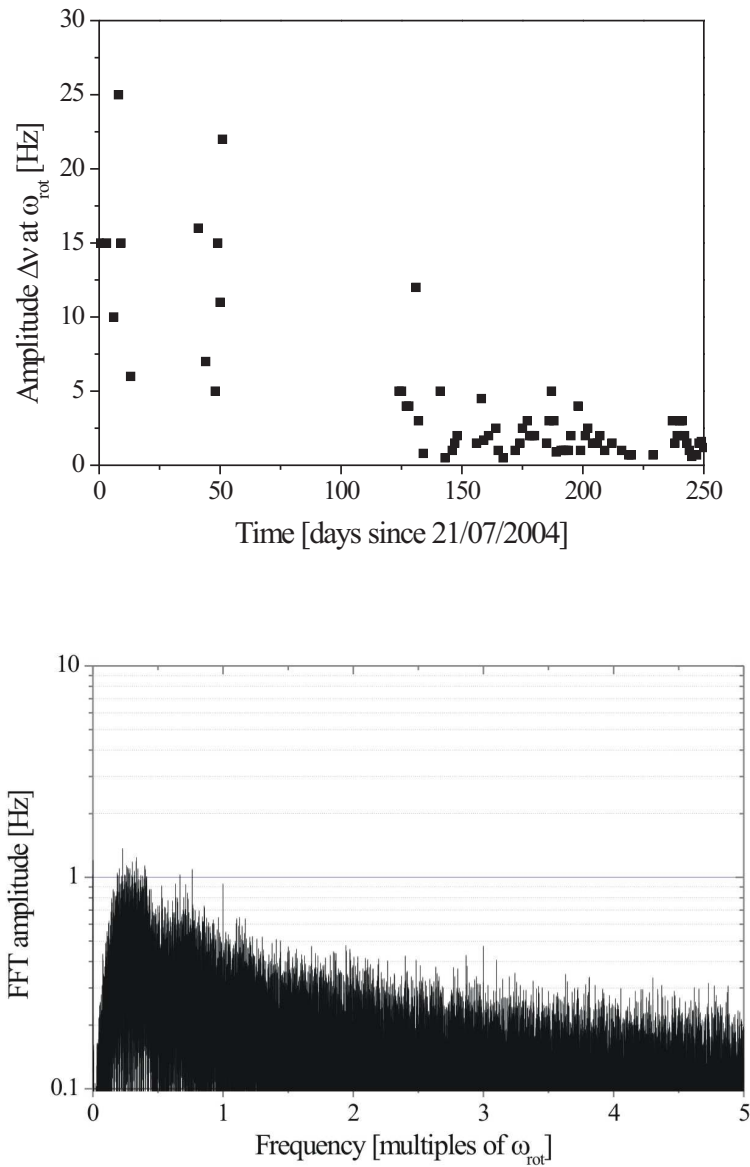
Figure 5.15: *Top: Improvements achieved with respect to suppression of systematic errors during the first 250 days after start of the measurements. Bottom: FFT of a beat frequency measurement extending over four days, after suppression of systematics. No systematic effect $> 1\,Hz$ is visible neither at ω_{rot} nor at $2\omega_{\mathrm{rot}}$.*

effect	sensitivity	typical variation	initial $\Delta\nu$ at ω_{rot}	suppression	final $\Delta\nu$ at ω_{rot}
rotation axis tilt	$\sim 0.1\,\mathrm{Hz}/\mu\mathrm{rad}$	$\alpha_r > 100\,\mu\mathrm{rad}$	$> 10\,\mathrm{Hz}$	$\alpha_r < 1\,\mu\mathrm{rad}$	$< 0.1\,\mathrm{Hz}$
rotation rate	$\sim 2\,\mathrm{Hz}/\Delta T_{\mathrm{rot}} = 1\,\mathrm{s}$	$\Delta T_{\mathrm{rot}} \sim 1\,\mathrm{s}$	$\sim 2\,\mathrm{Hz}$	$\Delta T_{\mathrm{rot}} < 0.05\,s$	$< 0.1\,\mathrm{Hz}$
center-of-mass	$\sim 1\,\mathrm{Hz}/\mathrm{cm}$	$r_o = 1\,\mathrm{cm}$	$\sim 1\,\mathrm{Hz}$	$r_o < 1\,\mathrm{mm}$	$< 0.1\,\mathrm{Hz}$
electrom. stray fields	-	-	$> 10\,\mathrm{Hz}$	n.q.	$< 0.1\,\mathrm{Hz}$
sampling errors	-	-	$> 10\,\mathrm{Hz}$	n.q.	$< 1\,\mathrm{Hz}$
temperature gradient	$< 5\,\mathrm{Hz}/°\mathrm{C}$	$\Delta T < 0.1°\mathrm{C}$	$< 0.5\,\mathrm{Hz}$	-	$< 0.5\,\mathrm{Hz}$
(parasitic etalons, mixer offset,...)					
PDH signal amplitude	$< 3\,\mathrm{Hz}/\mathrm{mV}$[a]	$\Delta A/A \sim 0.2\%$	$< 1\,\mathrm{Hz}$[b]	-	$< 1\,\mathrm{Hz}$
PDH signal offset	$\sim 30\,\mathrm{Hz}/\mathrm{mV}$[c]	$\Delta O < 10\,\mu\mathrm{V}$	$< 0.3\,\mathrm{Hz}$	-	$< 0.3\,\mathrm{Hz}$
Earth's magnetic field	-	-	$< 1\,\mathrm{Hz}$	-	$< 1\,\mathrm{Hz}$
total effect			$> \mathbf{10\,Hz}$		$< \mathbf{1\,Hz}$

Table 5.1: Overview of identified systematic effects and the suppression that has been achieved. n.q. = not quantified. [a] : assuming an error signal offset $< 10\%$ of the error signal amplitude. [b] : with the error signal offset adjusted to $< 3\%$ of the error signal amplitude. [c] : assuming an error signal amplitude of $A = 1$ V.

Chapter 6

Analysis and results

6.1 Course of the measurement

The basic measures to suppress systematic effects, mainly tilt control and stabilization of rotation rate, were implemented until November 2004. From December 2004 until March 2005 (phase 1), beat frequency measurements were taken at low systematic error and data could be taken regularly. Each data set consists of a continuous beat frequency measurement, sampled with a gate time of 1 s with the table rotating at a rate of one turn per T_{rot}. T_{rot} was set to 50 s for the initial measurements and decreased to 45 s in February, due to a modification of the rotation rate control system. During this period of 131 days, 14 data sets each spanning more than 24 h have been acquired. These data sets are rather equally distributed over phase 1 and all together cover 37 days including more than 71000 table rotations. The duty cycle, defined as the actual measurement time referred to the total time span, is about 28%. Phase one thus represents a time of intense data collection extending over four months (see Figure 6.1).

From April to June 2005, no measurements were performed, since additional heaters and thermistors were implemented in an attempt to actively stabilize the temperature of the resonator mount.

From June 2005 on, data collection continued and data was recorded at irregular intervals until January 2006. During this period of eight months, 13 data sets > 24 h were obtained, that all together cover 25 days and include 47000 rotations. This corresponds to a reduced duty cycle during phase 2 of ~12%. The main reasons for this are problems with the error-prone temperature stabilization and a breakdown of the pressurized air supply in late August. Acquisition and installation of a new compressor caused a second break of measurements from September to October 2005.

	phase 1	phase 2	total
total time span	12/04 - 03/05	06/05 - 01/06	12/04 - 01/06
	131 days	214 days	396 days
total measurements	66	41	107
usable measurements	14	13	27
total days	68	41	109
usable days	37	25	62
total rotations	130844	79680	210524
usable rotations	71000	47000	118000
duty cycle	28%	12%	16%
(usable days/time span)			

Table 6.1: *Overview of the duty cycle achieved during different phases of the measurement span of one year.*

In total, measurement data has been collected during a time span of more than one year. During this period the data is not equally distributed with two gaps of two months each.

6.2   Data of a single continuous measurement

As an example, the data recorded during a single continuous measurement is presented in more detail here. With a measurement span of four days, the example data set presented in Figure 6.2 constitutes the longest continuous measurement that was recorded. This and all other data sets are referred to a time axis t starting 0:00 UTC on January 1st, 2000. The example data set started at t = 1875.75 days, which is February 18th, and includes about 8000 rotations at a rotation period of $T_{\mathrm{rot}} = 45\,\mathrm{s}$.

Figure 6.2 shows the raw data, which exhibits an average frequency drift of $\sim -35\,\mathrm{Hz/s}$. This large drift compromized the application of an FFT, in order to determine the Fourier coefficients at $2\omega_{\mathrm{rot}}$ and the sidereal sidebands. The varying long term drift contributes to these Fourier components, irrespective of the applied windowing function. Thus, previous to a Fourier analysis a numerical high-pass filter (see Section 4.6) was applied to the data. The corner frequency of the high-pass filter was chosen as $\omega_{\mathrm{c}} = 1/(200\,\mathrm{s}) \ll \omega_{\mathrm{rot}}$. Note however, that such a filter distorts the amplitude and phase of the signal at $2\omega_{\mathrm{rot}}$. This is especially critical here, because the signal amplitudes in question ($\sim 0.1\,\mathrm{Hz}$) are about four orders of magnitude smaller than the frequency drift during a single table rotation ($\sim 1\,\mathrm{kHz}$).

Within the filtered data, characteristic peaks of $\sim 100\,\mathrm{Hz}$ amplitude can be
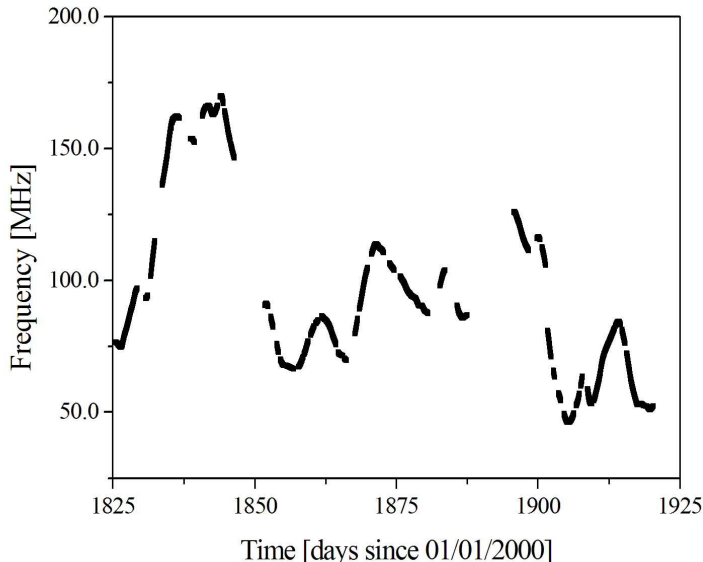
Figure 6.1: *Raw data collected during phase 1. The beat frequency measurements displayed here span from January 2005 to end of March 2005.*

observed at regular intervals of $\sim 1.2\,\text{h}$ and $\sim 3\,\text{h}$. Presumably, these peaks are caused by electromagnetic interference with stray fields from regularly switching electrical instruments located in the same building (e.g. motors of the air conditioning). Since this disturbance only affects approximately every hundredth table rotation, it results only in few outliers which can be excluded from the analysis without significant reduction of the data basis.

The Fourier transform of the filtered data (Figure 6.3) reveals no systematic effect $> \Delta\nu/\nu_0 = 1 \times 10^{-15}$ at the relevant frequency $2\omega_{\text{rot}}$. At ω_{rot} (not shown) a small peak indicates a residual systematic effect as large as $1\,\text{Hz}$. In principle, estimates of the coefficients $\tilde{B}_k$ and $\tilde{C}_k$ can be obtained from Figure 6.3 directly, if we consider the Fourier spectrum of a Lorentz violation signal as derived in Section 3.1. The Fourier coefficients are on the order of 1×10^{-15} and provide upper limits on the linear combinations of SME parameters given in Table C.2.

According to Table C.2, the same linear combinations of SME parameters enter the coefficients $\tilde{B}_k$ and the associated $\tilde{C}_k$. Thus, a measurement spanning a few days can only provide limits on five independent combinations of SME parameters. This is not sufficient to determine independent limits for all eight SME parameters.
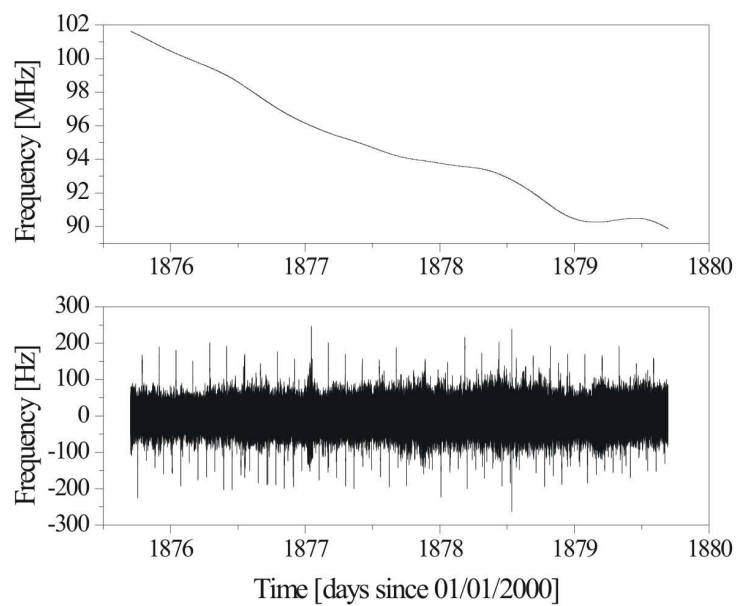
Figure 6.2: *Data from a single continuous measurement. The measurement starts February 18th, 2005, and extends over four days. Top: beat frequency raw data. Bottom: beat frequency after removal of drift applying a high-pass filter of corner frequency $\sim 1/(200\,s)$. The sampling rate is one data point per second.*
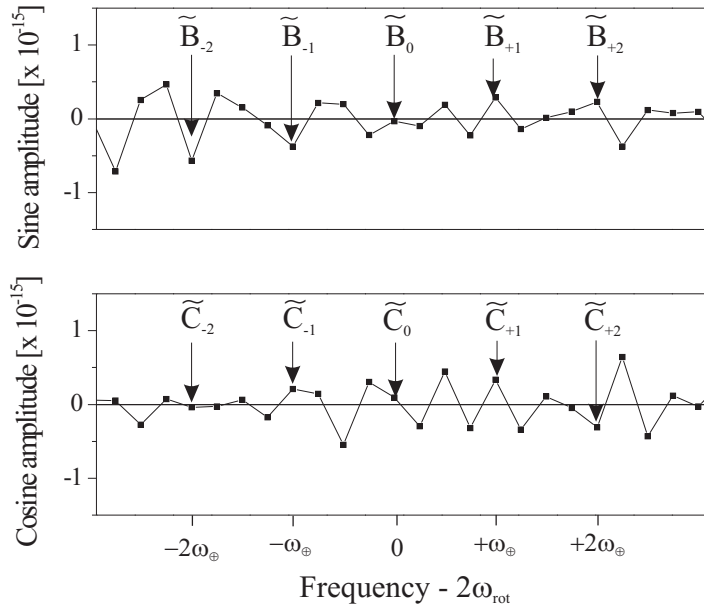
Figure 6.3: *Results of an FFT of the data displayed in Figure 6.2. The sine and cosine amplitudes in the vicinity of $2\omega_{\mathrm{rot}}$ are shown and the sidereal sideband amplitudes according to Table C.2 are assigned (compare to Figure 3.1). No systematic effect at $2\omega_{\mathrm{rot}}$ is visible.*

On the other hand, the Fourier amplitudes $\tilde{B}_k$ and $\tilde{C}_k$ could be determined for all 27 measurements as done for the example above. Then, the complete set of SME parameters could be determined from a fit of the annual variation of these amplitudes as given in Table C.2.

However, the signal distortions due to the applied filter are expected to limit the accuracy of such an FFT based analysis, though this has not been studied in detail here. However, from analyzing test data sets, an alternative method was found to well account for the large frequency drift and reproduce test signals at an accuracy $< \pm 0.1\,\text{Hz}$. This method is described below.

6.3   SME-analysis

For simplicity, the analysis focusses on the photonic sector of the SME. This also enables a direct comparison to similar experiments, which explicitly or implicitly assume no Lorentz violation in the electronic sector of the SME. As was shown in Section 3.1.3 however, Lorentz violation in the electronic sector of the SME can be taken into account by substituting $\tilde{\kappa}_{e-}^{IJ}$ with $\tilde{\kappa}_{e-}^{IJ} + 2\mathcal{M}_{\text{fs}}c_{IJ}$ in the final results.

6.3.1   Fit procedure

The analysis of the complete data is done in three subsequent fitting steps. In a first step, the amplitudes B and C are determined from a least squares fit of equation (3.13) to samples of few table rotations each. Then, the amplitudes B_k and C_k of equation (3.10) and (3.11) are determined for each single data set in a second step. In the last step, the annual modulation of these amplitudes as given in Table 3.1 is determined and estimates of the SME parameters are obtained. Each step includes data from an increased time span, thus the spectral resolution increases from step to step, until the complete signal for Lorentz violation is recovered.

Step 1

First, the data from each continuous measurement is divided into samples that extend over n rotations each. The sample size is chosen small enough to guarantee $n \times T_{\text{rot}} \ll T_{\text{sid}}$, such that B and C are approximately constant within each sample. Hereby the ith sample is attributed its mean time t_i on the adopted time axis and the amplitudes are labeled correspondingly, i.e. $B(t_i) = B^{(i)}$ and $C(t_i) = C^{(i)}$.
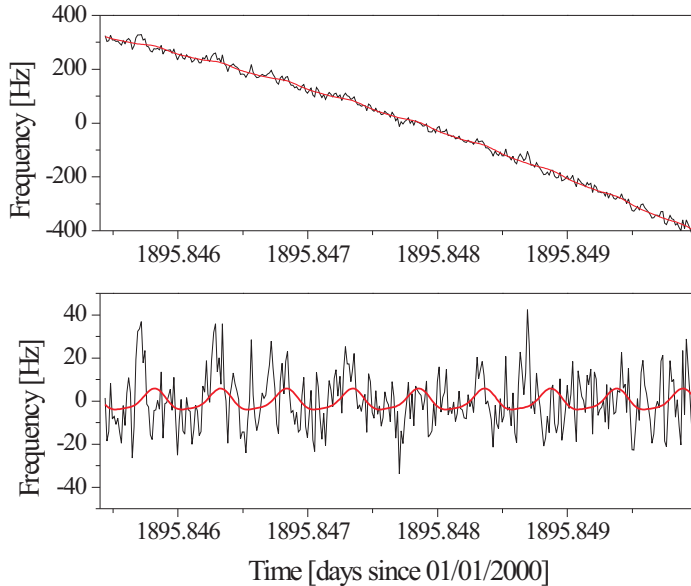
Figure 6.4: *A sample of the beat frequency measurement spanning ten rotations and a fit according to equation (6.2). Top: original data and fit. Bottom: linear and quadratic drift removed (for display only).*

The basic fit function to determine $B^{(i)}$ and $C^{(i)}$ from the ith sample is

$$\frac{\Delta\nu}{\nu_0} = B^{(i)}\sin(2\omega_{\mathrm{rot}}(t-t_0)) + C^{(i)}\cos(2\omega_{\mathrm{rot}}(t-t_0)) + A_0^{(i)} + A_1^{(i)}t, \quad (6.1)$$

where $A_0^{(i)}$ and $A_1^{(i)}$ are included to account for an arbitrary offset and a linear drift. t_0 is chosen such that $t - t_0 = T$, as defined in Section 3.1, i.e. it is set to the first instant within a measurement at which the optical axis of the rotating resonator and the laboratory x-axis coincide. The offset of this table rotation angle from the table's zero position is 41° and is included in t_0.

With the rotation rate control applied, deviations from an ideal rotation during a measurement are not an issue, as long as no strong disturbance of table rotation occurs (see Section 5.2). Nonetheless, the data was referred to the recorded table position when performing the fit, which guarantees that the fitted signal matches the phase of the table rotation at any instant of the measurement. This eventually involved corrections of the time axis on the order of few seconds, which however are not an issue within the following fit

117
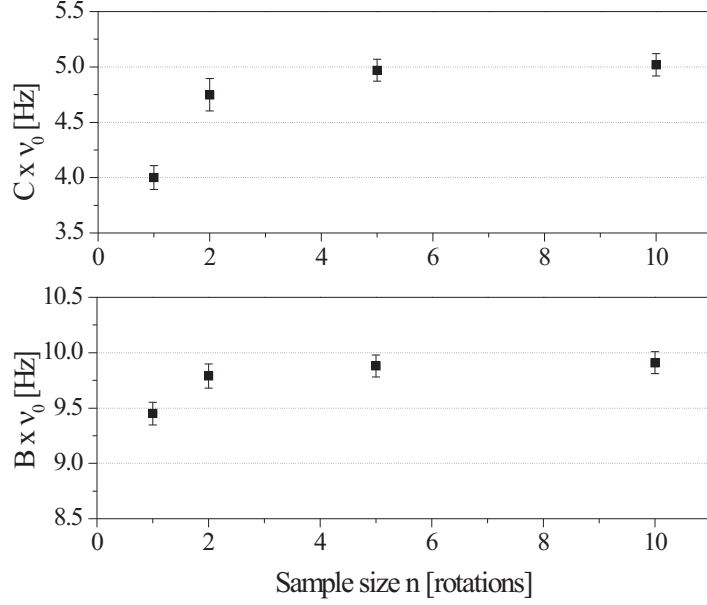
Figure 6.5: *Results of a fit of equation (6.1) to test data using different sample sizes. The graph gives the results obtained from fitting test data superimposed to the raw data of the four-day measurement, considered as an example in the previous section. For bin sizes $n \geq 10$ rotations, the test data amplitudes $B \times \nu_0 = 10\,Hz$ and $C \times \nu_0 = 5\,Hz$ are reproduced correctly within the $1\,\sigma$ error. The latter is on the order of $0.1\,Hz$. A small phase shift is observed though, which leads to a small systematic underestimation of the amplitudes B and a corresponding overestimation of amplitudes C. The absolute signal amplitude $\sqrt{B^2 + C^2}$ however remains unaffected.*

step concerning periods of 12 h and 24 h.

Optimum sample size in the presence of large frequency drift: A least squares fit to a sinusoidal signal at $2\omega_{\mathrm{rot}}$, superimposed with a linear frequency drift, does not give a correct estimate of the actual signal amplitude if the fit spans only a single period of a sinewave. However, the correlation of drift and sinusoidal signal decreases, if the number of periods included into the fit is increased. This is illustrated by results on test data, shown in Figure 6.5. The test data has been generated by superimposing a signal as described by equation (6.1) with $B \times \nu_0 = 10\,\mathrm{Hz}$ and $C \times \nu_0 = 5\,\mathrm{Hz}$ to the raw data of Figure 6.2. Dividing this test data set into samples of n rotations each (with

$n = 1, 2, 5, 10, 20$), fitting equation (6.1) to each sample, and averaging the results for $B^{(i)}$ and $C^{(i)}$, yields the mean values and standard errors shown in Figure 6.5. For sample sizes $n < 5$, the results differ significantly from the actual signal amplitudes. Thus, a sample size $n = 10$ was chosen, which yields results that are not affected by frequency drift, while it still meets the condition $10 \times T_{\mathrm{rot}} \sim 450\,s \ll T_{\mathrm{sid}} \sim 86400\,s$.

Optimum fit function: The fit function (6.1) has been extended by further parameters to better account for certain spectral characteristics of the data. Additional fit parameters $A_{\mathrm{S}}^{(i)}$ and $A_{\mathrm{C}}^{(i)}$ have been introduced to account for a potential systematic effect at ω_{rot}, where no Lorentz violation signal but only residual systematic effects are expected. Furthermore, as evinced by the Hadamard deviation shown in Figure 4.13, frequency drift is dominated by a nonlinear contribution above integration times of $\sim 100\,s$ corresponding to ~ 2 table rotations. With a sample size of 10 rotations this nonlinear drift becomes relevant and a quadratic term with fit parameter A_2 is added. The final fit function thus is:

$$
\begin{aligned}
\frac{\Delta \nu}{\nu_0} = {} & B^{(i)} \sin(2\omega_{\mathrm{rot}}(t - t_0)) + C^{(i)} \cos(2\omega_{\mathrm{rot}}(t - t_0)) \\
& + A_{\mathrm{S}}^{(i)} \sin \omega_{\mathrm{rot}}(t - t_0) + A_{\mathrm{C}}^{(i)} \cos \omega_{\mathrm{rot}}(t - t_0) \\
& + A_0^{(i)} + A_1^{(i)} t + A_2^{(i)} t^2.
\end{aligned}
\tag{6.2}
$$

As shown in Figure 6.6, inclusion of the additional parameters leads to a reduction of the average fit residuals of $\sim 10\%$.

Results of step 1: With a sample size $n = 10$ and $T_{\mathrm{rot}} = 45\,s$, the fit step 1 yields 192 equally distributed coefficients $B^{(i)}$ and $C^{(i)}$ from each 24 hour segment of data. For the example data set of Section 6.2, the resulting distributions are shown in Figure 6.7. We find a normal distribution around zero as evinced by the histograms and standard statistical tests. The standard deviation for both coefficients is $\sim 2.8\,\mathrm{Hz}$ and the standard error is on the order of $0.1\,\mathrm{Hz}$, which provides a first estimate of the sensitivity of the measurement. Similar distributions of $B^{(i)}$ and $C^{(i)}$ have been obtained from all other measurements as well. In total, we are thus left with 2×27 distributions, each spanning at least 24 h.

Step 2

In a second step, the 27 distributions of $B^{(i)}$ and $C^{(i)}$ versus time t_i are fitted with equations (3.10) and (3.11), respectively. This fit is performed as a
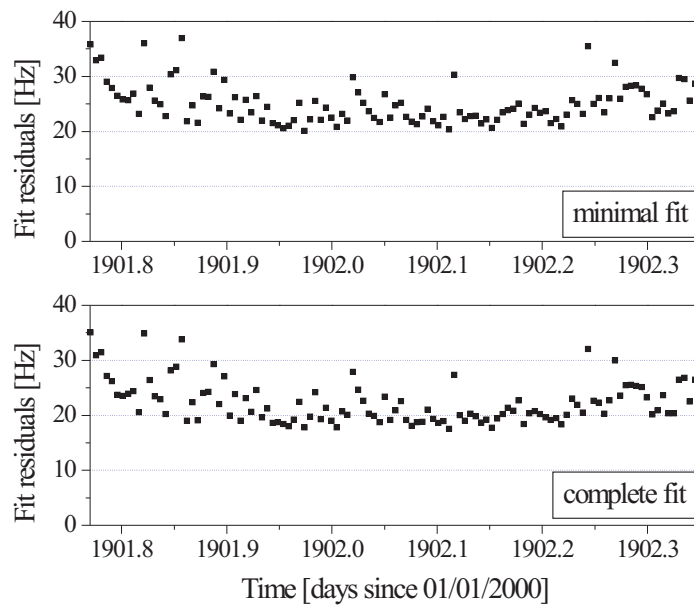
Figure 6.6: *Distribution of fit residuals of fit step 1 obtained from a data set that is affected by large drift and a systematic effect at ω_{rot} of $\sim 5\,Hz$. Each point gives the average $\sqrt{\chi^2}$ for a fit of equation (6.2) (bottom graph) or equation (6.1) (top graph) to a sample of ten rotations. A decrease of the average fit residuals of $\sim 10\%$ is observed, if the complete fit function (6.2) is applied.*
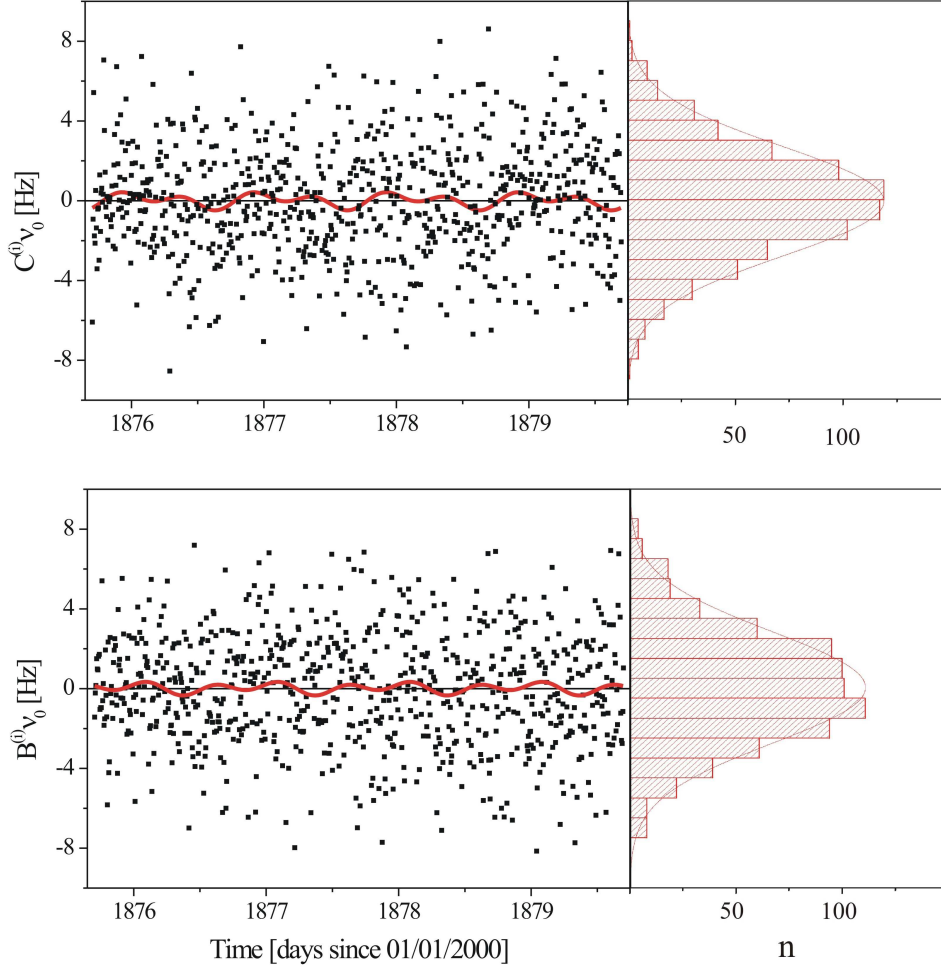
Figure 6.7: *Results for amplitudes $B^{(i)}$ and $C^{(i)}$ of the four-day measurement of Figure 6.2, involving ~ 800 samples. The values $B^{(i)}$ and $C^{(i)}$ are normally distributed around zero, which is further evinced by results of Shapiro-Wilks and t-tests. The associated standard error of both distributions is $0.1\,\mathrm{Hz}$, corresponding to a standard deviation of $\sim 2.8\,\mathrm{Hz}$. A fit of equation (6.3) and (6.4) according to fit step 2 is also displayed. These fits yield the modulation amplitudes B_k and C_k (all $\times 10^{-16}$): $C_0 = 0.7 \pm 3.3$, $C_{s1} = -1.4 \pm 4.7$, $C_{c1} = -8.8 \pm 4.7$, $C_{s2} = -9.1 \pm 4.7$, $C_{c2} = -3.1 \pm 4.7$, $B_0 = 1.0 \pm 3.3$, $B_{s1} = 3.4 \pm 4.7$, $B_{c1} = -4.2 \pm 4.7$, $B_{s2} = 5.9 \pm 4.7$, $B_{c2} = 5.7 \pm 4.7$.*

linear regression with B_k and C_k as the free parameters of the fit functions

$$\begin{aligned} B(t) &= B_0 + B_{\text{s1}} \sin(\omega_\oplus(t - t'_0)) + B_{\text{c1}} \cos(\omega_\oplus(t - t'_0)) \\ &\quad + B_{\text{s2}} \sin(2\omega_\oplus(t - t'_0)) + B_{\text{c2}} \cos(2\omega_\oplus(t - t'_0)), \end{aligned} \tag{6.3}$$

$$\begin{aligned} C(t) &= C_0 + C_{\text{s1}} \sin(\omega_\oplus(t - t'_0)) + C_{\text{c1}} \cos(\omega_\oplus(t - t'_0)) \\ &\quad + C_{\text{s2}} \sin(2\omega_\oplus(t - t'_0)) + C_{\text{c2}} \cos(2\omega_\oplus(t - t'_0)). \end{aligned} \tag{6.4}$$

The phase is set by t'_0 to a time when the laboratory y- and SCCEF Y-axis coincide such that $t - t'_0 = T_\oplus$. $t'_0 = 79.4681$ days denotes such an instant on the adopted time axis. According to data available from [US 06], this coincides with Sun's transit through the zenith for Berlin at vernal equinox (11:17 UTC, March 20th, 2000). Thus, at $t'_0 = 79.4681$ the SCCEF X-axis points towards the Sun, and the SCCEF Y-axis is oriented East-West, coinciding with the laboratory y-axis.

For the four-day measurement considered as an example before, the results of this fit are also displayed in Figure 6.7. Similar fits on all data sets all together yield 27 values for each coefficient B_k and C_k, which are presented in Figure 6.8. The mean value and standard deviation for each of the 2×5 coefficients is stated in each graph of Figure 6.8. The average applies weighting of the amplitudes according to their reciprocal squared fit error which accounts for the differing length and quality of the data sets.

Residual systematic effects at $2\omega_{\text{rot}}$ affect the coefficients C_0 and B_0, as evident from the top graphs in Figure 6.8 (note the different scale). On average, the systematic deviation of C_0 and B_0 for a single data set is on the order of five σ. However, the phase and magnitude of these systematics are different within separate data sets. This is also evident from the top graph of Figure 6.9. Thus, the systematic deviation from zero averages out to some extent, when combining the results of all measurements. However, this results in an increased error bar on the mean value of C_0 and B_0.

The other amplitudes are sensitive to a systematic effect modulated at 12 h or 24 h. Such a modulation might be caused by a daily modulation of temperature or tilt of the building floor. However, the results presented in Figure 6.8 are not significantly affected by such an effect. This is evinced by statistical checks, which have been performed on these results and which are summarized in Table 6.2. As shown there, the results are normally distributed around zero at the 95% level of confidence for most of the amplitudes.

Alternative schemes for fit step 2: As compared to the procedure described above, two slightly differing approaches to fit step 2 have been applied for an analysis of the data as presented in [HSK$^+$05] and [HSK$^+$06], respectively. While all three schemes provide similar estimates on SME parameters and

	C_0	C_{s1}	C_{c1}	C_{s2}	C_{c2}
$\sigma/\bar{\sigma}_i$	6.5	1.2	1.3	1.1	1.0
p_{SW}	0.30	0.60	0.96	0.87	0.40
C_{SW}	0.96	0.97	0.99	0.98	0.96
p_t	0.78	0.06	0.61	0.50	0.17
C_t	0.29	-1.98	0.51	-0.69	1.42
	B_0	B_{s1}	B_{c1}	B_{s2}	B_{c2}
$\sigma/\bar{\sigma}_i$	8.9	0.9	1.3	1.4	0.9
p_{SW}	**0.002**	0.89	0.17	0.54	**0.01**
C_{SW}	0.86	0.98	0.95	0.97	0.90
p_t	0.16	0.70	0.67	0.84	0.17
C_t	-1.46	-0.38	-0.44	-0.20	-1.41

Table 6.2: Statistics on the results of fit step 2 for B_k and C_k as displayed in Figure 6.8. σ is the standard error of the distribution of the 27 data points and $\bar{\sigma}_i$ denotes the average of the associated 27 single error bars. A value $\sigma/\bar{\sigma}_i \gg 1$ as for B_0 and C_0 thus indicates the presence of systematic effects differing among the single measurements. C_{SW} and p_{SW} give the results of the Shapiro-Wilks test, which tests for normal distribution of the data. $C_{SW} \sim 1$ and $p_{SW} > 0.05$ indicate normal distribution at the 95% confidence level. Whether the data is significantly different from a zero result, is indicated by the results of a t-test with $C_t > 1.7$ and $p_{SW} > 0.05$ verifying this hypothesis at the 95% confidence level.

error bars, the simple scheme described above (scheme A) has been chosen for the analysis presented here. It gives the most conservative estimate on the actual error bar, in accordance with results of an analysis of test data (see Appendix D). Nonetheless, we briefly outline the two refined approaches below:

The first is to divide the distributions of $B^{(i)}$ and $C^{(i)}$ into windows of exactly 24 hours, and to fit each window separately (scheme B). This scheme has been adopted in [HSK+05]. It reduces the correlation between Fourier components at $\omega_\oplus$ and $2\omega_\oplus$. A data set of $n \times 24 + \epsilon$ hours then yields n sets of amplitudes B_k and C_k, while ϵ hours of the measurement are lost. Each set of amplitudes B_k and C_k is then assigned with the mean time of the respective 24 h interval and is treated as an independent measurement result. Note however, that given a residual systematic effect, which is approximately constant during a single measurement run of a few days, such independence of 24 hour windows can not really be claimed.

In order to avoid the loss of measurement data that exceeds exact multiples of 24 hours, overlapping 24 h windows, each shifted by one hour with respect to the preceding window, have been considered as well (scheme C). This scheme was adopted in [HSK+06] and requires an asymmetric weighting scheme, such that data points in the center of a data set do not multiply enter the analysis, as opposed to data points at the beginning or end of a measurement. Consequently, each point is assigned the inverse of the number of windows it enters as a weighting factor. For a measurement spanning $n \times 24 + \epsilon$ full hours, $p = (n-1) \times 24 + \epsilon + 1$ windows have to be fitted. The resulting p sets of B_k and C_k are then averaged to one single set, weighted with the inverse of the squared fit error of each amplitude.

A comparison of results obtained from test data applying all three schemes can be found in Appendix D.

Step 3

In the final step, the annual variation of the amplitudes B_k and C_k as given in Table 3.1 is fitted to the data of Figure 6.8. Inserting the colatitude of Berlin $\chi = 37°$ and $\eta = 23°$ yields the fit functions:

$$
\begin{aligned}
C_0 &= 0.14\tilde{\kappa}_{e-}^{ZZ} - 0.07\beta_\oplus\tilde{\kappa}_{o+}^{XY}\cos(\Omega_\oplus(t-t_0'')) \\
&\quad + 0.08\beta_\oplus\tilde{\kappa}_{o+}^{XZ}\cos(\Omega_\oplus(t-t_0'')) - 0.09\beta_\oplus\tilde{\kappa}_{o+}^{YZ}\sin(\Omega_\oplus(t-t_0'')), \\
C_{s1} &= -0.24\tilde{\kappa}_{e-}^{YZ} + 0.22\beta_\oplus\tilde{\kappa}_{o+}^{XY}\cos(\Omega_\oplus(t-t_0'')) \\
&\quad - 0.09\beta_\oplus\tilde{\kappa}_{o+}^{XZ}\cos(\Omega_\oplus(t-t_0'')) \\
&= 0.8B_{c1},
\end{aligned}
$$

$$C_{c1} = -0.24\tilde{\kappa}_{e-}^{XZ} - 0.22\beta_\oplus\tilde{\kappa}_{o+}^{XY}\sin(\Omega_\oplus(t - t_0''))$$
$$+ 0.09\beta_\oplus\tilde{\kappa}_{o+}^{YZ}\cos(\Omega_\oplus(t - t_0''))$$
$$= -1.03B_{s1},$$
$$C_{s2} = 0.41\tilde{\kappa}_{e-}^{XY} - 0.38\beta_\oplus\tilde{\kappa}_{o+}^{YZ}\cos(\Omega_\oplus(t - t_0''))$$
$$- 0.41\beta_\oplus\tilde{\kappa}_{o+}^{XZ}\sin(\Omega_\oplus(t - t_0''))$$
$$= 1.03B_{c2},$$
$$C_{c2} = 0.20[\tilde{\kappa}_{e-}^{XX} - \tilde{\kappa}_{e-}^{YY}] + 0.41\beta_\oplus\tilde{\kappa}_{o+}^{YZ}\sin(\Omega_\oplus(t - t_0''))$$
$$- 0.38\beta_\oplus\tilde{\kappa}_{o+}^{XZ}\cos(\Omega_\oplus(t - t_0''))$$
$$= -2B_{s2}.$$

The phase is set by t_0'' which coincides with vernal equinox in the year 2000 such that $t - t_0'' = T'$, as defined in Section 2.2.1. According to data from [US 06], this is $t_0'' = 79.31597$ days on the adopted time axis.

For each distribution, this fit is performed by a linear regression with the eight SME coefficients as the free fit parameters. Each value of B_k and C_k is weighted with the reciprocal square of its fit error of step 2. Note, that each of the $\tilde{\kappa}_{e-}$ elements enters only one pair of B_k and C_k amplitudes, while the $\tilde{\kappa}_{o+}$ elements appear in different combinations. Thus, the SME parameters have to be adjusted to several distributions of Figure 6.8 simultaneously, i.e. the regression is performed by including all ten distributions and their respective fit functions and varying the complete set of SME parameters at a time. The implementation of this procedure in Mathematica has been described in detail in [Sen06]. Finally, this regression gives an estimate and a $1\,\sigma$ error for each SME parameter.

6.3.2 Results obtained from the complete data

In Table 6.3 and Figure 6.10 the results for the photonic SME parameters are presented, as obtained from an analysis of all 27 data sets. The results are consistent with a null result, since deviations from zero do not exceed $2\,\sigma$ (95% confidence) and only four of nine values exceed the $1\,\sigma$ level (68% confidence).

The correlation matrix obtained from the linear regression of step 3 (see Table 6.4) gives the residual correlations of the fit estimates. Most entries are < 0.1, however few off-diagonal entries ~ 0.25 remain, which is attributed to the fragmented distribution of the data over the measurement span.

Most of the $1\,\sigma$ limits are $< 10^{-15}$, apart from those of $\tilde{\kappa}_{e-}^{ZZ}$ and $\tilde{\kappa}_{e-}^{XX} - \tilde{\kappa}_{e-}^{YY}$, which feature increased error bars. The most stringent limits of $\sigma = \pm 2.5 \times 10^{-16}$ are obtained for $\tilde{\kappa}_{e-}^{XY}$ and $\tilde{\kappa}_{e-}^{XZ}$.

The parameter $\tilde{\kappa}_{e-}^{ZZ}$ enters the coefficient C_0 only. Thus, $\tilde{\kappa}_{e-}^{ZZ}$ may be most

sensitive to the residual systematic effects, that are evident in the distribution of C_0 values in Figure 6.8. Still, the deviation of $\tilde{\kappa}_{e-}^{ZZ} = (13.3 \pm 9.8) \times 10^{-16}$ from zero is only $\sim 1\,\sigma$, because the phases of the systematic effects vary among independent measurements and systematic deviations from zero of single data sets average out. This averaging results in an increased error bar for this SME parameter, reflecting the variation of residual systematic effects.

SME parameters other than $\tilde{\kappa}_{e-}^{ZZ}$ could be compromised by systematic effects that are modulated at a period of 24 h or 12 h, respectively. However, no such modulation has been observed during the measurements and no indication for it can be deduced, neither from the results on B_k and C_k, nor from the results on the SME-parameters.

The increased error bar on $\tilde{\kappa}_{e-}^{XX} - \tilde{\kappa}_{e-}^{YY} = (5.7 \pm 22.6) \times 10^{-16}$ remains an unresolved issue, which might be attributed to the irregular distribution of the data over the time span of one year.

6.3.3   Results obtained from a subset of the data

During phase 1 of this experiment, the focus was set on intensive data collection and data is more homogenously distributed as compared to the total measurement. Thus, an analysis of these measurements alone was considered worthwhile. However, the correlation matrix (Table 6.5) obtained from fit step 3 then exhibits many significantly nonzero off-diagonal entries. Thus, in order to provide a useful estimate on separate parameters, the set of fit parameters must be reduced by either dropping the $\tilde{\kappa}_{e-}$ terms or the $\tilde{\kappa}_{o+}$ terms within fit step 3. The obtained results for the SME parameters are given in Table 6.3 and are displayed in Figure 6.10. The values there provide limits on the respective parameters, based on the assumption that nonzero SME parameters do not cancel within the measurement signal.

Apart from $\tilde{\kappa}_{e-}^{ZZ}$, all values agree well with a zero result and none of the error bars exceeds the 10^{-15} level. In comparison to the analysis of the complete data, the error bar on $(\tilde{\kappa}_{e-}^{XX} - \tilde{\kappa}_{e-}^{YY}) = (-0.1 \pm 4.4) \times 10^{-16}$ is reduced by a factor of five. For κ_{e-}^{ZZ} the effect of residual systematics is much more pronounced as compared to the results from the complete data. The value of $\tilde{\kappa}_{e-}^{ZZ} = (-82.7 \pm 32.4) \times 10^{-16}$ features a deviation from zero of more than $2\,\sigma$ and at the same time a largely increased error bar. Presumably, this indicates that the systematic effect did not vary as much during the measurements of phase 1 as it did during the complete measurement span of one year.

parameter	complete	phase 1
$\tilde{\kappa}_{e-}^{XY}$	**-4.9 $\pm$ 2.5**	-2.5 ± 3.4
$\tilde{\kappa}_{e-}^{XZ}$	-1.4 ± 2.5	-0.1 ± 4.5
$\tilde{\kappa}_{e-}^{YZ}$	**4.1 $\pm$ 3.9**	2.7 ± 4.6
$\tilde{\kappa}_{e-}^{ZZ}$	**13.3 $\pm$ 9.8**	**-82.7 $\pm$ 32.4**
$\tilde{\kappa}_{e-}^{XX} - \tilde{\kappa}_{e-}^{YY}$	5.7 ± 22.6	-0.1 ± 4.4
$\tilde{\kappa}_{o+}^{XY}$	**5.7 $\pm$ 3.7**	**9.9 $\pm$ 9.5**
$\tilde{\kappa}_{o+}^{XZ}$	5.3 ± 6.3	3.3 ± 5.5
$\tilde{\kappa}_{o+}^{YZ}$	-0.2 ± 6.2	-1.4 ± 5.5

Table 6.3: *Results for photonic SME parameters obtained from the complete data and data from phase 1 only. All $\tilde{\kappa}_{e-}$ values are $\times 10^{-16}$, $\tilde{\kappa}_{o+}$ values are $\times 10^{-12}$. The results for phase 1 are based on the assumption that $\tilde{\kappa}_{e-}$ and $\tilde{\kappa}_{o+}$ terms do not cancel each other within a Lorentz violation signal. Deviations from zero exceeding 1σ are highlighted in bold face.*

parameter	$\tilde{\kappa}_{e-}^{XY}$	$\tilde{\kappa}_{e-}^{XZ}$	$\tilde{\kappa}_{e-}^{YZ}$	$\tilde{\kappa}_{e-}^{ZZ}$	$\tilde{\kappa}_{e-}^{XX-YY}$	$\tilde{\kappa}_{o+}^{XY}$	$\tilde{\kappa}_{o+}^{XZ}$	$\tilde{\kappa}_{o+}^{YZ}$
$\tilde{\kappa}_{e-}^{XY}$	1	0.00	0.01	-0.03	0.00	-0.03	**-0.30**	**0.22**
$\tilde{\kappa}_{e-}^{XZ}$	0.00	1	0.07	0.02	0.02	**0.31**	0.03	0.06
$\tilde{\kappa}_{e-}^{YZ}$	0.01	0.07	1	0.01	-0.01	**0.22**	-0.05	-0.01
$\tilde{\kappa}_{e-}^{ZZ}$	-0.03	0.01	0.01	1	-0.01	0.07	0.05	-0.07
$\tilde{\kappa}_{e-}^{XX-YY}$	0.00	0.02	-0.01	-0.01	1	0.01	**0.22**	**0.30**
$\tilde{\kappa}_{o+}^{XY}$	-0.03	**0.31**	**0.22**	0.07	0.01	1	0.09	-0.02
$\tilde{\kappa}_{o+}^{XZ}$	**-0.30**	0.03	-0.05	0.05	**0.22**	0.09	1	0.00
$\tilde{\kappa}_{o+}^{YZ}$	**0.22**	0.06	-0.01	-0.07	**0.30**	-0.02	0.00	1

Table 6.4: *Correlation matrix for the fit to data spanning one year. The parameter combination $(\tilde{\kappa}_{e-}^{XX} - \tilde{\kappa}_{e-}^{YY})$ is denoted $\tilde{\kappa}_{e-}^{XX-YY}$ for brevity. Due to the fragmented data basis several correlations exceed the level of 10% (highlighted in bold face).*

parameter	$\tilde{\kappa}_{e-}^{xy}$	$\tilde{\kappa}_{e-}^{XZ}$	$\tilde{\kappa}_{e-}^{YZ}$	$\tilde{\kappa}_{e-}^{ZZ}$	$\tilde{\kappa}_{e-}^{XX-YY}$	$\tilde{\kappa}_{o+}^{XY}$	$\tilde{\kappa}_{o+}^{XZ}$	$\tilde{\kappa}_{o+}^{YZ}$
$\tilde{\kappa}_{e-}^{XY}$	1	**0.17**	**0.11**	**-0.18**	-0.01	0.03	**-0.45**	**0.65**
$\tilde{\kappa}_{e-}^{XZ}$	**0.17**	1	**0.42**	**0.14**	**0.15**	**0.59**	0.04	**0.28**
$\tilde{\kappa}_{e-}^{YZ}$	**0.11**	**0.42**	1	**0.16**	-0.07	**0.71**	**-0.15**	0.07
$\tilde{\kappa}_{e-}^{ZZ}$	**-0.18**	**0.14**	**0.16**	1	**0.10**	**0.29**	**0.24**	**-0.12**
$\tilde{\kappa}_{e-}^{XX-YY}$	-0.01	**0.15**	-0.07	**0.10**	1	0.09	**0.65**	**0.43**
$\tilde{\kappa}_{o+}^{XY}$	0.03	**0.59**	**0.71**	**0.29**	0.09	1	0.07	0.09
$\tilde{\kappa}_{o+}^{XZ}$	**-0.45**	0.04	**-0.15**	**0.24**	**0.65**	0.07	1	-0.01
$\tilde{\kappa}_{o+}^{YZ}$	**0.65**	**0.28**	0.07	**-0.12**	**0.43**	0.09	-0.01	1

Table 6.5: *Correlation matrix for a fit of data of phase 1 spanning four months. The parameter combination $(\tilde{\kappa}_{e-}^{XX} - \tilde{\kappa}_{e-}^{YY})$ is denoted $\tilde{\kappa}_{e-}^{XX-YY}$ for brevity. Parameters are strongly correlated, thus a determination of independent limits on all parameters is not feasible.*

6.4 RMS-analysis

An analysis in the RMS framework can be based on the results of fit steps 1 and 2 of the previous section. In step 3, an annual variation of B_k and C_k as given in Table 3.2 is then fitted to the respective distributions of Figure 6.8, with the RMS parameter $P_{\mathrm{MM}} = (\beta - \delta - \frac{1}{2})$ as the fit parameter. Insertion of the colatitude of Berlin $\chi = 37°$ and $\eta = 23°$ into the expressions of Table 3.2 yields the fit functions

$$C_0 = [0.088 + 0.004\cos(\Omega_\oplus(t - t_0'')) - 0.014\sin(\Omega_\oplus(t - t_0''))] P_{\mathrm{MM}} \frac{v_c^2}{c^2},$$

$$C_{\mathrm{s1}} = [0.010 + 0.001\cos(\Omega_\oplus(t - t_0''))] P_{\mathrm{MM}} \frac{v_c^2}{c^2}$$

$$= -0.8 B_{\mathrm{c1}},$$

$$C_{\mathrm{c1}} = [-0.049 + 0.015\cos(\Omega_\oplus(t - t_0'')) + 0.004\sin(\Omega_\oplus(t - t_0''))] P_{\mathrm{MM}} \frac{v_c^2}{c^2}$$

$$= 0.8 B_{\mathrm{s1}},$$

$$C_{s2} = [0.165 + 0.060 \cos(\Omega_\oplus(t - t_0'')) - 0.014 \sin(\Omega_\oplus(t - t_0''))] \, P_{MM} \frac{v_c^2}{c^2}$$
$$= 1.03 B_{c2},$$

$$C_{c2} = [-0.370 + 0.013 \cos(\Omega_\oplus(t - t_0'')) + 0.065 \sin(\Omega_\oplus(t - t_0''))] \, P_{MM} \frac{v_c^2}{c^2}$$
$$= -1.03 B_{s2}.$$

Contrary to the SME analysis, these fits are largely constrained, because P_{MM} is the only free parameter. The effect of a non-vanishing parameter P_{MM} would be most pronounced in the distributions of C_{c2} and B_{s2}, resulting in a non-vanishing mean value of the respective coefficient and a relative annual variation of $\sim 20\%$ of this value.

To determine the RMS parameter P_{MM}, a constrained linear regression is performed in a similar way as done for the SME analysis. Accordingly, P_{MM} is determined such that it minimizes the sum of residuals obtained from all distributions of B_k and C_k and the respective equations at a time. The final result from an analysis of the complete data then is

$$P_{MM} = (0.5 \pm 3.2) \times 10^{-10}. \tag{6.5}$$

The RMS analysis applies only one free parameter and is thus not restricted to data from a measurement spanning a full year. Consequently, the analyzed data can be restricted to data of better quality such as that of phase 1. An analysis of this data however yields a similar result as before:

$$P_{MM} = (-2.7 \pm 3.0) \times 10^{-10}. \tag{6.6}$$

6.5   Comparison to results of similar experiments

6.5.1   Comparison to existing limits on SME parameters

A comparison of the above results on SME parameter to results that have been reported by preceding experiments [WBC+04, MHB+03a] is given in Table 6.3. The limits obtained from the present experiment improve these results by approximately one order of magnitude. Furthermore, previous experiments did not provide a limit on $\tilde{\kappa}_{e-}^{ZZ}$, because they were all relying on Earth's rotation. Since Earth's rotation axis is oriented along the SCCEF Z-axis, these experiments were insensitive to this coefficient.

Simultaneously to the work presented in this thesis, two similar experiments

have been performed by other groups at the Heinrich-Heine-Universität in Düsseldorf, Germany, and the University of Western Australia in Perth, Australia. A comparison to the results reported by these groups is presented in Table 6.6.

Stanwix *et al.* [STW$^+$05] utilize two cryogenically cooled sapphire cavities, operated in a microwave whispering gallery mode at $\sim 10\,\mathrm{GHz}$. The resonators are mounted with orthogonal axes inside a liquid-Helium dewar on a turntable, which can be rotated continuously at a period of $18\,\mathrm{s}$. In [STW$^+$05] five data sets of a continuous beat frequency measurement are analyzed. The longest data set extends over four days and all data measurements were done within a period spanning four months. The limits on the SME parameters that they derive are comparable to those obtained here, except for $\tilde{\kappa}_{e-}^{ZZ}$. Their value for this parameter $\tilde{\kappa}_{e-}^{ZZ} = (210 \pm 570) \times 10^{-16}$ is obscured by a systematic effect that is about one order of magnitude larger than achieved within the present work. As their published data does not span one year, they assume that no cancelation of $\tilde{\kappa}_{e-}$ and $\tilde{\kappa}_{o+}$ terms takes place, in the same way as was done for the analysis of data from phase 1 above. According to [Tob06], further data has been collected meanwhile, and now extends over more than one year as well. As this experiment applies cavities of different geometry, operates in the microwave regime and is performed at a different latitude of the southern hemisphere, it contributes complementary information with respect to a possible violation of Lorentz invariance. This is further considered below and in Appendix E, where Lorentz violation in the electronic sector of the SME is taken into account.

Antonini *et al.* [AOGS05b] reported on an optical Michelson-Morley experiment, however not applying continuous rotation. They compare the frequencies of two orthogonally oriented cryogenic sapphire resonators and have presented an analysis of a single data set spanning four days in [AOGS05b], later extended by additional data [AOGS05a]. The experiment is set up on a rotation stage, which can be rotated back and forth by 90° within several minutes. As they are not able to disentangle all SME parameters from that single measurement, they give limits on the B_k and C_k amplitudes only. Furthermore, they present an estimate of $\tilde{\kappa}_{e-}^{ZZ}$, which is approximately one order of magnitude less stringent than the limit reported in the present experiment, due to a large systematic effect.

In conclusion, the present experiment allows to determine a significantly more stringent limit on $\tilde{\kappa}_{e-}^{ZZ}$ as compared to [SKE$^+$03] and [AOGS05b] due to the achieved low level of systematics. Furthermore it relies on a much more extended data basis and provides the most stringent limits on independent SME parameters.

	this work	[STW$^+$05]	[AOGS05b]	[WBC$^+$04]	[MHB$^+$03a]
$\tilde{\kappa}_{e-}^{XY}$	-4.9 ± 2.5	-6.3 ± 4.3	-	-57 ± 23	17 ± 26
$\tilde{\kappa}_{e-}^{XZ}$	-1.4 ± 2.5	1.9 ± 3.7	-	-32 ± 13	-63 ± 124
$\tilde{\kappa}_{e-}^{YZ}$	4.1 ± 3.9	-4.5 ± 3.7	-	5 ± 13	36 ± 90
$\tilde{\kappa}_{e-}^{ZZ}$	13.3 ± 9.8	210 ± 570	-290 ± 220	-	-
$\tilde{\kappa}_{e-}^{XX-YY}$	5.7 ± 22.6	-13 ± 9	-	-32 ± 46	89 ± 49
$\tilde{\kappa}_{o+}^{XY}$	5.7 ± 3.7	2.0 ± 2.1	-	-18 ± 15	140 ± 140
$\tilde{\kappa}_{o+}^{XZ}$	5.3 ± 6.3	-9.1 ± 4.6	-	-14 ± 23	-12 ± 26
$\tilde{\kappa}_{o+}^{YZ}$	-0.2 ± 6.2	4.4 ± 4.6	-	27 ± 22	1 ± 27

Table 6.6: *Comparison of the results presented in this thesis to previous and concurrent work. The parameter combination $(\tilde{\kappa}_{e-}^{XX} - \tilde{\kappa}_{e-}^{YY})$ is denoted $\tilde{\kappa}_{e-}^{XX-YY}$ for brevity. All $\tilde{\kappa}_{e-}$ values are $\times 10^{-16}$, $\tilde{\kappa}_{o+}$ values are $\times 10^{-12}$. The results of [WBC$^+$04, AOGS05b] are of similar accuracy, apart from the significantly larger systematics affecting the value of $\tilde{\kappa}_{e-}^{ZZ}$.*

6.5.2 Comparison to existing limits on the RMS parameter

A comparison of the above result for the RMS parameter P_{MM} to previous results is presented in Table 6.7. The limit deduced from this measurement represents an improvement of about one order of magnitude as compared to preceding experiments. Similar accuracy has been obtained by the simultaneously performed experiments of Stanwix *et al.* [STW$^+$05] and Antonini *et al.* [AOGS05b].

Insertion of the value for P_{MM} into the basic equation (2.22), allows to derive a limit on $\Delta c/c$ as given by

$$\frac{\Delta c}{c} = (-0.15 \pm 4.8) \times 10^{-16}, \tag{6.7}$$

where $v = 370 \, \text{km/s}$ has been adopted as the average velocity of the laboratory with respect to the CMB. This allows to give a direct comparison to results of earlier Michelson-Morley experiments as presented in Figure 6.11.

6.6 Limits on electronic SME parameters

As discussed in Section 3.1.3 the extension of the present analysis to Lorentz violation in the electronic sector of the SME can be achieved by substituting

$$\tilde{\kappa}_{e-}^{IJ} \rightarrow \tilde{\kappa}_{e-}^{IJ} + 2\mathcal{M}_{\text{fs}} c_{(IJ)},$$
$$\tilde{\kappa}_{o+}^{IJ} \rightarrow \tilde{\kappa}_{o+}^{IJ}.$$

reference	$P_{\mathrm{MM}} \times 10^{-10}$
this work	(-0.1 ± 3.2)
[STW$^+$05] 2005	(-0.9 ± 2.0)
[AOGS05b] 2005	(-0.6 ± 3.3)
[MHB$^+$03a] 2003	(22 ± 15)
[WBC$^+$03] 2003	(12 ± 22)
[BH79] 1979	< 50

Table 6.7: *Comparison of the result for the RMS parameter P_{MM} to previous and concurrent measurements.*

parameter	this work	[Mül05]
$c_{XX} - c_{YY}$	1.0 ± 3.7	11.5 ± 6.4
$c_{(XY)}$	1.2 ± 4.5	7.6 ± 3.5
$c_{(XZ)}$	0.1 ± 1.9	-1.6 ± 6.3
$c_{(YZ)}$	0.3 ± 2.0	2.1 ± 4.6
c_3	56.8 ± 364.2	< 1000

Table 6.8: *Limits on electronic SME parameters obtained from a combined analysis of the present measurement and the measurement of Stanwix et al. All values are $\times 10^{-16}$.*

Thus, in the full context of the SME, the limits of Table 6.3 must be regarded as limits on a combination of electronic and photonic SME parameters.
A comparison of the present experiment to that of Stanwix *et al.* offers further interesting perspectives: The two experiments were performed on different hemispheres and feature cavities of different material and geometry. Thus, they have different sensitivity to Lorentz violation and the null results provided by either experiment can be used to derive limits on electronic parameters independent from photonic parameters. This derivation is given in Appendix E and the results are presented in Table 6.8. They represent an improvement by up to a factor of three compared to the limits previously reported on these parameters.

6.7   Conclusion

The results of this work are consistent with zero and do not provide any significant evidence for a violation of Lorentz invariance. Instead, they give an experimental confirmation of its validity in electrodynamics at the 10^{-16} level of accuracy. The analysis of the measurement provides limits on test

parameters of the SME and RMS, which are more stringent by up to one order of magnitude as compared to previous results. This improvement is mostly based on two achievements:

(i) A large data basis spanning one year and involving more than 100000 turntable rotations.

(ii) Suppression of systematic errors caused by active rotation below $1\,\mathrm{Hz}$. The level of systematic effects is one to two orders of magnitude below the level achieved in similar experiments. This is considered to be a promising basis for further improvements, which have already been started and are described in the following chapter.

Furthermore, the analysis includes effects from Lorentz violation in the matter sector of the standard-model of particle physics, which has often been neglected in similar past experiments. Thus, the analysis exploits the full generality provided by the SME framework. Even more, such an extended analysis allows to apply the complementary results obtained by the similar experiment of [SKE⁺03] to improve bounds on several SME parameters of the electronic sector.

The sensitivity of the measurement is limited by thermal noise of the cavities, which limits the achieved relative frequency stability during one rotation to a level of 10^{-14}. As shown in the next chapter this has already been overcome within an improved setup applying new cavities which will allow for another order of magnitude improvement in the near future.
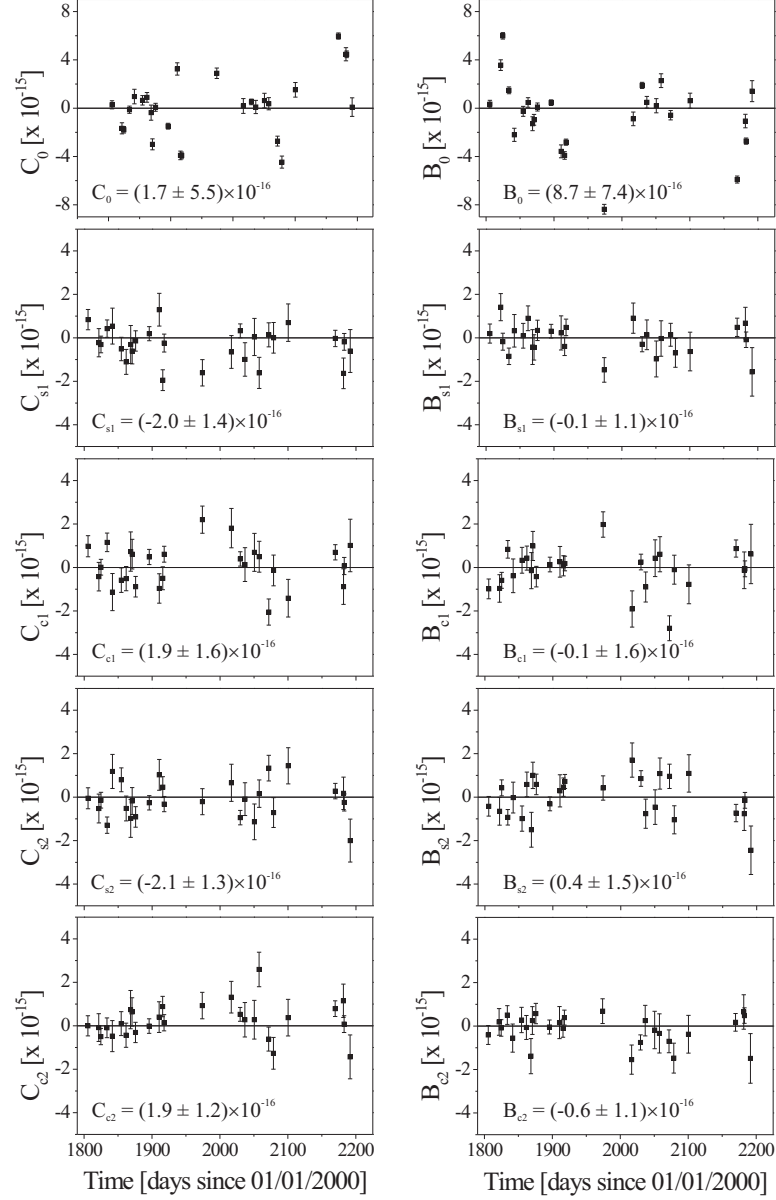
Figure 6.8: *Results for B_k and C_k of all 27 data sets. Each graph presents the results of fit step 2 for a certain coefficient B_k and C_k plotted against time. Each data point within a graph is obtained from one of the 27 data sets. The average value of the respective coefficient, weighted according to the fit error, is also stated within each graph. Note the different scale of the top graphs giving the results for C_0 and B_0, which are affected by small residual systematics.*

134
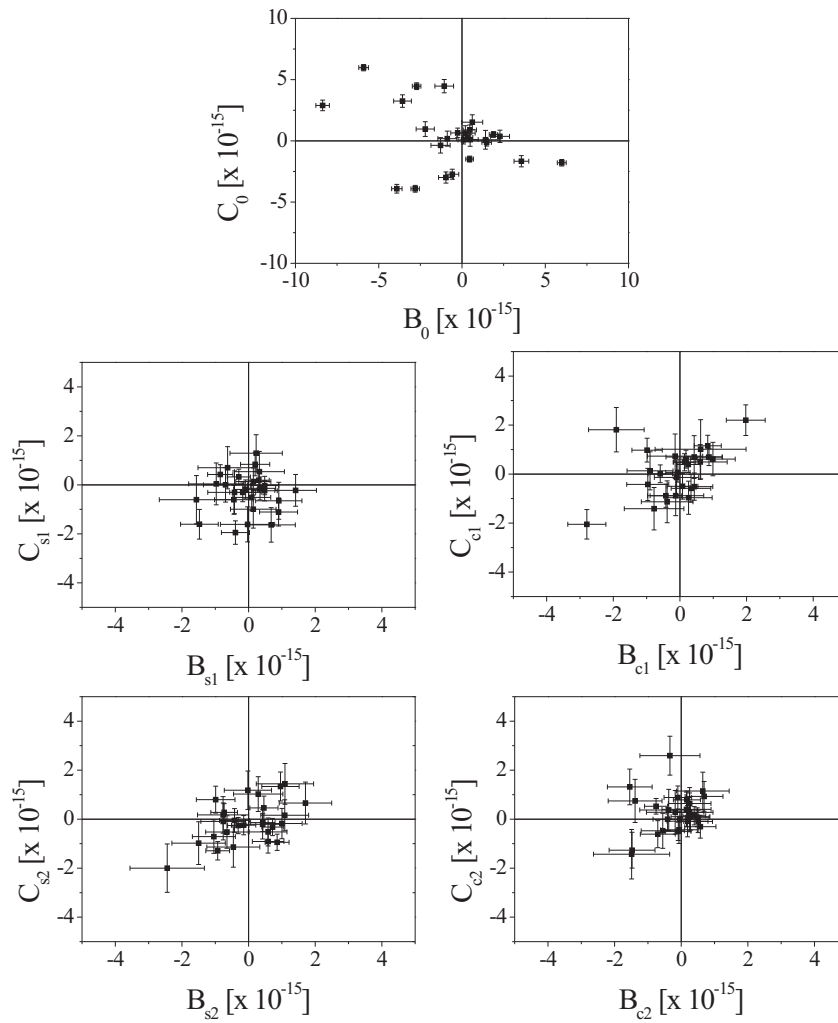
Figure 6.9: *Results for B_k and C_k, plotted against each other. The approximately random variations of the phase of the fitted sinusoidal signals becomes evident from these plots. Note again the different scale for the top graph.*
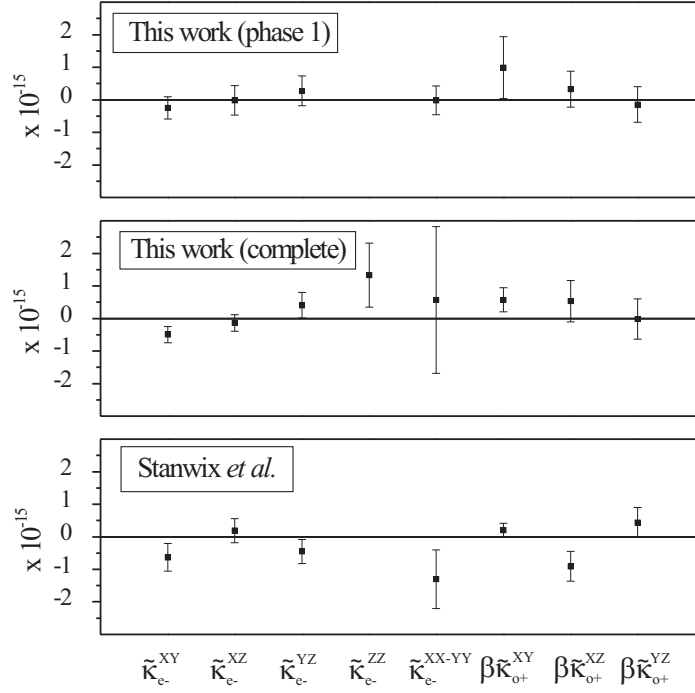
Figure 6.10: *Results for the photonic SME parameters determined from the complete data, respectively from phase 1 only, compared to results of a simultaneously performed experiment by Stanwix et al.. The SME parameter combination $(\tilde{\kappa}_{e-}^{XX} - \tilde{\kappa}_{e-}^{YY})$ is denoted $\tilde{\kappa}_{e-}^{XX-YY}$ for brevity. $\beta \sim 10^{-4}$ denotes Earth's orbital boost. For the results of phase 1 the SME parameter $\tilde{\kappa}_{e-}^{ZZ} = (-82.7 \pm 32.4) \times 10^{-16}$ is beyond the scale of the graph. This is also the case for the value $\tilde{\kappa}_{e-}^{ZZ} = (210 \pm 570) \times 10^{-16}$ of Stanwix et al., which is more than tenfold increased as compared to the present measurement.*
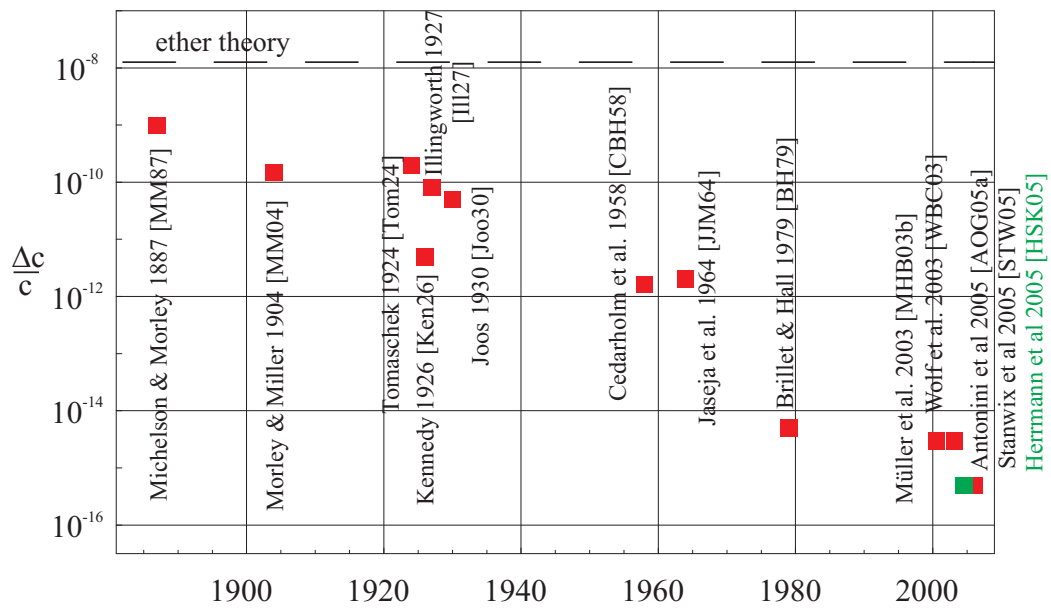
Figure 6.11: *Recent improvements of the Michelson-Morley experiment expressed in terms of the limit set on an anisotropy of the speed of light modeled in the RMS framework.*

6.   Analysis and results

Chapter 7

An improved setup

In February 2006, after completion of one year of measurement, a reconstruction of the setup was started. The new design incorporates several features that should improve the measurement sensitivity by one to two orders of magnitude. These features are: (i) new cavities with narrow linewidths and low thermal noise, (ii) an active vibration isolation, and (iii) a new vacuum chamber which specifically matches the needs of this experiment, i.e. it offers better thermal isolation and is capable to maintain ultra-high vacuum (UHV).

7.1   New cavities

Following an idea proposed in [Bra01], new high-finesse cavities have been designed, specifically for application in a Michelson-Morley experiment. The two cavities are implemented in one monolithic spacer block in a crossed configuration, in order to provide common mode rejection of length fluctuations. Two such pairs of crossed cavities have been fabricated by Advanced Thin Films, Inc.. The first pair is made from fused silica, which is of high mechanical quality ($Q > 10^6$). As estimated in Section 4.4, these cavities should provide a low level of thermal noise and thus should overcome the previous limitation of cavity frequency stability.

The second cavity block is made from Zerodur of expansion class 0, which features a low thermal expansion coefficient at room temperature (CTE $< 2 \times 10^{-8}$/K). Zerodur was chosen instead of ultra-low expansion (ULE) glass ceramics, because the latter is anisotropic with respect to the zero crossings of the CTE. These differ along different axes of the material, which deteriorates common mode rejection of temperature fluctuations. On the other hand, Zerodur has a low mechanical quality factor ($Q \sim 10^3$), which
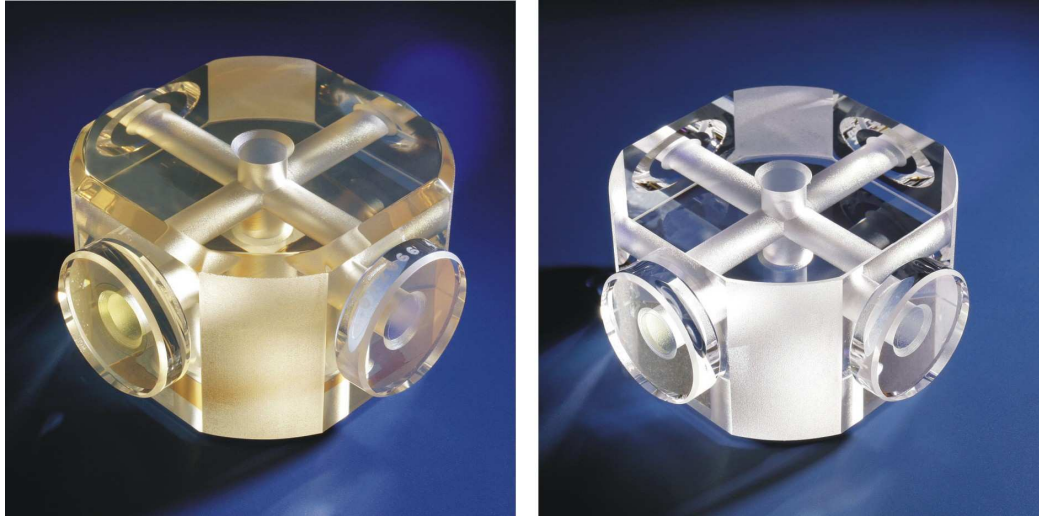
Figure 7.1: *New crossed resonators implemented in a block of Zerodur (left) and fused silica (right).*

leads to increased thermal noise. However, the decisive parts with respect to thermal noise are the mirror substrates only. Thus, an additional set of HR-coated mirrors made from fused silica has been purchased, which can be used to replace the present Zerodur mirrors. This will be done, after some preliminary measurements on the present cavities have been completed.

Figure 7.1 shows pictures of the two cavity pairs. A cavity length of $L = 5.5\,\text{cm}$ has been chosen for both items. Longer cavities ($L \geq 10\,\text{cm}$) would have been favorable, since this would decrease cavity linewidth and the effect of thermal noise. However, the size was limited to the above value in order to implement the setup in a compact chamber on the turntable. Furthermore, a reduced size minimizes tilt effects that increase with cavity length.

Each cavity's mirror pair consists of a planar and a concave mirror (r = $50\,\text{cm}$). This configuration allows for a better alignment of the optical axes, when contacting the mirrors to the spacer and minimizes the sensitivity of the resonance frequency to cavity deformations. The targeted Finesse was 300000, corresponding to a linewidth of $9\,\text{kHz}$. Larger Finesse would have been achievable only at the cost of reduced impedance matching. Table 7.1 gives the actual measured linewidths and achieved transmission for the TEM_{00} modes of the cavities. The impedance matching of all cavities allowed for a transmission of $\sim 60\%$ while the actual linewidths of $8\,\text{kHz}$ and $13\,\text{kHz}$ for the Zerodur resonators, and $7\,\text{kHz}$ for both fused silica resonators are close

to the desired value. The absolute lengths of the two cavities within each block have been determined from a comparison of the free spectral ranges to differ by $2\,\mu$m.

cavity	linewidth (TEM_{00})	Finesse (TEM_{00})
FS1	7 kHz	400000
FS2	7 kHz	400000
Zer1	8 kHz	340000
Zer2	13 kHz	210000

Table 7.1: *Properties of the new resonators. FS = fused silica, Zer = Zerodur.*

7.2 Modifications of the setup

Improved cavity mounting

The new cavity blocks are mounted inside another more compact cryostat now, one block at a time. This cryostat provides a rigid support for the resonator mount and no internal movements or oscillations have been observed so far. The (preliminary) resonator mount is a copper pot with a ring-edge milled into the bottom plate to provide a line contact to the cavity block placed inside. The turbo-molecular pump has been replaced by an ion pump, which further reduces external vibrations and does not require permanent rough pumping from outside through the vacuum feedthrough.
Having the cavities still mounted inside a cryostat, provides the interesting possibility to study the temperature dependence of thermal noise by cooling the cavities down to liquid-Helium temperature. These low-temperature measurements are scheduled to be done before this cryostat is replaced by a new room temperature vacuum chamber. Such a chamber, has been designed by A. Senger for this Michelson-Morley experiment [Sen06] and is currently being fabricated (see Appendix F).

Active vibration isolation

An active vibration isolation system (HWL 350-M) has been acquired, which now supports a breadboard that carries the optics and the vacuum chamber with the cavities inside. The system consists of two bench units ($600 \times 155 \times 120\,\text{mm}^3$) with a maximum applicable load of $350\,\text{kg}$ (see Figure 7.3). The unit provides both passive isolation at frequencies beyond $200\,\text{Hz}$ by means
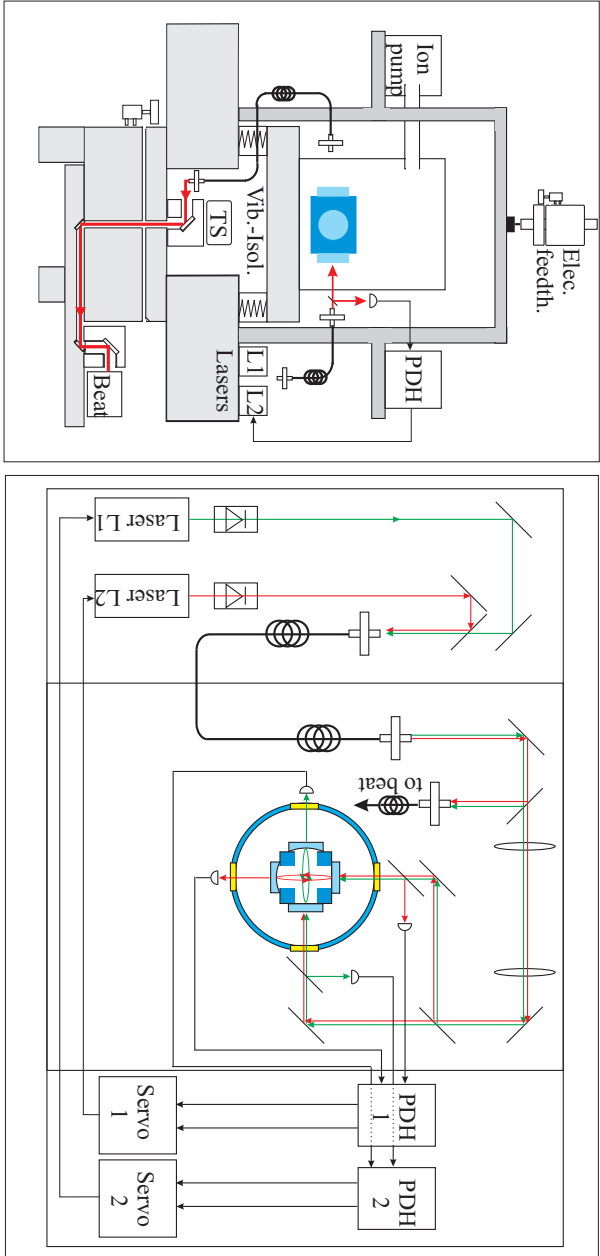
Figure 7.2: *Schematic of the new setup. Left: The new setup features a vibration-isolated breadboard on the turntable. The turbo-molecular pump has been replaced by an ion pump, that does not introduce vibrations to the setup and does not require a vacuum feedthrough. Right: Optical setup after reconstruction. The light of both lasers is coupled to the same polarization-maintaining single mode fiber for transfer to the isolated platform. The light paths to the two cavities now exhibit a maximum degree of symmetry.*

of springs, and active isolation at frequencies down to $1.2\,\mathrm{Hz}$ by means of electromagnetic actuators. The performance of the isolation unit is shown in Figure 7.3. Isolation sets in at $\sim 1\,\mathrm{Hz}$ and reaches approximately $-40\,\mathrm{dB}$ at $10\,\mathrm{Hz}$. Above $30\,\mathrm{Hz}$, the performance seems to decrease and further fine tuning will be required to improve on this.

Reconstruction of the optical setup

Laser L2 has been replaced by another NPRO Nd:YAG laser (LWE, model 124) and is placed on the turntable now. Both lasers were placed on the vibration isolated platform initially and coupled to the resonators free beam. The first measurements compared the frequencies of the two Zerodur cavities and were dominated by flicker noise at the 10^{-14} level, as shown in Figure 7.6. This is in good agreement with the estimate on thermal noise for this cavity configuration given in Table 4.4. To further investigate on the origin of this flicker noise, the two lasers were locked to two neighboring $\mathrm{TEM_{00}}$-modes of the same Zerodur resonator. Therefor, the two beams were overlapped and coupled to the cavities free beam, separately mode matched by means of two telescopes. This frequency comparison is insensitive to fluctuations of the resonator length such as those caused by thermal noise, and should thus reflect the performance of the laser stabilization electronics. As shown in Figure 7.6, the flicker noise in this measurement was reduced to a relative Allan deviation of 7×10^{-15}. This limit is set by beam pointing fluctuations of the two beams relative to each other on the photodetector, which cause phase shifts of the PDH error signal. To minimize these fluctuations, the optical setup was rebuilt as depicted in Figure 7.2. Now, both lasers are placed on the non-vibration-isolated breadboard and the beams are overlapped inside the same polarization-maintaining single-mode optical fiber for transfer to the isolated platform. This provides mode-cleaned, perfectly overlapped beams and enables to use the same single telescope for mode matching to the cavities. This scheme basically eliminates all relative beam movements among the two beams, when they are coupled to the same resonator and indeed helped to improve the relative Allan deviation to below 10^{-15} for integration times $> 1\,\mathrm{s}$. Still, the comparison of two Zerodur cavities again yields a flicker floor at a level above 10^{-14}, despite the reduction of beam pointing problems. This shows that this limit is set by an intrinsic property of the cavities, which we consider to be thermal noise.
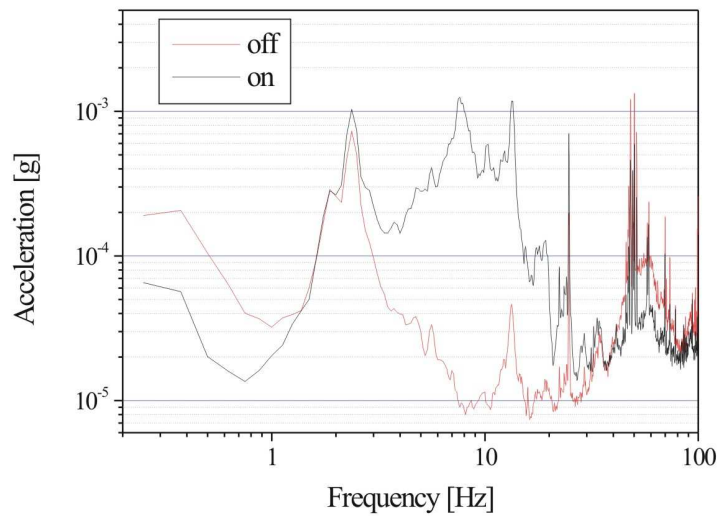
Figure 7.3: *Picture of the active vibration isolation and performance of the system. The active vibration isolation system is placed on the turntable and supports a breadboard that carries the optics and the vacuum chamber. Residual accelerations between 1.2 Hz and 20 Hz are suppressed by up to a factor of one hundred. The performance with respect to suppression of vibrations above still needs to be improved. (Note that the seismometer sensitivity above 60 Hz decreases as 1/f which is not corrected for in this graph.)*
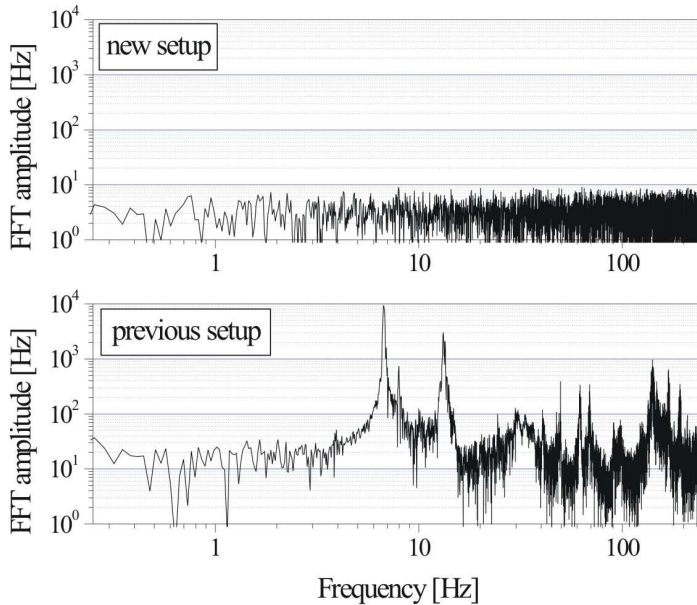
Figure 7.4: *Comparison of a Fourier transform of a beat frequency measurement of 10 s, sampled at 1 ms.*

7.3 Improvement of relative frequency stability

A frequency comparison of the two new fused silica cavities achieved a relative frequency stability of 2×10^{-15} at $\tau > 1$ s. This is almost an order of magnitude improvement, as compared to the measurements recorded from the Zerodur cavities and the previously applied cavities R1 and R2. The Hadamard deviation obtained from a comparison without rotating the table is given in Figure 7.6. This measurement was performed applying the same lock electronics and the optimized optical setup as for the Zerodur resonators. Again, the observed stability is in good agreement with the estimate on thermal noise for these cavities given in Table 4.4. However, further studies are required to investigate on other possible limitations at this level of sensitivity.

Furthermore, the improved rigid mounting of the cavities and the application of the active vibration isolation helped to greatly reduce frequency oscillations at timescales < 1 s caused by Doppler effect and vibrations. No significant such effect could be observed as evident from Figure 7.4. The beat
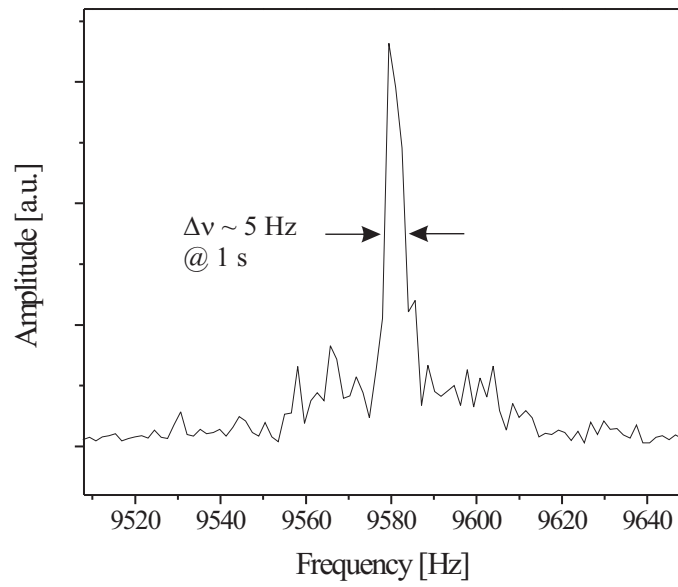
Figure 7.5: *Beat linewidth obtained from a comparison of the two fused silica cavities. The linewidth at 1 s integration time is $\sim 5\,Hz$.*

linewidth could thus be reduced to $\sim 5\,\mathrm{Hz}$ at an integration time of $1\,\mathrm{s}$ (see Figure 7.5).

Finally, also the relative long-term frequency stability of the new cavities significantly overcomes that of the previously applied cavities R1 and R2. The beat frequency drift is on the order of $1\,\mathrm{Hz/s}$, as compared to $\sim 100\,\mathrm{Hz}$ for the previous setup. If we assume that the temperature drift of a single cavity here is similar to that of R1 or R2, we can estimate that common mode rejection suppresses thermal length fluctuations by a factor of up to 100. Still, an accurate determination of thermal common mode rejection remains to be done.

7.4 First results obtained from the new rotating setup

The first measurement that compared the crossed fused silica resonators with rotating table ($T_{\mathrm{rot}} = 45\,\mathrm{s}$) showed a systematic effect at ω_{rot} on the order of a few Hertz. Due to the improved frequency stability, this effect could be observed from a few table rotations already as shown in Figure 7.7. This substantially simplifies the analysis of systematic effects at the Hertz level as compared to the previous setup, where effects of this magnitude could only be revealed by averaging data of hundreds of table rotations.

The initial systematic effect could be significantly reduced after replacing two windows of the vacuum chamber, which turned out to feature the wrong AR-coating. Thus these windows had formed parasitic etalons with the cavity mirrors, which got modulated by a small temperature gradient when rotating the setup. The reduction of systematic frequency oscillations by replacing these windows with properly AR-coated ones is shown in Figure 7.7 to the bottom.

A preliminary analysis of a measurement spanning three days yields the amplitudes B and C as shown in Figure 7.8. The values do not exceed one Hertz which is a reduction by factor of ~ 10 as compared to the results of the previous setup (see Figure 6.7). However, there is a modulation with a period of $12\,\mathrm{h}$. A corresponding, larger modulation with a $24\,\mathrm{h}$ period is observed for the systematic effect at ω_{rot} (see Figure 7.9). A closer consideration reveals, that the absolute magnitude of this systematic effect is approximately constant but the phase of this effect is continuously shifted by $360°$ within $24\,\mathrm{h}$. The signal at $2\omega_{\mathrm{rot}}$ with a modulation at half that period ,i.e. $12\,\mathrm{h}$, is considered to be leakage of the effect at ω_{rot}. Consequently, no indication for Lorentz violation may be drawn from this preliminary data.

147
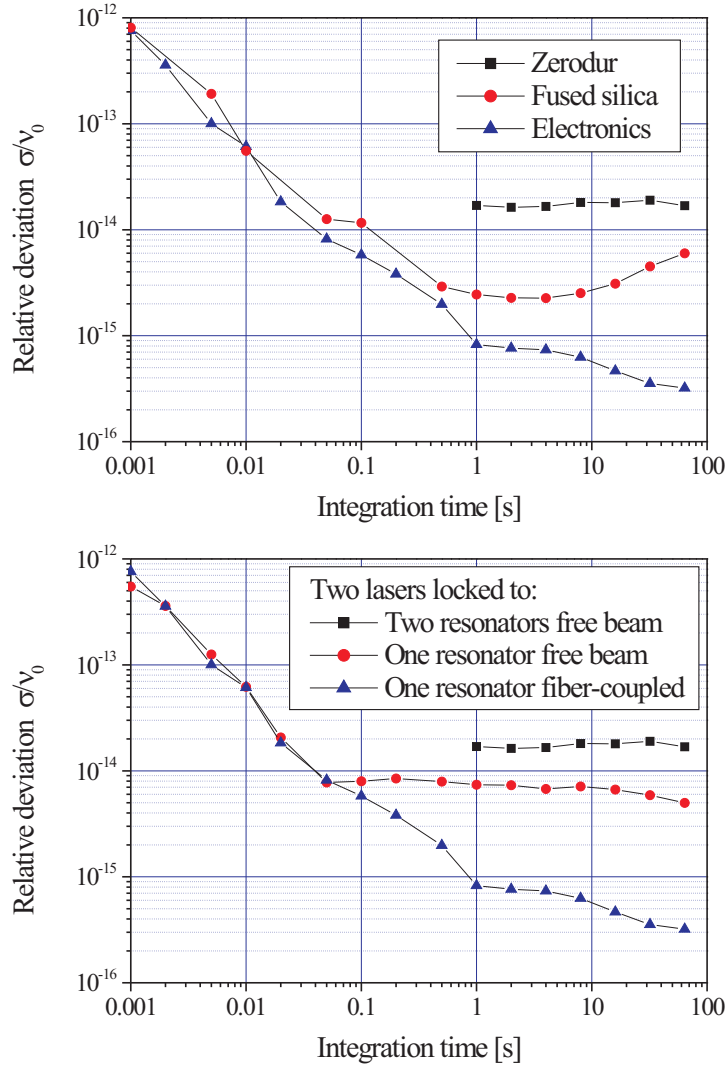
Figure 7.6: *Top: Relative frequency stability achieved with the new set of resonators and performance of the lock electronics. Bottom: Effect of improved beam pointing on relative frequency stability. The top most curve shows the relative frequency stability for a comparison of the two Zerodur resonators. The two lower curves show the relative frequency stability for comparisons of two neighboring TEM$_{00}$ modes of one of the Zerodur resonators, before and after improving the pointing stability.*
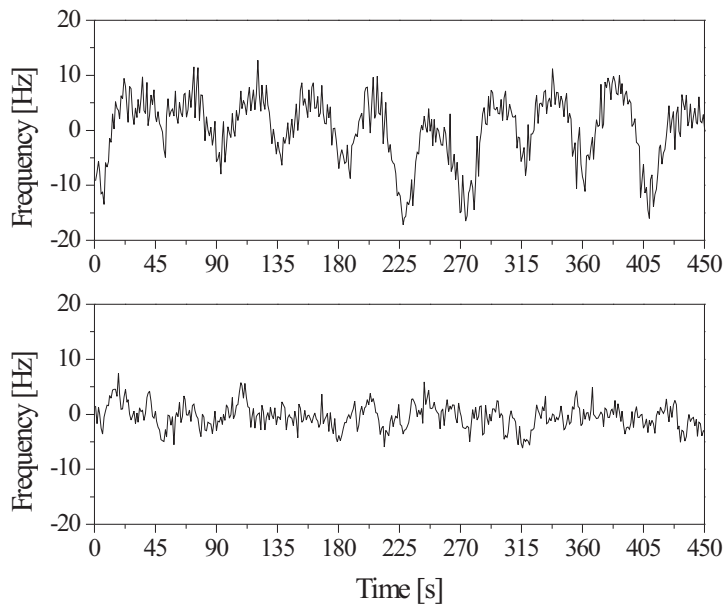
Figure 7.7: *First measurements of the new setup (top) exhibited a systematic effect of several Hertz ($T_{\mathrm{rot}} = 45\,\mathrm{s}$), which could however be reduced by straightforward measures (bottom).*

The cause of this phase modulated systematic effect remains to be determined. A simple explanation would be a malfunction of the turntable encoder readout. For an actually constant systematic effect, an increasing discrepancy of actual and measured rotation rate continuously shifts the phase of the fitted signal in the analysis of the data. However, no indication for such a malfunction could be found and there is no reason to assume that this phase shift exactly matches with the period of one day. A confusion of sidereal and non-sidereal days can be excluded as well, as this becomes only relevant within the subsequent steps of the analysis. First estimates on the effect of rotation axis tilt of the current setup indicate an increased sensitivity of $0.5\,\mathrm{Hz}/\mu\mathrm{rad}$. Thus, if the tilt control system leaves an unsuppressed varying effect on the order of $\pm 1\,\mu\mathrm{rad}$, this might be an explanation. Furthermore, there are several other effects that might be subject to a daily modulation of temperature and an investigation on these effects has yet to be done.

The amplitudes of the sidereal modulation B_k and C_k have been derived from a fit to the distribution of Figure 7.8 and are stated in Table 7.2. Clearly, the modulated residual systematic effect compromises the results obtained for some of the coefficients. However, the error bars already reach a level of $< 5 \times 10^{-17}$. Note further, that the current setup applies two rotating resonators, which increases its sensitivity to Lorentz violation parameters by another factor of 2. Thus, if the systematic effects can be further reduced, the new setup should enable an improvement of the previous results by more than one order of magnitude already from a measurement of few days only.

7.5 Next steps and estimated ultimate sensitivity

Based on the results of the above measurement of three days, the accuracy that could be obtained from a long-term measurement over ~ 100 days can be estimated. At the current noise, level further integration might allow to reduce the error bars on Lorentz violation parameters to below 10^{-17}. However, to fully exploit this sensitivity the major challenge will be to identify and reduce the residual systematic effects, which are currently on the order of 10^{-15}, by about two orders of magnitude.

The observed residual systematics are especially unfavorable, because they are modulated at a $24\,\mathrm{h}$ period. Thus, in a first step the origin of this modulation needs to be identified. Measures such as an improved temperature shielding of the setup, e.g. enclosing the rotating setup inside a box, or a further improvement of the tilt control system, might achieve this rather
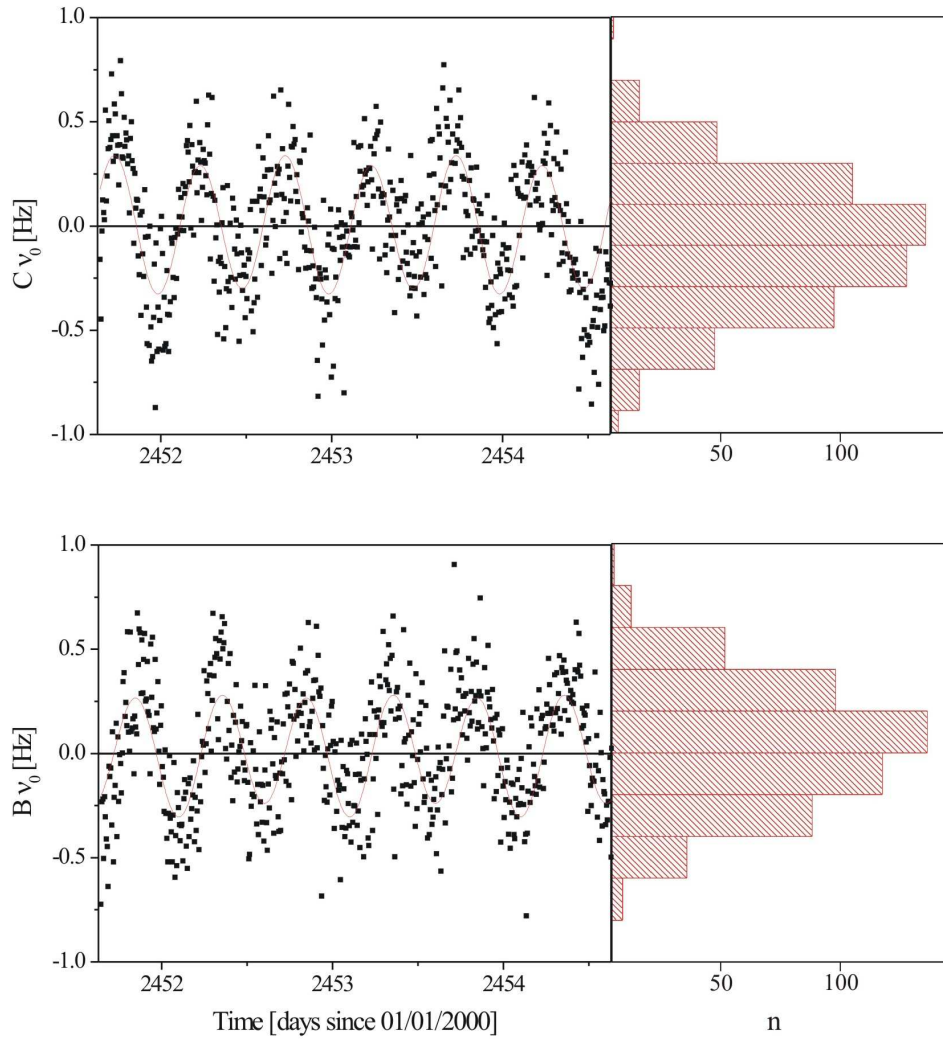
Figure 7.8: *B and C amplitudes (at $2\omega_{\mathrm{rot}}$) determined from step 1 of the analysis, applied to data that has been obtained from a three day comparison of the rotating new fused silica cavities. While the amplitudes are generally reduced by a factor of 10 as compared to the previous setup (see Figure 6.7), a modulated systematic effect with $12\,\mathrm{h}$ period is clearly visible.*
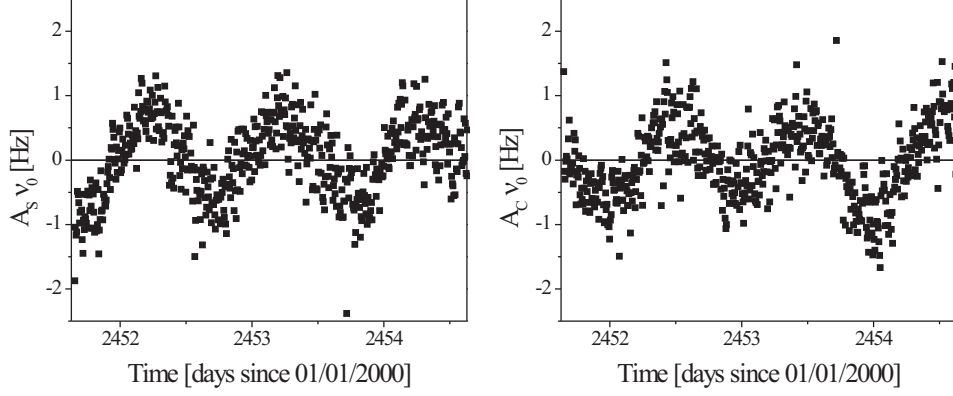
Figure 7.9: *Sine (A_S) and cosine (A_C) amplitudes at ω_{rot} are modulated with a 24 h period. Such a modulation at ω_{rot} is not a signal for a violation of Lorentz invariance. Presumably the modulation of amplitudes at $2\omega_{\mathrm{rot}}$ shown in Figure 7.8 can be traced to the same, not yet recovered systematic effect.*

parameter	value	previous
C_0	-2.6 ± 3.2	7 ± 33
C_{s1}	-4.9 ± 4.5	-14 ± 47
C_{c1}	-1.0 ± 4.6	-88 ± 47
C_{s2}	-16.7 ± 4.5	-91 ± 47
C_{c2}	-107.6 ± 4.5	-31 ± 47
B_0	10.7 ± 3.1	10 ± 33
B_{s1}	-6.2 ± 4.3	34 ± 47
B_{c1}	-12.3 ± 4.4	-42 ± 47
B_{s2}	-98.5 ± 4.3	59 ± 47
B_{c2}	12.4 ± 4.4	57 ± 47

Table 7.2: *Preliminary results from the new setup. All values are $\times 10^{-17}$. The error bars generally are in the mid 10^{-17} range which is a tenfold improvement over the results from the previous setup. However most components are severely affected by the modulated systematic effect, most prominently the amplitudes C_{c2} and B_{s2}.*

quickly. Furthermore, the new vacuum chamber is almost ready for implementation (Appendix F). This chamber will allow to reduce frequency drift due to temperature creep and thus enhance long-term frequency stability. As this chamber can also enclose most parts of the optics and the detection system, with the light coupled through optical fibers from outside, it might as well help to reduce systematic effects that are caused by temperature modulation.

With a constant systematic effect even as large as 10^{-15}, the experiment would already offer a largely increased sensitivity to all SME parameters but $\tilde{\kappa}_{e-}^{ZZ}$. A phase of intensive data collection could then be started, which would provide significantly improved bounds on combinations of SME parameters and the RMS parameter P_{MM}. All together a determination of Lorentz violation parameters at an accuracy improved by another order of magnitude should be possible with the current setup within the near future. Finally these results should be able to restrict a hypothetical anisotropy of the speed of light at a level well below 10^{-17}.

Bibliography

[AB81]   Allan, D. W.; Barnes, J. A.: A modified Allan variance with
              increased oscillator characterization ability. In: *Proceedings of
              the 35th Annual Frequency Control Symposium*, pp. 470–475,
              1981.

[ADD99]   Arkani-Hamed, N.; Dimopoulos, S.; Dvali, G.: Phenomenology,
              astrophysics, and cosmology of theories with submillimeter di-
              mensions and tev scale quantum gravity. In: *Phys. Rev. D*,
              volume 59:p. 086004, 1999.

[AEM$^+$98]   Amelio-Camelia, G.; Ellis, J.; Mavromatos, N. E.; Nanopoulos,
              D. V.; Sarkar, S.: Tests of quantum gravity from observations
              of γ-ray bursts. In: *Nature*, volume 393:pp. 763 – 765, 1998.

[All66]   Allan, D.: Statistics of atomic frequency standards. In: *Proc.
              IEEE*, volume 54:pp. 221 – 230, 1966.

[Alt06]   Altschul, B.: Limits on Lorentz violation from synchrotron and
              inverse Compton sources. In: *Phys. Rev. Lett.*, volume 96:p.
              201101, 2006.

[AMU02]   Alfaro, J.; Morales-Técotl, H. A.; Urrutia, L. F.: Loop quantum
              gravity and light propagation. In: *Phys. Rev. D*, volume 65:p.
              103509, 2002.

[AOGS05a]   Antonini, P.; Okhapkin, M.; Göklü, E.; Schiller, S.: Reply to
              "Comment on 'Test of constancy of speed of light with rotating
              cryogenic optical resonators' ". In: *Phys. Rev. A*, volume 72:p.
              066102, 2005.

[AOGS05b]   Antonini, P.; Okhapkin, M.; Göklü, E.; Schiller, S.: Test of
              constancy of speed of light with rotating cryogenic optical res-
              onators. In: *Phys. Rev. A*, volume 71:p. 050101, 2005.

[Bau71]   Baugh, R. A.: Frequency modulation analysis with the Hadamard variance. In: *Proc. Ann. Symp.*, pp. 222 – 225, 1971.

[BFM+92]   Bhat, P. N.; Fishman, G. J.; Meegan, C. A.; Wilson, R. B.; Brock, M. N.; Paciesas, W. S.: Evidence for sub-millisecond structure in a gamma-ray burst. In: *Nature*, volume 359:pp. 217 – 219, 1992.

[BGV99]   Braginsky, V. B.; Gorodetsky, M. L.; Vyatchanin, S. P.: Thermodynamical fluctuations and photo-thermal shot noise in gravitational wave antennae. In: *Phys. Lett. A*, volume 264:pp. 1 – 10, 1999.

[BH79]   Brillet, A.; Hall, J. L.: Improved laser test of the isotropy of space. In: *Phys. Rev. Lett.*, volume 42:pp. 549 – 552, 1979.

[BHK+95]   Berglund, C. J.; Hunter, L. R.; Krause, D.; Prigge, E. O.; Ronfeldt, M. S.; Lamoreaux, S. K.: New limits on Local Lorentz Invariance from hg and cs magnetometers. In: *Phys. Rev. Lett.*, volume 75:pp. 1879 – 1882, 1995.

[BK00]   Bluhm, R.; Kostelecký, V. A.: Lorentz and CPT tests with spin polarized solids. In: *Phys. Rev. Lett.*, volume 84:pp. 1381 – 1384, 2000.

[BKR99]   Bluhm, R.; Kostelecký, V. A.; Russell, N.: CPT and Lorentz tests in hydrogen and antihydrogen. In: *Phys. Rev. Lett.*, volume 82:pp. 2254 – 2258, 1999.

[BMP+02]   Braxmaier, C.; Müller, H.; Pradl, O.; Mlynek, J.; Peters, A.; Schiller, S.: Tests of relativity using a cryogenic optical resonator. In: *Phys. Rev. Lett.*, volume 88:p. 010401, 2002.

[Bra01]   Braxmaier, Claus: *Fundamentale Tests der Physik mit ultrastabilen optischen Oszillatoren.* PhD thesis, Universität Konstanz, Fachbereich Physik, Konstanz, 2001.

[BSW+00]   Bear, D.; Stoner, R. E.; Walsworth, R. L.; Kostelecký, V. A.; Lane, C. D.: Limit on Lorentz and CPT violation of the neutron using a two-species noble gas maser. In: *Phys. Rev. Lett.*, volume 85:pp. 5038 – 5041, 2000.

[CBR+04]   Cané, F.; Bear, D.; Rosen, D. F. Phillips M. S.; Smallwood, C. L.; Stoner, R. E.; Walsworth, R. L.; Kostelecký, V. A.: Bound

on Lorentz and CPT violating boost effects for the neutron. In: *Phys. Rev. Lett.*, volume 93:p. 230801, 2004.

[CCG+04] Crooks, D. R. M.; Cagnoli, G.; Gretarsson, M. M. Fejer A.; Harry, G.; Hough, J.; Nakagawa, N.; Penn, S.; Route, R.; Rowan, S.; Sneddon, P. H.: Experimental measurements of coating mechanical loss factors. In: *Class. Quantum Grav.*, volume 21:pp. S1059 – S1065, 2004.

[CCHP01] Cerdonio, M.; Conti, L.; Heidmann, A.; Pinard, M.: Thermoelastic effects at low temperature and quantum limits in displacement measurements. In: *Phys. Rev. D*, volume 63:p. 082003, 2001.

[CDS98] Connes, A.; Douglas, M.; Schwarz, A.: In: *J. High Energy Phys.*, volume 02:p. 003, 1998.

[CG52] Callen, H. B.; Greene, R. F.: On a theorem of irreversible thermodynamics. In: *Phys. Rev.*, volume 86:p. 702, 1952.

[CG99] Coleman, S.; Glashow, S. L.: High-energy tests of Lorentz invariance. In: *Phys. Rev. D*, p. 116008, 1999.

[CHK+01] Caroll, S. M.; Harvey, J. A.; Kostelecký, V. A.; Lane, C. D.; Okamoto, T.: Non commutative field theory and Lorentz violation. In: *Phys. Rev. Lett.*, volume 87:p. 141601, 2001.

[CHL+89] Chupp, T. E.; Hoare, R. J.; Loveman, R. A.; Oteiza, E. R.; Richardson, J. M.; Wagshul, M. E.; Thompson, A. K.: Results of a new test of local Lorentz invariance: A search for mass anisotropy in ^{21}Ne. In: *Phys. Rev. Lett.*, volume 63:pp. 1541 – 1545, 1989.

[CK97] Colladay, D.; Kostelecký, V. A.: CPT violation and the standard model. In: *Phys. Rev. D*, volume 55:pp. 6760 – 6774, 1997.

[CK98] Colladay, D.; Kostelecký, V. A.: Lorentz-violating extension of the standard model. In: *Phys. Rev. D*, volume 58:p. 116002, 1998.

[DGB92] Day, T.; Gustafson, E. K.; Byer, R. L.: Sub-Hertz relative frequency stabilization of two diode laser pumped Nd:YAG lasers locked to a Fabry-Pérot interferometer. In: *J. Quant. Electr.*, volume 28:pp. 1106 – 1117, 1992.

[DHK⁺83]   Drever, R. W. P.; Hall, J. L.; Kowalski, F. V.; Hough, J.; Ford, G. M.; Munley, A. J.; Ward, H.: Laser phase and frequency stabilization using an optical resonator. In: *Appl. Phys. B*, volume 31:pp. 97 – 105, 1983.

[DMVS99]   Dehmelt, H.; Mittleman, R.; VanDyck, R. S.; Schwinberg, P.: Past electron g-2 experiments yielded sharpest bound on CPT violation for point particles. In: *Phys. Rev. Lett.*, volume 83:pp. 4694 – 4696, 1999.

[DN01]   Douglas, M. R.; Nekrasov, N. A.: Noncommutative field theories. In: *Rev. Mod. Phys.*, volume 73:p. 977, 2001.

[Ein05]   Einstein, A.: Zur Elektrodynamik bewegter Körper. In: *Ann. Phys.*, volume 17:p. 891, 1905.

[EMN99]   Ellis, J.; Mavromatos, N. E.; Nanopoulos, D. V.: Search for quantum gravity. In: *Gen. Rel. Grav.*, volume 31:pp. 1257 – 1262, 1999.

[EMN00]   Ellis, J.; Mavromatos, N. E.; Nanopoulos, D. V.: Is nothing sacred? Vacuum energy, Supersymmetry and Lorentz breaking from recoiling D branes. In: *gr-qc/0005100v2*, pp. 1 – 28, 2000.

[GKH⁺94]   Grieser, R.; Klein, R.; Huber, G.; Dickopf, S.; Klaft, I.; Knoblock, P.; Merz, P.; Albrecht, F.; Grieser, M.; Habs, D.; Schwalm, D.; Kühl, T.: A test of special relativity with stored lithium ions. In: *App. Phys. B*, volume 59:p. 127, 1994.

[GKH⁺99]   Gabrielse, G.; Khabbaz, A.; Hall, D. S.; Heimann, C.; Kalinowsky, H.; Jhe, W.: Precision mass spectroscopy of the antiproton and proton using simultaneously trapped particles. In: *Phys. Rev. Lett.*, volume 83:pp. 3198 – 3201, 1999.

[Gök04]   Göklü, Ertan: *Tests der Lorentzinvarianz mittels elektromagnetischer Resonatoren.* Diploma thesis, Heinrich-Heine-Universität Düsseldorf, Institut für Experimentalphysik, Düsseldorf, 2004.

[GP99a]   Gambini, R.; Pullin, J.: Nonstandard optics from quantum space-time. In: *Phys. Rev. D*, volume 59:p. 124021, 1999.

[GP99b]   Gambini, R.; Pullin, J.: Quantum gravity experimental physics. In: *Gen. Rel. Grav.*, volume 31:pp. 1631 – 1637, 1999.

[HBG$^+$05]   Howe, D. A.; Beard, R. L.; Greenhall, C. A.; Vernotte, F.; Riley, W. J.; Peppler, T. K.: Enhancements to GPS operations and clock evaluations using a total Hadamard deviation. In: *IEEE transactions on ultrasonics, ferroelectrics and frequency control*, volume 52:pp. 1253 – 1261, 2005.

[HGL$^+$07]   Hohensee, M.; Glenday, A.; Li, C.-H.; Tobar, M. E.; Wolf, P.: Erratum: New methods of testing Lorentz violation in electrodynamics. In: *Phys. Rev. D*, volume 75:p. 049902, 2007.

[HH90]   Hils, D.; Hall, J. L.: Improved Kennedy-Thorndike experiment to test special relativity. In: *Phys. Rev. Lett.*, volume 64:pp. 1697 – 1700, 1990.

[HMW05]   Hooper, D.; Morgan, D.; Winstanley, E.: Lorentz and CPT invariance violation in high-energy neutrinos. In: *Phys. Rev. D*, volume 72:p. 065009, 2005.

[HNL03]   Hou, L.; Ni, W.; Li, Y. M.: Test of cosmic spatial isotropy for polarized electrons using a rotatable torsion balance. In: *Phys. Rev. Lett.*, volume 90:p. 201101, 2003.

[HPM$^+$03]   Humphrey, M. A.; Phillips, D. F.; Mattison, E. M.; Vessot, R. F. C.; Stoner, R. E.; Walsworth, R. L.: Testing CPT and Lorentz symmetry with hydrogen masers. In: *Phys. Rev. A*, volume 68:p. 063807, 2003.

[HSK$^+$05]   Herrmann, S.; Senger, A.; Kovalchuk, E.; Müller, H.; Peters, A.: Test of the isotropy of the speed of light using a continuously rotating optical resonator. In: *Phys. Rev. Lett.*, volume 95:p. 150401, 2005.

[HSK$^+$06]   Herrmann, S.; Senger, A.; Kovalchuk, E.; Müller, H.; Peters, A.: Test of Lorentz Invariance using a continuously rotating optical resonator. In: *Lect. Notes Phys.*, volume 702:pp. 385 – 400, 2006.

[HTY99]   Hall, J. L.; Taubmann, M. S.; Ye, J.: Laser stabilization. In: *OSA Handbook*, 1999.

[Hut96]   Hutsell, S. T.: Operational use of the Hadamard variance in GPS. In: *Proc. 28th PTTI meeting*, pp. 201 – 213, 1996.

[IS38]   Ives, H. E.; Stilwell, G. R.: An experimental study of the rate of a moving atomic clock. In: *J. Opt. Soc. Am.*, volume 28:pp. 215 – 226, 1938.

[IS42]   Ives, H. E.; Stilwell, G. R.: An experimental study of the rate of a moving atomic clock ii. In: *J. Opt. Soc. Am.*, volume 31:pp. 369 – 374, 1942.

[JJMT64]   Jaseja, T. S.; Javan, A.; Murray, J.; Townes, C. H.: Test of special relativity or of the isotropy of space by use of infrared masers. In: *Phys. Rev.*, volume 133:pp. 1221 – 1224, 1964.

[JK99]   Jackiw, R.; Kostelecký, V. A.: Radiatively induced Lorentz and CPT violation in electrodynamics. In: *Phys. Rev. Lett.*, volume 82:pp. 3572 – 3575, 1999.

[JKR64]   Jones, C. K.; Klemens, P. G.; Rayne, J. A.: Temperature dependence of ultrasonic attenuation in fused quartz up to $1\,\mathrm{kmc/s}$. In: *Phys. Lett.*, volume 8:p. 31, 1964.

[Joo30]   Joos, G.: Die Jenaer Wiederholung des Michelsonversuchs. In: *Ann. d. Physik*, volume 7:pp. 385 – 407, 1930.

[Kak99]   Kaku, M.: *Strings, conformal fields, and M-theory.* Springer, New York, Berlin, Heidelberg, second edition edition, 1999.

[KB85]   Kane, T. J.; Byer, R. L.: Monolithic, unidirectional single-mode ring laser. In: *Opt. Lett.*, volume 10:p. 65, 1985.

[KL66]   Kogelnik, H.; Li, T.: Laser beams and resonators. In: *Applied Optics*, volume 5:p. 1550, 1966.

[KL99]   Kostelecký, V. A.; Lane, C. D.: Constraints on Lorentz violation from clock comparison experiments. In: *Phys. Rev. D*, volume 60:p. 116010, 1999.

[KM01]   Kostelecký, V. A.; Mewes, M.: Cosmological constraints on Lorentz violation in electrodynamics. In: *Phys. Rev. Lett.*, volume 87:p. 251304, 2001.

[KM02]   Kostelecký, V. A.; Mewes, M.: Signals for Lorentz violation in electrodynamics. In: *Phys. Rev. D*, volume 66:p. 056005, 2002.

[KS89]   Kostelecký, V. A.; Samuel, S.: Spontaneous breaking of Lorentz symmetry in string theory. In: *Phys. Rev. D*, volume 39:p. 683, 1989.

[KS02]   Konechny, A.; Schwarz, A.: Introduction to M(atrix) theory and noncommutative geometry, part I. In: *Phys. Rept.*, volume 360:pp. 353 – 465, 2002.

[KT32]   Kennedy, R. J.; Thorndike, E. M.: Experimental establishment of the relativity of time. In: *Phys. Rev.*, volume 42:pp. 400 – 418, 1932.

[Lan05]   Lane, C. D.: Probing Lorentz violation with Doppler-shift experiments. In: *Phys. Rev. D*, volume 72:p. 016005, 2005.

[LJH+86]   Lamoreaux, S. K.; Jacobs, J. P.; Heckel, B. R.; Raab, F. J.; Fortson, E. N.: New limits on spatial anisotropy from optically pumped ^{201}Hg and ^{199}Hg. In: *Phys. Rev. Lett.*, volume 57:p. 3125, 1986.

[LNW+03]   Lipa, J. A.; Nissen, J. A.; Wang, S.; Stricker, D. A.; Avaloff, D.: New limits on signals of Lorentz violation in electrodynamics. In: *Phys. Rev. Lett.*, volume 90:p. 060403, 2003.

[LTS+96]   Lineweaver, C. H.; Tenorio, L.; Smoot, G. F.; Keegstra, P.; Banday, A. J.; Lubin, P.: The dipole observed in the DMR 4 year data. In: *Astrophys J.*, volume 470:pp. 38 – 42, 1996.

[Mak06]   Makdissi, A.: AlaVar 5.2, 2006. URL `http://www.alamath.com/alavar.html`.

[MHB+03a] Müller, H.; Herrmann, S.; Braxmaier, C.; Schiller, S.; Peters, A.: Modern Michelson-Morley experiment using cryogenic optical resonators. In: *Phys. Rev. Lett.*, volume 91:p. 020401, 2003.

[MHB+03b] Müller, H.; Herrmann, S.; Braxmaier, C.; Schiller, S.; Peters, A.: Precision test of the isotropy of light propagation. In: *App. Phys. B*, volume 77:pp. 719 – 731, 2003.

[MHS+03a] Müller, H.; Herrmann, S.; Saenz, A.; Peters, A.; Lämmerzahl, C.: Optical cavity tests of Lorentz invariance for the electron. In: *Phys. Rev. D*, volume 68:p. 116006, 2003.

[MHS⁺03b]   Müller, H.; Herrmann, S.; Schuldt, T.; Scholz, M.; Kovalchuk, E.; Peters, A.: Offset compensation by use of amplitude modulated sidebands in optical frequency standards. In: *Opt. Lett.*, volume 28:pp. 2186 – 2188, 2003.

[Mic81]   Michelson, A. A.: The relative motion of the Earth and the luminiferous ether. In: *Am. J. Sci.*, volume 22:pp. 120 – 129, 1881.

[MID99]   Mittleman, R. K.; Ioannou, I. I.; Dehmelt, H. G.: Bound on CPT and Lorentz symmetry with a trapped electron. In: *Phys. Rev. Lett.*, volume 83:pp. 2116 – 2119, 1999.

[MM87]   Michelson, A. A.; Morley, E. W.: On the relative motion of the Earth and the luminiferous ether. In: *Am. J. Sci.*, volume 34:pp. 333 – 345, 1887.

[MM97]   Michelson, A. A.; Morley, E. A.: On the relative motion of the Earth and the luminiferous ether. In: *Phil. Mag.*, volume 24:pp. 449 – 463, 1897.

[MS76]   Mansouri, R.; Sexl, R. U.: A test theory of special relativity. In: *Gen. Rel. Grav.*, volume 8:pp. 495, 515, 809, 1976.

[MTW73]   Misner, C. W.; Thorne, K. S.; Wheeler, J. A.: *Gravitation.* Freeman and company, New York, 1973.

[Mül04]   Müller, Holger: *Moderne optische Tests der Relativitätstheorie.* PhD thesis, Humbold-Universität zu Berlin, Mathematisch-Naturwissenschaftliche Fakultät I, Berlin, 2004.

[Mül05]   Müller, H.: Testing Lorentz invariance by the use of vacuum and matter filled cavity resonators. In: *Phys. Dev. D*, volume 71:p. 045004, 2005.

[MYH94]   Ma, L.-S.; Ye, J.; Hall, J. L.: Delivering the same optical frequency at two places: accurate cancellation of phase noise introduced by an optical fiber or other time-varying path. In: *Opt. Lett.*, volume 19, 1994.

[NAY⁺03]   Numata, K.; Ando, M.; Yamamoto, K.; Otsuka, S.; Tsubono, K.: Wide-band direct measurement of thermal fluctuations in an interferometer. In: *Phys. Rev. Lett.*, volume 91:p. 260602, 2003.

[NKC04]   Numata, K.; Kemery, A.; Camp, J.: Thermal-noise limit in the frequency stabilization of lasers with rigid cavities. In: *Phys. Rev. Lett.*, volume 93:p. 250602, 2004.

[NML$^+$06]   Notcutt, M.; Ma, L. S.; Ludlow, A. D.; Foreman, S. M.; Ye, J.; Hall, J. L.: Contribution of thermal noise to frequency stability of rigid optical cavity via Hertz-linewidth lasers. In: *Phys. Rev. A*, volume 73:p. 031804, 2006.

[NPZ05]   Nicolai, H.; Peeters, K.; Zamaklar, M.: Loop quantum gravity: an outside view. In: *Class. Quantum Grav.*, volume 22:pp. 193 – 247, 2005.

[PBIW85]   Prestage, J. D.; Bollinger, J. J.; Itano, W. M.; Wineland, D. J.: Limits for spatial anisotropy by use of nuclear-spin-polarized ^{9}Be$^+$ ions. In: *Phys. Rev. Lett.*, volume 54:pp. 2387 – 2390, 1985.

[PHM$^+$01]   Philips, D. F.; Humphrey, M. A.; Mattison, E. M.; Stoner, R. E.; Vessot, R. F. C.; Walsworth, R. L.: Limit on Lorentz and CPT violation of the proton using a hydrogen maser. In: *Phys. Rev. D*, volume 63:p. 111101, 2001.

[Pou46]   Pound, R. V.: Electronic frequency stabilization of microwave oscillators. In: *Rev. Sci. Instr.*, volume 17:pp. 490 – 505, 1946.

[Rob49]   Robertson, H. P.: Postulate versus observation in the special theory of relativity. In: *Rev. Mod. Phys.*, volume 21:pp. 378 – 382, 1949.

[Rut78]   Rutman, J.: Characterization of phase and frequency instabilities in precision frequency sources. In: *Proc. IEEE*, volume 66:pp. 1048–1075, 1978.

[Sau90]   Saulson, P. R.: Thermal noise in mechanical experiments. In: *Phys. Rev. D*, volume 42:pp. 2437 – 2445, 1990.

[SBS98]   Startin, W. J.; Beilby, M. A.; Saulson, P. R.: Mechanical quality factors of fused silica resonators. In: *Rev. Sci. Instr.*, volume 69:pp. 3681 – 3689, 1998.

[Sch03]   Schuldt, Thilo: *Frequenzstabilisierter Nd:YAG-Laser für Weltraumanwendungen*. Diploma thesis, Humboldt-Universität zu Berlin, Fachbereich Physik, Berlin, 2003.

[Sen06]   Senger, Alexander: *Ein modernes Michelson-Morley Experiment zum Test der Lorentzinvarianz.* Diploma thesis, Humboldt-Universität zu Berlin, Mathematisch-Naturwissenschaftliche Fakultät I, Berlin, 2006.

[SHH88]   Salomon, C.; Hils, D.; Hall, J. L.: Laser stabilization at the millihertz level. In: *J. Opt. Soc. Am. B*, volume 5:pp. 1576 – 1587, 1988.

[SKE+03]   Saathoff, G.; Karpuk, S.; Eisenbarth, U.; Huber, G.; Krohn, S.; Horta, R. Muoz; Reinhardt, S.; Schwalm, D.; Wolf, A.; Gwinner, G.: Improved test of time dilation in special relativity. In: *Phys. Rev. Lett.*, volume 91:p. 190403, 2003.

[ST58]   Schawlow, A. L.; Townes, C. H.: Infrared and optical masers. In: *Phys. Rev.*, volume 112:pp. 1940 – 1949, 1958.

[Sto98]   Storz, Rafael: *Frequenzstabilisierung auf kryogene optische Resonatoren.* PhD thesis, Universität Konstanz, Fachbereich Physik, Konstanz, 1998.

[STW+05]   Stanwix, P.; Tobar, M. E.; Wolf, P.; Susli, M.; Locke, C. R.; Ivanov, E. N.; Winterflood, J.; van Kann, F.: Test of Lorentz invariance in electrodynamics using rotating cryogenic sapphire microwave oscillators. In: *Phys. Rev. Lett.*, volume 95:p. 040404, 2005.

[Tob06]   Tobar, M.: Private communication, 2006.

[TR02]   Tartaglia, A.; Ruggiero, M. L.: Angular momentum effects in Michelson-Morley type experiments. In: *Gen. Rel. Grav.*, volume 34:pp. 1371 – 1382, 2002.

[Tro05]   Troebs, Michael: *Laser development and stabilization for the spaceborne interferometric gravitational wave detector LISA.* PhD thesis, Universität Hannover, Fachbereich Physik, Hannover, 2005.

[TSS+06]   Tobar, M. E.; Stanwix, P. L; Susli, M.; Wolf, P.; Locke, C. R.; Ivanov, E. N.: Rotating resonator-oscillator experiments to test Lorentz invariance in electrodynamics. In: *Lect. Notes Phys.*, volume 702:pp. 416 – 450, 2006.

[TWFH05] Tobar, M. E.; Wolf, P.; Fowler, A.; Hartnett, J. G.: New methods of testing Lorentz violation in electrodynamics. In: *Phys. Rev. D*, volume 71:p. 025004, 2005.

[US 06] US Naval Observatory: Data base of the astronomical association, 2006. URL `http://aa.usno.navy.mil/`.

[Vol01] Volovik, G. E.: Reentrant violation of special relativity in the low energy corner. In: *JETP Lett.*, volume 73:pp. 162 – 165, 2001.

[WBC⁺03] Wolf, P.; Bize, S.; Clairon, A.; Luiten, A. N.; Santarelli, G.; Tobar, M. E.: Test of Lorentz invariance using a microwave resonator. In: *Phys. Rev. Lett.*, volume 90:p. 060402, 2003.

[WBC⁺04] Wolf, P.; Bize, S.; Clairon, A.; Santarelli, G.; Tobar, M. E.; Luiten, A. N.: Improved test of Lorentz invariance in electrodynamics. In: *Phys. Rev. D*, volume 70:p. 051902, 2004.

[WCBC06] Wolf, P.; Chapelet, F.; Bize, S.; Clairon, A.: Cold atom clock test of Lorentz invariance in the matter sector. In: *Phys. Rev. Lett.*, volume 96:p. 060801, 2006.

[Wit86] Witten, E.: Non-commutative geometry and string field theory. In: *Nucl. Phys. B*, volume 268:p. 253, 1986.

[WTB⁺04] Wolf, P.; Tobar, M. E.; Bize, S.; Clairon, A.; Luiten, A. N.; Santarelli, G.: Whispering gallery resonators and tests of Lorentz invariance. In: *Gen. Rel. Grav.*, volume 36:pp. 2351 – 2371, 2004.

[YCIB99] Young, B. C.; Cruz, F. C.; Itano, W. M.; Bergquist, J. C.: Visible lasers with subhertz linewidths. In: *Phys. Rev. Lett.*, volume 82:pp. 3799 – 3801, 1999.

[ZH93] Zhu, M.; Hall, J. L.: Stabilization of optical phase/frequency of a laser system: application to a commercial dye laser with an external stabilizer. In: *J. Opt. Soc. Am. B*, volume 10:pp. 22802 – 816, 1993.

Appendix A

Estimators for frequency stability in the time domain

The present thesis applies two measures of frequency stability in the time domain: the Allan deviation and the Hadamard deviation. Here, definitions are given and the connection to the power-law model is briefly outlined.

Consider a time series of frequency data, where each frequency measurement y_i has been recorded within a sampling time τ_0, assuming no dead time among adjacent intervals. This time series can be divided into intervals extending over a time $\tau = m\tau_0$ each. $\bar{y}_k$ is the average value of the m frequency measurements within the k_{th} such interval. The average variance of these values $\bar{y}_k$ among N subsequent intervals of length τ, then is a general measure of frequency stability, as given by

$$\sigma_y^2(N, \tau) = \frac{1}{N-1} \sum_{k=1}^{N} (\bar{y}_k - \frac{1}{N} \sum_{j=1}^{N} \bar{y}_j)^2 \qquad (A.1)$$

The most common such measure of frequency stability is the Allan variance [All66, Rut78], which is the average 2-sample variance according to the above definition with N = 2. This results in

$$\sigma_y^2(2, \tau) = \langle \sum_{k=1}^{2} (\bar{y}_k - \frac{1}{2} \sum_{j=1}^{2} \bar{y}_j)^2 \rangle = \frac{1}{2} \langle (\bar{y}_2 - \bar{y}_1)^2 \rangle \qquad (A.2)$$

where the average $\langle \rangle$ ideally extends over an infinite number of adjacent pairs of $\bar{y}_k$. In practice, the finite size of any frequency measurement requires an approximation that involves only a finite number of m such pairs. Thus the practical definition of the Allan variance can be written as

$$\sigma_A^2 = \frac{1}{2(m-1)} \sum_{k=1}^{m-1} (\bar{y}_{k+1} - \bar{y}_k) \qquad (A.3)$$

167

A. Estimators for frequency stability in the time domain

Noise type	α	$S_f^2(f)$	$\sigma_A^2(\tau)$
random walk frequency	-2	$h_{-2}f^{-2}$	$\frac{2\pi^2}{3}h_{-2}\tau$
flicker frequency	-1	$h_{-1}f^{-1}$	$2\ln 2h_{-1}$
white frequency	0	h_0	$\frac{h_0}{2}\frac{1}{\tau}$
flicker phase	+1	$h_1 f$	$\frac{h_1(1.04+3\ln(2\pi f_h\tau))}{4\pi^2}\frac{1}{\tau^2}$
white phase	+2	$h_2 f^2$	$\frac{3h_2 f_h}{4\pi^2}\frac{1}{\tau^2}$

Table A.1: *Allan deviation and its connection to the power-law model.*

The square root σ_A of this is denoted the Allan deviation or root Allan variance (RAV). Beyond the above definition, several refinements of the Allan deviation exist such as the modified Allan deviation or the total Allan deviation, which are widely applied [AB81].

According to the so-called power-law model the spectral noise density of an oscillator can be modeled as

$$S_f^2 = \sum_{\alpha=-2}^{\alpha=+2} h_\alpha f^\alpha. \tag{A.4}$$

This expression includes the five characteristic noise types with their characteristic dependence (see Table A.1). To link the power law model to the Allan deviation, the transformation given in [Rut78] can be applied:

$$\sigma_A^2 = \int_0^\infty S_f^2(f)\frac{2\sin^4(\pi\tau f)}{(\pi\tau f)^2}df. \tag{A.5}$$

This expression diverges if $\alpha \geq 1$, thus an upper cut-off frequency f_h has to be stated if flicker phase- or white phase-noise are considered. The resulting connection of the Allan deviation to the different noise types of the power-law model are also stated in Table A.1. Furthermore, Figure A.1 depicts the characteristic slopes of the Allan deviation for the different noise types of an arbitrary oscillator.

The Hadamard deviation [Bau71] is a further estimator of frequency stability of an oscillator. It is an analogue to the Allan deviation where the 3-sample variance is considered, i.e. the second difference of frequency variations. The Hadamard variance is thus given as

$$\sigma_H^2 = \frac{1}{6(m-2)}\sum_{k=1}^{m-2}(\bar{y}_{k+2} - 2\bar{y}_{k+1} + \bar{y}_k) \tag{A.6}$$

The fundamental difference as compared to the Allan deviation is that the Hadamard deviation is insensitive to a linear drift. Thus it is commonly
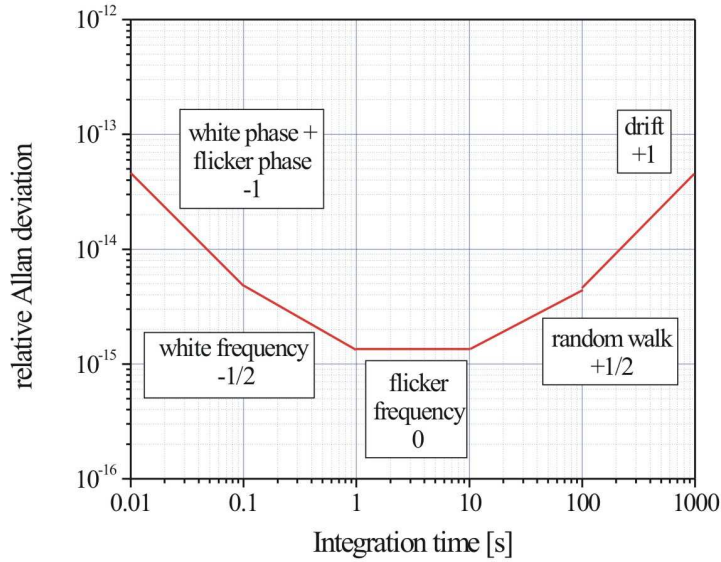
Figure A.1: *Typical appearance of power-law noise contributions within the Allan deviation.*

adopted for analysis of frequency stability where the interesting spectral features might be compromised by frequency drift [Hut96]. Furthermore, while the same power-law noise contributions can be identified within a plot of the Hadamard deviation as in the Allan deviation, the Hadamard deviation converges also for flicker walk and random walk frequency noise, with slopes of +1 and +3/2 respectively [HBG+05].

A. Estimators for frequency stability in the time domain

Appendix B

Full expressions of SME signal coefficients

The full expressions of amplitude modulation coefficients of equations (3.9), (3.10) and (3.11) are given here. Expressions are stated to first order in orbital boost only, including the full set of photonic SME parameters. For the analysis the κ_{e+} and κ_{o-} terms are neglected, as they are already restricted by astrophysical measurements well below the sensitivity of the measurement.

$$
\begin{aligned}
A_0 \;:\;\; & \frac{1}{16} \Big(-3 \Big(\tilde{\kappa}_{\text{e-}}^{\text{ZZ}} - 3\tilde{\kappa}_{\text{e+}}^{\text{ZZ}} + 6 \sin\left(\Omega_\oplus T\right) \beta_\oplus \tilde{\kappa}_{\text{o-}}^{\text{YZ}} - 4 \cos\left(\Omega_\oplus T\right) \sin(\eta) \beta_\oplus \tilde{\kappa}_{\text{o+}}^{\text{XY}} \\
& + 2 \cos(\eta) \cos\left(\Omega_\oplus T\right) \beta_\oplus \left(3\tilde{\kappa}_{\text{o-}}^{\text{XZ}} - \tilde{\kappa}_{\text{o+}}^{\text{XZ}} \right) - 2 \sin\left(\Omega_\oplus T\right) \beta_\oplus \tilde{\kappa}_{\text{o+}}^{\text{YZ}} \Big) \cos^2(\chi) \\
& - 16\tilde{\kappa}_{\text{tr}} + 3\sin^2(\chi)\tilde{\kappa}_{\text{e-}}^{\text{ZZ}} - \tilde{\kappa}_{\text{e-}}^{\text{ZZ}} - 9\sin^2(\chi)\tilde{\kappa}_{\text{e+}}^{\text{ZZ}} + 3\tilde{\kappa}_{\text{e+}}^{\text{ZZ}} \\
& + 18\sin^2(\chi)\sin\left(\Omega_\oplus T\right) \beta_\oplus \tilde{\kappa}_{\text{o-}}^{\text{YZ}} - 6\sin\left(\Omega_\oplus T\right) \beta_\oplus \tilde{\kappa}_{\text{o-}}^{\text{YZ}} \\
& - 12\cos\left(\Omega_\oplus T\right) \sin(\eta) \sin^2(\chi) \beta_\oplus \tilde{\kappa}_{\text{o+}}^{\text{XY}} + 4\cos\left(\Omega_\oplus T\right) \sin(\eta) \beta_\oplus \tilde{\kappa}_{\text{o+}}^{\text{XY}} \\
& - \cos(\eta)(3\cos(2\chi) - 1)\cos\left(\Omega_\oplus T\right) \beta_\oplus \left(3\tilde{\kappa}_{\text{o-}}^{\text{XZ}} - \tilde{\kappa}_{\text{o+}}^{\text{XZ}} \right) \\
& - 6\sin^2(\chi)\sin\left(\Omega_\oplus T\right) \beta_\oplus \tilde{\kappa}_{\text{o+}}^{\text{YZ}} + 2\sin\left(\Omega_\oplus T\right) \beta_\oplus \tilde{\kappa}_{\text{o+}}^{\text{YZ}} \Big) \\
A_{\text{s1}} \;:\;\; & -\frac{1}{4}\sin(2\chi) \Big(\tilde{\kappa}_{\text{e-}}^{\text{YZ}} - 3\tilde{\kappa}_{\text{e+}}^{\text{YZ}} + 3\sin\left(\Omega_\oplus T\right) \beta_\oplus \tilde{\kappa}_{\text{o-}}^{\text{YY}} - 3\sin\left(\Omega_\oplus T\right) \beta_\oplus \tilde{\kappa}_{\text{o-}}^{\text{ZZ}} \\
& + 3\cos(\eta)\cos\left(\Omega_\oplus T\right) \beta_\oplus \left(\tilde{\kappa}_{\text{o-}}^{\text{XY}} - \tilde{\kappa}_{\text{o+}}^{\text{XY}} \right) \\
& - 3\cos\left(\Omega_\oplus T\right) \sin(\eta) \beta_\oplus \left(\tilde{\kappa}_{\text{o-}}^{\text{XZ}} - \tilde{\kappa}_{\text{o+}}^{\text{XZ}} \right) \Big)
\end{aligned}
$$

B. Full expressions of SME signal coefficients

$$
\begin{aligned}
A_{\mathrm{c1}} \;:\;\; & -\frac{1}{4}\sin(2\chi)\left(\tilde{\kappa}_{\mathrm{e\text{-}}}^{\mathrm{XZ}} - 3\tilde{\kappa}_{\mathrm{e+}}^{\mathrm{XZ}} + 3\sin\left(\Omega_\oplus T\right)\beta_\oplus \tilde{\kappa}_{\mathrm{o\text{-}}}^{\mathrm{XY}}\right. \\
& \left. + 3\cos(\eta)\cos\left(\Omega_\oplus T\right)\beta_\oplus\left(\tilde{\kappa}_{\mathrm{o\text{-}}}^{\mathrm{XX}} - \tilde{\kappa}_{\mathrm{o\text{-}}}^{\mathrm{ZZ}}\right) + 3\sin\left(\Omega_\oplus T\right)\beta_\oplus \tilde{\kappa}_{\mathrm{o+}}^{\mathrm{XY}}\right. \\
& \left. + 3\cos\left(\Omega_\oplus T\right)\sin(\eta)\beta_\oplus\left(\tilde{\kappa}_{\mathrm{o\text{-}}}^{\mathrm{YZ}} - \tilde{\kappa}_{\mathrm{o+}}^{\mathrm{YZ}}\right)\right) \\[4pt]
A_{\mathrm{s2}} \;:\;\; & \frac{1}{4}\sin^2(\chi)\left(-\tilde{\kappa}_{\mathrm{e\text{-}}}^{\mathrm{XY}} + 3\tilde{\kappa}_{\mathrm{e+}}^{\mathrm{XY}} + 3\sin\left(\Omega_\oplus T\right)\beta_\oplus \tilde{\kappa}_{\mathrm{o\text{-}}}^{\mathrm{XZ}}\right. \\
& \left. + 3\cos\left(\Omega_\oplus T\right)\sin(\eta)\beta_\oplus\left(\tilde{\kappa}_{\mathrm{o\text{-}}}^{\mathrm{XX}} - \tilde{\kappa}_{\mathrm{o\text{-}}}^{\mathrm{YY}}\right) + 3\sin\left(\Omega_\oplus T\right)\beta_\oplus \tilde{\kappa}_{\mathrm{o+}}^{\mathrm{XZ}}\right. \\
& \left. + 3\cos(\eta)\cos\left(\Omega_\oplus T\right)\beta_\oplus\left(\tilde{\kappa}_{\mathrm{o\text{-}}}^{\mathrm{YZ}} + \tilde{\kappa}_{\mathrm{o+}}^{\mathrm{YZ}}\right)\right) \\[4pt]
A_{\mathrm{c2}} \;:\;\; & \frac{1}{8}\sin^2(\chi)\left(2\tilde{\kappa}_{\mathrm{e\text{-}}}^{\mathrm{YY}} + \tilde{\kappa}_{\mathrm{e\text{-}}}^{\mathrm{ZZ}} - 6\tilde{\kappa}_{\mathrm{e+}}^{\mathrm{YY}} - 3\tilde{\kappa}_{\mathrm{e+}}^{\mathrm{ZZ}} - 12\cos\left(\Omega_\oplus T\right)\sin(\eta)\beta_\oplus \tilde{\kappa}_{\mathrm{o\text{-}}}^{\mathrm{XY}}\right. \\
& \left. - 6\sin\left(\Omega_\oplus T\right)\beta_\oplus \tilde{\kappa}_{\mathrm{o\text{-}}}^{\mathrm{YZ}} + 6\cos(\eta)\cos\left(\Omega_\oplus T\right)\beta_\oplus\left(\tilde{\kappa}_{\mathrm{o\text{-}}}^{\mathrm{XZ}} + \tilde{\kappa}_{\mathrm{o+}}^{\mathrm{XZ}}\right)\right. \\
& \left. - 6\sin\left(\Omega_\oplus T\right)\beta_\oplus \tilde{\kappa}_{\mathrm{o+}}^{\mathrm{YZ}}\right)
\end{aligned}
$$

$$
\begin{aligned}
B_{0} \;:\;\; & 0 \\[4pt]
B_{\mathrm{s1}} \;:\;\; & \frac{1}{2}\sin(\chi)\left(\tilde{\kappa}_{\mathrm{e\text{-}}}^{\mathrm{XZ}} + \tilde{\kappa}_{\mathrm{e+}}^{\mathrm{XZ}} - \sin\left(\Omega_\oplus T\right)\beta_\oplus \tilde{\kappa}_{\mathrm{o\text{-}}}^{\mathrm{XY}}\right. \\
& \left. - \cos(\eta)\cos\left(\Omega_\oplus T\right)\beta_\oplus\left(\tilde{\kappa}_{\mathrm{o\text{-}}}^{\mathrm{XX}} - \tilde{\kappa}_{\mathrm{o\text{-}}}^{\mathrm{ZZ}}\right) - \sin\left(\Omega_\oplus T\right)\beta_\oplus \tilde{\kappa}_{\mathrm{o+}}^{\mathrm{XY}}\right. \\
& \left. - \cos\left(\Omega_\oplus T\right)\sin(\eta)\beta_\oplus\left(\tilde{\kappa}_{\mathrm{o\text{-}}}^{\mathrm{YZ}} - \tilde{\kappa}_{\mathrm{o+}}^{\mathrm{YZ}}\right)\right) \\[4pt]
B_{\mathrm{c1}} \;:\;\; & -\frac{1}{2}\sin(\chi)\left(\tilde{\kappa}_{\mathrm{e\text{-}}}^{\mathrm{YZ}} + \tilde{\kappa}_{\mathrm{e+}}^{\mathrm{YZ}} - \sin\left(\Omega_\oplus T\right)\beta_\oplus \tilde{\kappa}_{\mathrm{o\text{-}}}^{\mathrm{YY}} + \sin\left(\Omega_\oplus T\right)\beta_\oplus \tilde{\kappa}_{\mathrm{o\text{-}}}^{\mathrm{ZZ}}\right. \\
& \left. - \cos(\eta)\cos\left(\Omega_\oplus T\right)\beta_\oplus\left(\tilde{\kappa}_{\mathrm{o\text{-}}}^{\mathrm{XY}} - \tilde{\kappa}_{\mathrm{o+}}^{\mathrm{XY}}\right) + \cos\left(\Omega_\oplus T\right)\sin(\eta)\beta_\oplus\left(\tilde{\kappa}_{\mathrm{o\text{-}}}^{\mathrm{XZ}} - \tilde{\kappa}_{\mathrm{o+}}^{\mathrm{XZ}}\right)\right) \\[4pt]
B_{\mathrm{s2}} \;:\;\; & \frac{1}{4}\cos(\chi)\left(2\tilde{\kappa}_{\mathrm{e\text{-}}}^{\mathrm{YY}} + \tilde{\kappa}_{\mathrm{e\text{-}}}^{\mathrm{ZZ}} + 2\tilde{\kappa}_{\mathrm{e+}}^{\mathrm{YY}} + \tilde{\kappa}_{\mathrm{e+}}^{\mathrm{ZZ}} + 4\cos\left(\Omega_\oplus T\right)\sin(\eta)\beta_\oplus \tilde{\kappa}_{\mathrm{o\text{-}}}^{\mathrm{XY}}\right. \\
& \left. + 2\sin\left(\Omega_\oplus T\right)\beta_\oplus \tilde{\kappa}_{\mathrm{o\text{-}}}^{\mathrm{YZ}} - 2\cos(\eta)\cos\left(\Omega_\oplus T\right)\beta_\oplus\left(\tilde{\kappa}_{\mathrm{o\text{-}}}^{\mathrm{XZ}} + \tilde{\kappa}_{\mathrm{o+}}^{\mathrm{XZ}}\right)\right. \\
& \left. + 2\sin\left(\Omega_\oplus T\right)\beta_\oplus \tilde{\kappa}_{\mathrm{o+}}^{\mathrm{YZ}}\right) \\[4pt]
B_{\mathrm{c2}} \;:\;\; & \frac{1}{2}\cos(\chi)\left(\tilde{\kappa}_{\mathrm{e\text{-}}}^{\mathrm{XY}} + \tilde{\kappa}_{\mathrm{e+}}^{\mathrm{XY}} + \sin\left(\Omega_\oplus T\right)\beta_\oplus \tilde{\kappa}_{\mathrm{o\text{-}}}^{\mathrm{XZ}} +\right. \\
& \left. \cos\left(\Omega_\oplus T\right)\sin(\eta)\beta_\oplus\left(\tilde{\kappa}_{\mathrm{o\text{-}}}^{\mathrm{XX}} - \tilde{\kappa}_{\mathrm{o\text{-}}}^{\mathrm{YY}}\right) + \sin\left(\Omega_\oplus T\right)\beta_\oplus \tilde{\kappa}_{\mathrm{o+}}^{\mathrm{XZ}}\right. \\
& \left. + \cos(\eta)\cos\left(\Omega_\oplus T\right)\beta_\oplus\left(\tilde{\kappa}_{\mathrm{o\text{-}}}^{\mathrm{YZ}} + \tilde{\kappa}_{\mathrm{o+}}^{\mathrm{YZ}}\right)\right)
\end{aligned}
$$

$$C_0 \;:\; \frac{1}{8}\sin^2(\chi)\left(3\tilde{\kappa}_{\text{e-}}^{\text{ZZ}} + 3\tilde{\kappa}_{\text{e+}}^{\text{ZZ}} - 6\sin\left(\Omega_\oplus T\right)\beta_\oplus\tilde{\kappa}_{\text{o-}}^{\text{YZ}} + 4\cos\left(\Omega_\oplus T\right)\sin(\eta)\beta_\oplus\tilde{\kappa}_{\text{o+}}^{\text{XY}}\right.$$

$$\left. - 2\cos(\eta)\cos\left(\Omega_\oplus T\right)\beta_\oplus\left(3\tilde{\kappa}_{\text{o-}}^{\text{XZ}} - \tilde{\kappa}_{\text{o+}}^{\text{XZ}}\right) + 2\sin\left(\Omega_\oplus T\right)\beta_\oplus\tilde{\kappa}_{\text{o+}}^{\text{YZ}}\right)$$

$$C_{\text{s1}} \;:\; -\frac{1}{4}\sin(2\chi)\left(\tilde{\kappa}_{\text{e-}}^{\text{YZ}} + \tilde{\kappa}_{\text{e+}}^{\text{YZ}} - \sin\left(\Omega_\oplus T\right)\beta_\oplus\tilde{\kappa}_{\text{o-}}^{\text{YY}} + \sin\left(\Omega_\oplus T\right)\beta_\oplus\tilde{\kappa}_{\text{o-}}^{\text{ZZ}}\right.$$

$$\left. - \cos(\eta)\cos\left(\Omega_\oplus T\right)\beta_\oplus\left(\tilde{\kappa}_{\text{o-}}^{\text{XY}} - \tilde{\kappa}_{\text{o+}}^{\text{XY}}\right) + \cos\left(\Omega_\oplus T\right)\sin(\eta)\beta_\oplus\left(\tilde{\kappa}_{\text{o-}}^{\text{XZ}} - \tilde{\kappa}_{\text{o+}}^{\text{XZ}}\right)\right)$$

$$C_{\text{c1}} \;:\; -\frac{1}{4}\sin(2\chi)\left(\tilde{\kappa}_{\text{e-}}^{\text{XZ}} + \tilde{\kappa}_{\text{e+}}^{\text{XZ}} - \sin\left(\Omega_\oplus T\right)\beta_\oplus\tilde{\kappa}_{\text{o-}}^{\text{XY}}\right.$$

$$\left. - \cos(\eta)\cos\left(\Omega_\oplus T\right)\beta_\oplus\left(\tilde{\kappa}_{\text{o-}}^{\text{XX}} - \tilde{\kappa}_{\text{o-}}^{\text{ZZ}}\right) - \sin\left(\Omega_\oplus T\right)\beta_\oplus\tilde{\kappa}_{\text{o+}}^{\text{XY}}\right.$$

$$\left. - \cos\left(\Omega_\oplus T\right)\sin(\eta)\beta_\oplus\left(\tilde{\kappa}_{\text{o-}}^{\text{YZ}} - \tilde{\kappa}_{\text{o+}}^{\text{YZ}}\right)\right)$$

$$C_{\text{s2}} \;:\; \frac{1}{8}(\cos(2\chi) + 3)\left(\tilde{\kappa}_{\text{e-}}^{\text{XY}} + \tilde{\kappa}_{\text{e+}}^{\text{XY}} + \sin\left(\Omega_\oplus T\right)\beta_\oplus\tilde{\kappa}_{\text{o-}}^{\text{XZ}}\right.$$

$$\left. + \cos\left(\Omega_\oplus T\right)\sin(\eta)\beta_\oplus\left(\tilde{\kappa}_{\text{o-}}^{\text{XX}} - \tilde{\kappa}_{\text{o-}}^{\text{YY}}\right) + \sin\left(\Omega_\oplus T\right)\beta_\oplus\tilde{\kappa}_{\text{o+}}^{\text{XZ}}\right.$$

$$\left. + \cos(\eta)\cos\left(\Omega_\oplus T\right)\beta_\oplus\left(\tilde{\kappa}_{\text{o-}}^{\text{YZ}} + \tilde{\kappa}_{\text{o+}}^{\text{YZ}}\right)\right)$$

$$C_{\text{c2}} \;:\; -\frac{1}{16}(\cos(2\chi) + 3)\left(2\tilde{\kappa}_{\text{e-}}^{\text{YY}} + \tilde{\kappa}_{\text{e-}}^{\text{ZZ}} + 2\tilde{\kappa}_{\text{e+}}^{\text{YY}} + \tilde{\kappa}_{\text{e+}}^{\text{ZZ}}\right.$$

$$\left. + 4\cos\left(\Omega_\oplus T\right)\sin(\eta)\beta_\oplus\tilde{\kappa}_{\text{o-}}^{\text{XY}} + 2\sin\left(\Omega_\oplus T\right)\beta_\oplus\tilde{\kappa}_{\text{o-}}^{\text{YZ}}\right.$$

$$\left. - 2\cos(\eta)\cos\left(\Omega_\oplus T\right)\beta_\oplus\left(\tilde{\kappa}_{\text{o-}}^{\text{XZ}} + \tilde{\kappa}_{\text{o+}}^{\text{XZ}}\right) + 2\sin\left(\Omega_\oplus T\right)\beta_\oplus\tilde{\kappa}_{\text{o+}}^{\text{YZ}}\right)$$

B. Full expressions of SME signal coefficients

Appendix C

Fourier coefficients of a Lorentz violation signal

The Fourier coefficients that contribute to the signal of Lorentz violation as given in equation (3.16) are stated here. Table C.2 gives the Fourier components for the SME, Table C.3 those applying for the RMS framework. Referred to an appropriate time axis as described in Section 3.1.2, the amplitudes of equations (3.10) and (3.11) are related to these coefficients as denoted in Table C.1.

C_k	$\tilde{C}_k$	B_k	$\tilde{B}_k$
C_0	$\tilde{C}_0$	B_0	B_0
C_{s1}	$\tilde{B}_{+1} - \tilde{B}_{-1}$	B_{s1}	$\tilde{C}_{-1} - \tilde{C}_{+1}$
C_{c1}	$\tilde{C}_{+1} + \tilde{C}_{-1}$	B_{c1}	$\tilde{B}_{-1} + \tilde{B}_{+1}$
C_{s2}	$\tilde{B}_{+2} - \tilde{B}_{-2}$	B_{s2}	$\tilde{C}_{-2} - \tilde{C}_{+2}$
C_{c2}	$\tilde{C}_{+2} + \tilde{C}_{-2}$	B_{c2}	$\tilde{B}_{-2} + \tilde{B}_{+2}$

Table C.1: Relation of Fourier coefficients to amplitudes B_k and C_k of equations (3.10) and (3.11).

	SME amplitude
$\tilde{C}_0$	$\tilde{\gamma}_0\left(\frac{3}{2}\tilde{\kappa}_{e-}^{ZZ} - \beta_\oplus[(\cos\eta\tilde{\kappa}_{o+}^{XZ} + 2\sin\eta\tilde{\kappa}_{o+}^{XY})\cos\Omega_\oplus T_\oplus - \tilde{\kappa}_{o+}^{YZ}\sin\Omega_\oplus T_\oplus]\right)$
$\tilde{C}_{+1}$	$\tilde{\gamma}_1\left(-\tilde{\kappa}_{e-}^{XZ} + \beta_\oplus[\sin\eta\tilde{\kappa}_{o+}^{YZ}\cos\Omega_\oplus T_\oplus - \tilde{\kappa}_{o+}^{XY}\sin\Omega_\oplus T_\oplus]\right)$
$\tilde{C}_{+2}$	$\tilde{\gamma}_2\left(\frac{1}{2}[\tilde{\kappa}_{e-}^{XX} - \tilde{\kappa}_{e-}^{YY}] - \beta_\oplus[\cos\eta\tilde{\kappa}_{o+}^{XZ}\cos\Omega_\oplus T_\oplus - \tilde{\kappa}_{o+}^{YZ}\sin\Omega_\oplus T_\oplus]\right)$
$\tilde{C}_{-1}$	$-\frac{\tilde{\gamma}_3}{\tilde{\gamma}_1}\tilde{C}_{+1}$
$\tilde{C}_{-2}$	$-\frac{\tilde{\gamma}_4}{\tilde{\gamma}_2}\tilde{C}_{+2}$
$\tilde{B}_0$	0
$\tilde{B}_{+1}$	$\tilde{\gamma}_1\left(-\tilde{\kappa}_{e-}^{YZ} + \beta_\oplus[(\cos\eta\tilde{\kappa}_{o+}^{XY} - \sin\eta\tilde{\kappa}_{o+}^{XZ})\cos\Omega_\oplus T_\oplus]\right)$
$\tilde{B}_{+2}$	$\tilde{\gamma}_2\left(\tilde{\kappa}_{e-}^{XY} - \beta_\oplus[\cos\eta\tilde{\kappa}_{o+}^{YZ}\cos\Omega_\oplus T_\oplus + \tilde{\kappa}_{o+}^{XZ}\sin\Omega_\oplus T_\oplus]\right)$
$\tilde{B}_{-1}$	$\frac{\tilde{\gamma}_3}{\tilde{\gamma}_1}\tilde{B}_{+1}$
$\tilde{B}_{-2}$	$\frac{\tilde{\gamma}_4}{\tilde{\gamma}_2}\tilde{B}_{+2}$

Table C.2: *Fourier spectrum amplitudes according to equation (3.16) related to SME parameters.* $\tilde{\gamma}_0 = \frac{1}{4}\sin^2\chi$, $\tilde{\gamma}_1 = \frac{1}{4}(1+\cos\chi)\sin\chi$, $\tilde{\gamma}_2 = \frac{1}{8}(1+\cos\chi)^2$, $\tilde{\gamma}_3 = \frac{1}{4}(1-\cos\chi)\sin\chi$, *and* $\tilde{\gamma}_4 = -\frac{1}{8}(1-\cos\chi)^2$. *Relations are stated to first order in orbital boost.* $\beta_\oplus = 10^{-4}$ *is the boost parameter,* $\chi = 37°$ *is the colatitude of the Berlin laboratory and* $\eta = 23°$ *is the tilt of Earth's axis relative to the SCCEF Z-axis.*

	RMS amplitude $\left(\times P_{\mathrm{MM}}\frac{v_c^2}{c^2}\right)$
$\tilde{C}_0$	$\frac{1}{2}\tilde{\gamma}_0(-1+3\cos 2\beta)$ $+2\frac{v_\oplus}{v_c}\tilde{\gamma}_0(\sin\alpha\cos\beta\cos\eta-2\sin\beta\sin\eta)\cos\Omega_\oplus T_\oplus$ $+2\frac{v_\oplus}{v_c}\tilde{\gamma}_0\cos\beta\cos\alpha\sin\Omega_\oplus T_\oplus$
$\tilde{C}_{+1}$	$-\gamma_1\cos\alpha\sin 2\beta$ $-2\frac{v_\oplus}{v_c}\gamma_1\cos\alpha\cos\beta\sin\eta\cos\Omega_\oplus T_\oplus$ $-2\frac{v_\oplus}{v_c}\gamma_1\sin\beta\sin\Omega_\oplus T_\oplus$
$\tilde{C}_{+2}$	$-\tilde{\gamma}_2\cos 2\alpha\cos^2\beta$ $+2\frac{v_\oplus}{v_c}\tilde{\gamma}_2\sin\alpha\cos\beta\cos\eta\cos\Omega_\oplus T_\oplus$ $-2\frac{v_\oplus}{v_c}\tilde{\gamma}_2\cos\alpha\cos\beta\sin\Omega_\oplus T_\oplus$
$\tilde{C}_{-1}$	$-\frac{\tilde{\gamma}_3}{\tilde{\gamma}_1}\tilde{C}_{+1}$
$\tilde{C}_{-2}$	$-\frac{\tilde{\gamma}_4}{\tilde{\gamma}_2}\tilde{C}_{+2}$
$\tilde{B}_0$	0
$\tilde{B}_{+1}$	$-\tilde{\gamma}_1\sin\alpha\sin 2\beta$ $-2\frac{v_\oplus}{v_c}\tilde{\gamma}_1(\sin\beta\cos\eta+\sin\alpha\cos\beta\sin\eta)\cos\Omega_\oplus T_\oplus$
$\tilde{B}_{+2}$	$\tilde{\gamma}_2\sin 2\alpha\cos^2\beta$ $+2\frac{v_\oplus}{v_c}\tilde{\gamma}_2\cos\alpha\cos\beta\cos\eta\cos\Omega_\oplus T_\oplus$ $+2\frac{v_\oplus}{v_c}\tilde{\gamma}_2\sin\alpha\cos\beta\sin\Omega_\oplus T_\oplus$
$\tilde{B}_{-1}$	$\frac{\tilde{\gamma}_3}{\tilde{\gamma}_1}\tilde{B}_{+1}$
$\tilde{B}_{-2}$	$\frac{\tilde{\gamma}_4}{\tilde{\gamma}_2}\tilde{B}_{+2}$

Table C.3: *Fourier spectrum amplitudes according to equation (3.16) related to RMS parameter P_{MM}. $\tilde{\gamma}_0 = \frac{1}{4}\sin^2\chi$, $\tilde{\gamma}_1 = \frac{1}{4}(1+\cos\chi)\sin\chi$, $\tilde{\gamma}_2 = \frac{1}{8}(1+\cos\chi)^2$, $\tilde{\gamma}_3 = \frac{1}{4}(1-\cos\chi)\sin\chi$, and $\tilde{\gamma}_4 = -\frac{1}{8}(1-\cos\chi)^2$. χ denotes the laboratory colatitude, η the tilt of Earth's axis relative to the SCCEF Z-axis. Terms varying with Earth's orbital motion are suppressed by $v_\oplus/v_c \sim 0.08$. $\alpha = 168°$ and $\beta = -6°$ denote the orientation of v_c in the SCCEF.*

C. Fourier coefficients of a Lorentz violation signal

Appendix D

Validation of the analysis on test data

The performance of the final fit procedure including all three steps as well as schemes A, B and C for step 2 has been evaluated by analyzing test data sets. Each set of test data is a time series of simulated measurement data, that contains a Lorentz violation signal modeled using the expressions of Table 3.1, with certain or all of the respective SME parameters set to non vanishing values. Two kinds of test data have been applied:

(i) For all 27 measurement runs beat frequency measurement data has been replaced by pure test data without drift or noise. As the discrete time axis has been retained, the distribution of test data over one year remains the same as that for the actual measurements.

(ii) In order to obtain a more realistic simulation of measurement data, noise and large frequency drift have been added simply by superimposing the signals from (i) to the actual measurement data. Of course "noise" added this way is not white noise. An actual measurement signal or small residual systematic effects might add to the test data. However, as long as test data sets are generated from SME parameters that produce signals significantly above the level of residual effects, useful information can still be obtained from such an analysis. It can be used to reveal a wrong estimate of the actual mean values and error bars on SME parameters, or it can be used to compare the performance of different analysis schemes.

A typical test data set of type (i) has been generated from

$$\tilde{\kappa}_{e-}^{XY}, \tilde{\kappa}_{e-}^{YZ}, \tilde{\kappa}_{o+}^{XY}, \tilde{\kappa}_{o+}^{YZ} = 2 \times 10^{-14}$$
$$\tilde{\kappa}_{e-}^{XX} - \tilde{\kappa}_{e-}^{YY}, \tilde{\kappa}_{e-}^{XZ}, \tilde{\kappa}_{o+}^{YZ} = 1 \times 10^{-14}.$$

As an example Figure D.1 shows the test data set obtained from the above values which substitutes the four-day data set described in Section 6.2. The
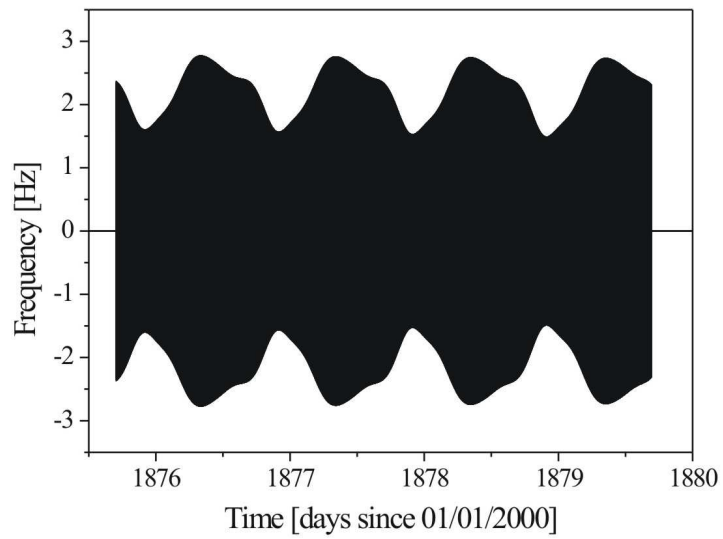
Figure D.1: *Simulated Lorentz violation signal for the four-day data set considered in Section 6.2. The actual variation with turntable rotation is not resolved within this graph.*
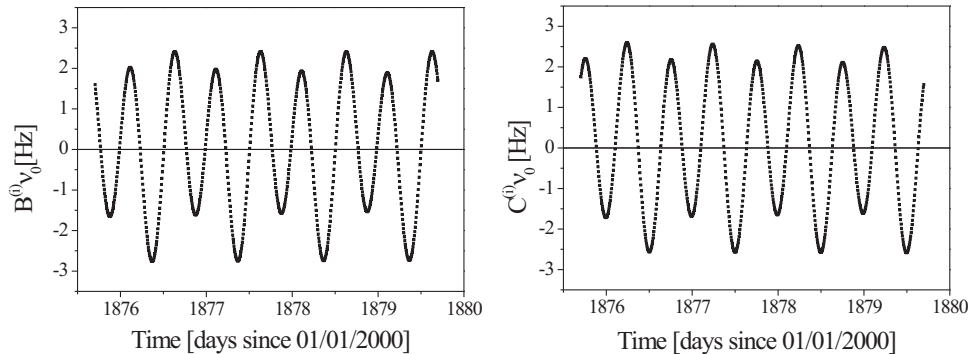
Figure D.2: *Results of fit step 1 for the simulated Lorentz violation signal of Figure D.1.*

sinusoidal oscillation of the beat frequency at the turntable rotation period is not resolved in the graph and merges into a black area. The envelope of the peak amplitudes is modulated at once and twice the period of a sidereal day. This modulation also becomes evident from the results of fit step 1 for this test data set (Figure D.2)

In total, test data substitutes for all 27 measurement runs have been generated and analyzed accordingly. Application of fit step 2 to these distributions of $B^{(i)}$ and $C^{(i)}$ gives the coefficients B_k and C_k shown in Figure D.3. Note, that the scale of these graphs is about twofold increased in comparison to Figure 6.8, while the test data values are about $10 - 50$ times larger than the limits deduced in Section 6.3.

The SME parameters extracted from the distributions of Figure D.3 in fit step 3 are presented in Figure D.4 to the top. All schemes A, B and C for step 2 reproduce the $\tilde{\kappa}$ values at an accuracy of $< 1.5\,\%$ deviation from the test value. Fit errors are not stated for the pure test data sets, because in the absence of measurement noise they do not provide any useful information.

Results on more realistic test data of type (ii), affected by measurement noise and large frequency drift, are given in the bottom graph of Figure D.4. The test values are recovered within reasonable error bars for schemes A and B, i.e. deviations do not substantially exceed the $1\,\sigma$ fit error for all parameters apart from $\tilde{\kappa}_{e-}^{ZZ}$. This parameter is associated to the coefficient C_0 which is affected by residual systematic effects that interfere with the SME parameter test value. Application of scheme C results in deviations from the test value, that exceed the $3\,\sigma$ level ($< 1\,\%$ probability) for several of the parameters. Following the results of scheme A and B we assume that

181

these deviations are not caused by a real signal hidden in the superimposed measurement data. Thus, we consider scheme C to produce less reliable estimates as compared to schemes A and B.
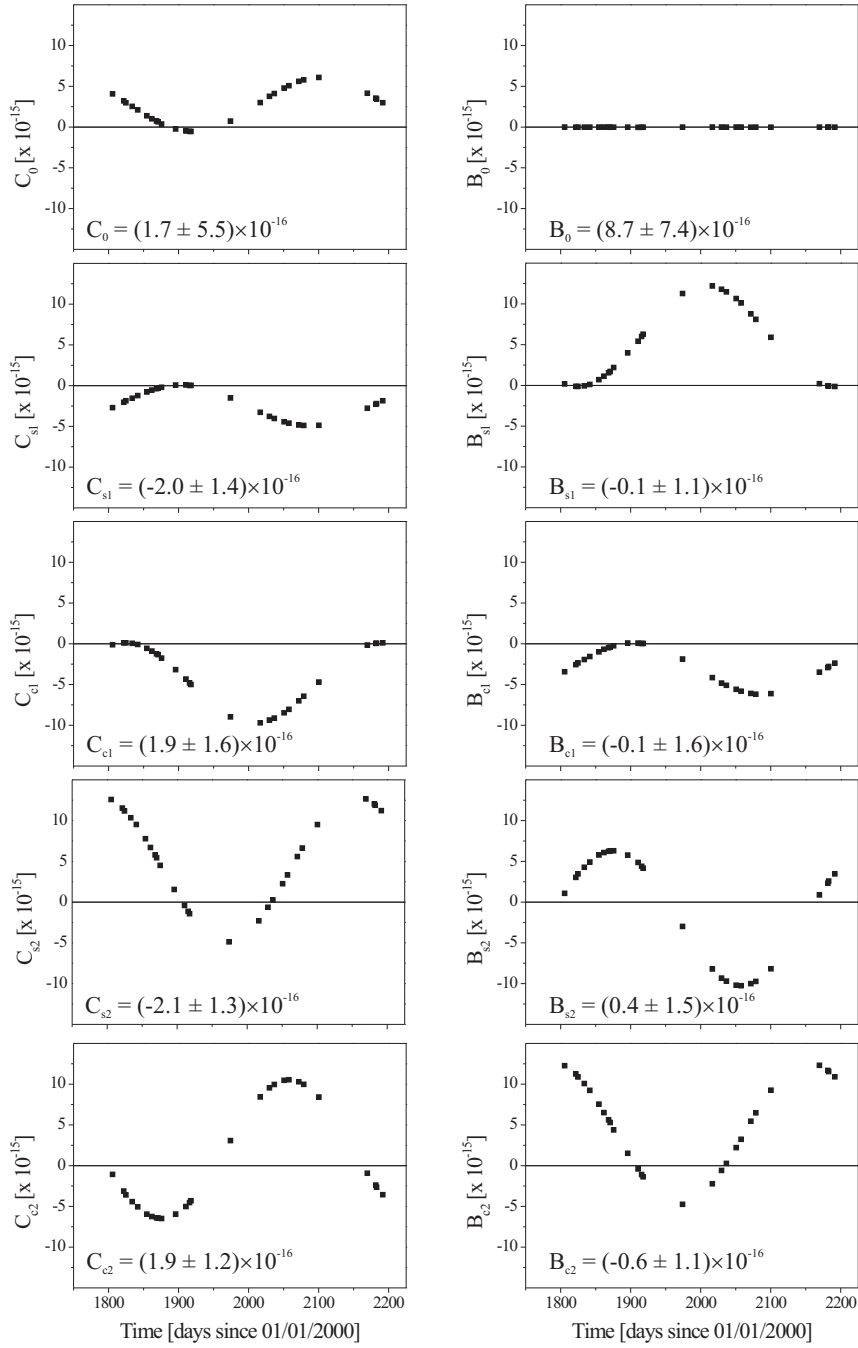
Figure D.3: *Results of step 2 of the analysis, obtained from the simulated Lorentz violation signal for the complete measurement.*
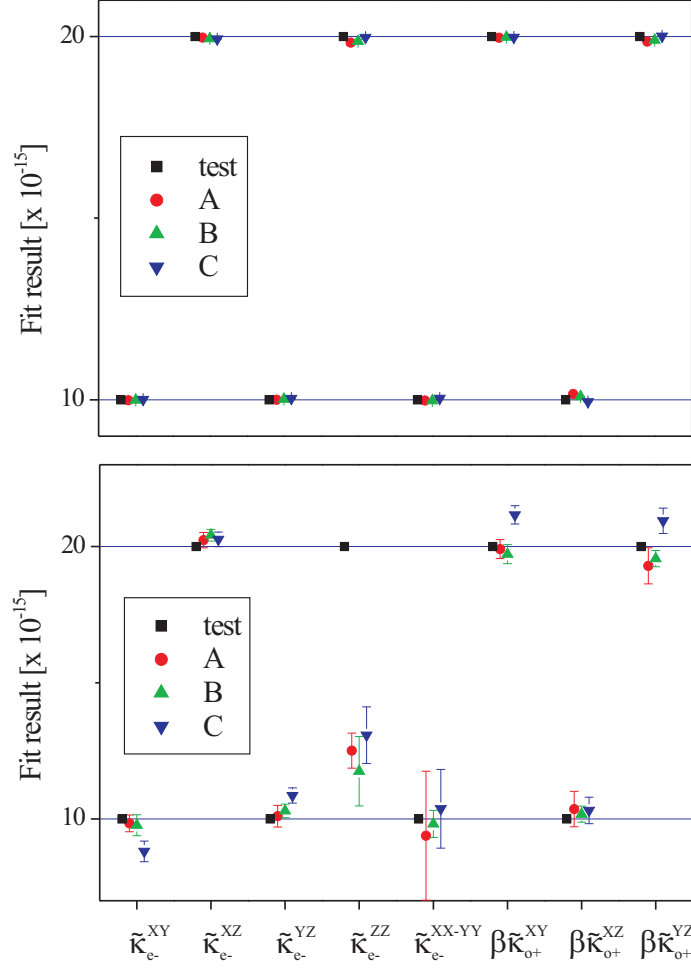
Figure D.4: *Top: Results obtained from application of the complete fitting procedure to pure test data generated from a set of non vanishing SME parameters. The parameter combination $(\tilde{\kappa}_{e-}^{XX} - \tilde{\kappa}_{e-}^{YY})$ is denoted $\tilde{\kappa}_{e-}^{XX-YY}$ for brevity. All three schemes within fit step 2 reliably reproduce the test values within an accuracy of $\sim 1\%$. Bottom: Results obtained from realistic test data superimposed with measurement noise and drift. Deviations for fitting scheme C generally exceed the 1σ level, while estimates produced by schemes A and B are more accurate.*

Appendix E

Limits on electronic SME parameters

Here, a derivation of independent limits on electronic and photonic SME parameters from combining the measurement results from this work with that of Stanwix *et al.* is given.

The sensitivity of the present experimental configuration to Lorentz violation in the electronic sector has been described in Section 3.1.3 following [MHS$^+$03a]. The sensitivity of the experiment of Stanwix *et al.* remains to be estimated. The effect of Lorentz violation in the electronic sector on the frequency of a single whispering gallery resonator made from crystalline sapphire has been estimated in [Mül05], taking into account geometrical changes as well as a change of the index of refraction of the monolithic whispering gallery resonators. The fractional change of the frequency of the whispering gallery mode in [Mül05] is modeled according to

$$\frac{\delta\nu}{\nu} = \mathcal{M}_{\mathrm{wg}} E_3',\tag{E.1}$$

where $E_3' = E_{xx} + E_{yy} - 2E_{zz}$ and the sensitivity coefficient is

$$\mathcal{M}_{\mathrm{wg}} = 3[-(\frac{1}{3} - \frac{1}{2}\mathcal{M}_{13}) + \beta_{\mathrm{wg}}].\tag{E.2}$$

Inserting the values for crystalline sapphire taken from [Mül05] we obtain

$$\mathcal{M}_{\mathrm{wg}} \approx -2.25.\tag{E.3}$$

Transformation from the SCCEF to the laboratory frame and taking the difference signal of two orthogonal rotating whispering gallery resonators gives the "electronic" signal coefficients of the Michelson-Morley experiment

$\tilde{B}_i/\tilde{C}_i$	parameter combination
$\tilde{C}_0$	$\frac{1}{2}\sin^2\chi[\tilde{\kappa}_{e-}^{ZZ} + \mathcal{M}_{\mathrm{wg}}c_3]$
$\tilde{C}_{-2}$	$-\cos^4(\chi/2)[(\tilde{\kappa}_{e-}^{XX} - \tilde{\kappa}_{e-}^{YY}) + \mathcal{M}_{\mathrm{wg}}(c_{XX} - c_{YY})]$
$\tilde{C}_{-1}$	$(\cos\chi + 1)\sin\chi[\tilde{\kappa}_{e-}^{XZ} + \mathcal{M}_{\mathrm{wg}}c_{(XZ)}]$
$\tilde{C}_{+1}$	$-\frac{(\cos\chi-1)}{(\cos\chi+1)}C_{-1}$
$\tilde{C}_{+2}$	$\tan^4(\chi/2)C_{-2}$
$\tilde{B}_0$	0
$\tilde{B}_{-2}$	$2\cos^4(\chi/2)[\tilde{\kappa}_{e-}^{XY} + \mathcal{M}_{\mathrm{wg}}c_{(XY)}]$
$\tilde{B}_{-1}$	$-(\cos\chi + 1)\sin\chi[\tilde{\kappa}_{e-}^{YZ} + \mathcal{M}_{\mathrm{wg}}c_{(YZ)}]$
$\tilde{B}_{+1}$	$\frac{(\cos\chi-1)}{(\cos\chi+1)}B_{-1}$
$\tilde{B}_{+2}$	$-\tan^4(\chi/2)B_{-2}$

Table E.1: *Amplitudes of a Lorentz violation signal from the Stanwix et al. experiment, involving electronic parameters, however neglecting the κ_{o+} terms. $\chi = 148.1°$ is the colatitude of Perth, Australia.*

performed by Stanwix *et al.*. It turns out, that these can be combined with the purely photonic ones of [TSS⁺06] using

$$\tilde{\kappa}_{e-}^{IJ} \rightarrow \tilde{\kappa}_{e-}^{IJ} + \mathcal{M}_{\mathrm{wg}}c_{(IJ)},$$
$$\tilde{\kappa}_{o+}^{IJ} \rightarrow \tilde{\kappa}_{o+}^{IJ}.$$

The signals neglecting the $\tilde{\kappa}_{o+}$ terms are given in Table E.1, stated in terms of Fourier coefficients in accordance with the presentation of [TSS⁺06].

Again, only five of these equations are linearly independent, because the same pair of electronic and photonic SME parameter is present within either two of these amplitudes. Unfortunately, the measured values for each $\tilde{B}_k$ and $\tilde{C}_k$ are not stated in [SKE⁺03]. Only the final results for each SME parameter assuming vanishing $\tilde{\kappa}_{o+}$ terms are given. Each of these parameters has been determined from two expressions in principle, however, one finds that one of these two coefficients exceeds the second by roughly a factor of ten. Thus, it is possible to reconstruct the measured values $v \pm \Delta v$ of the five dominant amplitudes among $\tilde{B}_k$ and $\tilde{C}_k$ from the values of SME parameters stated in [SKE⁺03].

From the present experiment another five independent equations can be obtained, restricting other combinations of electronic and photonic SME parameters as given in Table 3.1. This finally yields 10 independent equations involving five $\tilde{\kappa}_{e-}$ and five c_{IJ} terms. The three $\tilde{\kappa}_{o+}$ parameters are neglected, which allows to derive independent limits on photonic and electronic parameters from this equation system, assuming vanishing $\tilde{\kappa}_{o+}$ terms. The resulting

amplitude	IJ	$K_{\tilde{\kappa}}^{IJ}$	K_c^{IJ}	$v\ [\times 10^{-16}]$	$\Delta v\ [\times 10^{-16}]$
$\tilde{C}_0$	ZZ	0.21	-0.31	44.1	119.7
$\tilde{C}_{+1}$	XZ	-0.27	2.2	0.5	1.0
$\tilde{C}_{+2}$	XX-YY	-0.11	1.9	1.4	1.0
$\tilde{B}_{+1}$	YZ	-0.27	2.2	1.2	1.0
$\tilde{B}_{+2}$	XY	-0.23	-3.8	-1.7	1.2
C_0	ZZ	0.14	0.28	1.7	5.5
$C_{\mathrm{s}2}$	XY	0.41	2.4	-2.1	1.3
$C_{\mathrm{c}2}$	XX-YY	0.2	1.2	1.9	1.2
$B_{\mathrm{s}1}$	XZ	0.3	1.8	- 0.1	1.1
$B_{\mathrm{c}1}$	YZ	-0.3	-1.8	0.1	1.6

Table E.2: *The upper five amplitudes give the values $v = \Delta\nu/\nu$ for the five dominant Fourier coefficients determined from the Stanwix et al. experiment. The lower five amplitudes are those obtained from the present experiment.*

equation system is given by

$$v = K_{\tilde{\kappa}}^{IJ}\tilde{\kappa}_{e-}^{IJ} + K_c^{IJ}c_{IJ}, \tag{E.4}$$

where K_{κ}^{IJ} and K_c^{IJ} are given in Table E.2 and v denotes the signal amplitude $\Delta\nu/\nu$. Solving this equation system for electron and photon parameters finally yields the estimates presented in Table E.3.

parameter	value
$\tilde{\kappa}_{e-}^{XX} - \tilde{\kappa}_{e-}^{YY}$	3.8 ± 5.0
$\tilde{\kappa}_{e-}^{ZZ}$	125.7 ± 329.2
$\tilde{\kappa}_{e-}^{XY}$	-12.0 ± 5.7
$\tilde{\kappa}_{e-}^{XZ}$	-1.0 ± 2.6
$\tilde{\kappa}_{e-}^{YZ}$	-2.1 ± 3.4
$c_{XX} - c_{YY}$	1.0 ± 3.7
$c_{(XY)}$	1.2 ± 4.5
$c_{(XZ)}$	0.1 ± 1.9
$c_{(YZ)}$	0.3 ± 2.0
c_3	56.8 ± 364.2

Table E.3: *Limits on electronic and photonic SME parameters assuming vanishing $\tilde{\kappa}_{o+}$ terms. All values are $\times 10^{-16}$. (See Section 6.6 for a comparison to previous results.)*

Appendix F

A new vacuum chamber

A new vacuum chamber is currently being fabricated, that will provide better thermal isolation and thus improved long-term stability of the resonator frequencies. The details of the design have been elaborated by A. Senger and are described in [Sen06] in detail. A schematic drawing and a picture of the outer chamber are shown in Figure F.1.

The resonator pair is mounted inside an inner vacuum chamber (IVC), which is pumped by a combination of a getter and a small bakeable ion pump (Varian Inc., VacIon Plus 2 l/s) to ultra-high vacuum $< 10^{-10}$ mbar. The resonator block is placed on a 5 mm wide ring milled into a titanium disk. A diameter of ~ 4 cm has been chosen to provide minimum static deformation along the optical axis of the resonator according to a finite element simulation (see Figure F.2).

The IVC enclosing the cavity block is kinematically mounted on three glass spheres on the bottom of the first surrounding thermal shield. Kinematical mounting is provided by supporting the glass spheres inside circular shaped pits on the bottom of the first thermal shield and grooves on the bottom of the IVC. This support provides both mechanical stability and thermal isolation. In total, three layers of thermal shields are used. The inner two of these are made from stainless steel, whereas the outermost is made from copper. Each shield is kinematically mounted in a similar way as the IVC on three glass spheres within the next surrounding shield. The outermost copper shield, which is actively temperature-stabilized is 1 cm thick and contributes a rather large heat capacity. At the resonator site inside the IVC temperature stability is maintained passively only. It has been estimated to be at the nK-level [Sen06] (with no laser light dissipated inside the system). The most critical cause of heat transfer to the inside is thermal conduction via electrical connections to the getter and ion pumps. Thus, all cables have to be attached carefully to each successive thermal shield. Heat dissipation
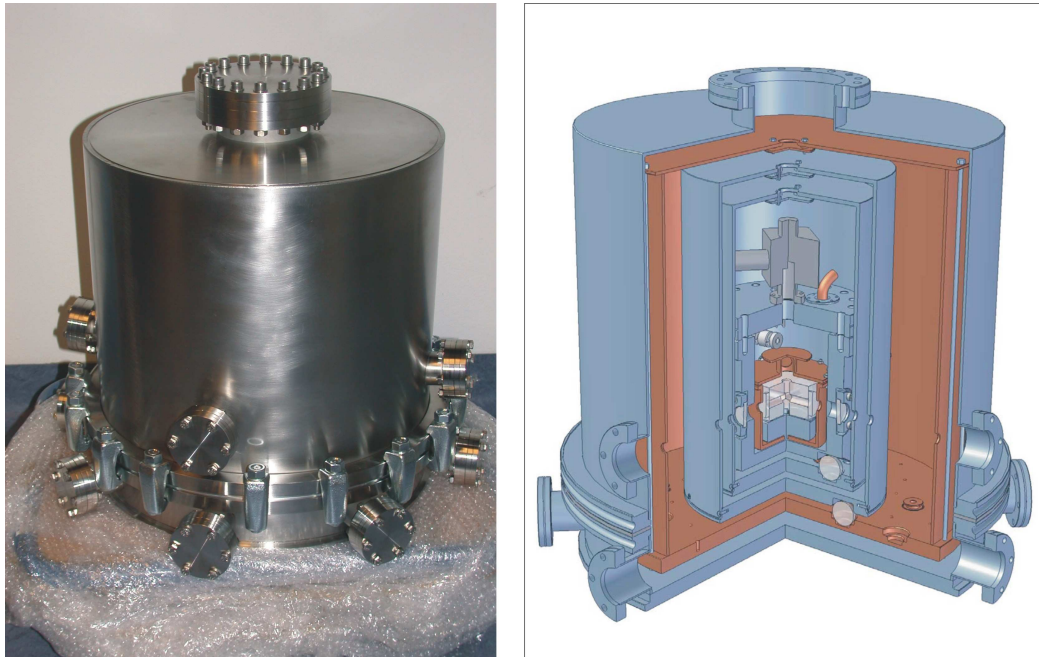
Figure F.1: *Picture of the outside part of the new vacuum chamber and a sketch of the inside design [Sen06]. The resonator block is placed inside an inner vacuum chamber pumped by an ion pump on top and surrounded by several thermal shields.*
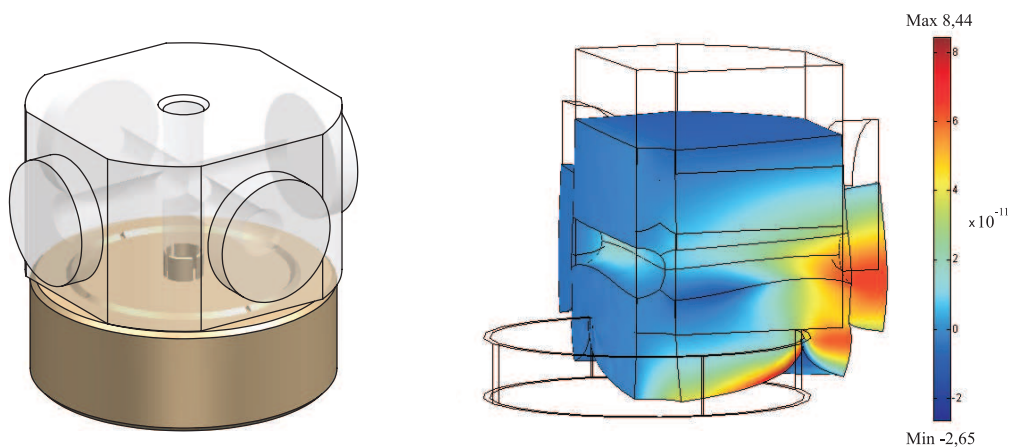

Figure F.2: *Resonator mounting on a titanium disk. To the right, the result of a finite element analysis of the static resonator deformation is illustrated graphically (largely exaggerated for display). The titanium ring diameter has been chosen to yield minimum deformation along the optical axis.*

by the ion pump is estimated to contribute $< 10\mu$W at the final pressure of $< 10^{-10}$ mbar.

The outer vacuum chamber is made from stainless steel and will be pumped by an ion pump to a background pressure of $< 10^{-6}$ mbar, which is sufficient to prevent heat transport between thermal shields by convection.

Preparation of the system for UHV will involve "baking out" the IVC and activation of the getter pump at $> 1000°$C. During this process, the resonators might be heated up to $> 300°$C, which they should endure without damage, provided that the ramping of the temperature is done slowly (~ 100 K/h). After rough-pumping the chamber the ion pump can be activated and the IVC can be enclosed inside the thermal shields and the outer vacuum chamber. The thermal time constant of the complete setup under vacuum has been calculated to be about one month. Thus, after assembly and before pumping, it will be thermalized introducing helium into the outer chamber as a contact gas.

Optical access from outside is provided through windows on four sides of each shield. Furthermore, several electrical feedthroughs allow to read out electrical signals, necessary for the active temperature stabilization. These feedthroughs also enable detection of the light, reflected or transmitted by the cavities, inside the chamber. This is considered necessary, in order to minimize possible beam pointing instabilities.

Finally, the chamber also offers the possibility to send the light in via an optical fiber, and to place most parts of the optics inside the outer vacuum chamber. This might help to substantially reduce systematic effects caused by temperature variations and parasitic etalons.

F. A new vacuum chamber

Acknowledgements

During my work on this thesis I could rely on the support and assistance of numerous people. I know that I am very much indebted to them and thus want to state my "thank you" to each of them.

Many thanks I owe to Achim Peters, who as my supervisor contributed a great deal of ideas and did not refrain from eventually putting hands on the experiment as well. His experience and insight into the technical details guided the course of this work. Without his steady trust in the experiment's success even in times, when future prospects appeared uncertain, the experiment would never have been possible.

Much of the work done here could build upon the excellent basis that had been laid by Holger Müller during his time as a PhD student at the Michelson-Morley experiment. Not only as a great expert on this topic but also as a good friend he was always willing to give his advice, which was required more than once. His effective help saved me from desperation more than once and I owe him many thanks for that.

During his time as a diploma student, Alexander Senger contributed a great deal to the experiment's progress. There could have been no better person to join the experiment, and up to now it benefits from his many contributions. His commitment to the design of the new vacuum chamber is highly appreciated.

The first results from the advanced new setup finally could never have been acquired in time without the help of Katharina Möhle and Roberto Vannucchi, who I am thus very much indebted to. I am sure they will make their way with the ongoing experiment and I wish them all the best for that.

To have an experienced and patient colleague as Evgeny Kovalchuk working next door is a benefit that I will certainly miss. He was always willing to have a closer look at the current problems and with him examining the setup I could be sure that no sloppiness is overlooked.

Thilo Schuldt and Matthias Scholz accompanied me throughout all the time since we moved here from Konstanz together. From time to time they saved me from getting stuck in the lab or mad with the work and I owe my

warmest thanks to them for that. Also, Thilo was so nice as to tolerate me having borrowed half his equipment at some time without any complain.

More than once Dipl. Ing. Klaus Palis was the man to address to, for all kinds of support required. His good connections to the Berlin locals helped to clear the way and organize help where non-Berliners as myself faced some cultural barriers. Vielen Dank, Klaus!

Finally, I would like to thank the whole bunch of nice people of the QOM, Nano and AMO groups I met during my time at the Hausvogteiplatz. The relaxed and harmonic atmosphere that they created there, I consider something really special, which I am sure that such is not encountered frequently in other working places.

At the Paul Drude Institute I was a frequent guest in search for whatever equipment I could borrow. There are few things left which I did not ask them for and I am very much indebted to their patience and willingness to help me out.

Many thanks also to Prof. Gerhard Ertl from the Fritz Haber Institute who supported us during the early phase of the experiment.

Throughout all my studies my parents gave me their unconditional support, which I am very much indebted for to them. And finally beyond all, it was Simone's support, encouragement and patience that helped me going on all the time. My gratitude to her is beyond words here.

Selbständigkeitserklärung

Hiermit erkläre ich, die vorliegende Arbeit selbständig ohne fremde Hilfe verfasst und nur die angegebene Literatur und Hilfsmittel verwendet zu haben.

Ich habe mich anderwärts nicht um einen Doktorgrad beworben und besitze einen entsprechenden Doktorgrad nicht.

Ich erkläre die Kenntnisnahme der dem Verfahren zugrunde liegenden Promotionsordnung der Mathematisch-Naturwissenschaftlichen Fakultät I der Humboldt-Universität zu Berlin.

Berlin, den 24. Oktober 2006

Sven Herrmann